Fluidized bed membrane reactors for water gas shift

Fluidized bed membrane reactors for water gas shift

Mass transfer, hydrodynamics and experimental demonstration

Cover design concept: Arash Helmi
Cover artwork: isontwerp.nl – Eindhoven

ISBN: 978-90-386-4243-7

Fluidized bed membrane reactors for water gas shift

Mass transfer, hydrodynamics and experimental demonstration

PROEFSCHRIFT

ter verkrijging van de graad van doctor aan de Technische Universiteit Eindhoven,
op gezag van de rector magnificus prof.dr.ir. F.P.T. Baaijens,
voor een commissie aangewezen door het College voor Promoties,
in het openbaar te verdedigen op
maandag 27 maart 2017 om 16:00 uur

door

Arash Helmi Siasi Farimani
geboren te Mashhad, Iran

Dit proefschrift is goedgekeurd door de promotoren en de samenstelling van de promotiecommissie is als volgt:

Voorzitter:	prof.dr.ir. R. Tuinier
1e promotor:	prof.dr.ir. M. van Sint Annaland
Copromotor(en):	dr. F. Gallucci
Leden:	prof.dr. J. Herguido (Universidad de Zaragoza)
	prof.dr.ir. J.R. van Ommen (TUD)
	prof.dr. V. Hessel
	prof.dr.ir. D.M.J. Smeulders
	Ing. G. Barbieri PhD (ITM-CNR)

Het onderzoek of ontwerp dat in dit proefschrift wordt beschreven is uitgevoerd in overeenstemming met de TU/e Gedragscode Wetenschapsbeoefening.

It was about a passion.

Dedicated to my beloved parents and family.

One day small snowflakes were falling on the ground.

One said "how nice we are flying!"

The other said "no we are not flying, we are just falling"

Then the other said, "we are going to die and disappear"

The other said, "no we will melt and we will go to the sea. We will live forever"

Another one said, "no people will walk on us"

In the end the snowflakes reached the ground and each of them, lived as they chose to live.

Summary

Fluidized bed membrane reactors for water gas shift

Water Gas Shift (WGS) is a widely used reaction for hydrogen production and synthesis gas upgrading. The conventional two-stage WGS process consists of a first reactor operated at high temperature to exploit faster kinetics and a second reactor that works at lower temperatures to take advantage of higher equilibrium conversions, followed by a separation step such as PSA. Pd-based membrane reactors are able to couple the WGS reaction and hydrogen separation and purification in one single unit and thus strongly intensify the process. The aim of this research is a detailed study of the reactor performance of fluidized bed membrane reactors using numerical studies and an experimental proof-of-principle of the concept for small-scale applications (viz. low-temperature PEM fuel cells).

The membrane reactor has been successfully demonstrated at lab-scale. The demonstration included the development and characterization of the membranes and the catalyst and subsequent integration of both inside the membrane reactor. A very stable performance of the fluidized bed membrane reactor with a capacity of 1 Nm^3/h of H_2 production was obtained over 900 hours of continuous work in the bubbling fluidization regime and at high temperature WGS conditions. A CO impurity of less than 10 ppm was achieved at the permeate side of the membranes. The produced ultra-pure H_2 can be directly fed to a highly efficient low-temperature fuel cell.

A Two-Fluid Model (TFM) was used to quantify the extent of concentration polarization and to visualize the concentration profiles near the membranes. The concentration profiles were simplified to a mass transfer boundary layer, which was implemented in a one-dimensional (1D) fluidized bed membrane reactor model to account for the concentration polarization effects.

Advanced non-invasive experimental techniques have been used to investigate the hydrodynamics inside fluidized bed membrane reactors in detail, using particle image velocimetry (PIV), digital image analysis (DIA) and 3D X-ray analysis. First, the hydrodynamics of the reactor was studied in a pseudo-2D geometry with the help of an endoscopic PIV/DIA technique and at room temperature. The study included the characterization of bubble and emulsion phases properties at the absence and at the presence of membranes module. Subsequently, the research was further extended in a real 3D geometry utilizing a high resolution X-ray analysis technique (in collaboration with TU Delft), quantifying the average bubble and emulsion phases properties for different particle types, inlet velocities and number of membranes inside the fluidized bed. In addition, the solids hold up in the close vicinity of the membranes were monitored at different gas extraction values through the membranes to characterize the nature and thickness of the so-called densified zones formed near the membranes. Results from these studies allow us to derive improved models to accurately describe and optimize

the performance of fluidized bed membrane reactors exploiting highly permeable membranes immersed in the catalytic bed.

The research leading to these results has received funding from the European Union Seventh Framework Programme (FP7/2007-2013) under grant agreement n° NMP3-LA-2011-262840 (DEMCAMER project)

Contents

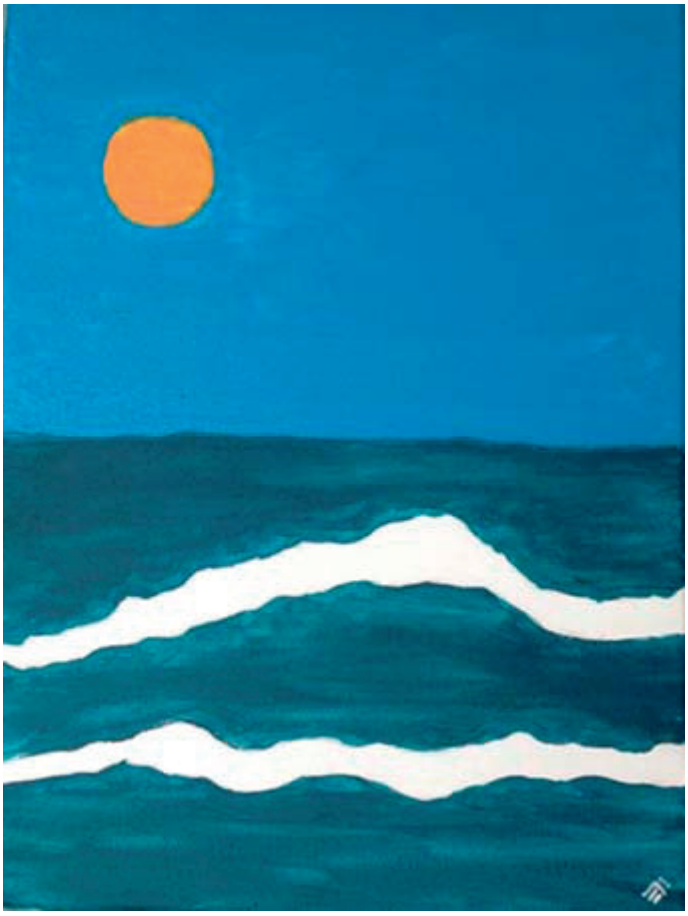

The novel ends when the ‘’story” begins, when the consequences of your actions start manifesting themselves.

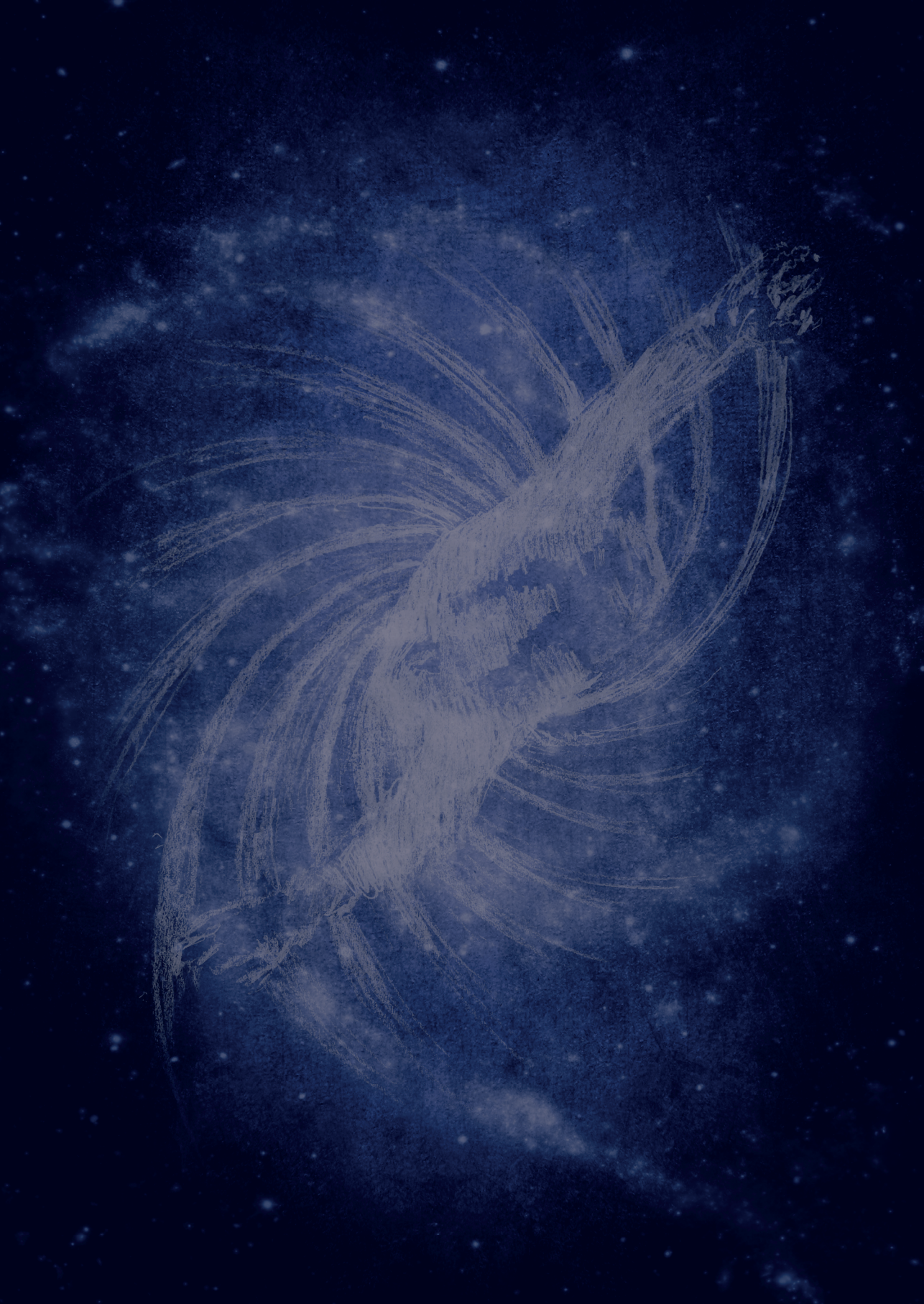

Chapter 1

General Introduction

1.1. Hydrogen as future energy career

Today's world population is constantly growing and the climate is radically changing all over the planet. It is estimated that the global population will reach between 8.3 and 10.9 billion people by 2050 [1,2], leading to a significant further increase in the demand for energy and food. Based on a report from the International Energy Agency, the worldwide demand for energy will increase at least 48% by the year 2040 (in comparison with 2012) [3], while the fuel share will remain in favor of fossil based fuels in comparison with other primary energy sources (viz. wind, geothermal, solar, biomass and nuclear) [4].

A great part of this energy demand is required for large scale industrial processes. Strikingly, between 20-50% of the energy usage in these industrial processes is lost in the form of exhaust gases, cooling water and other sources of heat loss [5]. In a global market with scarce conventional primary fossil-based energy sources, innovation of the chemical and process industries seems of the utmost importance to minimize the process energy requirements and diversify toward more versatile (e.g. bio-based) feedstocks.

Currently, numerous research investigations have been carried out on the potentials of different fuels, such as compressed natural gas, methanol, ethanol, synthetic natural gas liquids like Fischer-Tropsch liquids, and hydrogen, to replace fossil-based fuels. Among all, hydrogen attracted considerable attention owing to two major widely ackowledged features: firstly, it can be produced from many different primary energy resouces (viz. natural gas, biomass, wind, nuclear, geothermal, and waste) and secondly it can be fed to fuel cells and internal combustion engines with very high energy efficiencies and near zero greenhouse gas emissions [6].

Today, over 80% of the hydrogen used in industry is produced via the conventional catalytic conversion of fossil based fuels, mainly natural gas, using a series of high-temperature reactions, in particular: steam reforming of methane followed by a two-step water-gas-shift. This process is optimised to produce large amounts of hydrogen (more than 100 000 Nm^3/h) in centralized locations to be used in the production of many different chemicals (e.g. ammonia) in an energy-efficient process, but with a large carbon footprint.

To supply the produced H_2 to customers at other locations, the produced gas needs to be compressed and transported. Both compression and transporation are highly energy intensive processes. In this way two-third of the energy will be lost during the compression and transportation steps. Moreover, for many industrial sectors (fertilizer industry, food processing, glass manufacturing, etc.) a volumetric flow rate of 5-250 Nm^3/h of H_2 with a pressure of less than 10 bar is sufficient and large scale production of H_2 is not required [7]. The efficiency of the large scale conventional H_2 production processes is approximately 80% (equivalent hydrogen efficiency) and downscaling of such process is not economically viable [8]. Thus, for efficient production of H_2 at smaller scales, novel process methodologies need to be further developed.

1.2 Chemical process intensification

In 1995, owing to the pioneering work of Ramshaw, a new revolutionary concept was introduced to the chemical (engineering) society as ‘’Process Intensification (PI)’’. PI was originally defined as any strategy which will result in a dramatic reduction in the size of chemical plant keeping the production capacity at the same level. PI was later redefined as any attempt that results in an inherently smaller, cleaner and more energy efficient technology leading to a tremendous decrease in the process energy requirements [9].

The concept of PI has generated a considerable research interest within the last years due to its very high potential impact on the chemical market. It is widely believed that PI can be successfully applied to transform the current chemical industry to a more sustainable chemical process industry for the future. In a report by the European Technology platform for sustainable chemistry, PI is considered as one of the main strategic research areas forming the orientation of the future of chemical industry [5,10]. Figure 1.1 shows how PI can be introduced in the chemical industry, either by equipment-intensified processes or by novel process methodologies such as process integration in multifunctional reactors. Among different multifunctional reactor concepts, membrane reactor technology intends to overcome the limitations of the conventional H_2 production process providing high process efficiencies for on-site production of H_2 at small production volumes.

1.2. Membrane reactor technology

A membrane reactor is a device that can integrate reaction and separation steps in one single unit operation, thereby achieving a high degree of process intensification via a large reduction in the number of chemical process steps. Especially in case of thermodynamically limited chemical reactions (e.g. water gas shift), the reaction equilibrium can be shifted towards the products’ side by selective removal of one of the products from the reaction zone using the membranes (Le Châtelier’s principle). Therefore, a similar reactor capacity can be achieved in a smaller unit operating at milder conditions (e.g. lower operating temperatures) leading to significant improvements in the energy efficiency of the process.

Different membrane reactor configurations have been proposed in the literature. The simplest and the most studied configuration is the packed bed membrane reactor. Figure 1.2 shows a schematic representation of a packed bed membrane reactor, where catalyst particles are confined inside the membrane tube. When integrating highly permeable membranes in packed bed reactors the mass transfer limitations from the catalytic bed to the surface of the membrane (referred to as concentration polarization) can seriously hamper the overall performance of the reactor [11].

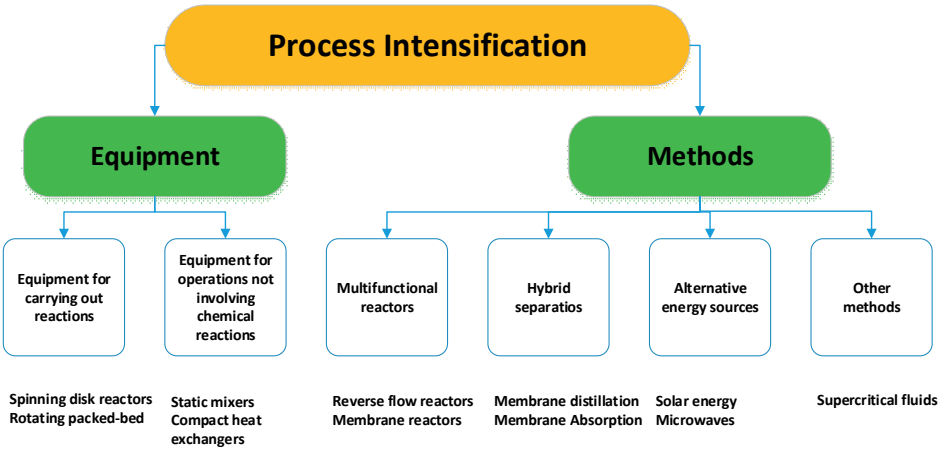

Figure 1.1 Process intensification components [9]

To circumvent these mass transfer limitations, more recently fluidized bed membrane reactors have been introduced with improved mass and heat transfer characteristics. Figure 1.3 shows the fluidized bed membrane reactor concept for the production of H_2 via water-gas-shift (WGS) using vertically immersed H_2 selective (palladium based) membranes.

In a bubbling fluidized bed an excellent gas-solid contact can be achieved due to the mixing of the particles (called emulsion phase) induced by the chaotic motion of the gas bubbles. The outstanding heat transfer rate in fluidized beds allows a virtually isothermal operation, reducing the possibility of hot spot formation to a large extent, contrary to packed bed membrane reactor configurations.

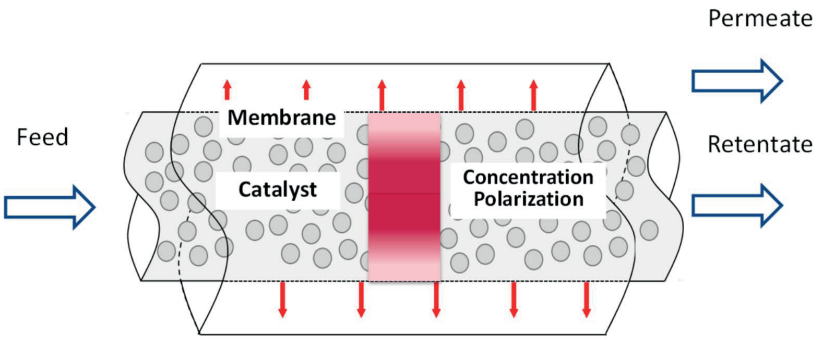

Figure 1.2 Packed bed membrane reactor concept

In addition, the pressure drop over the bed is very small due to the much smaller particle size compared to packed beds [12]. However, axial gas back-mixing and bubble-to-emulsion mass transfer limitations may adversely affect the performance of fluidized bed membrane reactors.

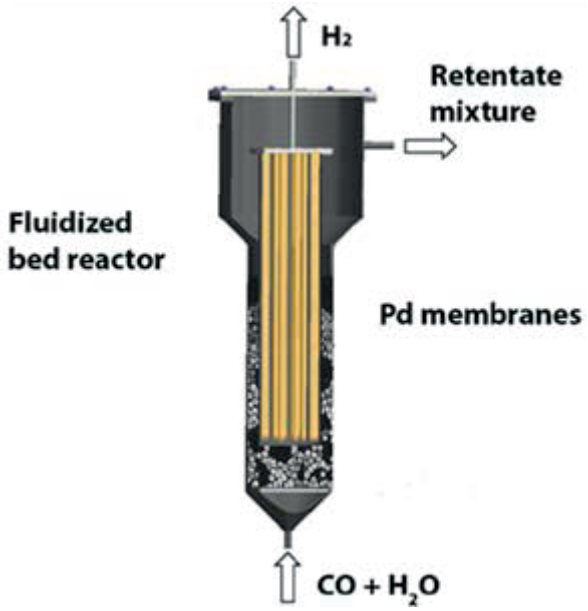

Figure 1.3 Fluidized bed membrane reactor concept with immersed vertical H_2 selective (palladium-based) membranes for intensified water-gas-shift (WGS)

Recently, the application of fluidized bed membrane reactors have been exploited as promising options for small-scale H_2 prodcution [7]. This can be achieved by integration of H_2 selective membranes inside a fluidizing bed of catalyst particles. Among the membranes for selective separation of H_2, Pd-based membranes show the highest permeability and exclusive selectivity for H_2 due to their unique permeation mechanism. Therefore, H_2 with very high purity directly suitable for micro-CHP units and PEM fuel cell applications can be effectively prodcued in small scales.

In addition, membrane technology can be applied for distributed production of highly pure H_2 suitable for many other sectors in industry circumventing enormous energy loss attributed to transportation from large scale H_2 prodcution units. Despite the very promising advantages that Pd-based fluidized membrane reactors can bring for the production of ultra-pure H_2, there are not many successful examples of full commercial-scale demonstration of such units in industry [13,14]. For full commercial exploitation of these units, there are still many technical challenges that need to be overcome.

1.4. Current challenges

Within the last few decades, the application of Pd-based membranes for the separation of H_2 have been widely investigated with special attention on the development of membranes with high mechanical, thermal and chemical stabilities [15]. Also due to the very high cost of Pd, more effort has been devoted to the development of thin and defect-free membranes with improved H_2 flux and durability suitable for membrane reactor applications [16].

In addition, due to a drastic reduction in reactor sizing, catalyst particles with improved activity, durability and cost effectiveness need to be developed, that can perform well at new operating conditions opened up by the integration of the membranes in the reactor. Once the catalyst and membrane(s) are developed, the compatibility between membranes and catalysts needs to be investigated at relevant operating conditions.

On the engineering part, the reactor design models heavily depend on closure equations that were originally derived for standard fluidized bed reactors. Despite many studies (both modeling and experimental) that have been conducted to investigate the prevailing phenomena inside these reactors, the influence of membranes on the heat and mass transfer characteristics of such reactor units is not fully explored yet. It is predicted that the presence of membranes with different configurations and permeation rates can strongly influence the hydrodynamics of this type of reactors as well. More research is needed to accurately describe and optimize the performance of fluidized bed membrane reactors exploiting highly permeable membranes immersed in the catalytic bed.

1.5 Outline of this thesis

This thesis focuses on the integration of Pd-based membranes for the production of ultra-pure hydrogen via water-gas-shift using a fluidized bed reactor unit. To fill the gap in literature, many aspects of such reactor unit (on the material level and engineering side) will be addressed and a better understanding on the prevailing phenomena inside the reactor will be obtained.

Chapter 2 focuses on the availability of Pd in the large quantities required for large scale applications and its potential impact on the global market. We will show that large-scale application of Pd-based membranes seems to be unfeasible and research on Pd-based membrane reactors should focus on small(er) scale applications (e.g. low temperature PEM-fuel cell applications).

Chapter 3 presents the development, characterization and stability tests of thin film Pd-based membranes for fluidized bed membrane reactor applications. We measure the performance of the membranes for single gas permeation, and afterwards for mixtures of gases and under fluidization conditions for various prepared thin-film membranes.

Chapter 4 focuses on the quantification of the extent of concentration polarization in fluidized bed membrane reactors. A simple one-dimensional (1D) phenomenological model is developed which can adequately capture the effect of concentration polarization in fluidized bed membrane reactors. A more sophisticated model (Two-Fluid Model) is used to estimate the mass transfer boundary layer thickness required for the 1D model. The predictions by both models are compared with results obtained from experiments showing good agreement, confirming that indeed concentration polarization can also prevail in fluidized bed membrane reactors with highly permeable membranes.

In **Chapter 5** the hydrodynamics of a fluidized bed reactor will be investigated in the presence of vertically immersed porous membranes in a real 3D reactor geometry using a fast X-ray analysis technique. With the help of this technique the hydrodynamics of the fluidized bed membrane reactor is monitored with very high spatial and temporal resolution enabling us to characterize the time-averaged gas and solids behavior at the presence of membrane reactor modules with different membranes configurations, particle sizes and gas permeation rates through the membranes.

Chapter 6 aims to extend the application of a coupled Particle Image Velocimetry/Digital Image Analysis (PIV/DIA) technique to dense bubbling gas-solid fluidized beds with vertically immersed tubular membranes in different module configurations. The solids flux and hold-up profiles and bubble phase properties, viz. equivalent bubble diameter and bubble rise velocity, will be described and discussed accordingly. Conclusions are drawn based on the obtained results and recommendations for the design of such reactor units is given.

Finally, in **Chapter 7** a demonstration unit with a capacity of 1 Nm^3/h of ultra-pure H_2 is designed, built and successfully operated over 900 h of continuous work under high temperature water-gas-shift operating conditions. The obtained results showed high hydrogen recovery factors, and very low CO concentrations at the permeate side (in average <10 ppm), so that the produced hydrogen can be directly fed to a low temperature PEM fuel cell.

Bibliography

[1] United Nations, World population prospects, (2015). https://esa.un.org/unpd/wpp/ (accessed October 16, 2016).

[2] United Nations, Department of Economic and Social Affairs, (2015). http://www.un.org/en/development/desa/news/population/2015-report.html (accessed December 16, 2016).

[3] U.S. Energy Information Administration, World energy demand and economic outlook, (2016). https://www.eia.gov/outlooks/ieo/world.cfm.

[4] The International Energy Agency IEA, Key World Energy Statistics 2012, Paris, 2012. http://www.iea.org/publications/freepublications/publication/kwes.pdf.

[5] P. Tello, R. Weerdmeester, Sustainable Process Industry through Resource and Energy Efficiency, 2013. www.spire2030.eu.

[6] J. Ogden, Hydrogen as an Energy Carrier: Outlook for 2010, 2030 and 2050, in: 10-50 Solut. Technol. Policies a lLow-Carbon Futur., The Pew center on Global Climate Change, and the National Commission on Energy Policy, University of California Davis, 2004.

[7] DEMCAMER, Design and manufacturing of catalitic membranes reactors by developing new nano-architectured catalytic and selective membrane materials, http://demcamer.org/ (accessed August 8, 2016).

[8] V. Spallina, D. Pandolfo, A. Battistella, M.C. Romano, M. van Sint Annaland, F. Gallucci, Techno-economic assessment of membrane assisted fluidized bed reactors for pure H_2 production with CO_2 capture, Energy Convers. Manag. 120 (2016) 257–273. doi:10.1016/j.enconman.2016.04.073.

[9] A.I. Stankiewicz, J.A. Moulijn, Process intensification: Transforming chemical engineering, Chem. Eng. Prog. 96 (2000) 22–33. doi:10.1002/btpr.305.

[10] SusChem stakeholders, SusChem: Strategic Innovation and Research Agenda, Brussels, 2015. http://www.suschem.org/cust/documentrequest.aspx?DocID=928.

[11] F. Gallucci, M. van Sint Annaland, J. A. M. Kuipers, Theoretical comparison of packed bed and fluidized bed membrane reactors for methane reforming, Int. J. Hydrogen Energy. 35 (2010) 7142–7150. doi:10.1016/j.ijhydene.2010.02.050.

[12] S. A. R.K. Deshmukh, S. Heinrich, L. Mörl, M. van Sint Annaland, J. A. M. Kuipers, Membrane assisted fluidized bed reactors: Potentials and hurdles, Chem. Eng. Sci. 62 (2007) 416–436. doi:10.1016/j.ces.2006.08.062.

[13] TOKYO GAS, http://www.tokyo-gas.co.jp/index_e.html (accessed October 9, 2016).

[14] MRT TECHNOLOGY, http://www.membranereactor.com/ (accessed October 9, 2016).

[15] F. Gallucci, E. Fernandez, P. Corengia, M. van Sint Annaland, Recent advances on membranes and membrane reactors for hydrogen production, Chem. Eng. Sci. 92 (2013) 40–66. doi:10.1016/j.ces.2013.01.008.

[16] H. Li, A. Caravella, H.Y. Xu, Recent progress in Pd-based composite membranes, J. Mater. Chem. A. 4 (2016) 14069–14094. doi:10.1039/c6ta05380g.

“Regard heaven as your father, Earth as your mother and all that lives as your brother and sister.”

- Native American proverb

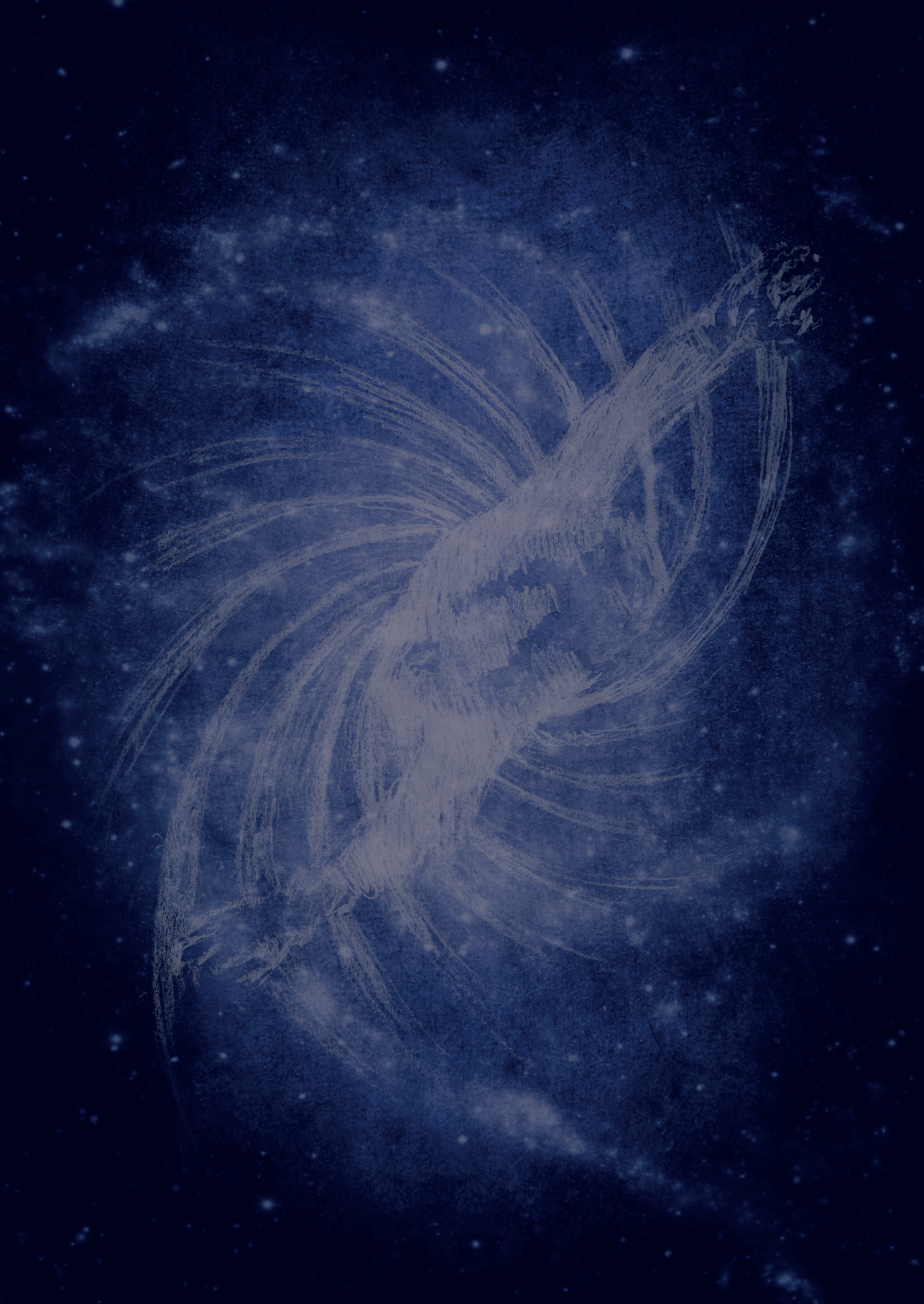

Chapter 2

Resource scarcity in palladium membrane applications for carbon capture in integrated gasification combined cycle units

Abstract

Recently, many reviews on pre-combustion CO_2 capture (CCS) in an IGCC plant have been focused on the techno-economic performance of palladium-based membrane reactor modules downstream of conventional steam reforming or shift reactors. Although the determination and minimisation of the amount of palladium necessary for a specific power production capacity has been the target of many research studies, surprisingly little attention has been paid in the open literature to the availability of this metal in the large quantities required for large scale applications. To fill this gap, the scope of this work was to compare the amount of palladium needed for pre combustion CCS with Pd-membranes and the available production capacity of palladium. Two specific techno-economic studies with a different net IGCC power output were selected from the literature. In each case, the amount of palladium that is necessary for the plant to be in operation was compared with the world supply and demand for palladium. The results show that even for a power plant of "only" 1 GWe net electricity production utilizing membranes with the best reported performance, a relatively large (~ 0.7%) amount of palladium is required compared to the total world supply. Considering the total worldwide electricity production from fossil fuels (14455 TWh in 2010) a tremendous increase in the world supply of Palladium would be required to redirect from the traditional IGCC power plants without CO_2 capture units to the new membrane technology. We conclude that large scale pre-combustion capture of CO_2 using palladium membranes seems to be unfeasible and research on Pd-based membrane reactors should focus on small(er) scale applications.

2.1. Introduction

Today's world population is rapidly growing and the climate is radically changing all over the planet. It is expected that the energy demand will strongly increase in the near future, while energy conversion will still heavily rely on combustion of fossil fuels. The worldwide electricity production from fuels shows a fast increase within last few decades. Key world energy statistics show an increase from 6115 TWh electricity production in 1973 to a value of 21431 TWh in 2010 (see Figure 2.1) [1]. The outlook for energy demand confirms that the demand for energy will grow at least until 2035, while fuel shares will remain unchanged in great favour to fossil fuels [2].

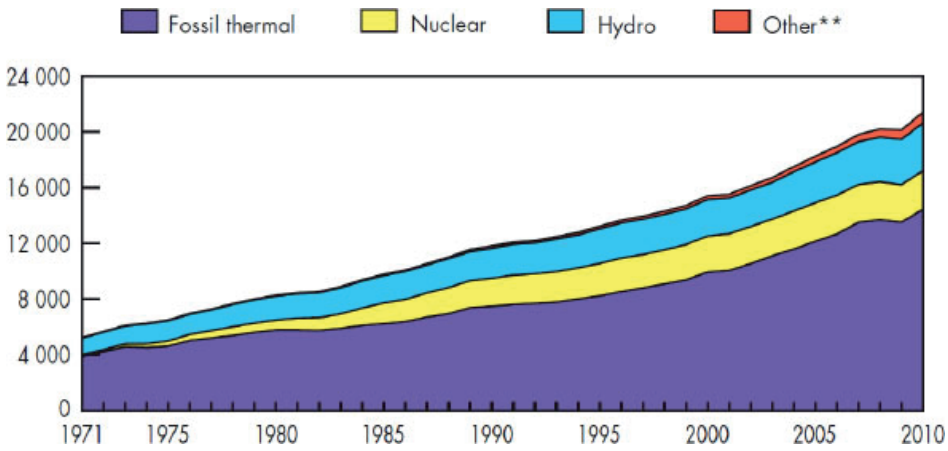

Figure 2.1 world electricity generation by fuel from 1973 till 2010 (TWh)[1]. ** Other includes solar, wind, geothermal and wave.

The combustion of fossil fuels for power production results in large amounts of anthropogenic carbon dioxide (CO_2) emissions. In 2010 more than 30 billion tonnes of CO_2 were released to the atmosphere from fuel combustion only (CO_2 emissions due to industrial waste and non-renewable municipal waste is not included) which is believed to contribute to the undesired global warming effect (recent global climate assessments show a rise of up to 2 °C in the average global temperature) [1]. In addition, CO_2 emissions also contribute to urban smog, acid rain and health problems [3]. Clearly, there is an inevitable need to strongly decrease the amount of anthropogenic CO_2 emissions to the atmosphere, in a relatively short period [4,5].

The growing concern regarding the effect of CO_2 on global climate change underlies several proposals to mitigate CO_2 emissions to the atmosphere. One concept is to capture released CO_2 from large source points and store it at large geological formations such as depleted oil and natural gas reservoirs, a process called as carbon capture and sequestration (CCS).

The Intergovernmental Panel on Climate Change (IPCC) report [4], summarizes the large points of concentrated stationary sources for CO_2 originating from fossil with a production

of more than 1 Mt CO_2/year (see Table 2.1). It can be concluded from the IPCC report that the main effort should be dedicated to capturing CO_2 from fossil fuel driven power plants which have the highest percentage contribution (78.8%) to the total global (concentrated) CO_2 emissions (Table 2.1).

Table 2.1 Distribution of worldwide large stationary CO_2 sources originating from fossil fuel [4].

Process/Industry	Emissions (Mt CO_2/yr)	% on the total
Power production	10539	78.8
Cement production	932	7.0
Refineries	798	6.0
Iron and steel industry	646	4.8
Petrochemical industry	379	2.8
Oil and gas processing	50	0.4
Other sources	33	0.2

A great research effort is being made on CCS that shows that this method seems to be a good mid-term solution to mitigate the amount of CO_2 in the atmosphere while non-fossil based options for energy production (renewable resources and nuclear fusion) are under development [6]. Despite the good promises, there still exist several challenges in the road of CCS commercialization that should be overcome in the short-term. The first challenge in the CCS process is how to capture the released CO_2 from the power plants. Carbon capture is capital (and energy) intensive and it often accounts for about 75% of the overall CCS cost [7].

Different processes have been introduced for CO_2 capture and several more are under investigation to be applied. A number of new carbon capture processes have been described recently. Li et al. found a number of 1297 patents on CO_2 capture solid sorbents, solvents, or membranes filed between 1836 to 2013 (over 80 countries) [3]. The proposed CO_2 removal processes can be divided into three main categories: solvent, sorbent and membrane based technologies. Among these processes, inorganic membranes seem to be a good candidate at high temperatures for H_2 or CO_2 separation [8][9]. In fact, (high temperature) CO_2 membranes are still further away from industrial application than H_2 (palladium based) membranes [10–13].

For several decades, palladium based membranes have been available but they seemed to be very expensive for large scale application in power plants. This is due to the substantial high thickness of the membranes that is required to achieve structural stability (and perm-selectivity) at reaction conditions. Recent years have seen the development of inorganic membranes of (supported) palladium or palladium alloys with much smaller thicknesses with high permeability and selectivity and with good reliability up to a temperature of 400-420 °C, in the presence of reformate gas mixtures [14]. For this reason the current studies have been directed to evaluating membrane system solutions for CO_2 capture in power plants. In

particular, several collaborative European research projects have been co-financed by the European Commission to determine the detailed technical and operational characteristics of such a carbon capture strategy to be integrated in IGCC power plants.

Many reviews on membrane-based CO_2 capture technologies have been published during last few years [5,15–17]. In all these studies, the main focus has been paid on the techno-economic performance of a Palladium-based membrane (reactor) module downstream of conventional shift/reforming reactor, in an IGCC plant with pre-combustion capture of CO_2. Although the amount of palladium which is necessary for a specific power production has been the focus of many research studies, surprisingly very little attention has been paid to the availability of palladium in the large quantities required. To fill this gap in the literature research, the scope of this work was to compare the amount of palladium needed for pre-combustion CCS and the available production capacity of palladium.

In particular, three specific techno-economic studies with a different net IGCC power output were selected from the literature. For each case, the amount of palladium that is necessary for a plant to be in operation will be compared with the world supply and demand for palladium. Subsequently, the worldwide supply and demand of palladium and the feasibility of converting to a palladium based CO_2 capture membrane technology in an IGCC plant will be discussed. In addition, the current status of the palladium market and the future outlook for palladium prices for the coming years will be highlighted.

2.1.1 Review on carbon capture and storage (CCS) technology

Several CCS strategies have been proposed within last few years [5,15,18,19] where the choice between these proposals depends on different power generation technologies. Pulverized coal-fired (PC), natural gas combined cycle (NGCC) and integrated gasification combined cycle (IGCC) are the main existing and advanced technologies for electricity production from fossil fuels. Due to the sharp increase in oil and natural gas prices in the last couple of years the use of coal for electricity production (IGCC) is still seen as a main player in the future market. In fact, coal is available across the globe in large amounts which are secured for centuries. Moreover, it is distributed more homogeneously than oil and gas in the world [10]. Many believe that IGCC will become the key route for electricity production in the future [15].

An IGCC mainly consists of a gasification unit (well-known technology such as in E-gas, Prenflo, Shell, Texaco and GE gasifiers) where the solid or liquid fuel such as oil residuals or biomass is gasified to produce the so called synthesis gas (mainly hydrogen and carbon monoxide). In the next step, the produced synthesis gas is directed to a cleaning unit for Sulphur and particulate matter removal. IGCC is more efficient than PC; however its relatively high implementation cost, (which regarded as the main bottleneck for commercialization of this technology), the lower availability and less operational flexibility are some of the disadvantages of an IGCC unit, while the main drawback with this technology is the large amount of CO_2 emissions into the atmosphere [16]. Therefore, the integrated IGCC unit with CCS

technology would be a striking solution to secure electricity production with stabilized CO_2 concentration in the atmosphere. In principle CO_2 removal from an IGCC plant can be done utilizing three main strategies: a) post-combustion capture, b) Oxy-fuel combustion and c) pre-combustion capture.

(A) Post-combustion capture

The principle is to remove CO_2 from flue gas after the combustion process. The separation process is carried out at low temperature and pressure where the CO_2 concentration is typically low. The partial pressure of CO_2 is typically less than 0.15 atm, which makes the post-combustion capture process relatively costly. In spite of this fact, post-combustion is relatively mature and can be simply retrofitted in existing power plants as a downstream process, so it can be considered as an option with great potential for near term CO_2 capture [7] and is the technology to be outperformed by new capture technologies.

(B) Oxy-fuel combustion

In this strategy, pure oxygen atmosphere is used to combust the fuel for energy production. CO_2 and /or steam is recycled in the process, and as a result, a CO_2 reach stream with steam can be obtained. In the final stage, CO_2 is separated from steam in a simple cooling stage. The high energy penalty associated with oxy-fuel combustion is due to the expensive cryogenic air separation unit.

(C) Pre-combustion capture (or fuel decarbonisation)

Typically, the synthesis gas produced by gasification of coal or biomass is followed by a water gas shift (WGS) process to improve the ratio of H_2/CO. Afterwards, the hydrogen reach stream is combusted in an adapted turbine for electricity and/or process heat production. In the pre-combustion scheme, CO_2 is captured from shifted synthesis gas at high pressures (can be up to 65 atm) in a physical or chemical scrubbing process [2,7]. CO_2 capture at elevated partial pressures can reduce the capture costs.

Each carbon capture strategy has its own positive and negative aspects, and there are various technical challenges associated with each capture strategy. The main advantages and disadvantages for each CO_2 capture technology are well summarized by the United States Department of Energy (DOE) [20]. There is as yet no existing viable CO_2 capture proposal, since emitting CO_2 into the atmosphere is at the moment much cheaper than any of the CO_2 capture technologies proposed. Integration of any of these strategies in an IGCC unit will decrease the thermal efficiency of the plant drastically in comparison with an IGCC plant without CO_2 capture unit. This is due to the fact that some part of the produced electricity should be utilized for carbon capture (mainly) and compression [20]. Also additional equipment is needed for the new process. Thus, there is a vital need for developing new and cost-efficient capture technologies to shift towards carbon neutral electricity production processes [7].

2.2. Approach

Pd-based membranes can be used for CO_2 capture both as high-temperature separators downstream the WGS reactors, or as integrated separation steps in the reactor (membrane reactors). As membrane reactors can integrate both reaction and separation steps in one single unit, their application results in a shift of the equilibrium and thus in an intensified process. This underlies the idea to integrate the membrane reactors for high temperature separation in IGCC plants. Therefore, power and H_2 production can occur simultaneously at moderately high temperatures, thus circumventing the equilibrium limitations (thus resulting in smaller reactor volumes and higher conversions).

Several case studies on the application of H_2 membranes for CO_2 capture in IGCC plants have been published in the literature focusing on different aspects [21–30]. Brunetti et al. [31] provided a review on the latest status of different membrane materials for CO_2 capture in power plants. Also, the advantages of membrane technology for CO_2 capture were evaluated using specific design parameters.

Lu et al. [32] reviewed the state-of-the-art of different inorganic membranes for H_2 purification, while Bredesen et al. [33] reviewed different high-temperature membranes for CO_2 capture in power generation plants and also discussed in detail the fabrication of these membranes and their application in power generation units. Peters et al. [34] have investigated the inhibition effect of CO and H_2S on the performance of several Pd and Pd-alloy membranes, reporting that in general only few ppm of CO can already deteriorate the membrane performance dramatically.

Ku et al. [35] presented three requirements in order to successfully integrate a membrane based CO_2 capture technology into IGCC power plants. The membrane selectivity and permeability were discussed, however without a discussion on the total membrane area required for a specific power production. The authors have also indicated that membrane technology should be able to recover 90% of the total shifted syngas in order to be competitive with conventional solvent-based CO_2 capture technologies.

Lee et al. [36] reported long term stability tests for (SS) 310S and 316L membrane modules. Results have shown the durability of the membrane performance over 1000 hr at 400 °C and under 40%CO_2/60%H_2. However, no information on the amount of membrane area that is required for a specific power production has been reported. Schiebahn et al. [37] have proposed an alternative process of a water gas shift membrane reactor (WGS-MR) for pre-combustion CO_2 capture in an IGCC plant with only 4.5 % efficiency penalty in comparison with an IGCC plant without CO_2 capture. No information on the real performance of a WGS-MR has been provided.

Gazzani et al. [38] have provided a detailed techno-economic assessment on the performance of Pd-based membranes for CO_2 capture in an IGCC plant. The selected design is the integration of several membrane modules between several high temperature water gas shift

reactors. Two different plant layouts have been investigated in this study. In the first layout the authors have assumed that all the produced H_2 is separated through the membrane and fed to the turbine. In this case the membrane module accounts for 25% of total investment at high efficiency penalties. In the second layout a portion of the H_2 is separated and the remaining is used to post-fire the heat recovery steam generator which results in large decrease in the required membrane area and consequently the costs of the membrane modules (which drops to 15% of the total investment). However, the authors have used a very conservative price for the Pd membrane modules as they did not include the effect of the enormous amount of Pd required for their plant on the actual Pd price (as will be discussed in subsequent sections of this paper).

Within an IGCC process, the gasifier unit is one of the key steps and to large extent it determines the performance of the whole power production process. With regard to commercially available technologies for the gasifier unit, two companies (Shell and GE) are leading the market. Among various techno-economic studies (that have already been discussed in the previous part), three promising cases - with Shell and GE gasifiers - were selected for further resource availability analysis.

Case 1

Koc et al., [39] presented an interesting work on the economic performance of a WGS membrane reactor integrated in an IGCC plant with a GE gasifier, where a two-dimensional model was used to study the characteristic performance of the shift membrane reactor integrated in an IGCC plant (IGCC-MR). In addition, a lab scale membrane reactor module was developed and the experimental results were used to validate the model predictions. The specific performance target levels for the shift membrane reactor were set at 98% CO conversion and 95% hydrogen recovery. Table 2.2 illustrates the specifications of the industrial scale membrane reactor for a net power output fixed at 550 MWe (The membrane used in this study will be indicated as Ma membrane) [39].

Case 2

Augello et al. [14] performed a techno-economic analysis of an IGCC plant utilizing a membrane reactor which operates at about 400 °C, downstream of a conventional shift reactor, for pre-combustion CO_2 capture using a Shell gasifier. Three different Pd-based membranes were used for the calculations.

Table *2.* summarizes the main characteristics of these membranes for an IGCC plant of 386 MWe net power production. In all cases (with different membranes), the authors used a one-dimensional (1D) mathematical model to calculate the necessary membrane area for a specific production capacity and membrane reactor performance analysis.

Case 3

Chiesa et al. [40] analysed the thermodynamic performance of an IGCC plant with H_2 selective Pd membrane for CO_2 capture and compared this configuration with solvent absorption for CO_2 removal. The calculation shows an increase of 1.7% in the efficiency of the process in comparison to the reference conventional CO_2 capture technology if 85% of the total inlet syngas is extracted as H_2. They also reported the membrane area that needs to be provided for the different cases. The permeation parameters for the membrane used in this study can also be found in Table 2.2 for two different cases reported by the authors. A plant with water gas shift membrane reactor followed by catalytic combustion as WGS-MR (CO) or a water gas shift membrane reactor followed by cryogenic capture as WGS-MR (CR).

Table 2.2 Membrane specifications for different case studies

Case	Membrane	Type	Permeance [(10^{-8} mol/ m^2.s.Pa)][a]	Thickness (µm)	Temperature (°c)	Driving force of H_2 (bar)[b]	Ref.
1	Ma	PdAu	181	6.8	400	10.13	[39]
2	HP1	Pd based	239	10	400	10	[14]
2	HP2	Pd based	334	10	400	10	[14]
2	HP3	Pd based	Lower than HP2	8	400	10	[14]
3	WGS-MR (CO)	Pd40Cu	23.8	20	450	~10	[41]
3	WGS-MR (CR)	Pd40Cu	23.8	20	450	~10	[41]

[a] Permeance values have been calculate for a H_2 partial pressure of 1 bar.
[b] The driving force of H_2 permeation at the inlet of the membrane reactor/separator module

The three selected cases will form the basis for our discussion and for the comparison of the resource feasibility of an IGCC-MR unit with best state-of-the-art membranes reported in the literature. Gallucci et al. presented a list of different palladium based membranes reported in the literature for H_2 separation with their main characteristics (permeation fluxes and perm-selectivity). Figure 2.2 shows a general overview of such membranes in terms of H_2/N_2 ideal selectivity vs. membrane permeability for hydrogen diffusion [42].

Among the listed membranes, the best membrane material in terms of hydrogen permeability is the one manufactured by Peters et al. [43] with acceptable long term stability performance at around 10 bar of pressure and temperatures up to 350 °C [44]. This membrane – hereafter indicated as SINTEF- was chosen as the state-of-the-art membrane material (with highest ever reported permeability and still very high selectivity) to be compared with selected case studies in terms of palladium requirement for a specific net power output. The SINTEF membrane thus corresponds to the lowest amount of palladium required for the different cases.

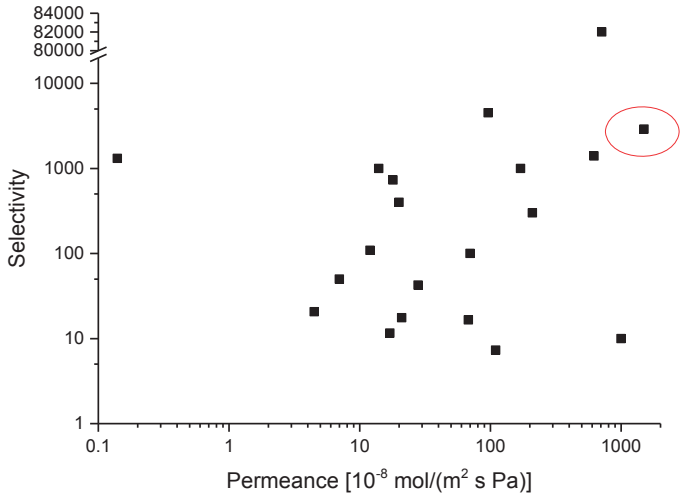

Figure 2.2 Permeance vs selectivity of different hydrogen separation membranes reported in literature [42]

2.3 Results and discussion

As discussed in the previous section, three different cases were selected (with GE and Shell gasifier) for further economical assessment and to investigate the amount of palladium that is needed for a specific MW of net electricity production. Figure 2.3 demonstrates results for an IGCC unit of 386 MWe utilizing HP1, HP2 and HP3 membranes [14] , 550 MWe utilizing Ma's membrane [44] and an IGCC unit of 422 and 367 MWe using different cases reported by Chiesa et al. as WGS-MR (CO) and WGS-MR (CR) respectively [40,45,46].

The results in Figure 2.3 suggest that an improvement in membrane permeability will result in a smooth decrease in the amount of palladium material needed for a specific net power output (HP1, HP2, HP3 and SINTEF), while this trend can be further accelerated by working at higher pressures, which is the case with the GE gasifier (Ma). Extrapolation of the results for 1 GWe electricity production shows a need of 9, 7.6, 7.37, 5.10, 4.82, 1.98 and 1.2 tonnes of palladium associated with WGS-MR (CR), WGS-MR(CO), HP1, HP2, HP3, Ma and SINTEF membranes, respectively (Figure 2.4).

Clearly the use of the state-of-the-art membrane represents a large decrease of palladium required for a 1 GWe power plant. It must be noted that the above results so far are only based on a comparison of what is already known in the literature. The various authors at this point proceed with economic evaluations based on the amount of palladium required and the actual price of palladium. However, the next comparison will show that this step (the actual cost of palladium) is arbitrary because nobody compared these numbers with the actual palladium available worldwide.

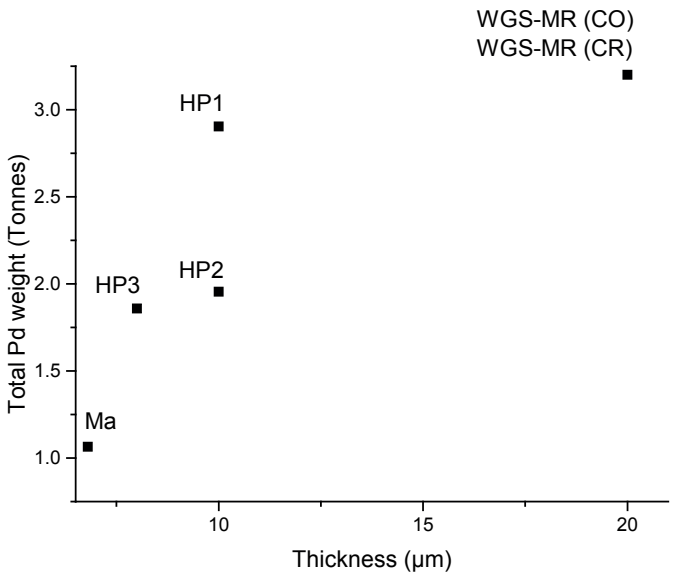

Figure 2.3 Tonnes of Palladium which is needed for specific amount of electricity production. HP1, HP2 , HP3: 386 MWe Ma: 550 MWe and 422 and 367 MWe using different cases reported by Chiesa et al. as WGS-MR (CO) and WGS-MR (CR) respectively

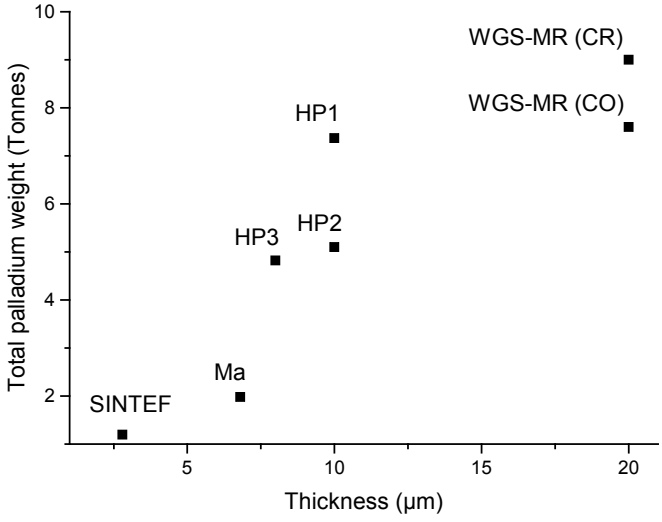

Figure 2.4 Tonnes of Pd that is needed for 1 GWe net power production

In fact, considering that the total world supply of Palladium in 2012 was 186 tonnes, it is obvious that even for a power plant of 1 GWe net electricity production utilizing the best possible membranes, still a relatively large amount of palladium (compared to the total available) is required. Furthermore, considering the total worldwide electricity production from fossil fuels (14455 TWh in 2012 [1]), a tremendous increase in the world supply of Palladium would be required to redirect to the new membrane technology from the previous traditional IGCC power plants without CO_2 capture units. For example, supposing that all the power production employed pre-combustion Pd-based membrane-based CO_2 capture units, the increase of palladium production would be as reported in the Figure 2.5. These numbers are only an indication, as it is clear that the total power production from fossil fuels is not only based on IGCC. For instance the use of NGCC (for natural gas) would require lower amount of membranes, but the implications of the data reported in the figure would not drastically change if all the exact amount of membranes were used for the various fossil fuels. These numbers are even more dramatic, if the reserves and use of palladium worldwide are considered in more detail, as discussed in the following sections.

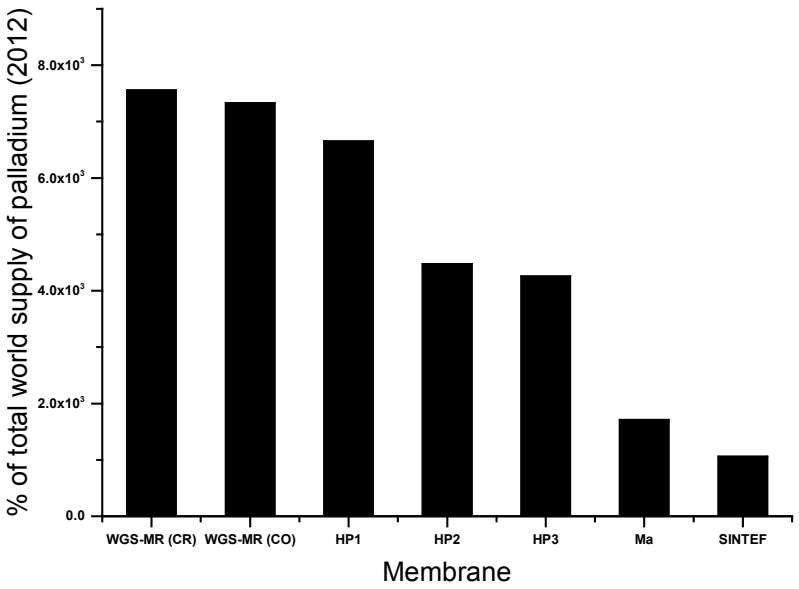

Figure 2.5 Percentage of increase in world total supply of Pd required to divert to the Pd-based membrane technology for pre-combustion CO_2 capture (worldwide production of electricity from fossil fuels: 14455 TWh in 2012 [1])

2.3.1 Palladium supply and demand

Since the 1970s, the demand for palladium has emerged in different industrial sectors (such as Electronics, Chemical, Fuel Cells, Oil Refining, Polyester, Water Treatment and Hydrogen Purification). Particularly the demand for Pd has increased in efforts to control emissions via

catalytic convertors of harmful automobile exhaust gases (hydrocarbons, carbon monoxide, and nitrogen oxide) to less harmful substances (nitrogen, carbon dioxide, and water vapor) [47,48]. The rare resources of palladium are located in few places on earth. More than 80% of world palladium production is concentrated in just two countries: the Russian Federation and South Africa [48] (see Figure 2.6).

Figure 2.6 (a) Palladium supply by region (total palladium supply in 2012:186 tonnes) (b) Palladium demand by sector (total palladium demand in 2012: 212 tonnes) [48] (reprinted with the permission of Johnson Matthey)

Palladium is usually extracted along with Platinum Group Metals (PGM). The extraction of palladium is capital intensive and large investments are needed for further developing existing production facilities. Figure 2.7 shows how the production facilities are distributed worldwide within the last few years. The projection of palladium production in time shows that this distribution will not change until at least 2020 [48,49].

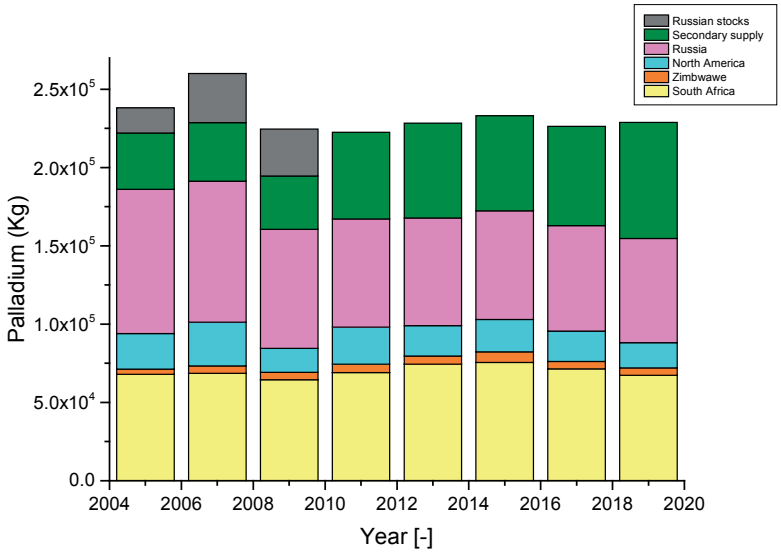

Figure 2.7 Worldwide palladium production distribution in time. (Adopted from Stillwater mining company) [49]

The global production of palladium increased by about 60% from 150000 kg/yr in 1950 to 242000 kg/yr in 2010. It is expected that palladium production capacity will increase by 14% between 2010 and 2015, but it will probably be lower due to the global recession. Also, from 2010 onwards, the recovery of PGMs from recycled automobile catalytic convertors, jewelry and electrical products has increased -up to 25% of total world supply- at a higher rate than the increase in production from natural resources [50].

Nearly 50% of the produced palladium is used in the automotive industry in catalytic convertors of gasoline vehicles. Due to this fact, the demand for palladium increased to the highest value of all times in 2012 (242 tonnes), mainly as a consequence of the rapid increase in the production of gasoline vehicles in growing economies such as China and India [48,51].

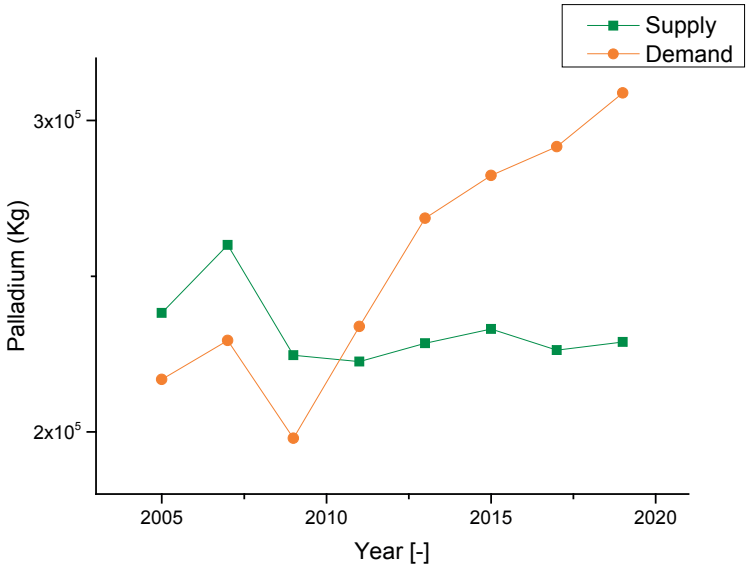

Figure 2.8 Projections for palladium supply-demand picture in time [49].

In this situation, Russian stockpiles are nearly depleted. Also, projections for recycled palladium show an increase up to double in size in the coming year, although this still cannot offset the deficit in the palladium market. This will change the supply-demand picture of palladium from being balanced to a severe deficit in 2020 (Figure 2.8) [49]. This figure shows that using the current price of palladium to evaluate the costs for a near-future CCS plant is very optimistic.

A complex link exists between supply, demand and market price for palladium. Most often, mineral exploration and production capacities will increase as a response to an increase in demand for the material in the market. In addition, several more factors can drastically influence the market price for Palladium such as depression era and geopolitical tensions (see

Figure 2.9)[52]. In early 2001, the palladium supply from Norilsk complex in Russia became unreliable. As a result, the market price for palladium reached to $33978 per kg [47,51].

As mentioned above, the supply-demand balance for palladium will determine an extra exploration of the material worldwide. In the case of palladium, although a severe increase in the worldwide demand is obvious, the extra exploration of palladium is further influenced by the demand for two other metals (nickel and copper), since palladium is usually mined as a byproduct in the process of nickel and copper production [50]. Data provided by mining companies show that, despite there will be new exploration sites in Australia, Brazil, China, Finland and the United States, but most of the global production for palladium will be from existing and already established production sites, at least until 2020 [50].

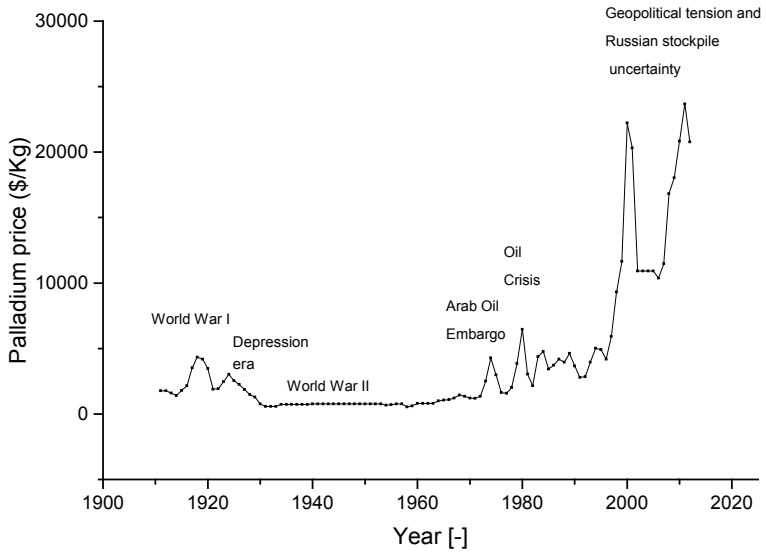

Figure 2.9 Yearly average historical price for palladium shows a dramatic increase in case of any anticipated interruption in palladium supply.

Today palladium is being demanded from various industrial sectors, while the production capacities for the metal is not enough to offset the (actual) deficit in the market. Hence, the palladium market will be so tight that any small changes in supply patterns will result in huge market price changes. And CCS based on membranes is not a small market change in this respect.

2.3.2 Outlook

The global economic recovery will be the main driver for palladium demand in the market. Specifically, the use of palladium in catalytic convertors in the automotive industry is growing

rapidly. At the same time, an increase in the gasoline vehicles production will move worldwide demand of palladium to a severe situation [51]. Existing supplies of palladium will fall more in the coming years due to a decrease in the output from Russia and South Africa. Also, new exploration efforts are decreasing. Therefore, the supply-demand picture for palladium will move from being nearly balanced to a severe deficit in the coming years.

These predictions do not consider the influence of new technologies (such as pre-combustion CO_2 capture with WGS-MR) on the worldwide demand of palladium. Considering the fact that even for only one relatively large scale IGCC plant (1 GWe) the total supply of palladium should increase to around 1% (with the most permeable membranes), it is clear that this will result in a tighter palladium market and an even more rapid growth in palladium prices. Therefore, pre-combustion capture of CO_2 using WGS-MR seems a non-practical option in relatively large scale plants and alternative (membrane) technologies should be considered. Additionally, more actions for recovery recyclability of palladium from used membranes have to be considered in future projects to make the Pd-based membrane technology more reliable. This important aspect should be also considered in a complete life cycle analysis of the palladium membrane production.

Although large scale CCS implementation seems a difficult market for Pd-based membrane technologies, it is clear that membrane reactors based on Pd membrane are still very interesting for smaller scale applications, where the amount of palladium required is small compared with the world supply.

2.4 Conclusions

According to a technical assessment, even for a power plant of 1 GWe net electricity production a large amount of palladium is required (with the most advanced membranes). Furthermore, considering the total worldwide electricity production from fossil fuels we need a tremendous increase in the world supply of palladium to redirect to the new membrane technology from the previous traditional IGCC power plants without CO_2 capture. Pre-combustion CO_2 capture using WGS-MR with palladium membranes seems a non-practical option for relatively large-scale plants. Other membrane materials have to be considered and studied. On the other hand, a smaller scale use of palladium membrane technology is still very interesting, especially because these applications will not greatly influence the palladium market. Moreover, recyclability of palladium membranes, often forgotten in research projects and almost never discussed in literature, should be studied as an important option to avoid an increase in the palladium price.

Bibliography

[1] International Energy Agency, Key World Energy, (2012). https://www.iea.org/publications/freepublications/publication/kwes.pdf.

[2] B.R. Peters T.A., Kaleta T., Lovvik O.M., Stange M., Pd-alloy membrane development for application in membrane Water-Gas-Shift in IGCC power plants, (2014). http://www.icimconference.com/ (accessed December 20, 2016).

[3] B. Li, Y. Duan, D. Luebke, B. Morreale, Advances in CO_2 capture technology: A patent review, Appl. Energy. 102 (2013) 1439–1447. doi:10.1016/j.apenergy.2012.09.009.

[4] B. Metz, O. Davidson, H. de Coninck, M. Loos, M.L. Metz bert, Davidson Ogunlade, de Coninck Heleen, Loos Manuela, IPCC special report on Carbon Dioxide Capture and Storage, 2005.

[5] P. Markewitz, W. Kuckshinrichs, Worldwide innovations in the development of carbon capture technologies and the utilization of CO_2, Energy & Environmental Sci. (2012). http://pubs.rsc.org/en/content/articlehtml/2012/ee/c2ee03403d (accessed May 31, 2013).

[6] CO_2 capture, Transport and storage in the Netherlands, http://www.co2-cato.org/ (accessed December 20, 2016).

[7] S.I. Plasynski, J.T. Litynski, H.G. McIlvried, R.D. Srivastava, Progress and New Developments in Carbon Capture and Storage, CRC. Crit. Rev. Plant Sci. 28 (2009) 123–138. doi:10.1080/07352680902776440.

[8] X. He, M.B. Hägg, Membranes for Environmentally Friendly Energy Processes, Membranes (Basel). 2 (2012) 706–726. doi:10.3390/membranes2040706.

[9] F. Gallucci, A. Basile, A. Iulianelli, H. Kuipers, A Review on Patents for Hydrogen Production Using Membrane Reactors, Recent Patents Chem. Eng. 2 (2009) 207–222. doi:10.2174/22113347109020302 07.

[10] M.C. Carbo, D. Jansen, W.G. Haije, Advanced Membrane Reactors in IGCC : H_2 or CO_2 separation? in: Fifth Annu. Conf. Carbon Capture Sequestration - DOE/NETL, 2006: pp. 1–9.

[11] J. Franz, V. Scherer, An evaluation of CO_2 and H_2 selective polymeric membranes for CO_2 separation in IGCC processes, J. Memb. Sci. 359 (2010) 173–183. doi:10.1016/j.memsci.2010.01.047.

[12] J.J. Marano, J.P. Ciferino, Integration of Gas Separation Membranes with IGCC Identifying the right membrane for the right job, Energy Procedia. 1 (2009) 361–368. doi:10.1016/j.egypro.2009.01.049.

[13] S. Shelley, Capturing CO_2: Membrane Systems Move Forward, CEP Mag. an AICHE Publ. (2009).

[14] L. Augello, M. Broglia, L. Calloni, F. Drago, P. Pinacci, C. Rinaldi, P. Savoldelli, Sviluppo e caratterizzazione di membrane di Pd per la separazione di H_2 da utilizzare in reattori di Water Gas Shift e reforming del gas naturale, 2012.

[15] J.C. Chow, J.G. Watson, A. Herzog, S.M. Benson, G.M. Hidy, W.D. Gunter, S.J. Penkala, C.M. White, Separation and capture of CO_2 from large stationary sources and sequestration in geological formations., J. Air Waste Manag. Assoc. 53 (2003) 1172–82. http://www.ncbi.nlm.nih.gov/pubmed/12828330.

[16] K. Damen, M. van Troost, A. Faaij, W. Turkenburg, A comparison of electricity and hydrogen production systems with CO_2 capture and storage—Part B: Chain analysis of promising CCS options, Prog. Energy Combust. Sci. 33 (2007) 580–609. doi:10.1016/j.pecs.2007.02.002.

[17] K.J. Rubin ES, Mantripragada H., Marks A., Versteeg P., The outlook for improved carbon capture technology, Prog. Energy Combust. Sci. 38 (2012) 630–671. http://www.sciencedirect.com/science/article/pii/S0360128512000184.

[18] N. MacDowell, N. Florin, A. Buchard, J. Hallet, A. Galindo, G. Jackson, C. S. Adjiman, C. K. Williams, N. Shah, P. Fennell, An overview of CO_2 capture technologies.pdf, Energy Environ. Sci. 3 (2010) 1645–1669. doi:10.1039/c004106h.

[19] E. S. Rubin, The Outlook for Advanced Carbon Capture Technology Outline of Talk, in: CAPD Energy Syst. Initiat. Semin., Pittsburgh, PA, 2010.

[20] DOE / NETL Carbon dioxide capture and storage R&D roadmap, 2010.

[21] P.N. Bracht M., Alderliesten P.T., Kloster R., Pruschek R., Haupt G., Xue E., Ross J.R.H., Koukou M.K., Water gas shift membrane for CO_2 control in IGCC systems: techno-economic feasibility study, Energy Convers. Manag. 38 (1997) S159–S164.

[22] S.K. Ryi, C.B. Lee, S.W. Lee, J.S. Park, Pd-based composite membrane and its high-pressure module for pre-combustion CO_2 capture, Energy. 51 (2013) 237–242. doi:10.1016/j.energy.2012.12.039.

[23] N. V. Gnanapragasam, B. V. Reddy, M. a. Rosen, Hydrogen production from coal gasification for effective downstream CO_2 capture, Int. J. Hydrogen Energy. 35 (2010) 4933–4943. doi:10.1016/j.ijhydene.2009.07.114.

[24] J.W. Dijkstra, J. a. Z. Pieterse, H. Li, J. Boon, Y.C. van Delft, G. Raju, G. Peppink, R.W. van den Brink, D. Jansen, Development of membrane reactor technology for power production with pre-combustion CO_2 capture, Energy Procedia. 4 (2011) 715–722. doi:10.1016/j.egypro.2011.01.110.

[25] S.H. Lee, J.N. Kim, W.H. Eom, Y.D. Ko, S.U. Hong, I.H. Back, Development of water gas shift/membrane hybrid system for precombustion CO_2 capture in a coal gasification process, Energy Procedia. 4 (2011) 1139–1146. doi:10.1016/j.egypro.2011.01.166.

[26] M.D. Dolan, R. Donelson, N.C. Dave, Performance and economics of a Pd-based planar WGS membrane reactor for coal gasification, Int. J. Hydrogen Energy. 35 (2010) 10994–11003. doi:10.1016/j.ijhydene.2010.07.039.

[27] J.H. Choi, M.J. Park, J. Kim, Y. Ko, S.-H. Lee, I. Baek, Modelling and analysis of pre-combustion CO_2 capture with membranes, Korean J. Chem. Eng. 30 (2013) 1–8. doi:10.1007/s11814-013-0042-7.

[28] L. Chen, M. Hill, N. Soundarrajan, Design Toward Integration of CO_2 Capture and Fuel Conversion Technologies for a 500 MWe Coal-Based Power Plant, (2006).

[29] N.S. Siefert, S. Litster, Exergy and economic analyses of advanced IGCC–CCS and IGFC–CCS power plants, Appl. Energy. 107 (2013) 315–328. doi:10.1016/j.apenergy.2013.02.006.

[30] F. Li, L. Zeng, L. Fan, Techno-Economic Analysis of Coal-Based Hydrogen and Electricity Cogeneration Processes with CO_2 Capture, Ind. Eng. Chem. Res. 49 (2010) 11018–11028. doi:10.1021/ie100568z.

[31] A. Brunetti, F. Scura, G. Barbieri, E. Drioli, Membrane technologies for CO_2 separation, J. Memb. Sci. 359 (2010) 115–125. doi:10.1016/j.memsci.2009.11.040.

[32] G.Q. Lu, J.C. Diniz da Costa, M. Duke, S. Giessler, R. Socolow, R.H. Williams, T. Kreutz, Inorganic membranes for hydrogen production and purification: a critical review and perspective., J. Colloid Interface Sci. 314 (2007) 589–603. doi:10.1016/j.jcis.2007.05.067.

[33] R. Bredesen, K. Jordal, O. Bolland, High-temperature membranes in power generation with CO_2 capture, Chem. Eng. Process. Process Intensif. 43 (2004) 1129–1158. doi:10.1016/j.cep.2003.11.011.

[34] T. A. Peters, T. Kaleta, M. Stange, R. Bredesen, Hydrogen transport through a selection of thin Pd-alloy membranes: Membrane stability, H_2S inhibition, and flux recovery in hydrogen and simulated WGS mixtures, Catal. Today. 193 (2012) 8–19. doi:10.1016/j.cattod.2011.12.028.

[35] A.Y. Ku, P. Kulkarni, R. Shisler, W. Wei, Membrane performance requirements for carbon dioxide capture using hydrogen-selective membranes in integrated gasification combined cycle (IGCC) power plants, J. Memb. Sci. 367 (2011) 233–239. doi:10.1016/j.memsci.2010.10.066.

[36] C.B. Lee, S.W. Lee, J.S. Park, D.W. Lee, K.R. Hwang, S.K. Ryi, S.H. Kim, Long-term CO_2 capture tests of Pd-based composite membranes with module configuration, Int. J. Hydrogen Energy. 38 (2013) 7896–7903. doi:10.1016/j.ijhydene.2013.04.053.

[37] S. Schiebahn, E. Riensche, M. Weber, D. Stolten, Integration of H_2-Selective Membrane Reactors in the Integrated Gasification Combined Cycle for CO_2 Separation, Chem. Eng. Technol. 35 (2012) 555–560. doi:10.1002/ceat.201100497.

[38] M. Gazzani, D.M. Turi, G. Manzolini, Techno-economic assessment of hydrogen selective membranes for CO_2 capture in integrated gasification combined cycle, Int. J. Greenhouse Gas Control. 20 (2014) 293–309. doi:10.1016/j.ijggc.2013.11.006.

[39] R. Koc, N.K. Kazantzis, W.J. Nuttall, Y. Hua, Economic assessment of inherently safe membrane reactor technology options integrated into IGCC power plants, Process Saf. Environ. Prot. 90 (2012) 436–450. doi:10.1016/j.psep.2012.07.004.

[40] P. Chiesa, T.G. Kreutz, G.G. Lozza, CO_2 sequestration from IGCC power plants by means of metallic membranes, J. Eng. Gas Turbines Power. 129 (2007) 123–134. doi:10.1115/1.2181184.

[41] P. Chiesa, T.G. Kreutz, G.G. Lozza, CO_2 Sequestration From IGCC Power Plants by Means of Metallic Membranes, J. Eng. Gas Turbines Power. 129 (2007) 123. doi:10.1115/1.2181184.

[42] F. Gallucci, E. Fernandez, P. Corengia, M. van Sint Annaland, Recent advances on membranes and membrane reactors for hydrogen production, Chem. Eng. Sci. 92 (2013) 40–66. doi:10.1016/j.ces.2013.01.008.

[43] T.A. Peters, T. Kaleta, M. Stange, Development of thin binary and ternary Pd-based alloy membranes for use in hydrogen production, (n.d.).

[44] R. Koc, N.K. Kazantzis, W.J. Nuttall, Y.H. Ma, Economic assessment of inherently safe membrane reactor technology options integrated into IGCC power plants, Process Saf. Environ. Prot. 90 (2012) 436–450. doi:10.1016/j.psep.2012.07.004.
[45] L. De Lorenzo, T.G. Kreutz, P. Chiesa, R.H. Williams, Carbon-Free Hydrogen and Electricity From Coal: Options for Syngas Cooling in Systems Using a Hydrogen Separation Membrane Reactor, J. Eng. Gas Turbines Power. 130 (2008) 31401. doi:10.1115/1.2795763.
[46] C.A. Scholes, K.H. Smith, S.E. Kentish, G.W. Stevens, CO_2 capture from pre-combustion processes—Strategies for membrane gas separation, Int. J. Greenh. Gas Control. 4 (2010) 739–755. doi:10.1016/j.ijggc.2010.04.001.
[47] D. McDonald, L.B. Hunt, A History of Platinum and Its Allied Metals, 1984. doi:10.2307/3104631.
[48] Platinum today, Available at:http://www.platinum.matthey.com/ Accessed: 17 July 2013,
[49] The Case for Palladium, Prescient or Perceptive Palladium View, 2010.
[50] D.R. Willburn, Global Exploration and Production Capacity for Platinum-Group Metals From 1995 through 2015, 2012. https://pubs.usgs.gov/sir/2012/5164/.
[51] P.J. Loferski, 2011 mineral yearbook, (2011). http://minerals.usgs.gov/minerals/pubs/commodity/platinum/myb1-2011-plati.pdf.
[52] H.E. Hilliard, Platinum-group metals, Available at :http://minerals.usgs.gov/minerals/pubs/commodity/platinum/55079, 1998.

"When a system at equilibrium is placed under stress, the system will undergo a change in such a way as to relieve that stress."

- Le Chatelier's principle

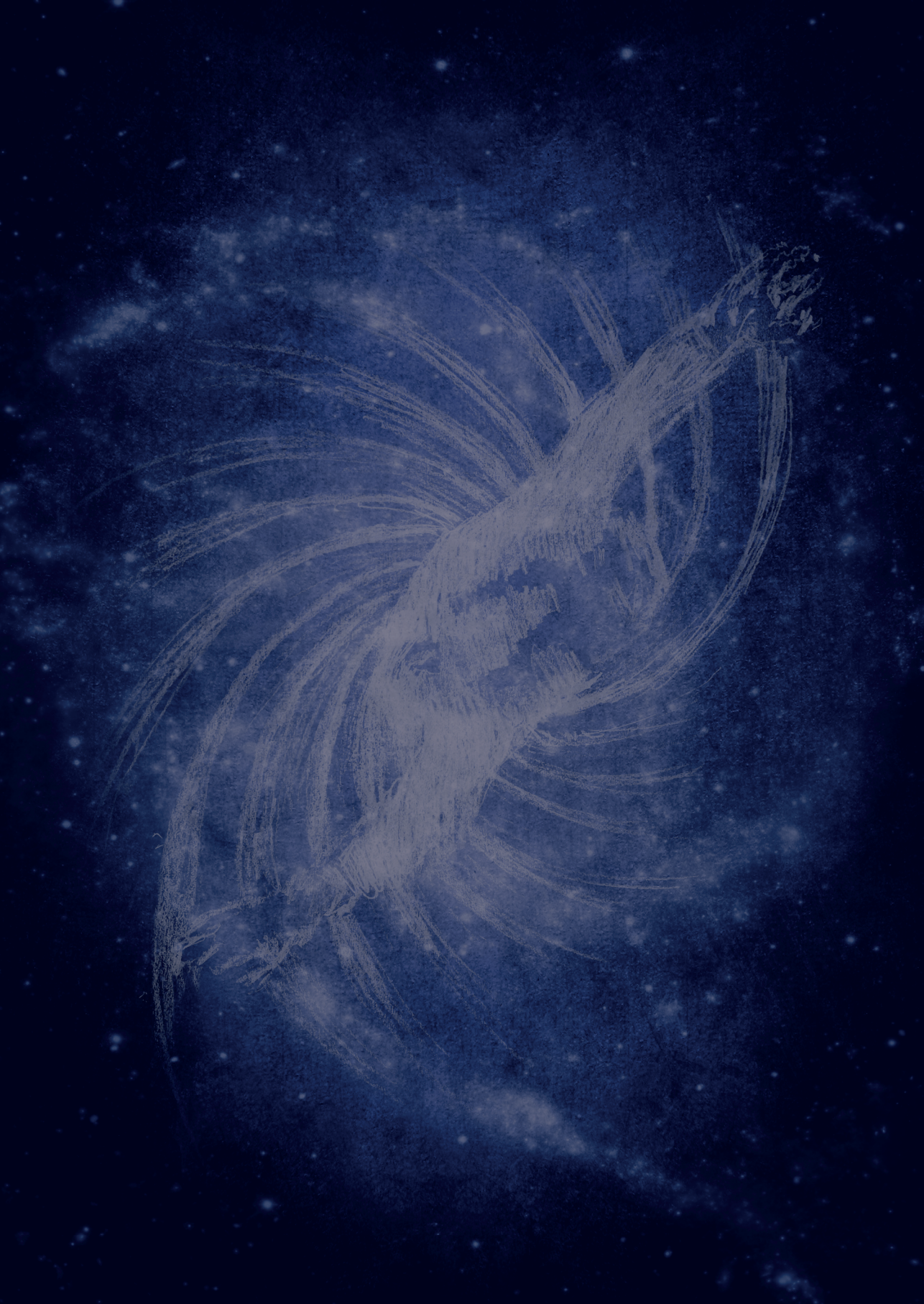

Chapter 3

Development of thin Pd-Ag supported membranes for fluidized bed membrane reactors including WGS related gases

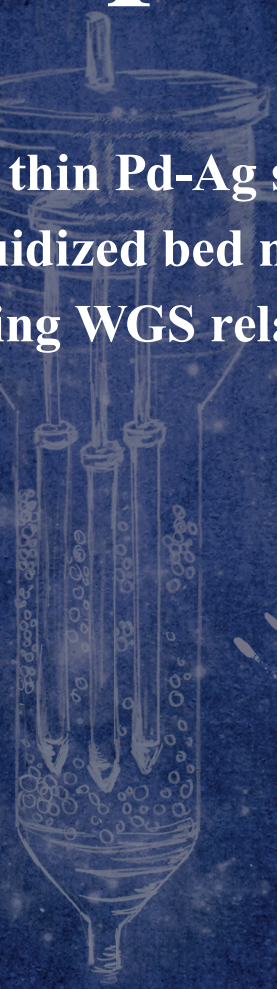

Abstract

This chapter reports the preparation, characterization and stability tests of Pd-based thin membranes for fluidized bed membrane reactor applications. Various thin membranes have been prepared by simultaneous Pd-Ag electroless plating. A simple technique for sealing of the produced membranes is reported and discussed. The membranes have been characterized for single gas permeation, and afterwards used for permeation of mixtures of gases and under fluidization conditions. The membranes have shown very high permeation rates and perm-selectivity when used as permeators. When applied in fluidized bed reactors it has been found that the membranes are stable as long as no interaction between the fluidization catalyst and the membrane surface occurs. For some catalysts a strong chemical interaction between the catalyst and the membrane surface has been observed which caused a drastic decrease in the membrane flux.

3.1 Introduction

High purity hydrogen is required in many processes, such as semiconductor manufacturing, fuel cells applications, chemical industry, analytical instruments, computer and aerospace industries, recovery of radioisotopes of hydrogen in nuclear reactors [1]. On the other hand, hydrogen production and separation can be also exploited for pre-combustion (decarbonization) route for carbon capture and sequestration (CCS) from fossil-fuel fired power stations [2]. Most of the hydrogen (> 80%) is currently produced by steam reforming of natural gas in large multi-tubular fixed-bed reactors. In small-scale applications, partial oxidation reactions and auto-thermal reforming (combination of partial oxidation (exothermic) and steam reforming (endothermic)) are also considered. These reactions are (generally) equilibrium limited and produce a hydrogen-rich gas mixture containing carbon oxides and other by-products. The carbon monoxide can be converted to carbon dioxide producing more hydrogen via the Water Gas Shift (WGS) reaction where steam is introduced as reactant (Eq. 3.1). WGS is thermodynamically favored at low temperatures and kinetically favored at high temperatures. The traditional two-stage WGS process consists of a first reactor operated at 300-450 °C (to efficiently convert the biggest part of CO) and a second reactor that works at lower temperatures at 200-300 °C to convert the last part of CO.

$$CO + H_2O \leftrightarrow H_2 + CO_2 \qquad \Delta H^0_{298} = -41\ kJ/mol \qquad \text{Eq.(3.1)}$$

During the last few years more attention has being paid on hydrogen perm-selective membrane reactors operated with commercial ferrochrome based catalysts which can integrate the WGS reaction and in-situ extraction of ultra-pure H_2 in one-stage and accordingly shift the equilibrium and thus intensify the process (improving yields and selectivities and reducing downstream separation costs, while also reducing the required reactor volume) [3]. New noble metal catalysts have been developed and have been tested in packed-bed membrane reactors. Results have shown that improving membrane characteristics enhances the reactor performance, but it would be more beneficial to develop a more active catalyst with higher activity to facilitate the use of thinner catalyst beds with a higher specific membrane area and lower concentration polarization across the catalyst bed. Most recently, fluidized bed membrane reactors have been introduced to overcome the mass transfer limitations prevailing in packed bed reactors because of their excellent gas-solid contact and heat and mass transfer characteristics [4,5]. However, these reactors have not been exploited yet for the WGS reaction.

Among the membranes for H_2 separation, the Pd-based membrane shows the highest permeability and exclusive selectivity for H_2 due to the unique permeation mechanism. In order to achieve the hydrogen separation targets defined by the Department of Energy of the United States (DOE) [6], very thin Pd membranes (less than 5 μm) are required. In

comparison to Pd, it is well known that Pd-Ag alloy membranes have higher H_2 permeability up to 70% ($Pd_{77}Ag_{23}$) and are stronger against hydrogen embrittlement (PdH α-β transition at low temperature) [1]. Common dense metal layer deposition technologies include physical vapor deposition (PVD, including magnetron sputtering, thermal evaporation or pulsed laser evaporation), chemical vapor deposition (CVD or MOCVD) and electroless plating (ELP) [7].

The electroless plating (ELP) method is the most used method for the preparation of thin Pd-based membranes particularly with respect to operational flexibility, simple equipment, cost performance and applicability to non-conductive materials of any shape. Pacheco Tanaka et al. developed a method for the simultaneous plating of Pd-Ag with the desired composition of metals [8]. This was achieved by uniform deposition of nano-particles of Pd nuclei on the surface of the substrate and careful control of the composition of the plating solution; various Pd-Ag ratios were prepared by this method and the H_2 permeation properties observed were studied and related to the embrittlement phenomenon [9].Recently, the method was improved and a synchronized deposition of Pd/Ag was obtained [10].

Thin Pd-based membranes are generally supported on porous substrates including stainless steel and ceramic materials of planar or tubular configuration [2]. Porous ceramics are the most common substrate material, owing to their excellent chemical stability. However, Pd-based membranes deposited on a ceramic support showed gas leak problems after some thermal cycles, due to the detachment of the Pd membrane layer that is deposited on the glass used to join ceramic dense and porous parts. The presence of leaks causes a decline in the hydrogen selectivity. The most promising sealing approach is based on using graphite. In some works, graphite gaskets were applied onto the faces of the two ends of the membrane tube [11,12], but the sealing is poorly gas-tight and the membrane can be easily broken by mechanical stress induced by the sealing compression. The membrane tube can be also sealed to a metal tube with connectors. The design of the connector is critical, because it should limit the pressing force and avoid damage to the thin membrane layer during operation [13,14].

In this chapter we will present results on Pd-Ag alloy supported on alumina tubes. The Pd-Ag membranes were prepared by simultaneous electroless plating. A membrane sealing procedure based on graphite ferrules and stainless steel connector was optimized to be able to connect the ceramic supported Pd-based membrane to dense metal tubes. These sealed membranes showed high hydrogen permeance and selectivity, in the order of the targets for DOE 2015. In addition, the resistance of the membranes to catalyst fluidization in novel fluidized bed WGS membrane reactors is investigated and discussed.

3.2. Experimental

3.2.1. Membrane preparation

Tubular alumina supports with an outside pore size of 100 nm were provided by Rauschert Kloster Veilsdorf. The supports have an external diameter of 10.0-10.5 mm and an internal diameter of 7 mm. For proper handling during membrane preparation, the alumina porous tubes were cut and connected to dense alumina tubes (provided by OMEGA with 6 mm OD and 4 mm I.D.), one end was closed, using an enameled glass (ASF1761, Asahi Glass Co., Ltd.) as shown in Figure 3.1. The glass was applied in the junction point between the porous and dense support and cures at 1000 ºC in air for 30 min (heating rates of 4 ºC/min from room temperature to 200 ºC and then of 12 ºC/min to 1000 ºC).

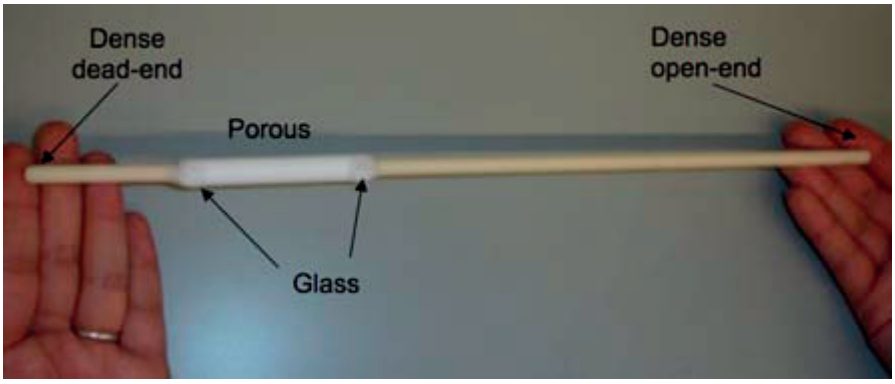

Figure 3.1 Assembled closed-end ceramic tubular support.

Pd-Ag thin layers were deposited on the alumina tubes by using a simultaneous (Pd and Ag) electroless plating technique. Firstly, the surface of the alumina tube was activated by seeding it with Pd nuclei prior to electroless plating following the procedure reported by Pacheco et al. [8]. The surface completely turned black due to uniform covering of palladium nuclei. By this procedure, a large number of fine palladium particles were deposited on the surface.

Pd and Ag were deposited by the simultaneous electroless plating method reported by Suzuki and Pacheco Tanaka [10]. The base plating process starts with the immersion of the activated alumina tube into a well stirred plating bath containing palladium acetate (11.70 mM), silver nitrate (0.64 mM), EDTA (0.15 M), ammonia (5 M) and hydrazine (15 mM). The whole system was placed in a thermostat bath maintained at 62-64 ºC. After 90 min of plating, a silver nitrate solution (12.5 mM) was added at 0.117 ml min^{-1} in order to increase the Ag content of the membrane. The total time of the plating was 210 min.

For some membranes, a second Pd-Ag sequential plating step was carried out in order to have a thicker final membrane to prevent any possible membrane failure due to catalyst fluidization in contact with the membrane surface. In this case the plating bath was composed

of palladium acetate (10 mM), silver nitrate (0.5 mM), EDTA (0.15 M), ammonia (5 M) and hydrazine (15 mM) (no additional adding of silver) and the plating deposition time was 30 min.

The characteristics of the membranes produced and tested are shown in Table 3.1. The membrane designated with E15 has undergone only the base plating process and both E54 and E56 membranes have had two plating steps (the base plating and the second plating).

Table 3.1 Prepared Pd-Ag supported membranes (Al_2O_3 100 nm porous support of 10 mm outside diameter).

Membrane code	Manufacturing method	Length (mm)
E15	ELP (1 plating)	36.3*
E54	ELP (2 platings)	68.0*
E56	ELP (2 platings)	74.6*
E62	ELP (2 platings)	50.0

*Membrane length after graphite attachment

After each plating step, the membrane layers were annealed at 550 ºC for 2 h; this temperature should be above the maximum operating temperature, which is around 500 ºC for the WGS membrane reactor, exposed to a 10% H_2/90 %N_2 gas mixture. The Pd-Ag deposited alumina tubes were introduced into a quartz tube that was placed in a cylindrical furnace (from Termolab with a homogeneous heating length of 80 cm). The temperature was increased at 3 ºC min^{-1} under nitrogen to the desired temperature and then heated at constant temperature. At 550 ºC, a hydrogen flow of 50 cm^3 min^{-1} and a nitrogen flow of 450 cm^3 min^{-1} were fed into the furnace. Nitrogen was used for the cooling step.

3.2.2. Physico-chemical characterization of membranes

The membrane E62 (Pd-Ag) prepared with the same procedure as for E54 and E56 was used for *as-prepared* physico-chemical characterization. The Pd and Ag contents of the membrane layer were determined by a Varian Vista MPX inductively coupled plasma optical emission spectrometer (ICP-OES). The cross-section images to analyze the morphology of the membrane layer and measure the membrane thickness were taken with an Environmental Scanning Electron Microscope (ESEM) (FEI Quanta 250 FEG). XRD of the membrane tube was measured with a Bruker D8 Advance to determine the alloying condition.

3.2.3. Membrane sealing by graphite gaskets

Sealing of Pd-based membrane layers deposited on ceramic tubular supports represents a challenging task: preliminary tests showed gas leak problems after some thermal cycles, due to the detachment of the Pd membrane layer that is deposited on the glass used to connect the ceramic dense and porous parts (see Figure 3.2).

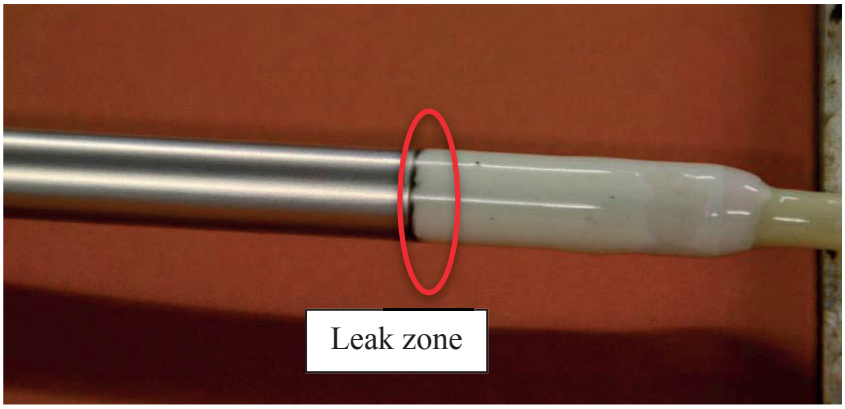

Figure 3.2 Leak zone of membranes found between Pd layer and glass used for join dense and porous parts after thermal cycles.

An extensive literature review was carried out in order to look for different options to solve this problem. Chen et al. [14] described a method using graphite ferrules instead of using standard metal ferrules. The authors have shown that these graphite ferrules could successfully seal the membrane with Swagelok® connectors. Even at very high pressures up to 50 bar, the nitrogen leakage rate over the connectors was only about 0.35 ml/min.

To seal the membranes with Swagelok® fittings of 10 mm I.D. (code: SS-10M0-6), graphite ferrules of 10 mm I.D. (purchased from CHROMalytic TECH(nology) Pty Ltd) were used instead of the standard metal ones. Ferrules were opened from inside with a rotating cutter with sharp edges to increase the inner diameter of the ferrules in order to make them fit to the membranes (with an O.D. between 10-10.4 mm).

Before sealing the membrane with the opened ferrules, the ferrules were first conditioned in the Swagelok® fitting with a dummy Stainless steel (316L) rod to form the ferrules to the right shape. The diameter of the dummy is equal to the diameter of the membrane to be sealed. The connectors were tightened with about 20 – 30 N.m (torque wrench) to form them with the right shape and to get a smooth inner surface (Figure 3.3).

Figure 3.3 Left: 316L dummy rod with graphite ferrule and Right: connector with pre-treated ferrule (shiny inner surface)

After shaping the ferrules, the membrane was fitted to the connectors. The connectors were carefully tightened to the membrane with a torque wrench. First a torque of 5 N.m was applied followed by increasing the force in two steps to 7 N.m. To verify whether the ferrules worked properly, Helium was fed from the inner part of the membrane up to a maximum pressure of 1 bar and introduced in a water bath. The formation of bubbles indicates that the connectors were not well-tightened and should be tightened more in order to avoid leaks. If no bubbles were formed, it indicated that the connected membrane was well sealed (confirmed later by permeation tests) and could be implemented later in the test reactor.

A disadvantage of this sealing method is the loss of membrane area. For a membrane with nearly 137 mm length, the usable length of hydrogen permeation is about 105 mm. The lost length because of the connectors is about 32 mm (in total for both sides). A typical membrane before and after connecting it to the Swagelok® connectors can be seen in Figure 3.4.

To further investigate the performance of the membrane sealing, a break test was carried out after the previous tests to determine the maximum tolerable torque on the membrane. The membrane was implemented in a new Swagelok® connector with a new graphite sealing. The graphite ferrules were treated as described before. The used torque for the sealing of the membrane was increased in steps from 1 N.m to 15 N.m to determine the breaking point of the membrane. At 14 N.m the membrane support was broken.

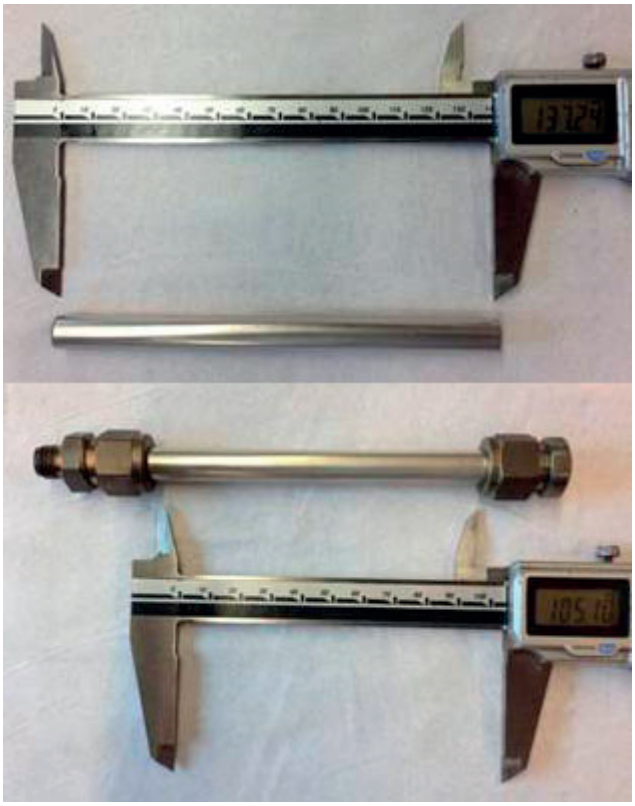

Figure 3.4 Pd membrane (E80 – Pd-Ag membrane, thickness 4.5 micron) before and after connecting to the Swagelok® connectors.

As can be seen in Figure 3.5, although the membrane broke at the exit of the Swagelok® connector, the cracks in the porous support actually started at the maximum load point of the graphite ferrule due to the excessive torque. For a proper sealing it is thus suggested to use the graphite ferrules and Swagelok® with a maximum torque up to 8 N.m to assure a very low level of leakage and prevent rupture of the ceramic support.

Figure 3.5 Broken Membrane after applying 14 N.m.

2.4 Permeation characterization of membranes and sealing performance

To test the applied sealing method, a membrane permeation setup was designed and constructed. Figure 3.6 illustrates details of the piping and instrumentation of the setup. The setup consists of three main sections: a feed section, a membrane module section and an analysis section. At the feed section mass flow controllers from BROOKS b.v. were used to set the desired gas composition (N_2, H_2, CO and CO_2) and flow rate.

The membrane module section consists of a stainless steel tube (3 cm i.d.) where the membrane is integrated from the top flange. The feed gas can be supplied to the module from the bottom part through a gas distributor. Thus, the module can also be used for fluidization tests. The whole membrane module (reactor) is placed in an electric furnace to be able to set the desired temperature inside the reactor (Figure 3.7). Three temperature indicators were placed at different positions in the module to measure and monitor the temperature. A back-pressure regulator was placed at the outlet of the module (retentate side) to set the required trans-membrane pressure difference (two pressure indicators were placed at permeate and the retentate side). Both retentate and permeate sections were connected to the analysis section (independently). The analysis section consists of a HORIBA film flow meter (minimum 0.2 ml/min) to measure the flow rate at the permeate side. At the retentate side a mass flow meter from BROOKS b.v. is placed. The outlet gases from both retentate and permeate sides can be analyzed with a μ-GC (CP-4900 series from Varian b.v.) or directed to the vent.

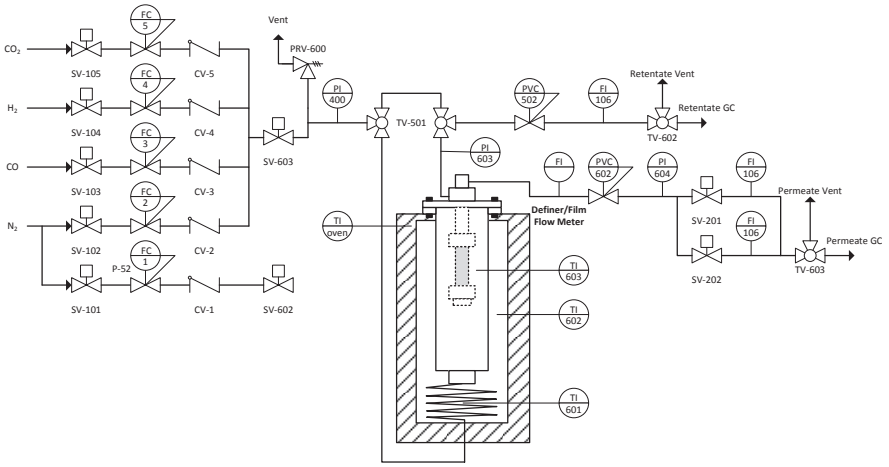

Figure 3.6 Process flow diagram for the permeation setup

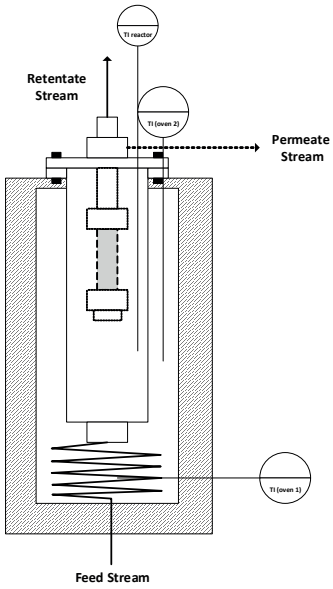

Figure 3.7 Details of the membrane reactor module including temperature and pressure indicators

First, permeation tests were carried out. Pure nitrogen (500 ml/min), pure hydrogen (1000-1500 ml/min) and mixtures of hydrogen and nitrogen were fed at different temperatures and pressures to the outside of the membrane and the permeation to the inner part of the membrane was quantified, while the inner part of the membrane was open to atmosphere and no sweep gas was used. For the permeation (leakage) of nitrogen, the Horiba Liquid Film Flow meter was used (0.2 – 10 ml/min). For the permeation of hydrogen two different Definer 550 (50 – 500 ml/min or 300 – 30000 ml/min) were used depending on the hydrogen partial pressure.

The range of temperatures for the nitrogen permeation tests was between 20 °C and 550 °C and between 300 °C – 500 °C for hydrogen. The permeance of hydrogen was measured at temperatures above 300 °C in order to prevent possible membrane embrittlement. The stability of the sealing and the permeance performance were tested for these different cases:

– Long-time measurement for N_2 and H_2 (48h test at 380-400 ºC and 2 bar of pressure difference) to ensure the stability of the membrane and the sealing performance over a longer times.
– Thermal cycling test for N_2 and H_2 (heating up and cooling down of minimum 7 cycles from room temperature to 400 ºC) to ensure that the sealing is not affected by thermal cycling possibly because of different expansion coefficients for the different materials (connectors, ferrules, membrane).
– Flow rate measurements for pure gas (N_2, H_2) at different pressures and temperatures to determine the membrane permeation parameters.

– WGS feed mixture gas (H_2, N_2, CO, CO_2) at 400 °C to ensure that the sealing is not affected by chemical reactions with some of the used gases at reaction conditions.
– Implementation of the membrane in a fluidized bed (at room temperature and at 400 °C) to ensure that the membrane works properly under fluidization conditions (using pure N_2, mixture of N_2/H_2 and dry WGS mixtures).
– Because it was observed during experiments with membrane E15 that mass transfer limitations and or CO poisoning effect can be important for this type of membranes, experiments under different feed gas compositions of H_2 to N_2 ratios and also the addition of different amounts of CO were done for membrane E56.
– Post characterization of membrane surface.

A typical composition of a reformate gas fed to a WGS reactor is reported in Table 3.2 and used as reference case in this work. Because steam and methane were not available in the permeation setup and are also not necessary for the experiments, the feed composition for the WGS permeation tests in this work was changed to the composition listed in the third column. The total feed flow rate was about 1000 ml/min.

Table 3.2 WGS gas feed composition

Species	Molar frac. (%) in industry	Molar frac. (%) used for the permeation tests
CH_4	3.8	-
H_2	44.8	72.8
CO	9.2	14.6
CO_2	4.7	7.6
H_2O	34.7	-
N_2	2.8	4.6

For the fluidization experiments, the gas flow rate was changed in such way that the bubbling fluidization conditions were maintained at different pressures and temperatures. All tested membranes and the tests carried out on each membrane have been summarized in Table 3.3.

Because a strong performance loss (in terms of hydrogen permeance) was observed for Membrane E15 during the first fluidization tests , a more structured test campaign has been carried out on the membranes E54 and E56 to further investigate the cause of this loss in performance. E54 was tested with pure gas and in fluidized conditions only to assess the effect of fluidization. The other membrane were tested with the complete test protocol.

Table 3.3 Tests performed on different sealed membranes

Membrane code	Pure gas exp.	H_2/N_2	Fluidization	WGS mixture
E15	X	X	X	X
E54	X		X	
E56	X	X	X	X

3.3. Results and discussions

3.3.1 Physico-chemical characterization results of as-prepared Pd-Ag supported membranes

ICP

The Pd and Ag composition of two pieces of the same membrane layer (E62) was analyzed by ICP-OES. First, the two samples were dissolved using concentrated nitric acid and then diluted to be able to analyze in a proper way. The Ag content of the E62 membrane layer is 13.4 ± 0.2 %.

SEM-EDX:

The cross-section SEM image of the E62 membrane consisting of the Pd-Ag layer (dark grey) on alumina porous support is shown in Figure 3.8. The Pd-Ag membrane thickness is around 3.6 μm. We assume that E54 and E56 membranes are also 3.6 μm, since they were prepared with the same procedure as E62.

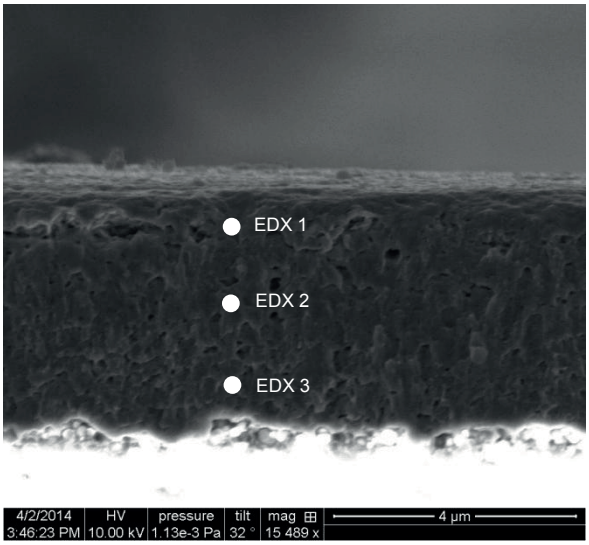

Figure 3.8 Pd-Ag layer on alumina 100 nm pore size (E62 membrane)

In addition, an EDX analysis was performed at the points marked in Figure 3.8 and the results have been summarized in Table 3.4.

Table 3.4 EDX analysis of a cross section of the membrane layer (E62 membrane).

EDX position	Pd (wt%)	Ag (wt%)
Point 1	86.2	13.9
Point 2	84.5	15.5
Point 3	86.1	13.9

XRD

Two samples of the E62 membrane were analyzed by XRD and the resulting spectra are presented in Figure 3.9. It can be seen that Pd and Ag were well alloyed, confirming that the annealing process performed is suitable. The crystalline structure of Pd-Ag alloy was face-centered cubic (FCC) and its lattice constant was 3.903 Å ("a").

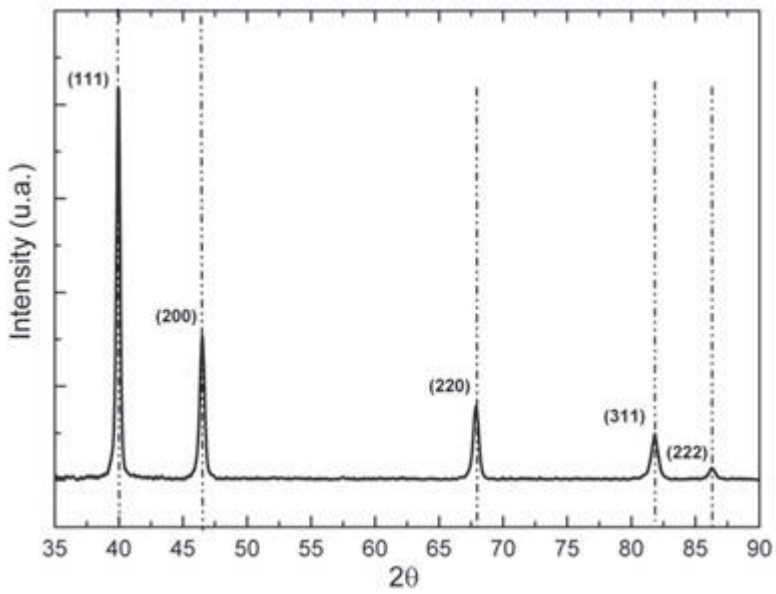

Figure 3.9 XRD spectra of E62 membrane (annealed Pd-Ag supported membrane).

3.3.2 Results on membranes performance and sealing stability.

Long-time permeation measurements of E15 membrane

Long-time measurements for 48 h at 380-400 ºC and 2 bar pressure difference were carried out to ensure stable membrane performance before carrying out the experiments to determine the membrane permeation parameters (the pre-exponential factor and activation energy). The hydrogen/nitrogen ideal perm-selectivity of the E15 membrane is shown in Figure 3.10.

The hydrogen permeance increases for the E15 membrane during the first few hours until it reaches a stable value, which is also reported in literature for Pd-membranes [15]. It is

reported in literature, that mainly two effects can responsible for the observed activation of the membrane [16]. First, there is the effect of surface contamination which can block the active sites on Pd layers for hydrogen transport. A second effect is considered as the induction period, which is related to the lattice rearrangements of Pd during hydrogen transport through the membrane.

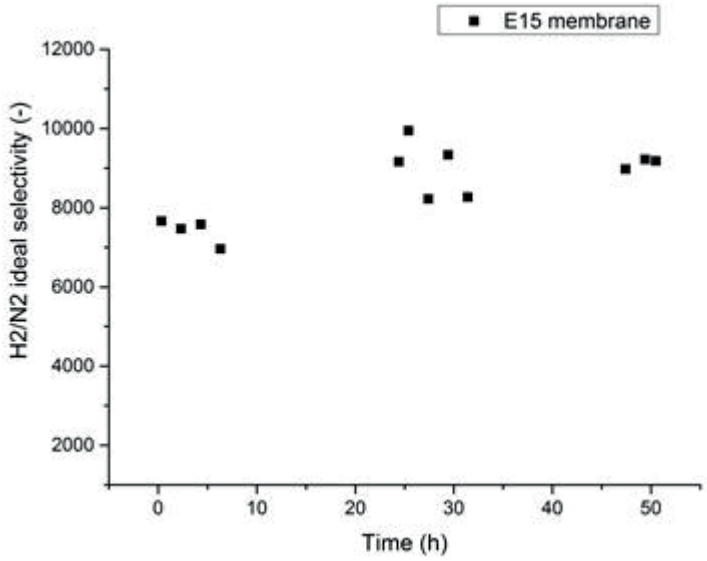

Figure 3.10 H_2/N_2 ideal perm-selectivity of E15 membrane during 48 hours experiment at 380-400 ºC and 2 bar of pressure difference.

Thermal cycling experiments for E15 membrane

To ensure that heating up and cooling down has no influence on the performance of the sealing and the membrane permeance, the E15 membrane performance was evaluated for several thermal cycles (Figure 3.11) after previous long term permeation tests and found to be quite stable.

For the E15 membrane, some small fluctuations in the nitrogen permeance can be discerned, related to the very low nitrogen flow rates (less or close to 0.2 ml/min), where the film flow meter could not be used for all measurements because the minimal detectable flow rate is 0.2 ml/min.

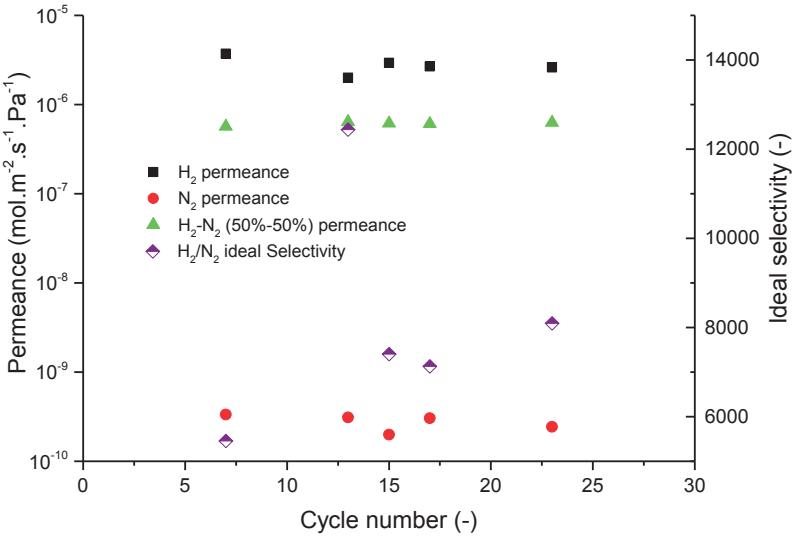

Figure 3.11 Performance of the E15 membrane with several thermal cycles after long term permeation tests (each thermal cycle indicates one heating-up and cooling-down step; from room temperature to 400 ºC)

Determination of membrane parameters

After the long-term measurements and the cycling experiments, the membranes were tested at different temperatures and pressures under N_2 and H_2. Table 3.5 shows the N_2 permeance for the E15 membrane as a function of temperature and partial pressure difference across the membrane. Because the N_2 flow rate is very low for E15, it could only be detected at pressure differences above about 4 bar, which is the maximum pressure difference available in the test setup.

Table 3.5 N_2 permeance for the E15 membrane at different temperatures and transmembrane pressure differences.

P_{eff} retentate (bar)	Temperature (°C)	Permeance (10^{-10} mol.m^{-2}.s^{-1}.Pa^{-1})
4.16	309	3.1
4.16	348	2.8
4.15	397	3.1
4.08	449	2.6

Results for the hydrogen permeation experiments are shown in Figure 3.12. The permeation of hydrogen is increasing with increasing transmembrane partial pressure difference. The E15 membrane exhibits an almost perfect linear behavior for the exponential factor n=0.5 (R^2>0.999), which is typical for Pd-Ag membranes at low pressures if bulk-diffusion through

the membrane is the rate limiting step [17]. The activation energy of the membrane ($E_{a,Pd}$) was determined at 7.8 kJ/mol.

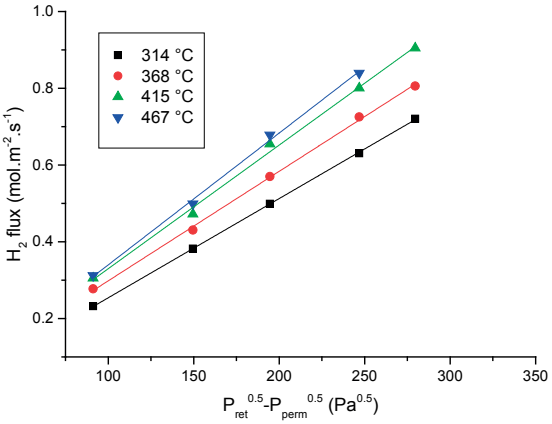

Figure 3.12 H_2 flux versus H_2 pressure difference at different temperatures for the E15 membrane.

Table 3.6 compares permeation parameters for different membranes reported in the literature with the membrane used in this work.

Table 3.6 Comparison of different Pd based membranes reported in literature with the E15 membrane

Membrane material	Preparation method	Selective layer thickness	T	Permeance H_2	Permeability H_2	Ideal selectivity	Ref
		[µm]	[°C]	[10^{-8} mol/ m^2sPa][a]	[10^{-13} mol m/ m^2sPa]	-	-
Pd-Au/YSZ/PSS	ELP	2.3	400	710	160	82000 (H_2/N_2)	[18]
Pd-Au/Al_2O_3	ELP	2 – 3	500	620	160	1400 (H_2/N_2)	[19]
Pd-Ag/PSS[b]	PVD-MS	2.8	400	1500	420	2900 (H_2/N_2)	[20]
Pd-Au-Pt[b]	PVD-MS	25	400	54	130	-	[21]
Pd/Inconel	ELP	7	450	96	67	4,500 (H_2/He)	[22]
Pd-Ag/Al_2O_3	ELP	3.2	400	310	100	8000-10,000 (H_2/N_2)	this work

[a] Permeance values have been calculated for a H_2 partial pressure of 1 bar.
[b] Self-supported membranes.

Tests at WGS conditions

The E15 membrane performance was also investigated at WGS conditions (see Table 3.2) measuring the H_2 permeance of the membranes before and after exposing the membrane to the WGS gas mixture at different pressure differences (see Figure 3.13).

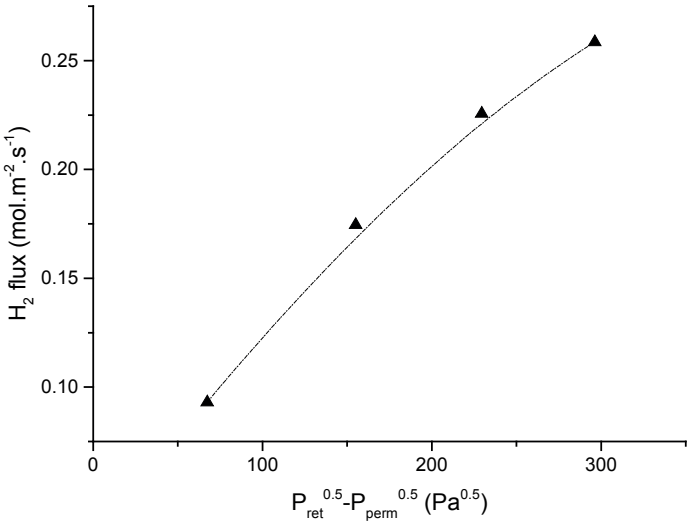

Figure 3.13 Performance of the E15 membrane at WGS conditions at different pressure differences (feed composition listed in Table 3.2).

In contrast with the pure gas experiments, the flux does not show a linear dependency on the partial pressure difference and indicates a concentration polarization effect (i.e. external mass transfer resistances). At higher pressure differences the flux through the membranes is higher and the effect of concentration polarization will more pronounced.

The H_2 and N_2 permeances of the E15 membrane before and after exposure to the WGS gas mixture is presented in Table 3.7, and the results confirm that the performance of the membrane (and the sealing) is not affected under WGS conditions.

Table 3.7 Permeation of H_2 and N_2 before and after exposure to a WGS gas mixture (400 °C).

Gas	Condition	P_{ret}-P_{perm} (bar)	Permeance ($mol.m^{-2}.s^{-1}.Pa^{-1}$)
N_2	Before WGS mixture	4.15	$2.21\ 10^{-10}$
	After WGS mixture	5.18	$2.32\ 10^{-10}$
H_2	Before WGS mixture	2.08	$3.58\ 10^{-6}$
	After WGS mixture	2.12	$3.48\ 10^{-6}$

Tests under fluidization conditions

To check the performance of the membranes under fluidization conditions the membranes were tested for long time in the bubbling fluidization regime. The characteristics of the materials used for the fluidization tests have been listed in Table 3.8:

Table 3.8 Characteristics of the particle beds used in the fluidization tests.

Bed	Catalyst		Filler	
	Material	Particle size (μm)	Material	Particle size (μm)
#1	0.16%Re0.34%Pt6%Ce/TiO_2	75-106	TiO_2	100-125
#2	Noble based CPO cat.*	50-75	Al_2O_3	104

* Provided by Shell Global Solutions.

Firstly, the E15 membrane was tested in a fluidized bed (#1) and the results showed a sharp drop in the performance of the membrane after several minutes. The nitrogen and hydrogen permeance was measured during 26 hours until the membrane showed nearly constant flow for both, hydrogen and nitrogen (Figure 3.14). The fluidization seems to affect the performance of the membrane significantly. The Nitrogen permeance increased and the hydrogen permeance decreased. After 20 hours of fluidization, the membrane showed stable behavior. Flushing the reactor with air (to remove possible contamination on the membrane surface), the hydrogen permeance could be increased, but only for a few minutes. After the fluidization tests, the membrane showed the same low permeance as before flushing with air.

The permeate flux as a function of the partial pressure difference is shown in Figure 3.15a for the empty reactor and fluidized bed cases. The permeance under fluidization conditions with bed #1 (after 30 hr of fluidization conditions) has decreased a factor 14 compared to an empty reactor (tube) as shown in the Figure 3.15b.

There are different phenomena that could have caused the observed loss of performance. First of all, as described by Dang et al. [23], when small particles are used in the fluidized bed membrane reactor, the extraction of a large amount of gas may lead to the formation of densified zones close to the membranes. It is possible that these densified zones have created additional mass transfer limitations for hydrogen permeation. However, as the strong decrease in flux is observed also when using pure hydrogen flow, the densification of the bed around the membranes cannot be the only cause for the loss of performance described above. Another possible phenomenon occurring in the fluidized bed membrane reactor is a possible erosion of the palladium layer, which would be detrimental for the performance of the membranes [1]. However, erosion of the Pd layer should lead to an increase in hydrogen flux rather than a (strong) decrease.

A possible phenomenon that could explain the decrease in hydrogen flux is a possible chemical interaction between the palladium and (some components of) the catalyst used in the tests. In fact, previous tests with Pd membranes on alumina, have shown strong chemical interaction (and eventually alloying) of Pd with alumina at higher temperatures [24]. Most probably, a similar kind of interaction may have occurred with the catalyst used in these tests but at lower temperatures.

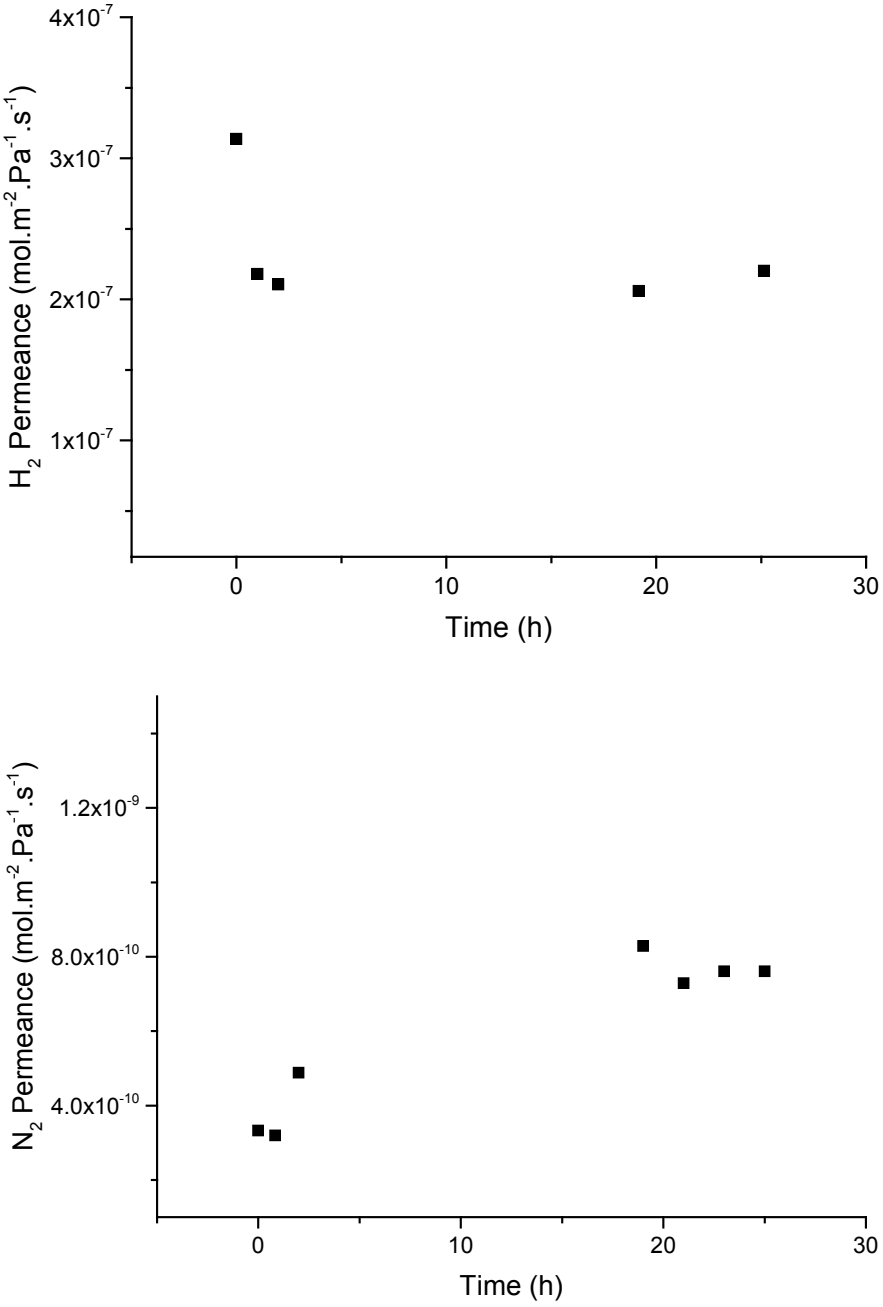

Figure 3.14 N_2 and H_2 permeances at fluidization (bed #1) for E15 membrane (400 °C).

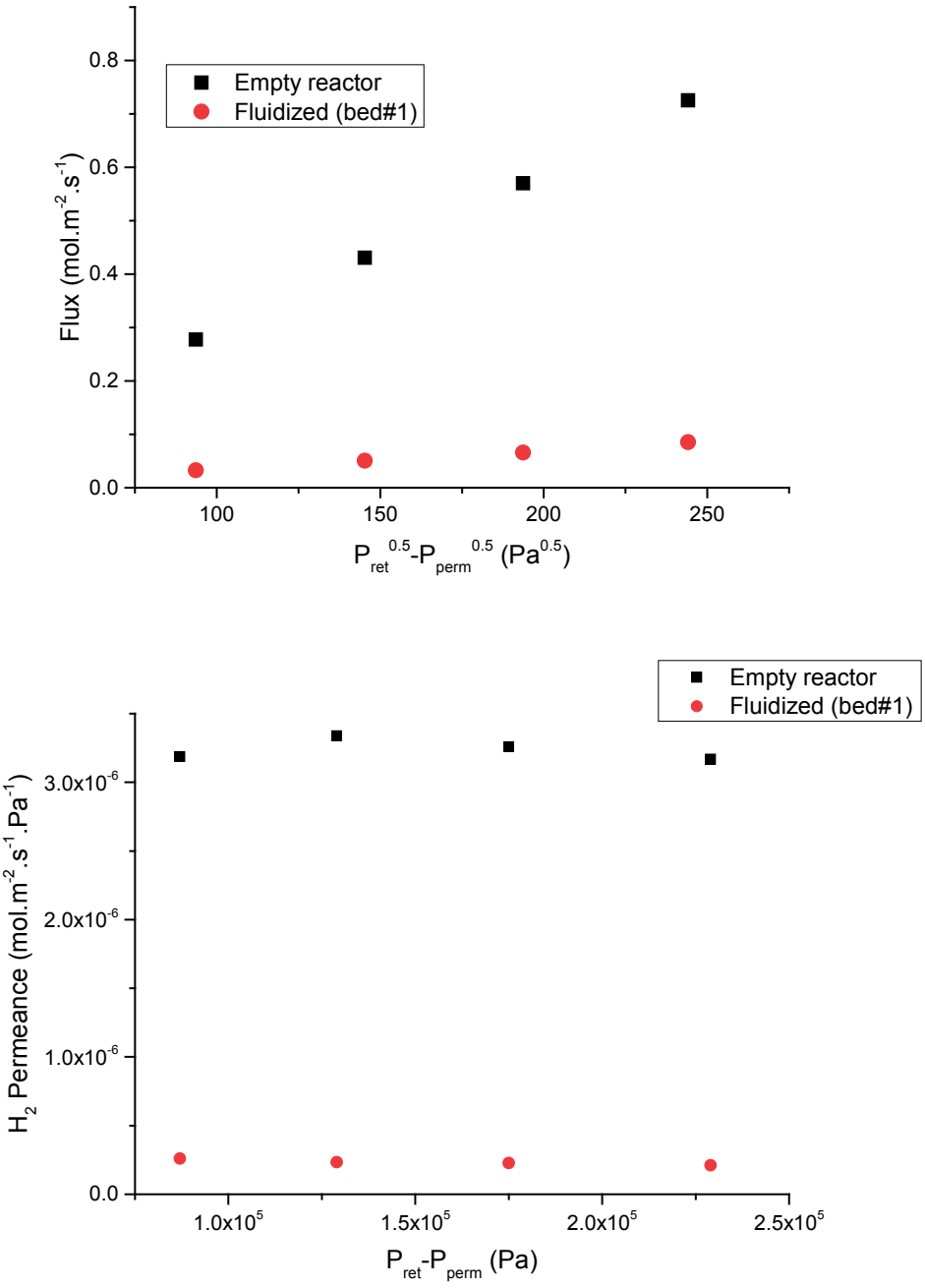

Figure 3.15 (a) H_2 Flux at different pressure differences and (b) H_2 permeance under fluidization conditions (bed #1) in comparison with the case in an empty reactor for the E15 membrane (400 °C).

To demonstrate this, new tests have been carried out at lower pressure to minimize the flux of hydrogen through the membrane and thus rule out the formation of densified zones as a possible cause [23]. Figure 16a shows the results of the long term permeation experiment of membrane E54 under relatively low hydrogen flux. As can be seen, the hydrogen permeance decreases with a sharp slope during the first 20 hours of the tests also for this membrane under low hydrogen flux conditions. After this time a stable membrane performance could be achieved. A comparison of the performance of membrane E54 after different tests is reported in Figure 16b. The membrane performance loss is about 10 times at stable fluidization conditions in comparison to the tests before the fluidization (permeation tests with empty tube). These tests clearly indicate that the possible densification of particles around the membrane cannot be the cause and thus further tests were carried out to elucidate the reason for this behavior.

Figure 3.17 shows the E54 membrane before and after the fluidization tests. As can be seen the membrane surface has changed due to the fluidization tests and the interaction with the catalyst and the inert particles. The membrane was cleaned with pressurized air and demineralized water in order to clean the surface without damaging it. However, no changes in the performances are observed after cleaning of the surface. This suggests that there is a strong interaction on the membrane surface with (components of) the catalyst.

Additional fluidization tests were carried out with the new membrane E56. Firstly, this membrane was protected with a thin layer of glass wool before the fluidization tests. This kind of tests were performed to understand whether the interaction between the particles and the membranes are enhanced by attrition. Additionally, before testing the WGS catalyst with the new membrane, another catalyst has been used (bed #2) for fluidization tests, as this material was already been used for steam methane reforming in fluidized bed membrane reactors without detrimental effects to the membrane performance [25]. After a successful test with the glass wool, the membrane E56 was tested without the glass wool protection (thus in direct contact with bed material #2). In the final test E56 was tested with a protective layer of glass wool together with bed #1 under fluidization conditions (bubbling fluidization regime).

Figure 3.18 shows the results of the performance of the E56 membrane for different test conditions:

a. Without bed before fluidization
b. With glass wool
c. Empty reactor after fluidization test
d. With Bed #2 & glass wool
e. With Bed #2
f. With Bed #1 & glass wool

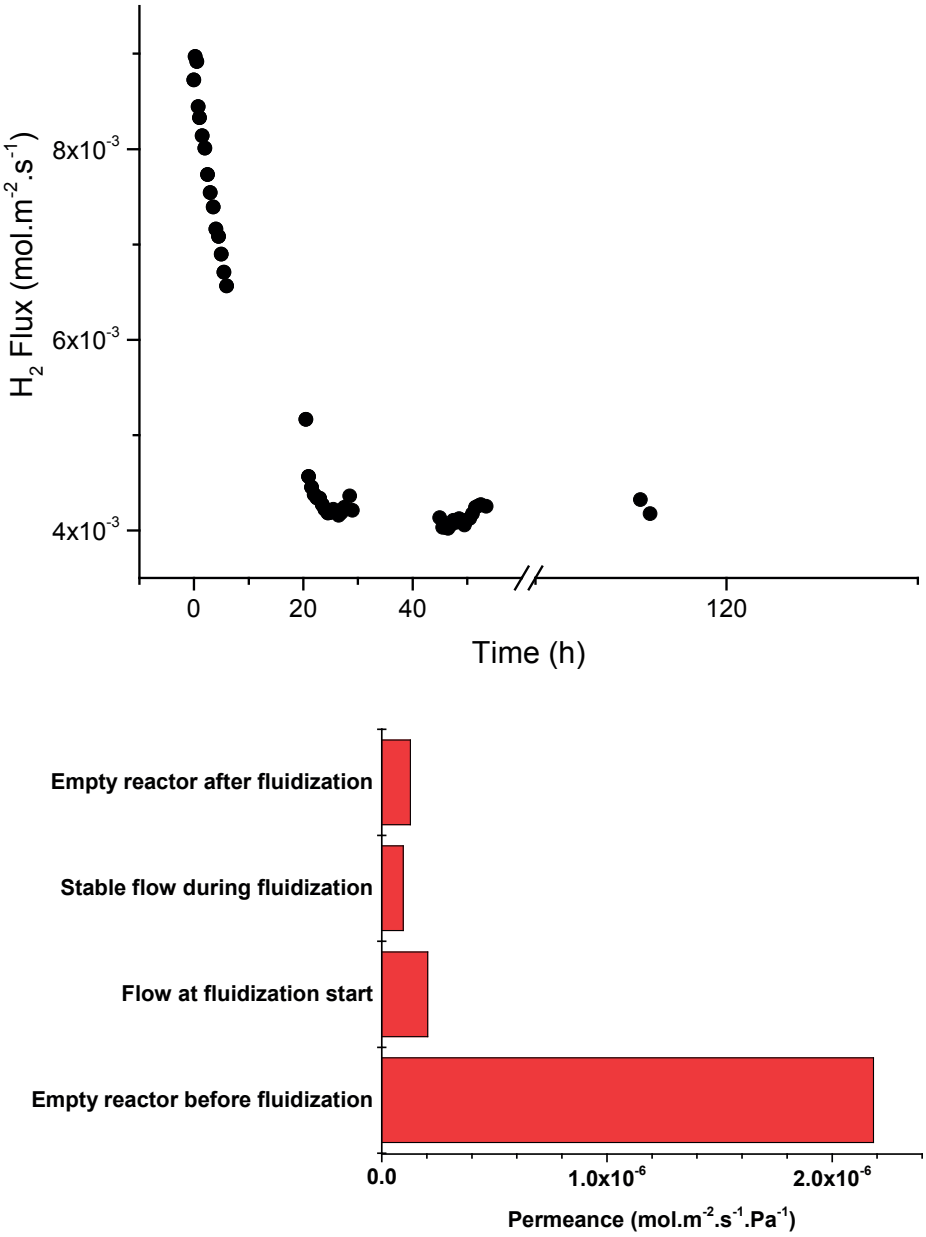

Figure 3.16 (a) H_2 flow evolution of E54 membrane in bed #1 fluidization and at low pressure difference and (b) comparison with results before fluidization (400 °C), H_2 flow rate in the feed up to 1100 ml/min.

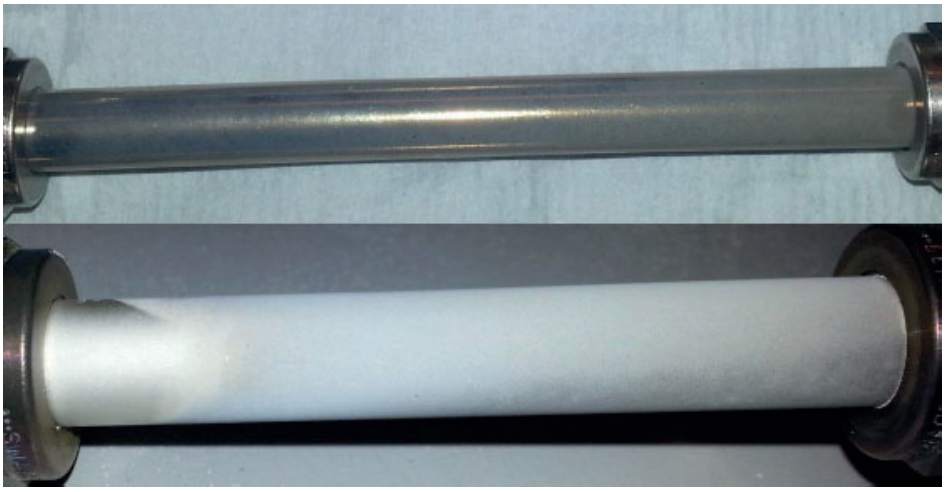

Figure 3.17 E54 membrane before and after fluidization tests with bed #1.

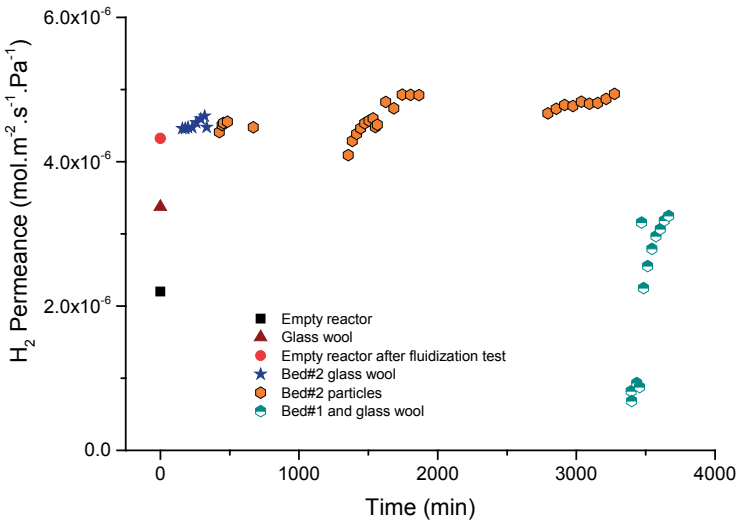

Figure 3.18 E56 membrane performance in different test configurations (400 °C) H_2 flow rate in the feed up to 1100 ml/min.

The figure shows that the membrane permeance increased between the first test (empty reactor case) and the test with glass-wool protection. No decrease of permeance has been detected as the porous glass wool does not induce any additional mass transfer limitation. The reason for the increase of permeance during the tests is the activation of the membrane being exposed to hydrogen at high temperature.

The test with bed material #2 and the protective layer of glass wool shows no decrease in permeance. During the almost 6 hours of test it can be seen that the permeance of the membrane was even slightly increasing over time, again related to the activation of the membrane. Wang et al. [16] reported a reactivation time of about 800 minutes of H_2 exposure before the membrane reached its original value for hydrogen permeance again. After this test, the protective layer of glass wool was removed and the membrane was tested during 48 hours under fluidization conditions with direct contact between the bed material and the membrane. The results obtained show that the membrane performance is not affected by fluidization when bed material #2 was used, in contrast to the tests performed with E54 using bed material #1. This confirms the assumption that the catalyst particles or the filler particles from bed #1 are the cause of the performance loss of the membranes under fluidization conditions. Mechanical stresses due to the fluidization regime has been found not to be responsible for any performance loss of the membrane.

To finalize the study, membrane E56 was protected with glass wool and used under fluidization conditions with bed material #1. It can be observed that the hydrogen permeance was lower than for any of the other cases. After exposing the membrane to air (to remove possible contaminations) the permeance starts to increase. After 6.5 hours of test under fluidization conditions, however, the hydrogen permeance was not yet at the same level as before this last test. So, most probably there is an interaction with the particles even if the membrane is protected by glass wool. After removing the glass wool, it was indeed observed that some particles had reached the membrane surface and probably interacted with the membrane, thereby decreasing its permeance. These tests indicate that in case of reactive particles, a better protection of the membrane should be adopted, while for inert particles, the membrane can be safely used in fluidized beds without any protection.

Figure 3.19a shows the nitrogen permeance of membrane E56 measured over time during the tests with bed material #2 (without glass wool). As can be observed, the permeance of nitrogen increases during the time of fluidization, which leads to a loss of selectivity (see Figure 3.19b). However, after the fluidization tests the selectivity was still above 10,000. A more detailed study is required to assess the influence of fluidization on the sealing material.

Mass transfer limitations and CO poisoning effect

It is well known that the higher the membrane permeation flux, the more important other mass transfer limitations may become. In this section external mass transfer limitations (concentration polarization) and mass transfer limitations due to possible CO poisoning of the membrane surface are further investigated. Different tests were carried out at different H_2/N_2 ratios. The results for the hydrogen flux at different H_2/N_2 mixtures are shown in Figure 3.20.

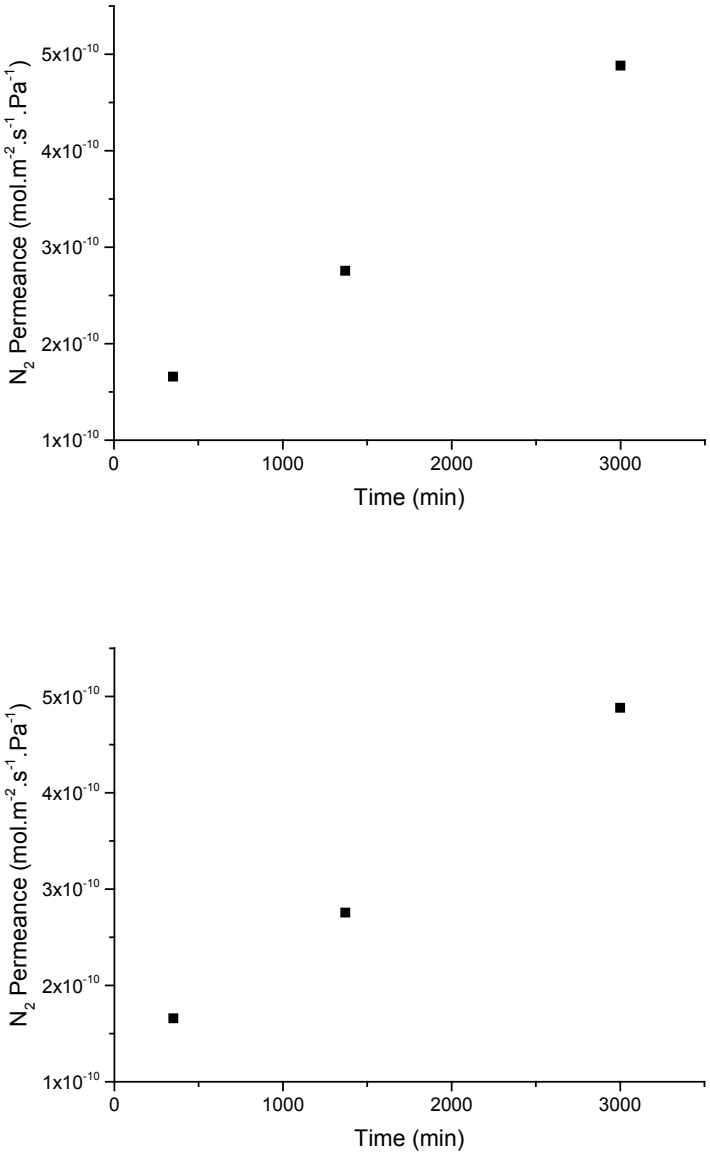

Figure 3.19 a) N_2 permeance and b) H_2/N_2 ideal permselectivity for the E56 membrane during 48h fluidization test with bed #2 (400 °C) gas flow rate (H_2 or N_2) in the feed up to 1100 ml/min.

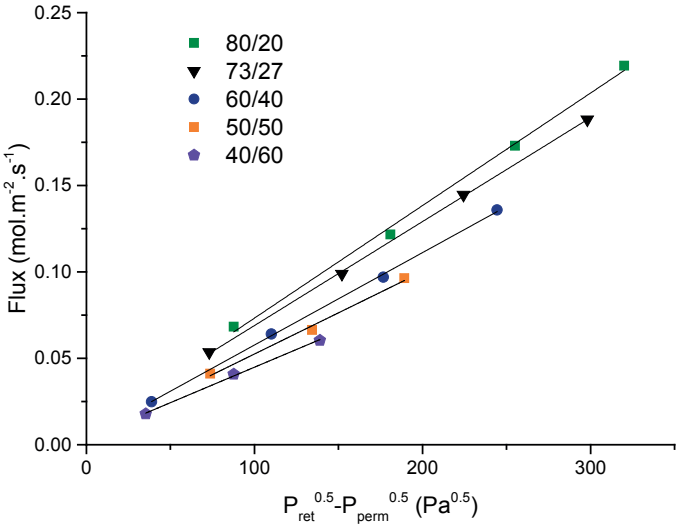

Figure 3.20 Hydrogen permeate flux of E56 membrane at different H_2/N_2 feed compositions (400 °C) gas flow rate in the feed up to 1500 ml/min.

The hydrogen flux through the membrane is plotted as a function of the partial pressure difference of hydrogen (inlet conditions). At the same partial pressure difference the driving force for the permeation for all experiments is the same. The results show that the hydrogen flux decreases when the concentration of hydrogen decreases in the feed gas stream (at the same driving force over the membrane). This behavior confirms that external mass transfer limitations (concentration polarization) are prevailing using gas mixtures, as was anticipated for highly permeable membranes.

These external mass transfer limitations (due to gas phase diffusion) could be decreased in case of fluidization, as the additional mixing induced by the solids circulation patterns in the bubbling (and turbulent) fluidization regime increases the local driving force for permeation. Indeed, comparing the experiments with fluidized particles in the reactor and the experiments with an empty reactor it could be observed that the hydrogen permeance was higher for the fluidized bed cases. This effect can be clearly seen from Figure 3.21, showing a comparison between two experiments carried out at the same conditions (temperature, feed flow rate and composition and transmembrane pressure difference), for an empty membrane reactor and for the fluidized bed membrane reactor. These results confirm once more that the fluidized bed membrane reactor is a preferred reactor concept for highly permeable membranes.

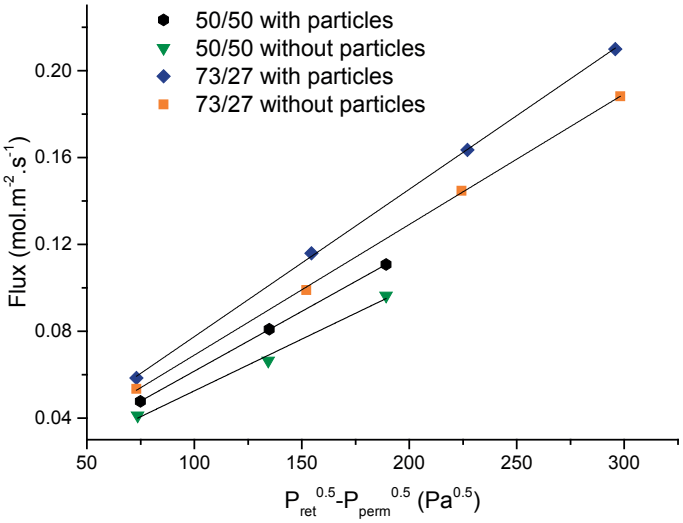

Figure 3.21 H_2 flux through the E56 membrane for the empty reactor and the fluidized bed reactor for different feed compositions (400 °C) gas flow rate in the feed up to 1500 ml/min.

As far as the membrane poisoning is concerned, it is well known that CO can block the active sites of the membrane (CO poisoning effect) and deteriorate the performance of the membranes [26]. This effect can be more pronounced for the highly permeable membranes. The CO poisoning effect was measured in a gas mixture containing 80% of hydrogen and increasing the amount of CO from 0 to 15% in steps of 5%. The results obtained can be seen in the Figure 3.22.

The effect of CO poisoning detected for a maximum amount of 15% CO in the feed gas mixture, is quite low (as expected considering the relatively high temperature). However, this effect is also not negligible, as the permeance of hydrogen decreased about 7% for 15% of CO in the feed gas stream. At higher temperatures this effect should be less significant, since the poisoning effect of CO is dependent on temperature and it is higher at lower temperatures [27].

3.3.3. Post-mortem characterization results of Pd-Ag supported membranes

XPS analysis of membrane E54

Experimental observations on the membranes E54 and E56 confirmed that either the filler (TiO_2) or the catalyst (0.16%Re0.34%Pt6%Ce/TiO_2) from bed material #1 were responsible for the loss of the hydrogen permeance during the fluidization tests. Therefore, XPS analysis was carried out on membrane E54 to elucidate the reason for the loss of permeance.

Figure 3.23 shows the sample of the E54 membrane that was used for the XPS analysis, which represents approximately half of the membrane. As a reference, one piece of E54 was

cut before the test, which has also been analyzed with XPS. The XPS measurements were carried out without etching, which makes the results being representative for the first 10 nm of the membrane surface. The area of each measurement was about 400 µm in diameter.

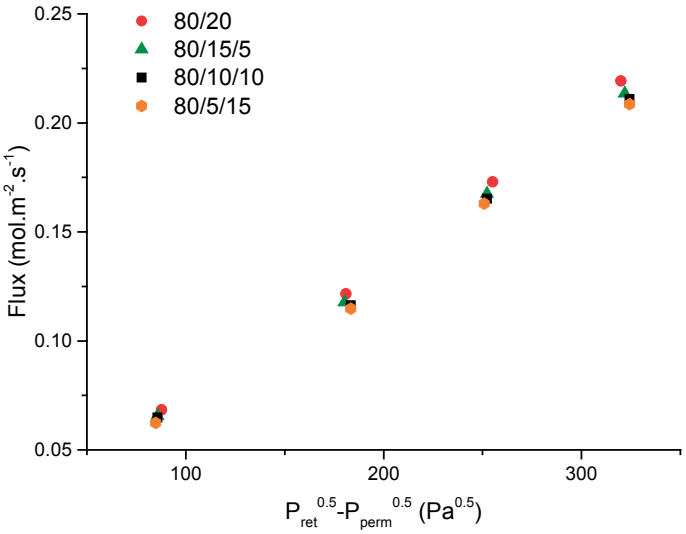

Figure 3.22 Effect of CO poisoning on hydrogen flux of E56 membrane (400 °C, the legend indicates the feed composition $H_2/CO/N_2$) gas flow rate in the feed up to 1500 ml/min.

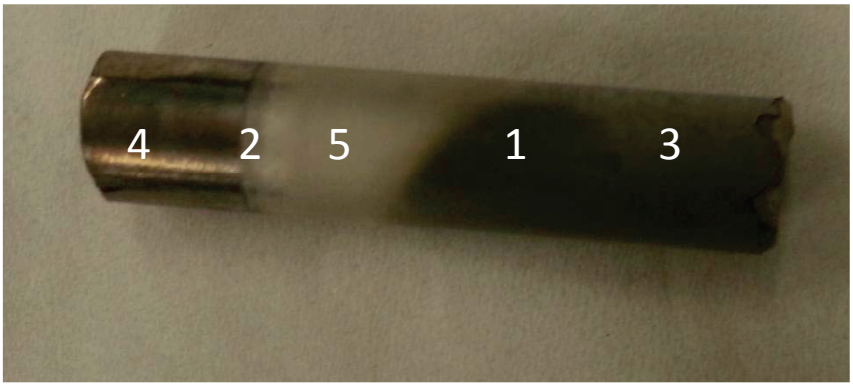

Figure 3.23 Post-mortem E54 sample used for the XPS analysis: (1) Membrane surface was carefully cleaned with paper to remove "dust"; (2) Area that is between the Swagelok® connector and the membrane without graphite; (3) Surface which was under fluidization without removing the "dust"; (4) Area where the graphite sealing was placed; (5) surface with less signs of interaction (defined hereafter as stagnant zone).

The results of the XPS analysis have been summarized in Table 3.9.

Table 3.9 Results of XPS analysis for E54

Sample Identifier		Ag 3d %	Ce 3d %	O 1s %	Pd 3d %	S 2p %	Si 2p %	C 1s %	Ti 2p %
1	Cleaned part	4	0.2	53.6	4	1	0	19.2	18.1
2	Swagelok® part	4.6	0	0	35.3	10.6	0	48.5	1.1
3	Fluidized part	3.8	0.2	56	4.4	1.2	0	14.6	19.8
4	Sealing part	0.3	0	12.2	2.6	0.3	0	84.4	0.2
5	Stagnant zone part	16.2	0	0	55.2	5.7	0	21.6	1.3
6	Ref membrane1	0	0	0	27.7	2.5	2.7	67.1	0
7	Ref membrane2	0	0	0	28.6	0	3.3	68.1	0
8	Ref membrane3	0	0	0	28.2	2.5	3.5	65.9	0

As can be seen in the results of Table 3.9, Ti and O are found in high amounts on the membrane surface (1,3), where the effect of fluidization was more pronounced. Comparing these results to the stagnant zone (5), it is evident that this zone is nearly free of Ti and completely free of O which implies that the interaction between the membrane and the solids occurs where there is more contact between the two. In the part where the Swagelok® fitting is close to the membrane a significant amount of sulfur was found, which could possibly have been released by the Swagelok® fitting due to reaction with gases under high temperature, since sulfur is present in the stainless steel parts of Swagelok [28].

The results for the measurements for the reference membrane show that there is no Ti and no O before the fluidization tests, as expected. It is interesting to mention that no Ag was detected on the surface of the membrane in the XPS analysis, which is probably related to the measuring method. XPS with etching would lead to a correct detection of Ag and Pd, but would lead to an incorrect detection of Ti and O that are the components leading to a decrease of permeance according to our previous observations.

A reason for the high amount of carbon found in the sealing part is the graphite ferrule attached to the membrane surface. Nevertheless, a significant amount of carbon is also detected for the samples under fluidization regime due to the contamination by the paper used for cleaning the surface before the tests. In general, it can be concluded that the catalyst active species seems not to be the reason for the decrease in permeance, since no Re, Ce or Pt could be found on the membrane surface, pointing towards the support material as the cause for the decrease in membrane permeance while the main responsible seems to be the interaction of Ti with the palladium layer. Interaction of TiO_2 and Pd was already observed by Dittmeyer and co-workers [29]. It is thus suggested to use a catalyst support based on a material that does not have interaction with palladium like alumina or zirconia-based supports. In a future work we will further investigate the interaction of the Pd-based membranes with different catalysts/supports at different operating conditions.

3.4. Conclusions

In this chapter a series of thin membranes have been produced with sequential electroless plating and tested as permeators and in fluidized bed conditions. A simple technique for membrane sealing has been implemented and discussed in the chapter based on standard connectors and graphite ferrules. The membranes have shown very high and stable permeation rates (with high selectivities), such that external mass transfer limitations start to be a limiting factor for the hydrogen permeation. It has been demonstrated that a fluidized bed reactor can decrease the extent of external mass transfer limitations as a result of increased gas mixing. However, the tests under fluidization conditions show that there may be an interaction between some bed materials and the membranes, which may result in a decrease in the membrane permeation. The fluidized bed reactor should thus be operated with catalyst/supports that have no interaction with the membrane such as alumina (as demonstrated in this chapter) or zirconia-based supports.

Bibliography

[1] S.N. Paglieri, J.D. Way, Innovations in Palladium Membrane Research, Sep. Purif. Rev. 31 (2002) 1–169. doi:10.1081/SPM-120006115.

[2] F. Gallucci, E. Fernandez, P. Corengia, M. van Sint Annaland, Recent advances on membranes and membrane reactors for hydrogen production, Chem. Eng. Sci. 92 (2013) 40–66. doi:10.1016/j.ces.2013.01.008.

[3] G. Barbieri, A. Brunetti, G. Tricoli, E. Drioli, An innovative configuration of a Pd-based membrane reactor for the production of pure hydrogen. Experimental analysis of water gas shift, J. Power Sources. 182 (2008) 160–167. doi:10.1016/j.jpowsour.2008.03.086.

[4] F. Gallucci, M. van Sint Annaland, J. A. M. Kuipers, Pure hydrogen production via autothermal reforming of ethanol in a fluidized bed membrane reactor: A simulation study, Int. J. Hydrogen Energy. 35 (2010) 1659–1668. doi:10.1016/j.ijhydene.2009.12.014.

[5] F. Gallucci, M. van Sintannaland, J. A. M. Kuipers, Theoretical comparison of packed bed and fluidized bed membrane reactors for methane reforming, Int. J. Hydrogen Energy. 35 (2010) 7142–7150. doi:10.1016/j.ijhydene.2010.02.050.

[6] The Department of Energy Hydrogen and Fuel Cells Program Plan, 2011. doi:DOE/EE-0651.

[7] N. Iniotakis, C.B. Von Der Decken, H. Fedders, W. Froehling, F. Sernetz, Hydrogen Permeation Membrane, 4699637, 1987.

[8] D.A. Pacheco Tanaka, M.A. Llosa Tanco, S.I. Niwa, Y. Wakui, F. Mizukami, T. Namba, T.M. Suzuki, Preparation of palladium and silver alloy membrane on a porous α-alumina tube via simultaneous electroless plating, J. Memb. Sci. 247 (2005) 21–27. doi:10.1016/j.memsci.2004.06.002.

[9] J. Okazaki, D. Tanaka, M. Tanco, Y. Wakui, F. Mizukami, T. Suzuki, Hydrogen permeability study of the thin Pd–Ag alloy membranes in the temperature range across the α–β phase transition, J. Memb. Sci. 282 (2006) 370–374. doi:10.1016/j.memsci.2006.05.042.

[10] T.M. Suzuki, D.A. Pacheco Tanaka, Composite palladium membranes with improved durability toward hydrogen embrittlement, in: Handb. Membr. Res. Prop. Perform. Appl., Nova Science Publishers, 2009: pp. 1–10.

[11] X. Hu, Y. Huang, S. Shu, Y. Fan, N. Xu, Toward effective membranes for hydrogen separation: Multichannel composite palladium membranes, J. Power Sources. 181 (2008) 135–139. doi:10.1016/j.jpowsour.2008.02.091.

[12] P. Quicker, V. Höllein, R. Dittmeyer, Catalytic dehydrogenation of hydrocarbons in palladium composite membrane reactors, Catal. Today. 56 (2000) 21–34. doi:10.1016/S0920-5861(99)00259-X.

[13] F. Rusting, P.P.A.C. Pex, J.A.J. Peters, G.D. Jong, Sealing socket and method for arranging a sealing socket to a tube, EP 1257758, 2005.

[14] W. Chen, X. Hu, R. Wang, Y. Huang, On the assembling of Pd/ceramic composite membranes for hydrogen separation, Sep. Purif. Technol. 72 (2010) 92–97. doi:10.1016/j.seppur.2010.01.010.

[15] F. Van Berkel, C. Hao, C. Bao, C. Jiang, H. Xu, J. Morud, T. Peters, E. Soutif, J.W. Dijkstra, D. Jansen, B. Song, Pd-membranes on their way towards application for CO_2-capture, Energy Procedia. 37 (2013) 1076–1084. doi:10.1016/j.egypro.2013.05.204.

[16] W. Wang, X. Pan, X. Zhang, W. Yang, G. Xiong, The effect of co-existing nitrogen on hydrogen permeation through thin Pd composite membranes, Sep. Purif. Technol. 54 (2007) 262–271. doi:10.1016/j.seppur.2006.09.016.

[17] A.M. Adris, C.J. Lim, J.R. Gracc, The fluidized-bed membrane reactor for steam methane reforming: model verification and parametric study, Chem. Eng. Sc. 52 (1997) 1609–1622.

[18] Ø. Hatlevik, S.K. Gade, M.K. Keeling, P.M. Thoen, A.P. Davidson, J.D. Way, Palladium and palladium alloy membranes for hydrogen separation and production: History, fabrication strategies, and current performance, Sep. Purif. Technol. 73 (2010) 59–64. doi:10.1016/j.seppur.2009.10.020.

[19] L. Shi, A. Goldbach, H. Xu, High-flux H_2 separation membranes from (Pd/Au)n nanolayers, Int. J. Hydrogen Energy. 36 (2011) 2281–2284. doi:10.1016/j.ijhydene.2010.11.056.

[20] T. A. Peters, T. Kaleta, M. Stange, R. Bredesen, Development of thin binary and ternary Pd-based alloy membranes for use in hydrogen production, J. Memb. Sci. 383 (2011) 124–134. doi:10.1016/j.memsci.2011.08.050.

[21] K.E. Coulter, J.D. Way, S.K. Gade, S. Chaudhari, G.O. Alptekin, S.J. DeVoss, S.N. Paglieri, B. Pledger, Sulfur tolerant PdAu and PdAuPt alloy hydrogen separation membranes, J. Memb. Sci. 405–406 (2012) 11–19. doi:10.1016/j.memsci.2012.02.018.
[22] Y.H. Ma, Composite Pd and Pd alloy porous stainless steel membranes for hydrogen production and process intensification, 2009.
[23] N.T.Y. Dang, F. Gallucci, M. van Sint Annaland, Micro-structured fluidized bed membrane reactors: Solids circulation and densified zones distribution, Chem. Eng. J. 239 (2014) 42–52. doi:10.1016/j.cej.2013.11.001.
[24] J. Okazaki, T. Ikeda, D. A. Pacheco Tanaka, M. a Llosa Tanco, Y. Wakui, K. Sato, F. Mizukami, T.M. Suzuki, Importance of the support material in thin palladium composite membranes for steady hydrogen permeation at elevated temperatures., Phys. Chem. Chem. Phys. 11 (2009) 8632–8638. doi:10.1039/b909401f.
[25] F. Gallucci, M. van Sint Annaland, J. A. M. Kuipers, Autothermal Reforming of Methane with Integrated CO_2 Capture in a Novel Fluidized Bed Membrane Reactor. Part 2 Comparison of Reactor Configurations, Top. Catal. 51 (2008) 146–157. doi:10.1007/s11244-008-9127-7.
[26] A. Basile, F. Gallucci, Membranes for Membrane Reactors, John Wiley & sons, 2011.
[27] F. Gallucci, F. Chiaravalloti, S. Tosti, E. Drioli, a. Basile, The effect of mixture gas on hydrogen permeation through a palladium membrane: Experimental study and theoretical approach, Int. J. Hydrogen Energy. 32 (2007) 1837–1845. doi:10.1016/j.ijhydene.2006.09.034.
[28] Swagelok, Stainless Steel Seamless Tubing, Febr. 2013. (2013) 1–4.
[29] Y. Huang, R. Dittmeyer, Preparation and characterization of composite palladium membranes on sinter-metal supports with a ceramic barrier against intermetallic diffusion, J. Memb. Sci. 282 (2006) 296–310. doi:10.1016/j.memsci.2006.05.032.

''Now it would be very remarkable if any system existing in the real world could be exactly represented by any simple model. However, cunningly chosen parsimonious models often do provide remarkably useful approximations. For example, the law PV = RT relating pressure P, volume V and temperature T of an "ideal" gas via a constant R is not exactly true for any real gas, but it frequently provides a useful approximation and furthermore its structure is informative since it springs from a physical view of the behavior of gas molecules. For such a model there is no need to ask the question "Is the model true?". If "truth" is to be the "whole truth" the answer must be "No". The only question of interest is "Is the model illuminating and useful?"

George Box, 1978

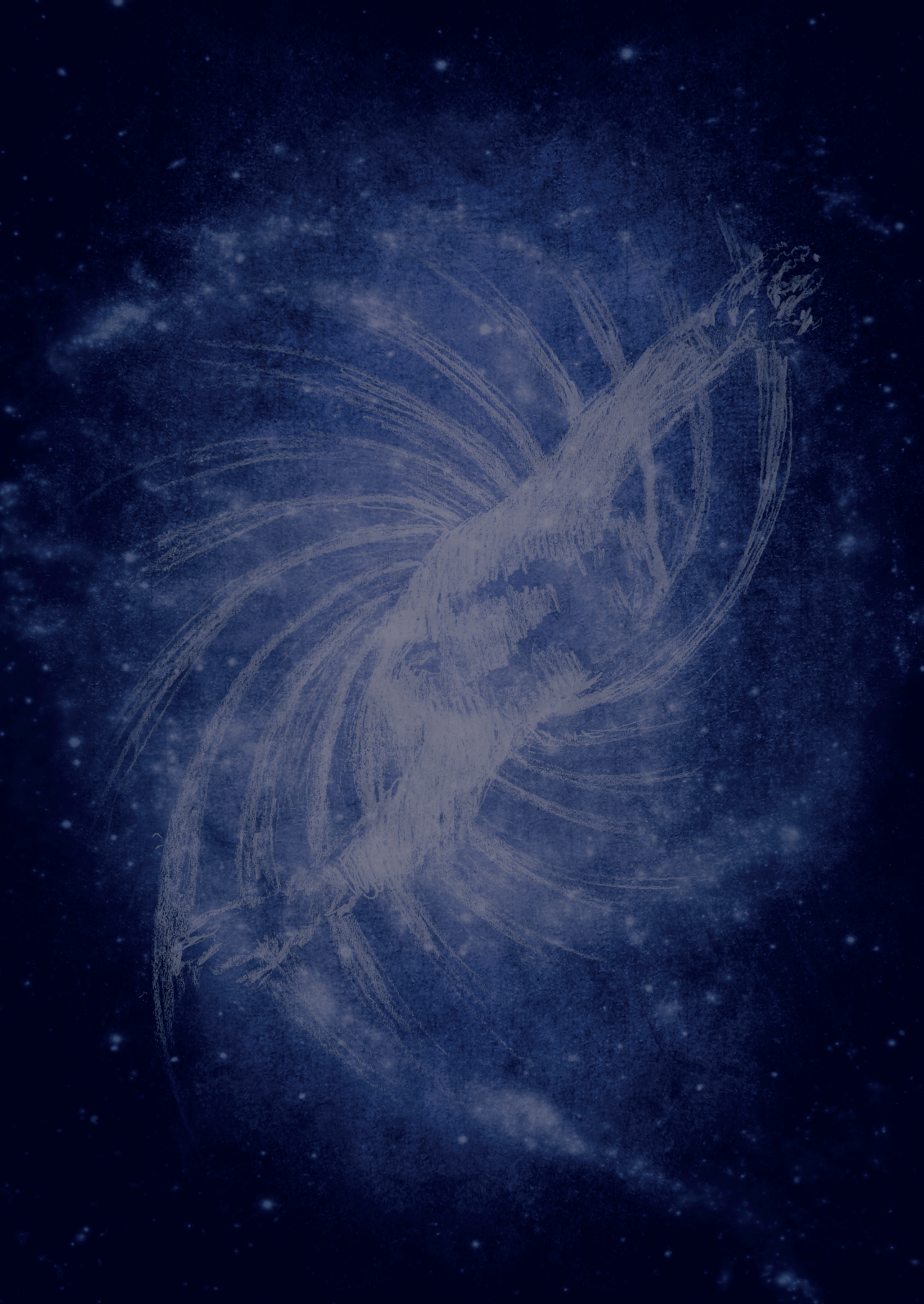

Chapter 4

On concentration polarization in fluidized bed membrane reactors

Abstract

Palladium-based membrane-assisted fluidized bed reactors have been proposed for the production of ultra-pure hydrogen at small scales. Due to the improved heat and mass transfer characteristics inside such reactors, it is commonly believed that they can outperform packed bed membrane reactor configurations. It has been widely shown that the performance of packed bed membrane reactors can seriously suffer from mass transfer limitations from the bulk of the catalyst bed to the surface of the membranes (concentration polarization) when using modern highly permeable membranes. The extent of concentration polarization in fluidized bed membrane reactors has not yet been researched in detail. In this work, we have quantified the concentration polarization effect inside fluidized bed membrane reactors with immersed vertical membranes with high hydrogen fluxes. A Two-Fluid Model (TFM) was used to quantify the extent of concentration polarization and to visualize the concentration profiles near the membrane. The concentration profiles were simplified to a mass transfer boundary layer (typically 1 cm in thickness), which was implemented in a 1D fluidized bed membrane reactor model to account for the concentration polarization effects. Predictions by the TFM and the extended 1D model showed very good agreement with experimental hydrogen flux data. The experiments and models show that concentration polarization can reduce the hydrogen flux by a factor of 3 even at low H_2 concentrations in the feed (10%), which confirms that concentration polarization can also significantly affect the performance of fluidized bed membrane reactors when integrating highly permeable membranes, but to a somewhat lesser extent than packed bed membrane reactors. The extraction of hydrogen also affects the gas velocity and solids hold-up profiles in the fluidized bed.

Nomenclature

Symbols

A	Area	m^2
C_1, C_2	Constants in frictional stress model	-
B	Exchange of fluctuation energy	kg m^{-1} s^{-3}
C	Concentration	mol m^{-3}
C_d	Drag coefficient	-
D	Diffusion/dispersion coefficient	m^2s^{-1}
d	Diameter	m
E_a	Activation energy	J mol^{-1}
e	Coefficient of restitution	-
f	Fraction	-
Fr	Constant in frictional stress model	N m^{-2}
g	Gravitational acceleration	m s^{-2}
g_0	Radial distribution function	-
H	Height	m
	Unit tensor	-
J	Membrane flux	mol m^2 s
K	Mass transfer coefficient	m s^{-1}
k_d	Mass transfer coefficient bulk to membrane	m s^{-1}
M_w	Molecular weight	kg mol^{-1}
N	Flux	mol m^2 s
P	Partial pressure	Pa
P_m	Permeability	mol m^{-1} s^{-1} $Pa^{-0.5}$
$P_{m,0}$	Permeation constant	mol m^{-1} s^{-1} $Pa^{-0.5}$
p	Pressure	Pa
Q_{Pd}	Permeance	mol m^{-2} s^{-1} $Pa^{-0.5}$
R	Universal gas constant	J mol^{-1} K^{-1}
r	Radial position	m
Re	Reynolds number	-
S	Strain rate	s^{-1}
S	Source term	-
Sh	Sherwood number	-
t	Time	-
t_m	Membrane thickness	m
T	Temperature	-
u	Velocity	m s^{-1}
V	Volume	m^3
X	Molar fraction	-
Y	Mass fraction	-
Z	Axial position	m

Greek letters

α	Volume fraction	-
β	Interphase drag coefficient	kg m^{-3} s^{-1}
γ	Dissipation of granular energy	kg m^{-1} s^{-3}
δ	Film layer thickness	m
θ	Granular temperature	m^2 s^{-2}
κ	Conductivity of granular energy	kg m^{-1} s^{-1}
λ	Bulk viscosity	kg m^{-1} s^{-1}
μ	Shear viscosity	kg m^{-1} s^{-1}
ρ	Density	kg m^{-3}
$\imath$	Shear stress tensor	N m^{-2}
ϕ^{fric}	Angle of internal friction	°

Subscripts & superscripts

avg	Average
b	Bubble
bc	Bubble to cloud
be	Bubble to emulsion
bulk	Bulk
ce	Cloud to emulsion
cell	Cell(s)
e	Emulsion
fric	Frictional
g	Gas
h	Hydraulic
m	Membrane
max	Maximum
mf	Minimum fluidization
min fr.	Minimum friction
mol	Molecular
n	Number of CSTRs
p	Particle
pp	Particle-particle
pw	Particle-wall
perm	Permeate
r	Radial
reac	Reactor
rise	Rise
s	Solid
sim	simulation
T	Transposed
tot	Total

4.1 Introduction

Currently, hydrogen is mainly produced on large scale via steam reforming of methane (SMR) [1]. In this process, methane is first reformed with steam (Eq. 4.1) in high temperature multi-tubular packed bed reactors. In the second step the carbon monoxide is converted via the water gas shift (WGS) reaction (Eq. 2) in packed bed reactors. Typically, a two stage WGS is used to take advantage of fast reaction rates at high temperatures (450 °C) and higher equilibrium conversions at lower temperatures (200 °C). Finally, the hydrogen produced is further purified using pressure swing adsorption (PSA).

Steam methane reforming reaction (SMR):

$$CH_4 + H_2O \leftrightarrow CO + 3H_2 \qquad \Delta H_r = 206 \ kJ/mol \qquad \text{Eq.(4.1)}$$

Water gas shift reaction (WGS):

$$CO + H_2O \leftrightarrow CO_2 + H_2 \qquad \Delta H_r = -41 \ kJ/mol \qquad \text{Eq.(4.2)}$$

The efficiency of the whole process is approximately 80% (equivalent hydrogen efficiency) thanks to steam/electricity export [2]. The heat integration between the different stages becomes more complicated at smaller scales, while heat export cannot be realized in distributed hydrogen production applications. For this reason the system becomes inefficient and non-economical at smaller scales. The cost of the hydrogen produced at large scale is around 0.2 €/Nm^3 while it increases up to 0.4-0.5 €/Nm^3 at smaller scales [2].

The efficiency of the hydrogen production via methane reforming can be increased by integrating hydrogen production and separation in a single multifunctional reactor. This can be achieved by using perm-selective palladium-based membranes in membrane reactors. Recovering the hydrogen during the reaction, results in a shift of the equilibrium towards the products, thus allowing achieving much higher conversions at lower temperatures. The shifting effect (Le Chatelier's principle) allows to minimize the reactor volume up to 80% for WGS [3] and maximize the efficiencies, as total conversion can be achieved already at lower temperatures [4].

In literature, both packed bed and fluidized-bed membrane reactor configurations have been proposed for SMR and WGS reactions. The latest developments in the fabrication of ultra-thin membranes with high permeation rates [5], have once more sparked the debate on the inherent bed-to-membrane mass transfer limitations (concentration polarization) in packed bed membrane reactors [6,7].

From an experimental point of view, Hara et al. [8] studied the decline of hydrogen permeation in a packed bed membrane reactor by injecting the reactor with H_2-Ar and H_2-CO mixtures. It was found that the reduction in hydrogen permeation was caused by CO poisoning of the Pd based membrane and concentration polarization near the membrane wall. It was

concluded that in order to fairly predict the membrane reactor performance, concentration polarization needs to be taken into account.

Mori et al. [9] investigated the influence of concentration polarization on hydrogen production via SMR in a packed bed membrane reactor with a highly permeable membrane. They performed experiments and compared them with a simple model that did not take into account the effect of concentration polarization. By increasing the reactor pressure, they found that the experimental methane conversion was lower than the simulated conversion. This implies that concentration polarization is occurring in the reactor and affects the methane conversion. The presence of concentration polarization was confirmed with experiments with a binary mixture of hydrogen and nitrogen.

Caravella et al. [6] made a model predicting the permeance of hydrogen in a hydrogen nitrogen mixture including the effect of concentration polarization in an empty annular tube. It was found that the effect of polarization is relevant not only for the very thin membranes (1-5 μm) with high fluxes but also for the thicker ones (100 μm) at certain operating conditions.

In a CFD study by Nekhamkina et al. [10], the mass transfer processes in two configurations were studied: an empty reactor with (i) the membrane at the wall, and (ii) an annular cylinder with the membrane as the inner tube. A model was developed to predict the membrane flux considering the effect of concentration polarization. A parameter Γ was defined which represents the ratio of the diffusion to the permeation flux. It was concluded that only when $\Gamma>6$ the effect of concentration polarization can be neglected.

To circumvent the mass transfer limitations typical of empty or packed bed membrane reactor configurations, fluidized bed membrane reactors were suggested, because of their improved heat and mass transfer characteristics. Patil et al. [11] and Gallucci et al. [12] successfully demonstrated this membrane reactor concept for the SMR reaction with relatively low flux membranes. No concentration polarization effects were reported, but the flux of the membrane used was 5-10 times lower than recently available high permeable membranes.

More recently, Helmi et al. [13] successfully demonstrated the long term (>900 h) performance of a fluidized bed membrane reactor utilizing very high flux membranes for ultra-pure hydrogen production via WGS. Although the long term stability of this membrane reactor has been confirmed (with CO content in the permeate side <10 ppm), no independent study has been performed yet on the concentration polarization effects in fluidized bed membrane reactors where a large amount of gas is extracted via the membranes.

This work focuses on the quantification of the extent of concentration polarization in fluidized bed membrane reactors. A simple one-dimensional phenomenological model is developed which can capture the effect of concentration polarization in fluidized bed membrane reactors. The Two-Fluid Model, an Euler-Euler model using the Kinetic Theory of Granular Flow to describe the solids phase rheology, is used to estimate the mass transfer boundary layer thickness required by the 1D model. The predictions by both models are compared with

results obtained from experiments showing good agreement, confirming that concentration polarization can also prevail in fluidized bed membrane reactors.

4.2 Modeling

4.2.1 1D phenomenological model

In this work a one-dimensional, two-phase flow model for bubbling fluidized beds was used. This model was originally proposed by Kato and Wen [14] for standard fluidized beds without internals, and was later extended to membrane assisted fluidized bed reactors by Deshmukh et al. [15]. In this model the fluidized bed is divided into a number of CSTR's in series for both the emulsion and bubble phases, while mass transfer limitation from the bulk of the bed to the surface of the membranes is not accounted for.

In a fluidized bed membrane reactor, the extraction of a large amount of gas may induce the formation of a densified zone (a region with higher solids hold-up) around the membranes [16,17]. This is caused by the high flux through the membrane relative to the fluidization velocity, resulting in a drag force of the particles towards the membranes, which is more pronounced for smaller particles [16]. In the densified zone the mixing is worse than in the bulk of the bed because the particles have much lower velocities (eventually behaving like a slowly moving bed). Because of the good mixing properties of fluidized beds, it is expected that the concentration gradient mainly resides in the densified zone around the membrane, and not in the bulk of the fluidized bed. However, this assumption needs to be validated and implemented in the phenomenological model.

Several theories exist to describe the mass transfer from the bulk of the bed to the surface of the membranes, where the simplest model is the film layer model [18]. In this model it is assumed that the concentration gradient resides entirely in a thin stagnant film (mass transfer boundary layer) with a thickness d around the membrane. Figure 4.1 shows a schematic representation of the one-dimensional fluidized bed membrane reactor model considering a film layer around the membrane. Furthermore it is assumed that:

- Bulk concentration is constant in the radial direction
- There is no axial convection in the film layer
- Dispersion only occurs in the radial direction (axial dispersion is neglected)
- The flux is independent of the radial distance from the membrane
- Isobaric and isothermal conditions

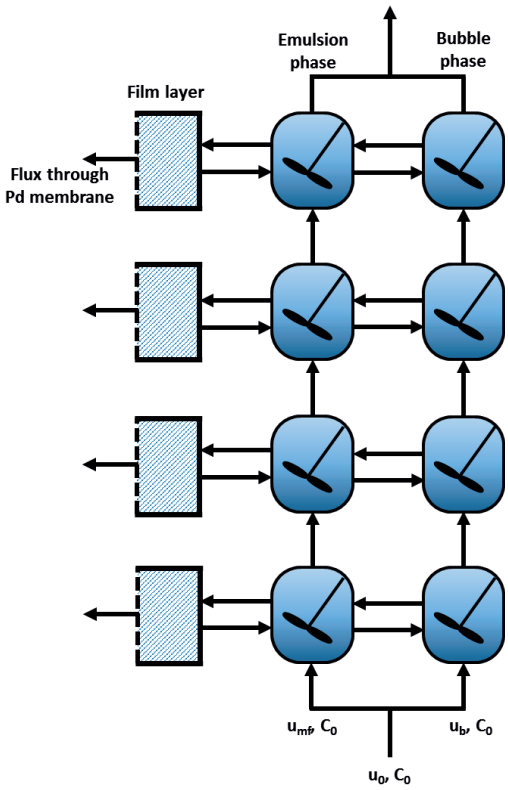

Figure 4.1 Schematic representation of the 1D phenomenological fluidized bed membrane reactor model

Using the before-mentioned assumptions and Fick's law to describe the H_2 flux through the boundary layer while accounting for the induced net (convective) drift flux, the H_2 flux towards the membrane can be written as:

$$N_{H_2} = \frac{J_{H_2}}{1 - X_{H_2}} = \frac{DC_{tot}}{1 - X_{H_2}} \frac{dX_{H_2}}{dr} \qquad \text{Eq.(4.3)}$$

Integration of equation 4.3 yields:

$$N_{H_2} = k_d C_{tot} \ln\left(\frac{1 - X_{H_2,m}}{1 - X_{H_2,bulk}}\right) \qquad \text{Eq.(4.4)}$$

with the mass transfer coefficient from the bulk to the membrane wall defined as

$$k_d = \frac{D}{\delta} \qquad \text{Eq.(4.5)}$$

which can be determined from a Sherwood correlation:

$$Sh = \frac{k_d d_H}{D}$$

Eq.(4.6)

Thus, for the thickness of the film layer:

$$\delta = \frac{d_H}{Sh}$$

Eq.(4.7)

In the literature, no Sherwood correlation was found that can describe the mass transfer from the bulk of a fluidized bed to an immersed wall. Moreover, also no generally applicable correlation for the radial dispersion in fluidized beds is available. Therefore, the radial dispersion in the densified zone of the mass boundary layer close to the membranes is estimated using the correlation by Tsotsas and Schlünder [19] for the dispersion coefficient in packed beds (see Table A.1 in appendix A). It should be noted that the dispersion coefficient is likely to be somewhat under-predicted.

The mass transfer of hydrogen through the Pd based membrane is described with the solution diffusion mechanism [20]. In this approach, diffusion through the dense Pd layer is considered as the rate limiting step for H_2 permeation. The flux through the membrane is induced by the H_2 partial pressure gradient between the retentate (reaction zone) and the permeate side (inside the tubes) of the membrane. It is assumed that there is no concentration gradient (nor pressure gradient) across the porous ceramic support layer of the membrane, and also mass transfer limitations at the permeate side are assumed to be negligible (Figure 4.2). In principle, the model could be extended to account for these factors.

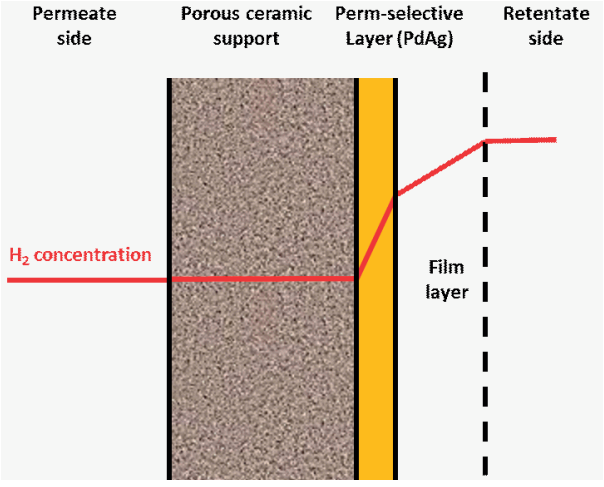

Figure 4.2 H_2 concentration profile across the membrane.

The membrane flux is thus described by Sieverts' law [20]:

$$J_{H_2} = \frac{P_m}{t_m}(P_{H_2,\mathrm{m}}^{0.5} - P_{H_2,per}^{0.5}) \qquad [mol/m^2 s]$$

Eq.(4.8)

$$P_m = P_{m_0} exp\left(-E_a \diagup RT\right)$$

Eq.(4.9)

in which P_m is the membrane permeability, $P_{m0}$is the permeation constant, E_a is the membrane activation energy and t_m is the membrane selective layer thickness.

Furthermore, from the bubble phase it is assumed that there is only mass transfer to the emulsion phase, not directly to the membrane, because of the relatively small bubble hold-up in bubbling fluidized beds and especially near the vertically immersed membrane tubes. From the emulsion phase the hydrogen transfers to the film layer and from there it permeates through the membrane. Therefore the component mass balance for the bubble phase reads:

$$\frac{d(u_{b,rise} f_b C_b)}{dz} = u_{b,rise} f_b \frac{dC_b}{dz} + f_b C_b \frac{du_{b,rise}}{dz} + u_{b,rise} C_b \frac{df_b}{dz} = -K_{be} f_b (C_b - C_e)$$

Eq.(4.10)

The rise velocity of bubbles in a swarm ($u_{b,rise}$), the bubble fraction (f_b) and the bubble to emulsion phase mass transfer coefficient K_{be} is determined from correlations reported in [21]. The total superficial velocity in CSTR number n ($u_{tot,n}$), is calculated by subtracting the flow through the membrane from the axial flow in CSTR number n-1:

$$u_{tot,n} = u_{tot,n-1} - \frac{J_{H_2}.A_m}{A_{reac} C_{tot}}$$

Eq.(4.11)

The emulsion phase exchanges hydrogen with the bubble phase and transports it via the film layer to the membrane wall. This can be described as:

$$\frac{dC_e}{dz} = \frac{1}{u_{mf} A_{reac}} \left[f_b K_{be} A_{reac} (C_b - C_e) - k_d C_{tot} \ln\left(\frac{1 - X_m}{1 - X_e}\right) \right]$$

Eq.(4.12)

The flux entering the film layer should be equal to the flux through the membrane, thus:

$$J_{H_2} = \frac{P_m}{t_m}(P_{H2,m}^{0.5} - P_{H2,per}^{0.5}) = k_d C_{tot} \ln\left[\frac{1-X_m}{1-X_e}\right]$$

Eq.(4.13)

An overview of all the hydrodynamic parameters is provided in Table A.1 (appendix A). For a detailed discussion on the model equations and assumptions the interested reader is referred to [22].

4.2.2 Two-Fluid Model

To supplement the one-dimensional phenomenological model with an estimate of the thickness of the mass transfer boundary layer, simulations using the Two-Fluid model (TFM) have been performed, using OpenFOAM twoPhaseEulerFoam version 2.3.1. This solver has been extended with gas-phase species balance equations and realistic membrane models to simulate the selective extraction of hydrogen.

The TFM considers the gas and solids phases as interpenetrating continua. The governing and constitutive equations are presented in Table B.1 (see appendix B). The gas phase is described as an ideal gas with Newtonian behavior, whereas the rheology of the solids phase is modeled with the Kinetic Theory of Granular Flow (KTGF). Extraction of hydrogen via the membrane is accounted for with a source term (S) in the gas phase continuity equation, which is applied to all grid cells adjacent to a membrane boundary.

The drag between the solids and the gas phase is calculated with the Gidaspow drag model [23], which combines the drag model of Ergun [24] and Wen & Yu [25]. Ergun's model is valid for high solids hold-ups (20% and higher) and Wen & Yu's model is valid at lower solids hold-ups (below 20%). The drag coefficient C_d is determined based on the particle Reynolds number.

To approximate the rheological properties of the particulate phase in a fluidized bed, the KTGF closure equations are used. The closure equations used in this work are presented in Table B.2 [26]. A number of closure equations were not available in the original OpenFOAM TFM, so they were added to the model. Further details on the TFM and KTGF can be found in literature [23,27–31]. Detailed information on the OpenFOAM TFM specifically has also been published by other authors [32,33].

To model mass transfer phenomena and extraction of hydrogen via membranes, a hydrogen species balance was added to the TFM (Eq. 4.14). The effect of the membranes on the system was taken into account via the source term, S_m, which is applied to the computational cells adjacent to a membrane boundary (illustrated by the red cells in Figure 4.3). The source term in equation 4.14 is the membrane flux calculated with Sieverts' law, multiplied by the boundary cell's area A_c, divided by the cell volume V_c, see equation 4.15. This approach to simulate perm-selective membranes was also used by Coroneo et al. [34].

$$\frac{\partial \alpha_g \rho_g Y_{H_2}}{\partial t} + \nabla \cdot \left(\alpha_g \rho_g \mathbf{u}_g Y_{H_2} \right) = \nabla \cdot \left(\alpha_g \rho_g D_{H_2} \nabla Y_{H_2} \right) + S_m$$

Eq.(4.14)

$$S_m = \frac{A_{cell}}{V_{cell}} Q_{Pd} \cdot \left[\left(X_{H_2}^{m} p_{tot} \right)^{0.5} - \left(X_{H_2}^{perm} p_{tot} \right)^{0.5} \right]$$

Eq.(4.15)

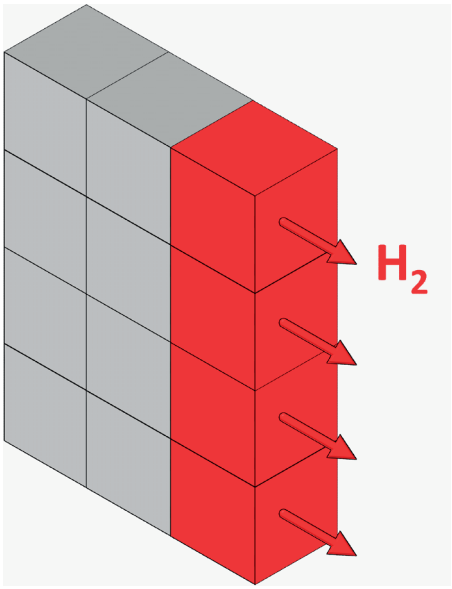

Figure 4.3 Schematic representation showing where the membrane source term and boundary condition have been applied.

Previous research has shown that extraction of gas from a fluidized bed can create densified zones which may affect the flow patterns of the solids [16,35]. In the case of selective hydrogen extraction, the removal of momentum from the system is expected to have a limited effect due to low molecular weight of hydrogen. However, when modelling extraction or addition of a component with a higher molecular weight, the extraction of momentum may become more significant. Therefore, a boundary condition for the momentum balances was modified in the TFM which accounts for the extraction of momentum due to the membrane permeation. The boundary condition effectively imposes a velocity, whose magnitude is correlated to the membrane flux and in the normal direction to the membrane boundary as given in equation 4.16.

$$u_m = \frac{S_m RT}{pM_w} \frac{V_{cell}}{A_{cell}}$$

Eq.(4.16)

The experimental setup is a cylindrical fluidized bed reactor with a single submerged membrane in the center of the reactor. This system was approximated with a 2D simulation. A sketch of the experimental set-up and how it has been approximated with the model is presented in Figure 4.4. The hydrogen was extracted via the left boundary, to which the membrane velocity boundary condition described by equation 4.16 was applied. On the right boundary a no-slip condition was imposed. For the solids phase, a Johnson & Jackson partial slip boundary condition with a specularity coefficient of 0.50 was applied on both the left and right walls (see Table B.3 in appendix B).

The settings for the vertical membrane simulations are presented in Table B.4 and Table B.5 (in appendix B). The domain width is equal to the radius of the experimental reactor and the domain height is equal to the membrane length. The selected grid was 0.5625 by 0.5625 mm, which is sufficiently fine to yield converged solutions. Temporal discretization was done with the second order Crank-Nicolson scheme. A combination of two second order schemes, the Gauss linear scheme and the Van Leer scheme, were used for spatial discretization. The TFM simulations were performed for three different inlet hydrogen molar fractions and four different outlet pressures.

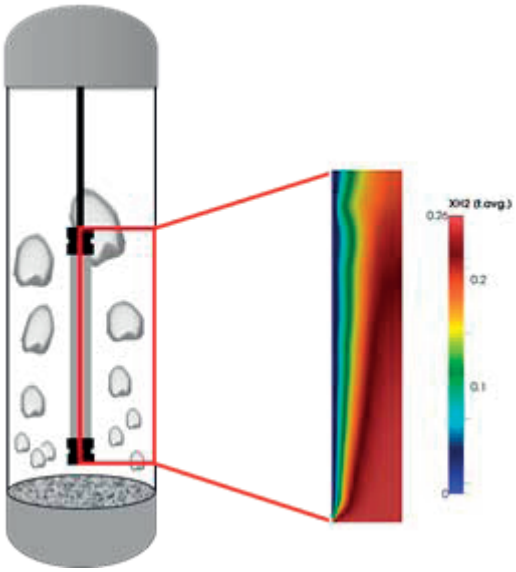

Figure 4.4 Schematic representation of the 2D simulation grid.

4.3. Experimental

Pt/Al_2O_3 particles with an average particle size of 200 μm and density 1400 kg m^{-3} were used for the experiments (provided by JM®). Detailed information on particle size measurement, minimum fluidization velocity and Geldart classification can be found in [13]. In a previous study it was ensured that particles do not chemically interact with the Pd membrane surface [36].

A 365 mm long cylindrical stainless steel tube with an inner diameter of 45 mm was used for the experiments. The gas distributor was a porous stainless steel plate of 40 μm pore size. Two thermocouples were placed inside and outside of the membrane (close by the surface of the membrane). In the fluidized bed experiments, 180 g of Pt/Al_2O_3 particles were integrated inside the reactor to ensure full immersion of the membrane at minimum fluidization conditions. For more detailed information on the experimental setup, see [13].

In the center of the reactor a 113 mm long $Pd_{0.85}$-$Ag_{0.15}$ based membrane supported on porous Al_2O_3 (100 nm pore size at the surface) was placed. The outer diameter of the membrane was 1 cm and was placed 3 cm above the distributor plate. The supported membrane was fabricated with an electroless plating technique with an average selective layer thickness of 4.5 microns along the membrane. The membrane was first integrated into the reactor module without catalyst particles to activate the membrane (see [36]). Subsequently, the membrane permeation properties (P_{m0} and E_a) were characterized at different retentate side pressures (1.2-1.6 bar) and at different temperatures (350, 400, and 450 °C) under pure hydrogen flow (P_{m0} =1.76·10^{-8} mol $m^{-1}s^{-1}Pa^{-0.5}$, E_a = 7.1 kJ mol^{-1}). The obtained permeation properties from the experiments were used in the models (phenomenological model and TFM) to describe the H_2 flux through the membrane. The permeate side was kept at 1 bar for the entire characterization period. To ensure that the membrane was leak tight, the nitrogen leakage rate was monitored during the experimental work at identical operating pressures (measured average ideal H_2/N_2 selectivity was 5000).

After the characterization procedure, experiments were performed with binary gas mixtures of N_2 and H_2 to quantify the concentration polarization effect. Experiments with pure hydrogen at the inlet was used to monitor the stability of the membrane over time. All the experiments were performed at 400 °C and hydrogen mole fractions of 0.1, 0.25 and 0.45 were used. Finally, the relative fluidization velocity (U/U_{mf}) was varied between 1.3 and 3.3 and the membrane performance was measured at constant pressure of 1.3 bar at the retentate side.

4.4 Results and discussion

The experiments reported hereafter were performed for various H_2 mole fractions. For every mole fraction experiments were carried out at different H_2 partial pressure differences across

the membrane. First the experimental results will be compared with the results obtained with the TFM to obtain a proper estimation of the radial dispersion coefficient for the fluidized suspension. As described in section 4.2, in the phenomenological model the concentration polarization is modelled by assuming a mass transfer boundary layer with thickness d around the membrane with an external mass transfer coefficient of k_d. The thickness of the film layer will be determined using the optimized dispersion coefficient in the TFM.

The effect of densified zones on concentration polarization is looked into and the effect of the hydrogen mole fraction and reactor pressure on the boundary film layer thickness will also be investigated. Subsequently, results from the phenomenological model without considering concentration polarization (referred to as 1D) and with accounting for concentration polarization (indicated by 1D/k_d) will be compared with experimental results for identical conditions. Finally, it will be discussed whether the bubble-to-emulsion, emulsion-to-membrane or the mass transfer across the membrane is the rate limiting step for gas extraction in fluidized beds.

4.4.1 Film layer thickness

In order to use the 1D/k_d model which is developed in this work, the thickness of the film layer needs to be estimated. To help estimating the magnitude of d, and the corresponding radial dispersion coefficient D_r, the Two-Fluid Model (TFM) was used. To the authors' knowledge, there are currently no generally accepted relations that describe the radial dispersion term for fluidized beds with internals. Resorting to correlations for packed beds, e.g. by Tsotsas and Schlünder (yielding $D_r = 5 \cdot 10^{-5}$ m^2 s^{-1} for the considered conditions), understandably does not yield satisfying results for fluidized beds. Hence, we have resorted to performing a sensitivity analysis to obtain a more accurate estimate for the radial dispersion coefficient. Figure 4.5 shows a comparison between the obtained results from experiments and results from the TFM using a gas phase dispersion coefficient of $5 \cdot 10^{-5}$ and $1 \cdot 10^{-4}$ m^{2}s^{-1}.

According to Figure 4.5, a very good match between TFM and experimental observations was obtained when using a radial dispersion coefficient of $1 \cdot 10^{-4}$ m^{2}s^{-1}. Therefore, and due to the fact the no validated correlation exists for the radial dispersion coefficient inside fluidized bed membrane reactors, this value was selected for all other reported simulations.

Investigating the concentration profiles in the vicinity of the membrane as computed by the TFM, the concentration of hydrogen significantly decreases from a bulk concentration to a minimum value close to the membrane for all the cases. This confirms the existence of a mass transfer boundary layer near the membrane imposing a mass transfer resistance from the bulk of the fluidized suspension to the surface of the membranes. Simulations were performed for different inlet H_2 mole fractions of 0.1, 0.2, 0.45 and 1 to investigate the thickness of this boundary layer for various operating conditions (see Figure 4.6 and Figure 4.7). The computed results clearly show a thinner film layer at the bottom of the membrane that increases significantly as a function of the axial position. This shows that the assumption of a film layer with a constant thickness is obviously a simplification. The description could be extended

using boundary layer theory to account for this, but the results shown later will show that the assumption of a constant film layer thickness seems more than sufficient.

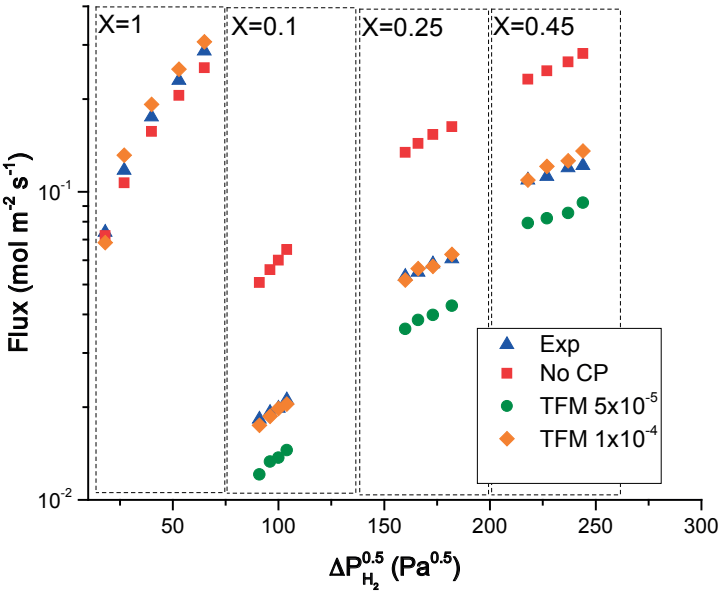

Figure 4.5 Comparison of the experimentally determined and TFM computed membrane flux as a function of the hydrogen partial pressure, two different gas phase radial dispersion coefficients have been used in the TFM ($D_r = 5 \cdot 10^{-5}$ and $1 \cdot 10^{-4}$ $m^2 s^{-1}$), $P_{reactor}$=1.5-1.8 bar, U/U_{mf} =3.3

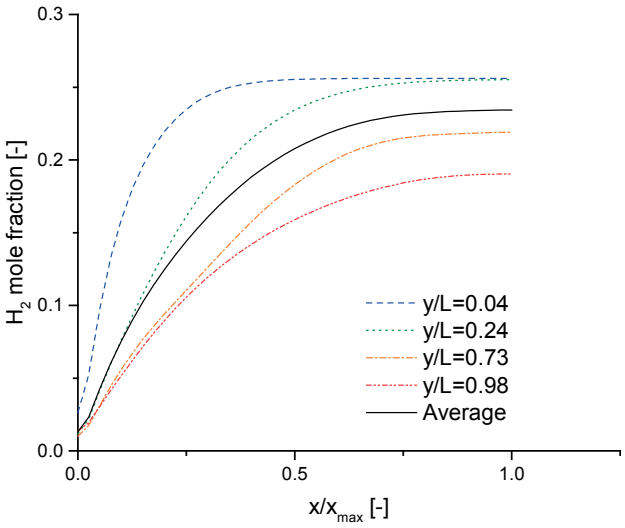

Figure 4.6 Time-averaged TFM predicted film layer thickness at different axial positions, y: axial distance from the membrane bottom, L: the membrane length, X: distance from the membrane in radial direction, ΔP: 0.5 bar, X=0.25

The film layer thickness decreases slightly for higher H_2 mole fractions in the inlet, whereas the pressure indeed seems to have a very small influence. Based on the obtained results from the TFM at different operating conditions and various axial positions, an average film layer thickness of 0.01 m was estimated for the considered geometry, which will be used in the 1D/k_d model.

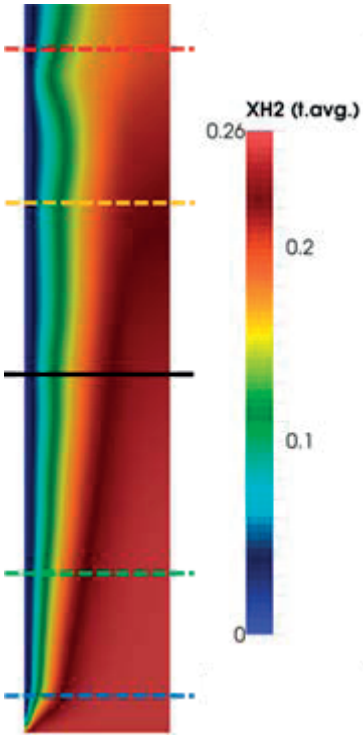

Figure 4.7 Time averaged concentration profiles of H_2 computed with the TFM (X=0.25), the dashed lines refer to the axial positions where the lateral concentration profiles are shown in Figure 4.6

4.4.2 Densified zones

The two-dimensional TFM simulations were used to investigate the formation of densified zones near the membrane and their effect on concentration polarization. Snapshots of the instantaneous hydrogen mole fractions and gas bubbles (defined as regions with a gas porosity above 0.85) show that the bubbles do not come close to the membrane (Figure 4.8). The hydrogen molecules therefore have to depend on diffusion to reach the membrane, the distance of the bubbles to the membrane is too large to convectively refresh the hydrogen at the membrane.

Figure 4.9 presents the time-averaged solids hold-up profiles for a fluidized bed injected with binary gas mixtures with 10, 25 and 45 mol% hydrogen. The 25 mol% case was also performed for the same bed without hydrogen extraction. When hydrogen is extracted, the

solids shift more towards the membrane. At higher hydrogen molar fractions, the solids hold-up near the membrane increases slightly compared to lower hydrogen molar fractions, because the momentum flux of the hydrogen towards the membrane is higher.

The solids hold-up at the wall opposite to the membrane simultaneously decreases by about 1 to 2%, indicating that the solids shift slightly more towards the membrane at higher extraction fluxes. However, when no extraction takes place, the solids hold-up near the membrane and right wall is higher than for the case with extraction. The extraction of hydrogen thus did not significantly alter the extent of the densified zones, and these small changes in the solids hold-up near the membrane cannot be the main cause of concentration polarization.

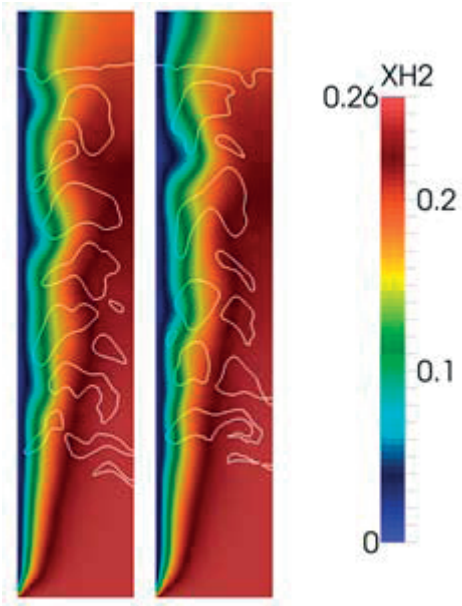

Figure 4.8 Instantaneous TFM snapshots of hydrogen molar fraction and bubble contours (white).

To better elucidate the effects of extraction, in Figure 4.10 the gas velocity profiles in an empty membrane tube with and without hydrogen extraction are compared, where all the conditions were kept the same as for the FBMR case with 25 mol% hydrogen at 1.5 bar pressure but without solids. A clear shift of the gas velocity profile towards the membrane was observed, which explains the slight reduction in the solids hold-up near the membrane and the overall shift of the solids hold-up profile towards the membrane.

4.4.3 1D/kd model verification

In an independent experimental observation by Patil et al. [37] for a FBMR with a Pd-based membrane with much lower permeation properties (P_m = 1.35·10^{-12} mol m^{-1} s^{-1} Pa) in comparison with the membrane used in this work, no influence of concentration polarization was

reported. Therefore, it was investigated whether the 1D/k_d model is able to describe these experiments with negligibly small film layer thickness. Figure 4.11 compares the reported experimental observation for a case at 400 °C, with a superficial gas velocity between u_0=3 and u_0=5 cm s^{-1}, and the H_2 partial pressure drop was between ΔP=0.5 and ΔP=3 bar, with the predictions from the phenomenological model.

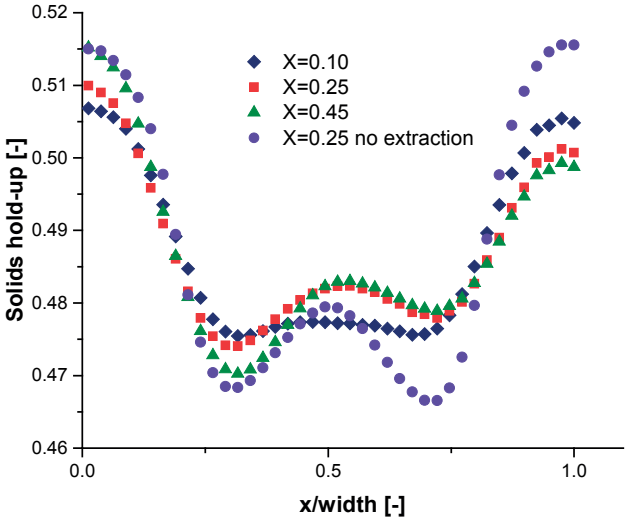

Figure 4.9 Time-averaged TFM solids hold-up data for a fluidized bed with membrane (X=0.10, 0.25 and 0.45) and one case with membrane without gas extraction (X=0.25), $P_{reactor}$=1.5 bar.

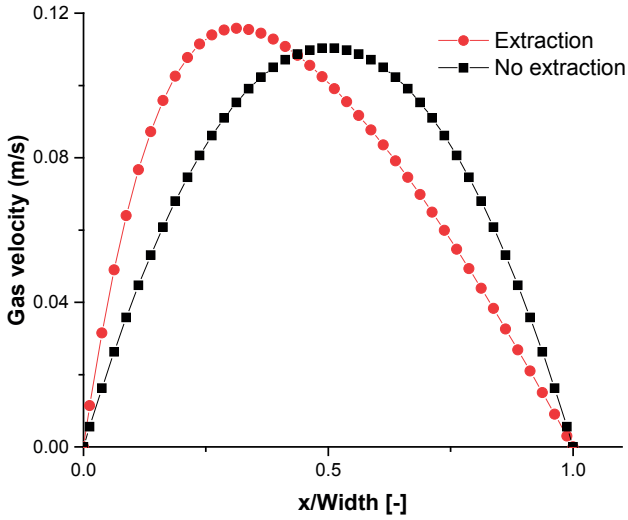

Figure 4.10 Gas velocity profiles for a gas reactor with and without extraction at X=0.25 and $P_{reactor}$=1.5 bar.

The model without considering concentration polarization (1D) predicts the experimental results very well. To validate the 1D/k_d model, a film layer thickness of $1 \cdot 10^{-6}$ m around the membrane was assumed with a radial dispersion coefficient of $1 \cdot 10^{-4}$ $m^2 s^{-1}$, and the model reduces indeed to the results from the 1D model confirming the absence of concentration polarization for the membrane used in the work by Patil *et al.* at the specified operating condition.

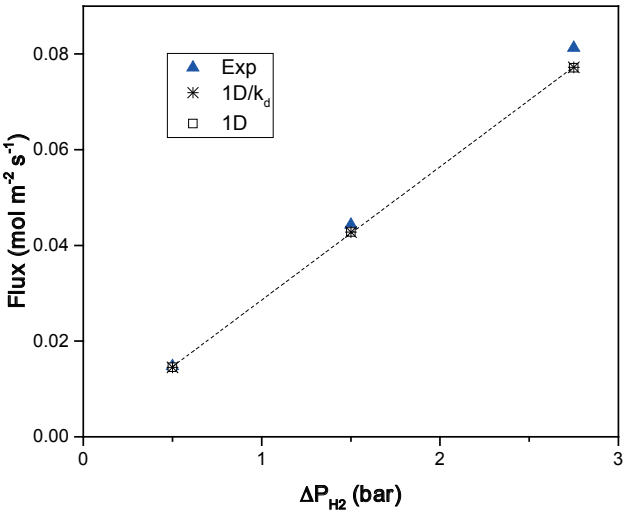

Figure 4.11 1D and 1D/kd model predictions for the H_2 flux compared with experiments by Patil et al. [36]

4.4.4 Model vs. experiments

In this section results from the one-dimensional models (1D and 1D/k_d) for the fluidized bed will be compared with the experimental observations at identical operating conditions. Experiments in the fluidized bed were performed with an inlet superficial gas velocity of u_0 = 0.05 m s^{-1} (u/u_{mf} = 3.3). The membrane permeance was determined to be $P_m = 1.76 \cdot 10^{-8}$ mol m^{-1} s^{-1} $Pa^{-0.5}$, the operating temperature was 400 °C, the reactor pressure was varied between 1.44 and 1.8 bar and the H_2 mole fraction was varied between 0.1 and 1.0, and the model parameters were set up accordingly. Figure 4.12 summarizes the experimental observations in comparison with the obtained results from simulations with the 1D and 1D/k_d models for different H_2 partial pressure differences. The figure clearly shows that the 1D model ignoring concentration polarization effects largely overestimates the membrane flux for all transmembrane pressure differences and the discrepancies further increase for smaller hydrogen concentrations, whereas the 1D/k_d model that accounts for concentration polarization effects accurately predicts the membrane flux for all the considered cases.

Furthermore, the simulation results of the 1D/k_d model for the case without bubble-to-emulsion mass transfer resistance were virtually identical to the results when bubble-to-emulsion mass transfer was taken into account, from which it can be concluded that the bubble-to-emulsion mass transfer resistance is negligible compared to the external mass transfer resistance to the membrane wall for the considered cases.

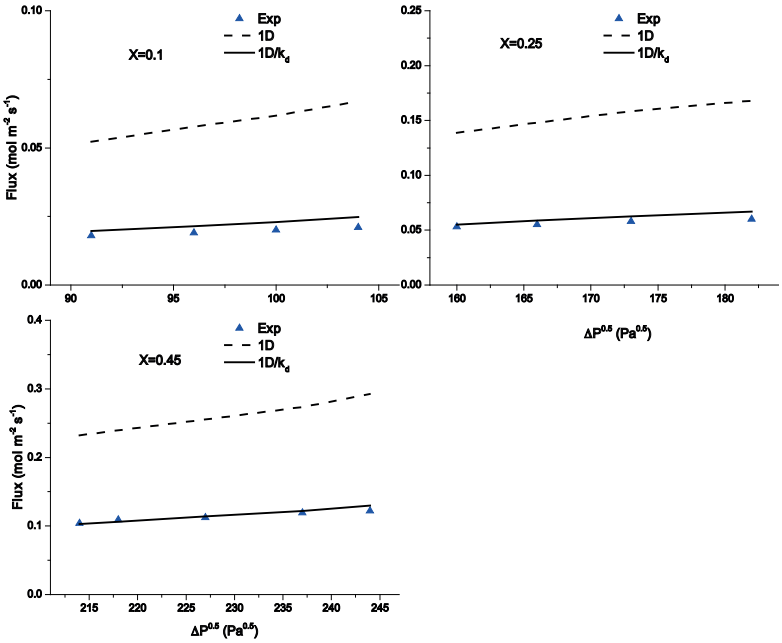

Figure 4.12 Experimental data versus model predictions for different H_2 concentrations; (1D): one-dimensional model without considering concentration polarization; (1D/kd): one-dimensional model accounting for concentration polarization considering a film layer thickness of 1 cm and a radial gas dispersion coefficient D_r of $1 \cdot 10^{-4}$ m^2/s.

In Figure 4.13 the axial H_2 mole fraction profiles along the membrane length are plotted for the bubble phase, emulsion phase and at the surface of the membrane. This is shown for one selected experiment, but all the other showed the same trend. Since the concentration differences between the bubble and the emulsion phase and along the membrane are small compared to the concentration differences between the emulsion and the membrane wall, it can be concluded that the external bed-to-membrane mass transfer is rate limiting.

To figure out the effect of inlet flow velocity on concentration polarization, Experiments were performed with different inlet flow velocities for three different inlet compositions. Binary mixtures of H_2 and N_2 were chosen with a H_2 content of 10, 25 and 45% at the inlet. For each inlet flow composition, the inlet velocity was varied to investigate the performance of the model at higher inlet flow rates in the bubbling fluidization regime (Figure 4.14).

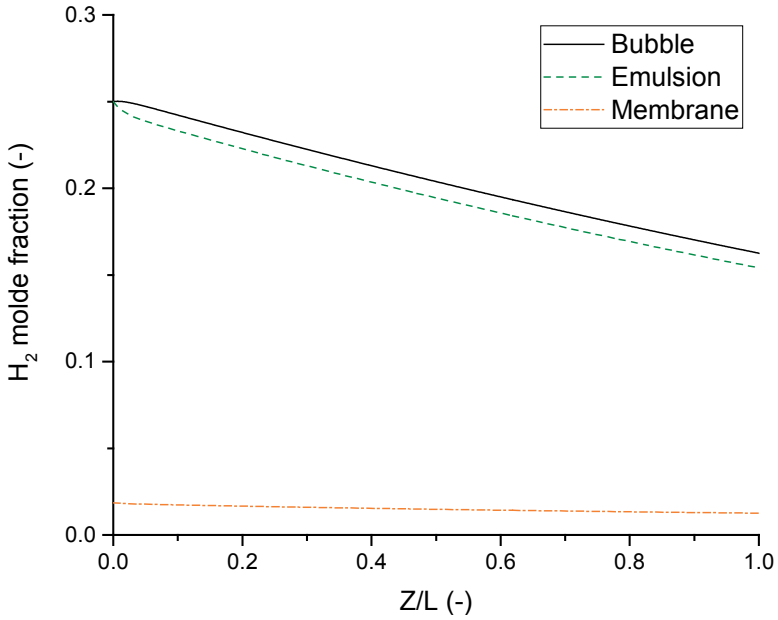

Figure 4.13 Axial hydrogen mole fraction profiles at the membrane surface, in the emulsion and in the bubble phase. Experiment: X=0.25, u=0.05 m s^{-1}, $P_{reactor}$=1.44 bar, P_m=1.76·10^{-8} mol m^{-1} s^{-1} $Pa^{-0.5}$.

According to the obtained results, in general the 1D/k_d model can predict accurately the flux through the membrane for different inlet flow rates and inlet gas compositions. Considering the fact that the thickness of the film layer was considered with a constant value of 0.01 m, it can be concluded that this constant can be a good estimate for the average thickness of the film layer for a wide range of inlet flow velocities. Investigating the obtained modeling results with and without considering concentration polarization, the effect of concentration polarization becomes more pronounced for higher inlet gas velocities and lower hydrogen inlet concentrations, and the developed 1D/k_d model can accurately capture this.

In general, for the phenomenological fluidized bed model a lot more research needs to be done. The influence of the membrane immersion on the hydrodynamic properties of the bed needs to be further investigated. The 1D/k_d model gives a very good prediction of the experimental observations when using a radial dispersion coefficient estimated from TFM simulations. However, an accurate correlation for the radial dispersion in fluidized beds (and preferably accounting for the presence of immersed objects) would facilitate the modelling. Another complicating factor is that the film layer thickness is quite large compared to the annular space between the membrane and the reactor wall (d = 0.01 m and d_r = 0.045 m). Although for this research a lab-scale reactor with a relatively small diameter was used and it may be well the case that for larger diameters is less important. On the other hand, often membrane modules are inserted into the bed, where the effect of the presence and permeation

through neighboring membranes might need to be accounted for in the estimation of the mass transfer boundary layer thickness.

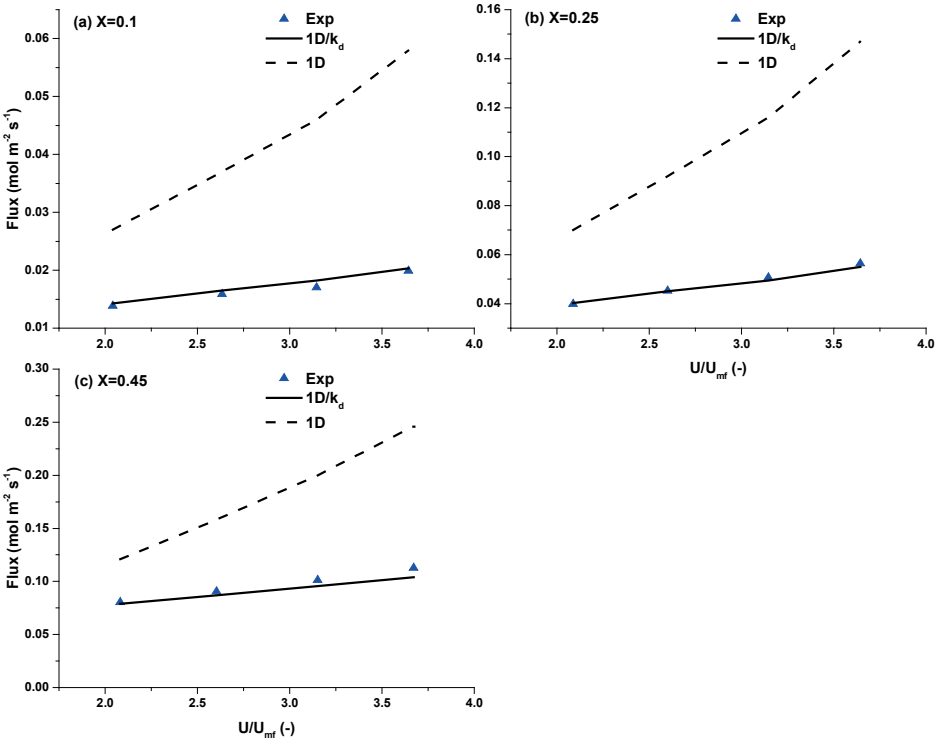

Figure 4.14 Model predictions versus experiments at different inlet velocities at constant H_2 partial pressure differences (a) $\Delta P_{H2}^{0.5}(Pa^{0.5}) = 86$, (b) $\Delta P_{H2}^{0.5}(Pa^{0.5}) = 150$, (c) $\Delta P_{H2}^{0.5}(Pa^{0.5}) = 205$

4.5 Conclusions

A simple one-dimensional two-phase phenomenological model was developed that captures the effect of concentration polarization in fluidized bed membrane reactors (1D/k_d). In this model the fluidized bed was divided into a number of CSTR's in series for both the emulsion and bubble phase while accounting for mass transfer limitations from the bed bulk to the surface of the membranes assuming that this occurs entirely in a thin stagnant film layer with constant thickness around the membrane. The H_2 flux through the membranes was described by Sieverts' law.

A more detailed Euler-Euler CFD model, the Two-Fluid Model, was developed in Open-FOAM where the solver was extended with species mass balance equations and membrane models to simulate the selective extraction of hydrogen. The model was used to quantify the extent of concentration polarization in a lab-scale experimental reactor and to determine the

mass transfer boundary layer thickness which is required by the one-dimensional phenomenological model.

Comparing the results obtained from experiments with the TFM model a very good agreement was found when an appropriate value for the gas phase dispersion coefficient was selected. The computed concentration profiles near by the membrane, confirmed the existence of a concentration boundary layer in the vicinity of the membrane that imposes a mass transfer resistance from the bulk of the fluidized bed to the surface of the membranes. Although the thickness of the film layer increases with the axial position, and decreases slightly for higher mole fractions, an average film layer thickness was estimated at 0.01 m for all the different operating conditions and was assumed constant. This film layer thickness and gas dispersion coefficient was used in the phenomenological 1D/k_d model.

The results of the 1D/k_d model for the membrane flux were compared with experimental observations over a wide range of inlet concentrations, operating pressures and inlet gas velocities, and a very good agreement was found, despite the fact that the film layer thickness was assumed constant. It was also found that the bubble-to-emulsion phase mass transfer limitations are much less pronounced relative to the emulsion-to-membrane wall mass transfer resistances for the investigated cases. Comparison with the 1D model results that do not account for concentration polarization, clearly indicates the very pronounced effect of concentration polarization, also for fluidized bed membrane reactors.

Bibliography

[1] K. Aasberg-Petersen, J.H. Bak Hansen, T.S. Christensen, I. Dybkjaer, P.S. Christensen, C. Stub Nielsen, S.E.L. Winter Madsen, J.R. Rostrup-Nielsen, Technologies for large-scale gas conversion, Appl. Catal. A Gen. 221 (2001) 379–387. doi:10.1016/S0926-860X(01)00811-0.

[2] V. Spallina, D. Pandolfo, A. Battistella, M.C. Romano, M. van Sint Annaland, F. Gallucci, Techno-economic assessment of membrane assisted fluidized bed reactors for pure H2 production with CO_2 capture, Energy Convers. Manag. 120 (2016) 257–273. doi:10.1016/j.enconman.2016.04.073.

[3] G. Barbieri, A. Brunetti, G. Tricoli, E. Drioli, An innovative configuration of a Pd-based membrane reactor for the production of pure hydrogen. Experimental analysis of water gas shift, J. Power Sources. 182 (2008) 160–167. doi:10.1016/j.jpowsour.2008.03.086.

[4] L. Roses, F. Gallucci, G. Manzolini, S. Campanari, M. van Sint Annaland, Comparison between fixed bed and fluidized bed membrane reactor configurations for PEM based micro-cogeneration systems, Chem. Eng. J. 171 (2011) 1415–1427. doi:10.1016/j.cej.2011.05.061.

[5] F. Gallucci, E. Fernandez, P. Corengia, M. van Sint Annaland, Recent advances on membranes and membrane reactors for hydrogen production, Chem. Eng. Sci. 92 (2013) 40–66. doi:10.1016/j.ces.2013.01.008.

[6] A. Caravella, G. Barbieri, E. Drioli, Concentration polarization analysis in self-supported Pd-based membranes, Sep. Purif. Technol. 66 (2009) 613–624. doi:10.1016/j.seppur.2009.01.008.

[7] F. Gallucci, M. van Sintannaland, J. A. M. Kuipers, Theoretical comparison of packed bed and fluidized bed membrane reactors for methane reforming, Int. J. Hydrogen Energy. 35 (2010) 7142–7150. doi:10.1016/j.ijhydene.2010.02.050.

[8] S. Hara, K. Sakaki, N. Itoh, Decline in Hydrogen Permeation Due to Concentration Polarization and CO Hindrance in a Palladium Membrane Reactor, Ind. Eng. Chem. Res. 38 (1999) 4913–4918. doi:10.1021/ie990200n.

[9] N. Mori, T. Nakamura, K. Noda, O. Sakai, A. Takahashi, N. Ogawa, H. Sakai, Y. Iwamoto, T. Hattori, Reactor Configuration and Concentration Polarization in Methane Steam Reforming by a Membrane Reactor with a Highly Hydrogen-Permeable Membrane, Ind. Eng. Chem. Res. 46 (2007) 1952–1958. doi:10.1021/ie060989j.

[10] O. Nekhamkina, M. Sheintuch, Effective approximations for concentration-polarization in Pd-membrane separators, Chem. Eng. J. 260 (2015) 835–845. doi:10.1016/j.cej.2014.09.049.

[11] C.S. Patil, M. van Sint Annaland, J. A. M. Kuipers, Fluidised bed membrane reactor for ultrapure hydrogen production via methane steam reforming: Experimental demonstration and model validation, Chem. Eng. Sci. 62 (2007) 2989–3007. doi:10.1016/j.ces.2007.02.022.

[12] F. Gallucci, M. van Sint Annaland, J. A. M. Kuipers, Autothermal Reforming of Methane with Integrated CO_2 Capture in a Novel Fluidized Bed Membrane Reactor. Part 2 Comparison of Reactor Configurations, Top. Catal. 51 (2008) 146–157. doi:10.1007/s11244-008-9127-7.

[13] A. Helmi, E. Fernandez, J. Melendez, D.A. Pacheco Tanaka, F. Gallucci, M. van Sint Annaland, Fluidized Bed Membrane Reactors for Ultra Pure H_2 Production-A Step forward towards Commercialization., Molecules. 21 (2016). doi:10.3390/molecules21030376.

[14] K. Kato, C.Y. Wen, Bubble assemblage model for fluidized bed catalytic reactors, Chem. Eng. Sci. 24 (1969) 1351–1369. doi:10.1016/0009-2509(69)85055-4.

[15] S. A. R.K. Deshmukh, J. A. Laverman, A. H.G. Cents, M. van Sint Annaland, J. A. M. Kuipers, Development of a Membrane-Assisted Fluidized Bed Reactor. 1. Gas Phase Back-Mixing and Bubble-to-Emulsion Phase Mass Transfer Using Tracer Injection and Ultrasound Experiments, Ind. Eng. Chem. Res. 44 (2005) 5955–5965. doi:10.1021/ie049102e.

[16] N.T.Y. Dang, F. Gallucci, M. van Sint Annaland, Micro-structured fluidized bed membrane reactors: Solids circulation and densified zones distribution, Chem. Eng. J. 239 (2014) 42–52. doi:10.1016/j.cej.2013.11.001.

[17] J.F. De Jong, M. van Sint Annaland, J.A.M. Kuipers, Experimental study on the effects of gas permeation through flat membranes on the hydrodynamics in membrane-assisted fluidized beds, Chem. Eng. Sci. 66 (2011) 2398–2408. doi:10.1016/j.ces.2011.02.059.

[18] E.N. Lightfoot, R. B. Bird, W. E. Stewart, Transport phenomena, 2007.

[19] E. Tsotsas, E.U. Schlünder, On axial dispersion in packed beds with fluid flow, Chem. Eng. Process. Process Intensif. 24 (1988) 15–31. doi:10.1016/0255-2701(88)87002-8.

[20] G.B. Enrico Drioli, ed., Membrane Engineering for the Treatment of Gases : Volume 2: Gas-separation Problems Combined with Membrane Reactors, in: RSC publishing, n.d.: pp. 110–136.
[21] C.S. Patil, M. van Sint Annaland, J. A. M. Kuipers, Design of a Novel Autothermal Membrane-Assisted Fluidized-Bed Reactor for the Production of Ultrapure Hydrogen from Methane, Ind. Eng. Chem. Res. 44 (2005) 9502–9512. doi:10.1021/ie050244y.
[22] S. A. R.K. Deshmukh, J. A. Laverman, M. van Sint Annaland, J. A. M. Kuipers, Development of a Membrane-Assisted Fluidized Bed Reactor. 2. Experimental Demonstration and Modeling for the Partial Oxidation of Methanol, Ind. Eng. Chem. Res. 44 (2005) 5966–5976. doi:10.1021/ie049092h.
[23] D. Gidaspow, Multiphase Flow and Fluidization: Continuum and Kinetic Theory Descriptions, Academic Press, 1994.
[24] S. Ergun, Fluid flow through packed columns, Chem. Eng. Prog. 48 (1952) 89–94. doi:10.1029/JB088iS01p0B353.
[25] C.Y. Wen, Y.H. Yu, A generalized method for predicting the minimum fluidization velocity, AIChE J. 12 (1966) 610–612. doi:10.1002/aic.690120343.
[26] J.J. Nieuwland, M. van Sint Annaland, J. A. M. Kuipers, W.P.M. van Swaaij, Hydrodynamic modeling of gas/particle flows in riser reactors, AIChE J. 42 (1996) 1569–1582. doi:10.1002/aic.690420608.
[27] C.K.K. Lun, S.B. Savage, D.J. Jeffrey, N. Chepurniy, Kinetic theories for granular flow: inelastic particles in Couette flow and slightly inelastic particles in a general flowfield, J. Fluid Mech. 140 (1984) 223. doi:10.1017/S0022112084000586.
[28] J.A.M. Kuipers, K.J. van Duin, F.P.H. van Beckum, W.P.M. van Swaaij, Computer simulation of the hydrodynamics of a two-dimensional gas-fluidized bed, Comput. Chem. Eng. 17 (1993) 839–858. doi:10.1016/0098-1354(93)80067-W.
[29] B. van Wachem, Derivation, Implementation, and Validation of Computer Simulation Models for gas-solid fluidized beds, (2000).
[30] M.A. van der Hoef, M. Ye, M. van Sint Annaland, A.T. Andrews, S. Sundaresan, J.A. Kuipers, Multiscale Modeling of Gas-Fluidized Beds, Adv. Chem. Eng. 31 (2006) 65–149. doi:10.1016/S0065-2377(06)31002-2.
[31] H. Rusche, Computational Fluid Dynamics of Dispersed Two-Phase Flows at High Phase Fractions, 2002. doi:10.1145/1806799.1806850.
[32] A. Passalacqua, R.O. Fox, Implementation of an iterative solution procedure for multi-fluid gas-particle flow models on unstructured grids, Powder Technol. 213 (2011) 174–187. doi:10.1016/j.powtec.2011.07.030.
[33] Y. Liu, O. Hinrichsen, CFD modeling of bubbling fluidized beds using OpenFOAM®: Model validation and comparison of TVD differencing schemes, Comput. Chem. Eng. 69 (2014) 75–88. doi:10.1016/j.compchemeng.2014.07.002.
[34] M. Coroneo, G. Montante, J. Catalano, A. Paglianti, Modelling the effect of operating conditions on hydrodynamics and mass transfer in a Pd–Ag membrane module for H_2 purification, J. Memb. Sci. 343 (2009) 34–41. doi:10.1016/j.memsci.2009.07.008.
[35] L. Tan, I. Roghair, M. van Sint Annaland, Simulation study on the effect of gas permeation on the hydrodynamic characteristics of membrane-assisted micro fluidized beds, Appl. Math. Model. 38 (2014) 4291–4307. doi:10.1016/j.apm.2014.04.044.
[36] E. Fernandez, A. Helmi, K. Coenen, J. Melendez, J.L. Viviente, D.A. Pacheco Tanaca, M. van Sint Annaland, F. Gallucci, Development of thin Pd-Ag supported membranes for fluidized bed membrane reactors including WGS related gases, Int. J. Hydrogen Energy. 40 (2015) 3506–3519. doi:10.1016/j.ijhydene.2014.08.074.
[37] C.S. Patil, M. van Sint Annaland, J. A. M. Kuipers, Experimental Study of a Membrane Assisted Fluidized Bed Reactor For H_2 Production by Steam Reforming of CH_4, Chem. Eng. Res. Des. 84 (2006) 399–404. doi:10.1205/cherd05028.
[38] C.S. Patil, Membrane Reactor Technology for Ultrapure Hydrogen Production, (2005) 90.

Appendix

Table A.1 Summary of the hydrodynamic parameters used in the 1D phenomenological model [38]

Parameter	Equation
Archimedes number	$Ar = \frac{d_p^3 \rho_g (\rho_p - \rho_g) g}{\mu_g^2}$
Minimum fluidization velocity	$u_{mf} = \left(\frac{\mu_g}{\rho_g d_p}\right)\left(\sqrt{(27.2)^2 + 0.0408 Ar} - 27.2\right)$
Bed voidage at minimum fluidization velocity	$\varepsilon_{mf} = 0.586 Ar^{-0.029}\left(\frac{\rho_g}{\rho_p}\right)^{0.021}$
Initial bubble diameter (porous plate Distributor)	$d_{b0} = 0.376\left(u_0 - u_{mf}\right)^2$
Maximum bubble diameter	$d_{b,\max} = \min\left(d_H, 0.65\left(\frac{\pi}{4} d_H^2 \left(u_0 - u_{mf}\right)\right)^{0.4}\right)$
Average bubble diameter	$d_{b,avg} = d_{b,\max} - (d_{b,\max} - d_{b,0}) e^{\left[\frac{-0.15H}{d_h}\right]}$
Bubble diameter	$d_b = d_{b,\max} - \left(d_{b,\max} - d_{b,0}\right) e^{\left[\frac{-0.3H}{d_h}\right]}$
Velocity of rise of swarm of bubbles	$u_{b,avg} = u_0 - u_{mf} + 0.711\left(g d_{b,avg}\right)^{1/2}$
Bubble phase fraction	$f_b = \frac{u_0 - u_{mf}}{u_{b,avg}}$
Emulsion phase fraction	$f_e = 1 - f_b$
Gas exchange coefficient	$K_{bc} = 4.5\left(\frac{u_{mf}}{d_{b,avg}}\right) + 5.85\left(\frac{\sqrt{D} g^{1/4}}{d_{b,avg}^{5/4}}\right)$ $K_{ce} = 6.77\left(\frac{\alpha_{mf} D u_{b,avg}}{d_{b,avg}^3}\right)^{1/2}$ $\frac{1}{K_{be}} = \frac{1}{K_{bc}} + \frac{1}{K_{ce}}$
Fuller equation	$D_{mol} = 0.001 \frac{T^{1.75}\sqrt{M_w}}{p\left(V_A^{1/3} + V_B^{1/3}\right)}$
Totsas and Schlünder	$D_r = \left(1 - \sqrt{1 - \alpha_{mf}}\right) D_m + \frac{u_0 d_p}{8}$

Table B.1. Summary of all governing and constitutive equations used in the TFM

Continuity equation of the gas phase

$$\frac{\partial \alpha_g \rho_g}{\partial t} + \nabla \cdot (\alpha_g \rho_g \mathbf{u}_g) = S_m$$

Continuity equation of the solids phase

$$\frac{\partial \alpha_s \rho_s}{\partial t} + \nabla \cdot (\alpha_s \rho_s \mathbf{u}_s) = 0$$

Momentum equation gas phase

$$\frac{\partial \alpha_g \rho_g \mathbf{u}_g}{\partial t} + \nabla \cdot (\alpha_g \rho_g \mathbf{u}_g \mathbf{u}_g) = -\left(\nabla \cdot \alpha_g \boldsymbol{\tau}_g\right) - \alpha_g \nabla p - \beta(\mathbf{u}_g - \mathbf{u}_s) + \alpha_g \rho_g \boldsymbol{g}$$

Momentum equation solids phase

$$\frac{\partial \alpha_s \rho_s \mathbf{u}_s}{\partial t} + \nabla \cdot (\alpha_s \rho_s \mathbf{u}_s \mathbf{u}_s) = -\left(\nabla \cdot \alpha_s \boldsymbol{\tau}_s\right) - \alpha_s \nabla p - \nabla p_s + \beta(\mathbf{u}_g - \mathbf{u}_s) + \alpha_s \rho_s \boldsymbol{g}$$

Granular temperature equation (non-equilibrium)

$$\frac{3}{2}\left(\frac{\partial (\alpha_s \rho_s \theta)}{\partial t} + \nabla \cdot (\alpha_s \rho_s \mathbf{u}_s \theta)\right) = \left(-p_s \bar{\bar{I}} + \alpha_s \boldsymbol{\tau}_s\right) : \nabla \mathbf{u}_s + \nabla \cdot (\kappa_s \nabla \theta) - \gamma_s - J_s$$

Viscous stress tensor gas phase

$$\boldsymbol{\tau}_g = -\left[\mu_g \left(\nabla \mathbf{u}_g + (\nabla \mathbf{u}_g)^T\right) + \frac{2}{3}\mu_g \left(\nabla \cdot \mathbf{u}_g\right)\bar{\bar{I}}\right]$$

Viscous stress tensor solids phase

$$\boldsymbol{\tau}_s = -\left[\mu_s \left(\nabla \mathbf{u}_s + (\nabla \mathbf{u}_s)^T\right) + \left(\lambda_s - \frac{2}{3}\mu_s\right)\left(\nabla \cdot \mathbf{u}_s\right)\bar{\bar{I}}\right]$$

Inter-phase drag coefficient

$$\beta = 150 \frac{\alpha_s^2 \mu_g}{\alpha_g d_p^2} + 1.75 \frac{\alpha_s \rho_g \left|\mathbf{u}_g - \mathbf{u}_s\right|}{d_p} \qquad \text{for } \alpha_s \geq 0.20$$

$$\beta = \frac{3}{4} C_d \frac{\alpha_g \alpha_s \rho_g}{d_p} \left|\mathbf{u}_g - \mathbf{u}_s\right| \alpha_g^{-2.65} \qquad \text{for } \alpha_s < 0.20$$

$$C_d = \frac{24}{\mathrm{Re}_p}\left(1 + 0.15\,\mathrm{Re}_p^{0.687}\right) \qquad \text{for } \mathrm{Re}_p \leq 1000$$

$$C_d = 0.44 \qquad \text{for } \mathrm{Re}_p > 1000$$

$$\mathrm{Re}_p = \alpha_g \frac{\rho_g d_p \left|\mathbf{u}_g - \mathbf{u}_s\right|}{\mu_g}$$

Table B.2. Summary of all KTGF closure equations used in the TFM [26].

Solids shear viscosity

$$\mu_s = 1.01600\frac{5}{96}\pi\rho_s d_p\sqrt{\frac{\theta}{\pi}}\frac{\left(1+\frac{8}{5}\frac{(1+e)}{2}\alpha_s g_0\right)\left(1+\frac{8}{5}\alpha_s g_0\right)}{\alpha_s g_0}+\frac{4}{5}\alpha_s\rho_s d_p g_0(1+e)\sqrt{\frac{\theta}{\pi}}$$

Solids bulk viscosity

$$\lambda_s = \frac{4}{3}\alpha_s\rho_s d_p g_0(1+e)\sqrt{\frac{\theta}{\pi}}$$

Solids pressure

$$p_s = \alpha_s\rho_s\theta\left(1+2(1+e)\alpha_s g_0\right)$$

Frictional pressure

$$p_s^{fric} = Fr\cdot\frac{\left[\max\left(\left(\alpha_s-\alpha_s^{\min.fric}\right),0\right)\right]^{c_1}}{\left[\max\left(\left(\alpha_s^{\max}-\alpha_s\right),5\cdot10^{-2}\right)\right]^{c_2}} \quad \text{with: } \alpha_s^{\min.fric}=0.50,\ Fr=0.05,\ c_1=2,\ c_2=3$$

Frictional shear viscosity

$$\mu_s^{fric} = \frac{p_s^{fric}\sqrt{2}\sin\phi^{fric}}{2\alpha_s\sqrt{\boldsymbol{S}:\boldsymbol{S}+\frac{\theta}{d_p^2}}} \quad \text{with: } \boldsymbol{S}=\frac{1}{2}\left(\left(\nabla\mathbf{u}_s\right)+\left(\nabla\mathbf{u}_s\right)^T\right)-\frac{1}{3}\nabla\cdot\mathbf{u}_s\bar{\bar{I}} \quad \text{with: } \phi^{fric}=28$$

Radial distribution function

$$g_0 = \frac{1+2.5\alpha_s+4.5904\alpha_s^2+4.515439\alpha_s^3}{\left[1-\left(\frac{\alpha_s}{\alpha_s^{\max}}\right)^3\right]^{0.67802}} \quad \text{with: } \alpha_s^{\max}=0.62$$

Conductivity of fluctuation energy

$$\kappa_s = 1.02513\frac{75}{384}\pi\rho_s d_p\sqrt{\frac{\theta}{\pi}}\frac{\left(1+\frac{12}{5}\frac{(1+e)}{2}\alpha_s g_0\right)\left(1+\frac{12}{5}\alpha_s g_0\right)}{\alpha_s g_0}+2\alpha_s\rho_s d_p g_0(1+e)\sqrt{\frac{\theta}{\pi}}$$

Dissipation of granular energy

$$\gamma_s = 3(1-\mathrm{e}^2)\alpha_s^2\rho_s g_0\theta\left[\frac{4}{d_p}\sqrt{\frac{\theta}{\pi}}-\left(\nabla\cdot\mathbf{u}_s\right)\right]$$

Fluctuating velocity/force correlation

$$B_s = 3\beta\theta$$

Table B.3. Boundary conditions of the TFM simulations.

	$\mathbf{u}_g$	$\mathbf{u}_s$	ρ	α_g, α_s	Y_{H2}	θ
Inlet	Dirichlet (*3.33 U_{mf}*)	Dirichlet (*zero*)	Neumann	Neumann	Dirichlet (*Table B.4*)	Neumann (*initial value set at t = 0*)
Outlet	Neumann	Dirichlet (*zero*)	Dirichlet (*Table B.4*)		Neumann	
Membrane	$u_m = \frac{S_m RT}{pM_w} \frac{V_{cell}}{A_{cell}}$	Partial slip (*spec. coef. = 0.50*)	Neumann			Partial slip (*spec. coef. = 0.50*)
Right wall	Dirichlet (*no-slip*)					

Table B.4. Simulation settings.

Quantity	**Setting**
Width (x)	0.0225 m
Height (y)	0.113 m
Cells width	40
Cells height	200
d_p	200 µm
ρ_p	1400 kg/m^3
E_{pp}, e_{pw}	0.90
U/U_{mf}	3.33
D_{H2}	1.10^{-4} m^2/s
Q_{pd}	$4.3.10^{-3}$ mol/m^2/Pa/Pa^n
A_m	$1.836.10^{-3}$ m^2
T	405 °C
t_{sim}	15 s
Δt	2.10^{-5} s

Table B.5. Simulated hydrogen mole fraction and outlet pressures.

$\mathbf{X_{H2}}$ **[-]**	$\mathbf{P_{outlet}}$ **[Pa]**	$\mathbf{P_{perm}}$ **[Pa]**
0.10	$1.5.10^5$	$0.01.10^5$
0.25	$1.6.10^{-5}$	
0.45	$1.7.10^{-5}$	
	$1.8.10^{-5}$	

If you tell them they don't believe you.

If you show them they have no other chance than to accept it.

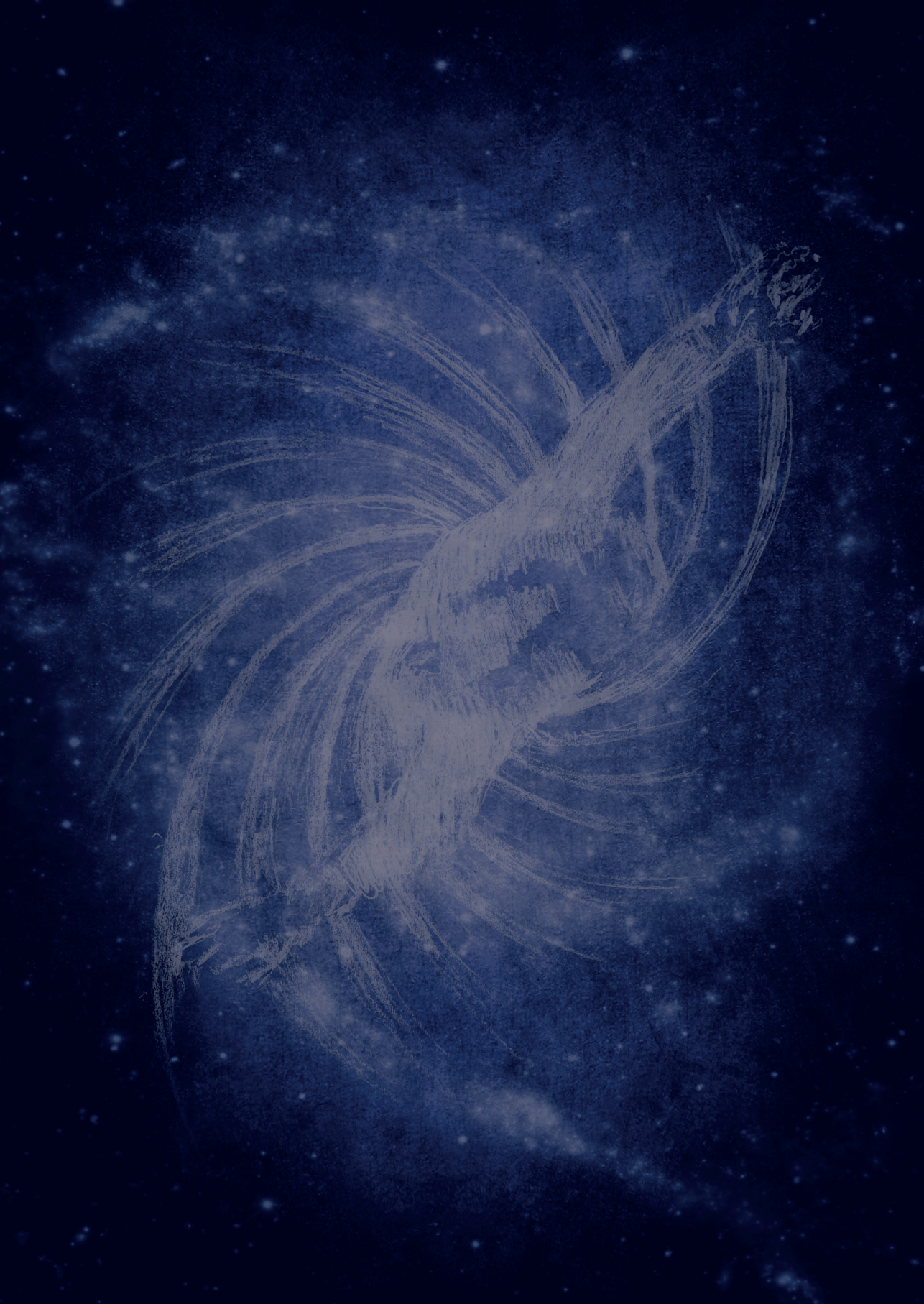

Chapter 5

On the hydrodynamics of membrane assisted fluidized bed reactors - A 3D X-ray analysis

Abstract

The application of membrane assisted fluidized bed reactors for distributed energy production has generated considerable research interest during the past few years. It is widely accepted that, due to better heat and mass transfer characteristics inside fluidized bed reactors, the reactor efficiency can outperform other reactor configurations such as packed bed units. Although many experimental studies have been performed to demonstrate and monitor the long term performance of membrane assisted fluidized bed reactors, the hydrodynamics of membrane-assisted fluidized bed reactors has thus far only been studied in pseudo-2D geometries. In this work the solids concentration inside a real 3D fluidized bed reactor geometry was measured using a fast X-ray analysis technique. Experiments were conducted in absence and presence of two different membrane modules with different configurations and number of membranes (porous Al_2O_3 tubes) for two types of particles, viz. 400-600 μm polystyrene (Geldart B type) and 80-200 μm Al_2O_3 (Geldart A/B type). Results from the experiments with Geldart B type particles revealed that the membrane modules (both the membranes and the spacers) can significantly reduce bubble growth along the fluidized bed resulting in a smaller average bubble diameter, expected to improve the bubble-to-emulsion mass transfer, whereas for the experiments with fine Geldart A/B particles, and at a very high extraction values (40% of the inlet flow), a densified layer with high solids concentration was formed near the membrane, which may impose an additional mass transfer resistance for gas components to reach the surface of the membranes (concentration polarization). The results from this study help designing and optimizing the positioning of the membranes and membrane spacers for optimal performance of fluidized bed membrane reactors.

5.1 Introduction

The application of membrane assisted fluidized bed reactors for distributed power production has attracted quite some research interest over the last few years [1]. In a membrane assisted reactor, reaction and separation steps are integrated in one single unit and a high degree of process intensification can be achieved, thereby strongly reducing the required reactor volume and increasing the energy efficiency of the process [2]. It is widely accepted that fluidized bed membrane reactors can outperform packed bed membrane reactor configurations due to their better mass and heat transfer properties [3]. Most of the literature on this topic has been devoted to provide a proof-of-concept at lab-scale or to monitor the long term performance of the membranes at different operating conditions and fluidization velocities [4].

On the material part, the main research effort has being paid on the fabrication of membranes with lower price and better permeation properties, i.e. increased permeability and perm-selectivity [3,5–9], whereas for the efficient demonstration of such units it is essential to understand and quantify the reactor design and scale-up parameters that account for the presence of membranes with different permeation values. De Jong et al. performed an extensive study on the hydrodynamics of fluidized beds in the presence of horizontally integrated membranes inside a pseudo 2D fluidized bed [10]. For this study a combined particle image velocimetry and digital image analysis (PIV/DIA) technique was used. The experimental results confirmed that for the membrane assisted bed the average equivalent bubble diameter was decreased by a factor of about 3 in comparison with the case where no membrane was integrated due to the increased bubble break-up (while the average bubble size was hardly affected by the permeation ratio through the membranes). In another study it was confirmed that the presence of horizontal membranes in the bed decreases the average bubble size, but the formation of gas pockets around the tubes need to be properly accounted when determining the average bubble size to avoid underestimation, while these gas pockets may also decrease the performance of the membrane reactor [11].

Dang et al. [12] and De Jong et al. [10] experimentally studied the solids circulation patterns in pseudo 2D fluidized beds (from relatively large beds to micro-structured beds) with gas extraction via membranes (filters) installed in the walls of the reactor also applying the combined PIV/DIA technique. It was found that in the cases where a large amount of gas is extracted via the membranes, the solids concentration in the near vicinity of the membrane increases and may result in the formation of so-called densified zones, which may impose an additional mass transfer resistance for gas components to reach the surface of the membranes. These findings are in accordance with a discrete particle simulation study done by Tan et al. [13]. These results have also been confirmed in case membranes (filters) are installed at the back plate of the pseudo 2D reactor [14].

Although these studies all point towards the possibility of the formation of densified zones close to the membrane surface thereby inducing external mass transfer limitations that can

limit the performance of fluidized bed membrane reactors, an extension of the study to 3D fluidized beds in the presence of and with permeation through vertically immersed membranes is required for a better understanding and improved design of membrane assisted fluidized bed reactors. Unfortunately, the technique used so far (PIV/DIA) is restricted to 2D geometries only, as it requires visual access to the reactor.

Recently, a detailed study was devoted on the effect of vertically immersed internals on the performance of a lab-scale and a pilot-scale fluidized bed heat exchanger in a real 3D reactor geometry utilizing an ultra-fast X-ray tomography technique [15–17]. It was generally found that the immersion of internals results in a lower average bubble size along the fluidized bed. In the present work the hydrodynamics of a fluidized bed reactor will be investigated in the presence of vertically immersed porous membranes in a real 3D reactor geometry using a fast X-ray analysis technique. With the help of this technique the hydrodynamics of the fluidized bed membrane reactor is monitored with very high spatial and temporal resolution. The chapter is outlined as follows: first the materials, set-up, the technique and data processing methods used in this study will be described in detail. Subsequently, the obtained results for different operating conditions will be presented and discussed, followed by a summary of the main conclusions.

5.2 Materials and methods

5.2.1 Experimental

In this study the solids concentration inside the fluidized bed was measured using the fast X-ray analysis technique developed by Mudde et al. [18]. The setup originally consisted of three standard medical type X-ray sources (Yxlon International GmbH) with a maximum energy of 150 Kev working in fan beam mode. Detailed information on the specification of the X-ray sources can be found elsewhere [19]. Each X-ray source generates a fan beam that can be detected by a detector plate on the opposite side of each X-ray source. For this study the experiments were performed with one X-ray source and one detector plate to obtain the projected 2D output signals from the 3D bed.

For the experiments a lab scale fluidized bed reactor was placed (inclination ±2 mm/m) in the center of the setup and 1140 mm from the X-ray source and 501 mm from the detector plate. For each experimental condition the attenuation of the X-ray beam was measured with a frequency of 35 Hz at the detector plate purchased from Xineos CMOS X-ray Flat Detectors (Xineos-3131® 30x30 cm in size). The theoretical spatial resolution of the detector is 0.2 mm per pixel. The measured data at the detector plate were stored on a PC for further analysis.

The entire experimental procedure was controlled with a workstation outside the setup room (covered with a lead sheet) ensuring a safe working condition. Using the workstation it was possible to trigger the X-ray source and read out the signals from the detector plate.

Further details on the setup and the measurement technique can be found in [15,16,18]. Each result reported in the present study is an average of 2100 frames (35 Hz) of one minute of continuous recording from one source and one detector plate. The sampling time of one minute allows to obtain sufficient data for statistics with a minimum error from the mean [15].

The lab-scale fluidized bed reactor was constructed of Perspex® and 10 cm in inner diameter (5 mm wall thickness) and 100 cm in length. The inlet was connected to compressed air controlled by a Bronkhorst® type mass flow controller. The size of the reactor is similar to the size of small scale fluidized bed reactors for micro heat and power applications [20]. The gas distributor plate was made of sintered stainless steel (40 μm pore size, 3.2 mm thick from Van Borselen Filters) to ensure a homogenous distribution of the gas at the bottom of the column. To minimize particle entrainment from the column a freeboard was designed and installed at the top part the reactor. Figure 5.1a shows a picture of the fluidized bed column placed between the X-ray source and the detector plate.

The immersed membranes were porous Al_2O_3 (100 nm pore size at the surface). Each membrane was 20 cm in length and 1 cm in outer diameter sealed to a plastic cap from one side and to a stainless steel Swagelok component (with graphite ferrule) from the other side [6]. At the outlet of the column, the membranes were connected to a 12 mm outlet tube that was connected to a vacuum pump (TRIVAC Leybold LH) with a capacity of 40 ln/min of air, which could be controlled with a Brooks® mass flow controller (0-44 ln/min) using Labview software. Due to the pressure drop in the lines from the outlet of the membrane module to the vacuum pump, a total flow rate of 10 ln/min of air could be maximally extracted via each membrane at room temperature and 1 bar pressure difference across the membrane. It should be noted that without the pressure drop in the lines a total flow rate of 22 ln/min could be extracted via each membrane at similar operating conditions [21].

Two different membrane modules were designed: one module with one membrane in the center of the reactor and one module with five membranes in a star configuration. For each membrane module, two spacer plates made from Perspex® were used to keep the membrane(s) in place and avoid any movement during fluidization. Such spacers are generally used when submerging membranes in fluidized bed reactors [20,22]. Figure 5.2 shows a schematic representation of the membrane spacers and their specifications.

Table 5.1 summarizes the relative area of the spacers to the reactor cross-sectional area. Although it is important to use spacers to keep the membranes in place and avoid breakage of the membrane tubes, it is expected that the spacer plates may also affect the fluidization due to their presence. Also the influence of the spacers on the hydrodynamics is investigated in this chapter.

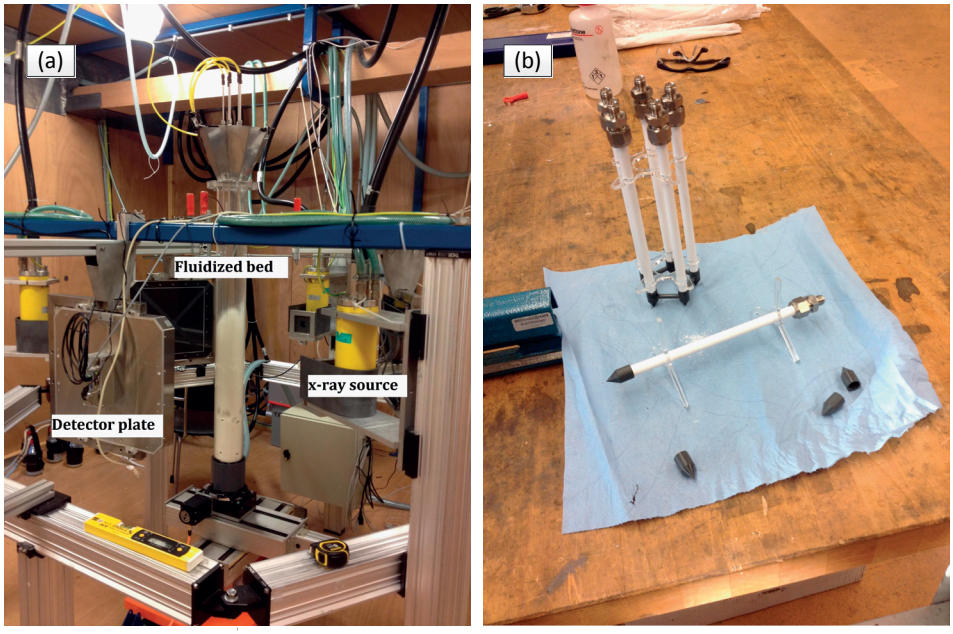

Figure 5.1 (a) The designed fluidized bed placed between the X-ray source and the detector plate (b) Membrane modules of one and five membranes with spacer plates and sealing

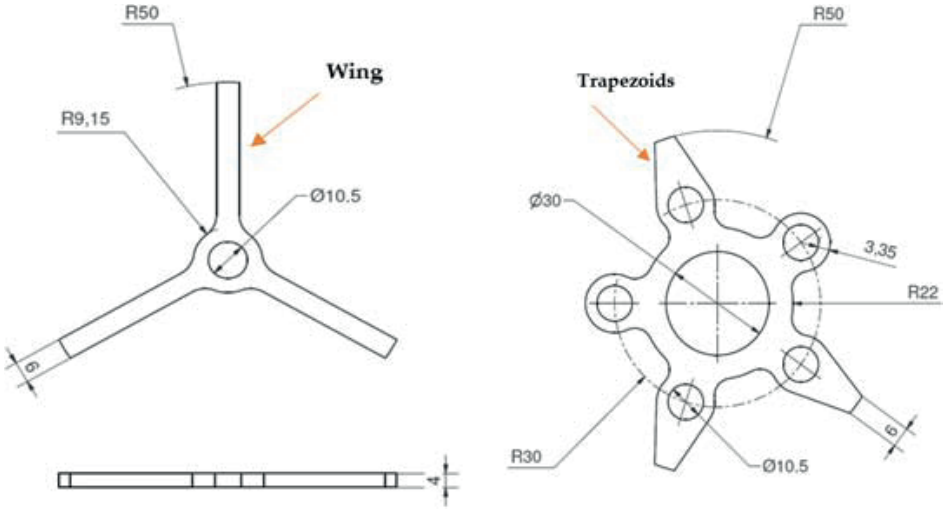

Figure 5.2 Spacer plates (left) spacer designed for the membrane module with one single membrane in the middle of the reactor and (right) spacer plate designed for the membrane module with five membranes in a star shape configuration (all measures are in mm).

Table 5.1 Relative area of the spacers to the reactor cross sectional area

Module	Number of membranes	Spacer section area 10^{-4} m^2	Reactor cross section area 10^{-4} m^2	Spacer area / Reactor cross section area (%)
I	1	9.12	78.5	11.6
II	5	19.8	78.5	25.2

Two different types of particles were used in this study. The first batch was 400-600 μm polystyrene particles and the second batch was 80-200 μm Al_2O_3 particles. For all the experiments the stagnant bed height of the particles was 30 cm from the distributor plate (bed aspect ratio of 3) to ensure full immersion of the membranes inside the bed at minimum fluidization conditions. Table 5.2 summarizes the physical properties of the used particles.

Table 5.2 Physical properties of the used particles

Material	Avg. particle diameter[1] [μm]	Apparent Density (g/cc)[2]	Minimum fluidization velocity[3](U_{mf}) [cm/s]	Geldart classification [23] [-]
Polystyrene	500	1.06*	22.0	B
Al_2O_3	160	1.691	2.4	A/B

[1] FRITSCH ANALYSETTE22; [2] ThermoFisher SCIENTIFIC Pascal 140 series; [3] by measuring the pressure drop over the distributor plate and the bed; *from [19]

To capture the behavior over the full length of the bed, and due to the fact that the detector plate and the X-ray source were fixed in place, the reactor module was relocated vertically using an adjustable table. For each single experiment, measurements were performed four times and at four different distances of the X-ray source from the distributor plate (H value in Figure 5.3), allowing to compare the average properties of the bed at vertical positions in the bed for the different cases.

The column was filled with particles and aligned in the middle of the X-ray source and the detector plate. According to the performed contrast tests at bubbling fluidization conditions, the X-ray source and camera settings were determined to ensure a very good contrast between the bubble and the emulsion phases. First, experiments were performed without the membrane modules (standard fluidized bed) to monitor the bed behavior at different fluidization numbers (0-3.5) and particle types (both Geldart B and Geldart A/B particles). Subsequently, the membrane modules with one and five membranes were immersed inside the bed and experiments were repeated at identical conditions (compared to the standard fluidized bed) without gas extraction via the membranes to quantify the effects of only the presence of the vertically immersed internals. In the last set of experiments, different amounts of gas (compressed air,

up to 40 % of the inlet flow rate) was extracted through the membranes and the bed behavior was monitored at otherwise identical operating conditions.

5.2.2 Image analysis

For each experiment, the attenuation of the X-ray beam was measured for each pixel at the detector plate to have the projected 2D intensity map of the bed in time. For each obtained single frame, initially the image was corrected for dead pixels caused by imperfections of the detector plates: the measured attenuation of each dead pixel was replaced by the mean value of the neighboring cells. Then, the frames were cropped to the desired region of interest for each experiment. To have the actual view of the column each frame was rotated 90° and flipped. Figure 5.4 shows the result of the performed image correction protocol for a typical single frame image.

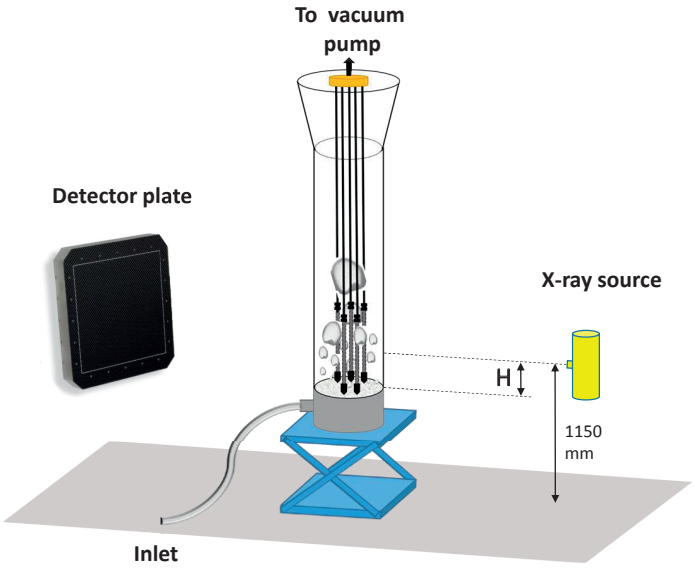

Figure 5.3 A schematic representation of the experimental setup with the reactor in the center of the setup. The reactor was scanned at four different axial positions H (mm):0, 80, 160 and 240 mm

To convert the measured attenuation (intensity) to a solids concentration (path length), a calibration protocol was performed. A dummy calibration module made of identical material (Perspex®) and with identical inner diameter (100 mm) and wall thickness (5 mm) as the fluidized bed reactor was constructed (Figure 5.5). The height of the dummy column was 10 cm.

Initially the dummy module was placed (1140 mm from the X-ray source and 501 mm from the detector plate) and aligned (±2 mm/m) between the X-ray source and the detector plate. The height of the column was adjusted to ensure that the whole module was covered at

the detector plate. Afterward, the module was filled in a segment wise mode (using a separation wall for the different segments) with different amount of particles (polystyrene or Al_2O_3). For each case the attenuation of the outlet X-ray beam from the column was measured at a pixel pocket (50x50) at the detector plate. Figure 5.5 shows the dummy module half filled with polystyrene particles when the separation wall was perpendicular and parallel to the X-ray source.

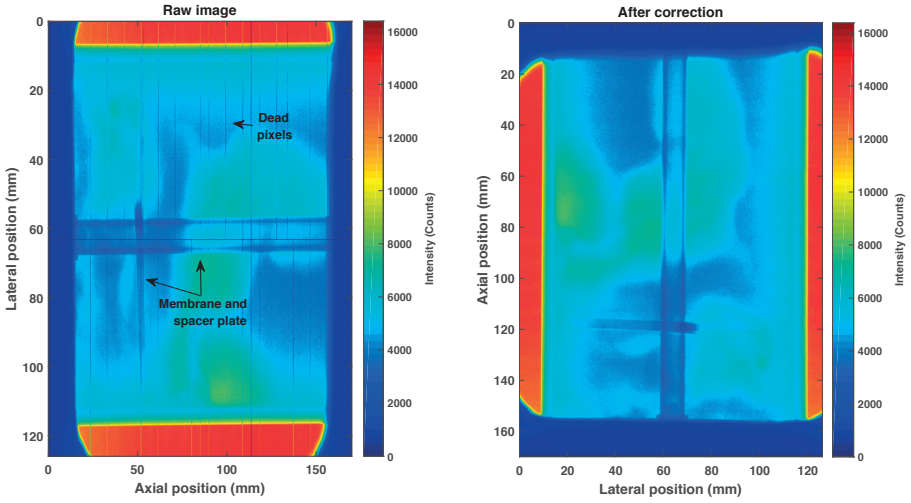

Figure 5.4 (left) Raw intensity map recorded at the detector plate. Frame needs to be corrected for dead pixels, orientation and contrast (right) dead pixels have been replaced by the average value of the neighboring cells; image has also been corrected for contrast and orientation. Geldart B type particles at 2 U/U_{mf}, H = 80 mm.

For all the experiments it was ensured that the separation wall (used to fill the column in segments) was parallel to the X-ray source (90° rotation from the case where the separation wall is perpendicular to the X-ray source). Knowing the exact thickness (path length) of the particle slice, the attenuation of the X-ray beam was converted to a path length of material inside the bed. Five different segments (empty bed, $1/4^{th}$, $2/4^{th}$, $3/4^{th}$ and full bed) were chosen for the calibration curve.

Figure 5.6 shows the fitted (2^{nd} order logarithmic) calibration curves for polystyrene (Geldart B) and Al_2O_3 (Geldart A/B) particles (error is below 3% or 2 mm of bed depth). Detailed information on the fitting parameters can be found in Table 5.3.

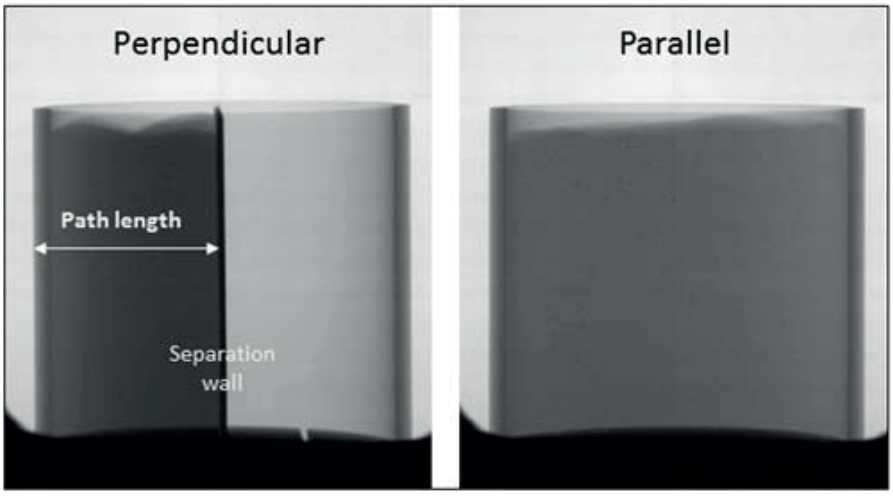

Figure 5.5 Calibration module filled 2/4th with polystyrene particles and (a) Separation wall is perpendicular to the X-ray source (b) Separation wall is parallel to the X-ray source.

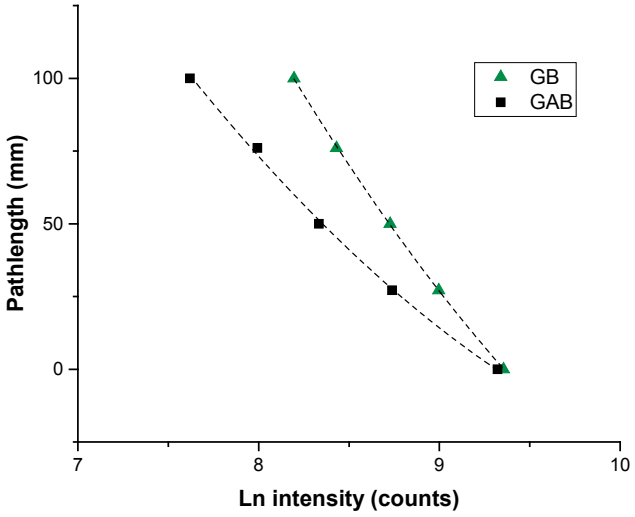

Figure 5.6 Fitted calibration curves for different particles. GB: polystyrene and GAB:Al_2O_3 particles (2nd order logarithmic)

Table 5.3 Fitting parameters for the calibration curves

Particle	Intercept		B1		B2		Statistics
Al_2O_3	Value	Standard error	Value	Standard error	Value	Standard error	Adj. R^2
Path length	1292.6	3.05×10^{-12}	-235.5	7.22×10^{-13}	10.38	4.26×10^{-14}	1
Polystyrene	Value	Standard error	Value	Standard error			Adj. R^2
Path length	1827.36	1.04×10^{-11}	-320.1	2.37×10^{-12}	13.34	1.35×10^{-13}	1

Membrane correction

For the experiments using the membrane modules, the intensity maps needed to be corrected for the effect of the membranes on the output intensity. To correct for the presence of the membrane(s) in each frame and for each experiment, two cases with and without membrane presence at 0 U/U_{mf} were selected. Theoretically, if an X-ray beam with initial attenuation of I_0 passes through a stagnant bed of particles with a bed thickness of d_p, and reactor wall thickness of d_w, the outlet intensity (I) of the beam can be calculated with Eq.(5.1).

$$I/I_0 = e^{[-\mu_w d_w - \mu_p d_p]} \qquad \text{Eq.(5.1)}$$

where μ represents the attenuation coefficient of the media (using subscripts w and p to refer to the reactor wall and particles respectively). If a single membrane is submerged in the middle of the bed, for the outlet intensity of the X-ray beam in the presence of the membrane (I¢), Eq.(5.1) can be rewritten as:

$$I'/I_0 = e^{[-\mu_w d_w - \mu_p d_{p'} - \mu_m d_m]} \qquad \text{Eq.(5.2)}$$

where $d_{p'}$ is the corrected thickness of the bed at the presence of the membrane (d_m is the outer diameter of the membrane):

$$d_{p'} = d_p - d_m \qquad \text{Eq.(5.3)}$$

so that

$$\alpha = \ln I/I' = d_m(\mu_m - \mu_p) \qquad \text{Eq.(5.4)}$$

where α represents the net contribution of the membrane presence on the intensity profile. Also where the membrane spacers are located, α will include the effect of spacers as well.

For each frame, the α value at each pixel was added to the logarithm of intensity at the corresponding pixel. Later the exponential of the product was calculated to obtain the corrected intensity map. Figure 5.7 shows the results of the membrane correction and calibration steps for a selected frame.

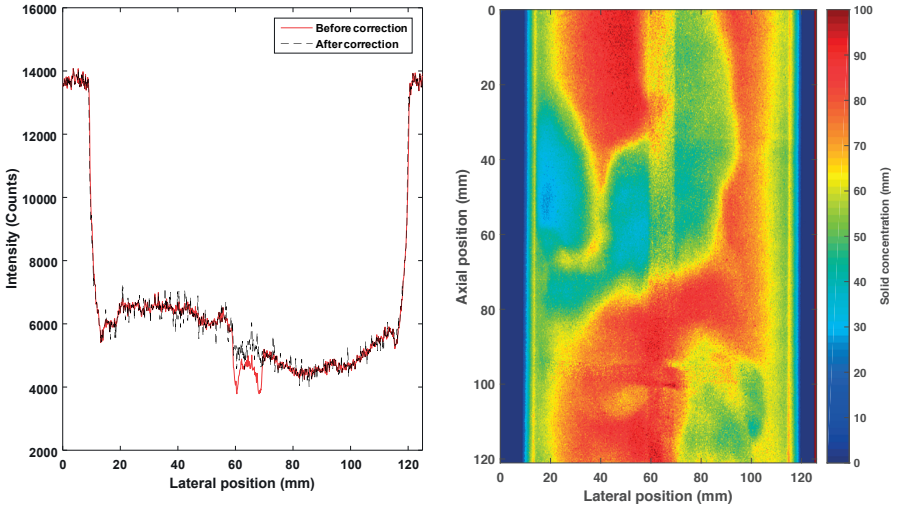

Figure 5.7 (left) Output intensity profile at a certain reactor height (70 mm above the distributor plate) across the bed width before and after image correction for the presence of the membrane (right) converted intensity map to solids concentrations (path length); at 2 U/U_{mf} and H = 80 mm.

For each experiment a standard sample of 2100 frames (35 fps) equal to 1 minute of continuous recording was chosen. Each frame was corrected according to previously described image correction protocol. In the next section the output results from the experiments will be analyzed and the main conclusions will be drawn accordingly.

5.3 Results and discussion

The obtained results from the experiments at different operating conditions and membrane reactor configurations will be discussed and analysed in two parts. In the first part, the average solids concentration maps for the cases with and without membrane presence will be discussed for the polystyrene particles (Geldart B), showing the effect of the different number of inserted membranes and the extent of gas extraction on the average solids concentration maps. Subsequently, the dynamics of the bubble phase along the reactor module will be discussed and recommendations will be given on the design of such membrane reactor units.

The second part of the discussion focuses on the results obtained with alumina particles (Geldart A/B) and the bed behaviour in the absence and presence of the membrane modules

and together with different extraction values. Specifically the average solids concentration fields at different positions in the lateral position of the column (from the membrane surface to the reactor wall) will be inspected to investigate the probability of formation of densified zones, and quantification of their thickness, in the case of very high gas extraction values.

5.3.1 Geldart B

Effect of internals

First the effect of internals on the hydrodynamics of the fluidized bed filled with polystyrene particles was studied. Three cases were selected: (1) standard fluidized bed without internals, (2) fluidized bed with the membrane module containing one single membrane in the middle of the reactor, but without gas extraction, and (3) fluidized bed with the membrane module with five membranes arranged in a star shape, also without gas extraction. For all these cases the outlet velocity was kept the same, implying that the inlet flow rate was corrected for the presence of the membrane(s). Figure 5.8 shows the obtained time-averaged (over 1 min of recording) solids concentration fields (in mm of solids path length) for the three cases. The color bar represents the normalized solid concentrations (in mm of solids path length), where 100 represents the maximum solids packing of a fixed bed (inner diameter of the reactor is 100 mm) and zero stands for an empty bed.

Figure 5.8a shows that for the standard fluidized bed case without immersed membranes the time-averaged normalized solids concentration decreases in the axial direction, as expected, corresponding to the well-known bubble growth and coalescence. However, the measured values of the solids concentration were relatively low. Inspecting the snapshots from the experiments (Figure 5.9) heavy slugging of the bed is clearly visible, as may have been expected related to the small bed diameter and relatively large size of the particles. Once the membrane module with one single membrane in the middle of the bed was immersed, the degree of slugging was largely decreased (Figure 5.8b). This is attributed to increased bubble break-up because of the presence of the immersed membrane and membrane spacer.

Figure 5.8c shows the time-averaged solids concentration for the case with the membrane module consisting of five membranes immersed inside the fluidized bed. In comparison with the case with one single membrane in the middle, the solids concentration is increased along the membrane module and around the membranes. The maximum solids concentration was found at the bottom spacer plate and close to the membranes. It should be noted that for all the cases higher solids concentrations were observed close to the surface of the membrane(s) than in the bulk of the fluidised bed.

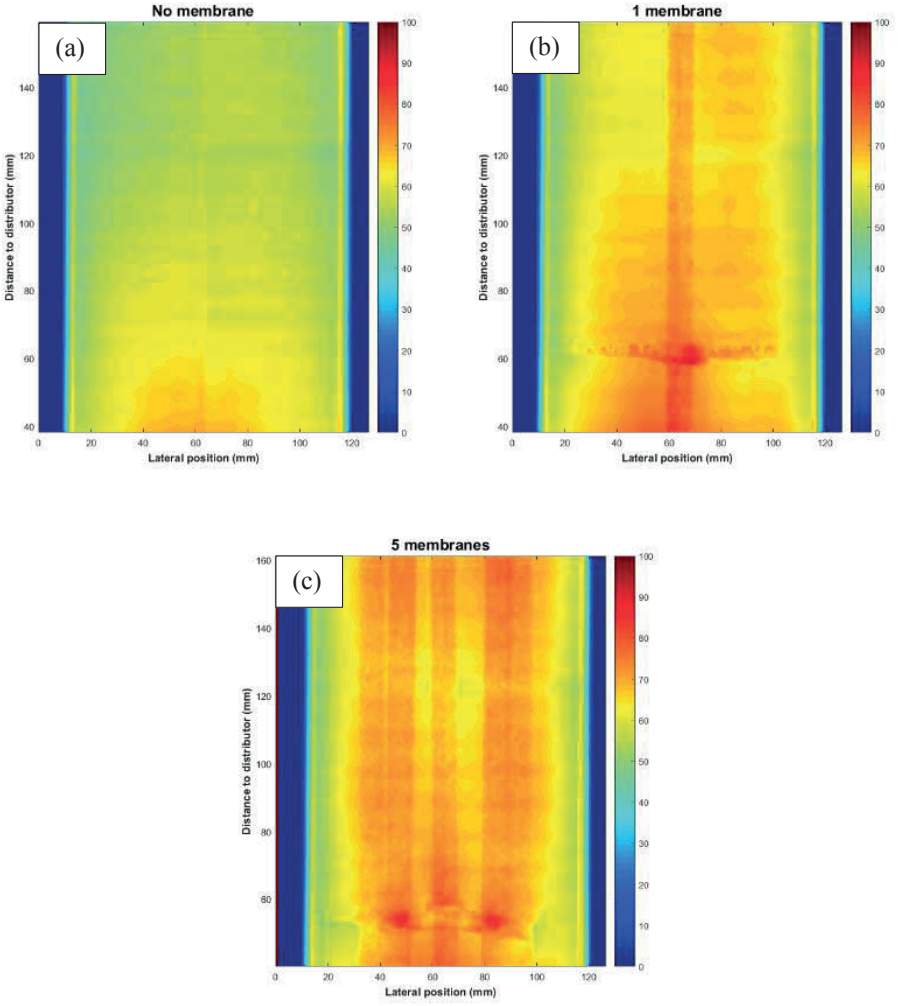

Figure 5.8 Time-averaged normalized solids concentration map for three cases: (a) standard fluidized bed without membrane module; (b) Fluidized bed with one single membrane in the middle without gas extraction; (c) Fluidized bed with 5 membranes in a star configuration without gas extraction. The color bar represents the normalized solid concentrations, where 100 mm represents the maximum solids packing of a fixed bed (inner diameter of the reactor is 100 mm).

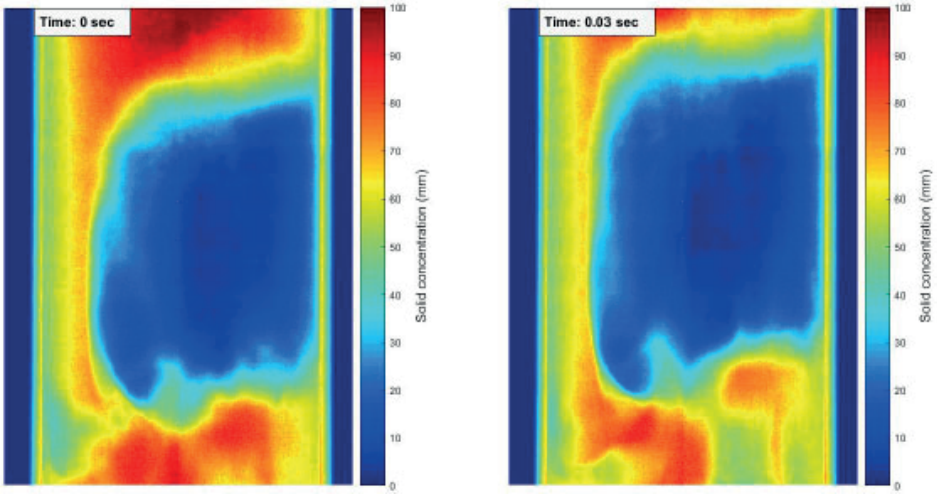

Figure 5.9 Snapshots from the experiments without membrane modules; Geldart B (Polystyrene) particles; 2 U/U_{mf}, H = 80 mm.

Effect of spacers

Figure 5.10a shows the time-averaged solids concentration field for the case with one single membrane immersed in the middle of the bed at 2 U/U_{mf} for different vertical positions. It can be seen from the results at plane 2 (i.e. at H = 80 mm) that at the bottom of the membrane and close to bottom spacer the solids concentration is somewhat higher indicating that there more gas bubbles move along the reactor walls. Passing over the membrane spacer the gas bubbles tend to travel back to the middle of the reactor where the membrane is. Moving higher in the fluidized bed to plane 3 (H = 160 mm), the average bubble size increases and the average solids concentration decreases. For the single membrane module the effect of the second spacer at the top on the hydrodynamics is much less pronounced in comparison to the effects of the bottom spacer. This may imply that there is an optimum distance between the spacers for maximum bubble cutting.

When the membrane module with five membranes was immersed inside the reactor, the average equivalent bubble diameter did not increase as much as for the single-membrane module, while the effect of the second spacer is more pronounced (Figure 5.10b). At the second spacer the bubbles tend to pass more frequently close to the wall and later back again to the middle part of the reactor.

The lateral solids concentration profiles for the case of the module with one single membrane in the middle were plotted and compared at different distances from the bottom distributor plate and for the cases with and without membranes. Also the experimental results for the case with gas extraction (10 ln/min equal to 5% of inlet flow) was included. For all the cases the outlet velocity was kept at 2 U/U_{mf} (the inlet flow rates were corrected for the reduced projected area of the membranes and for gas extraction).

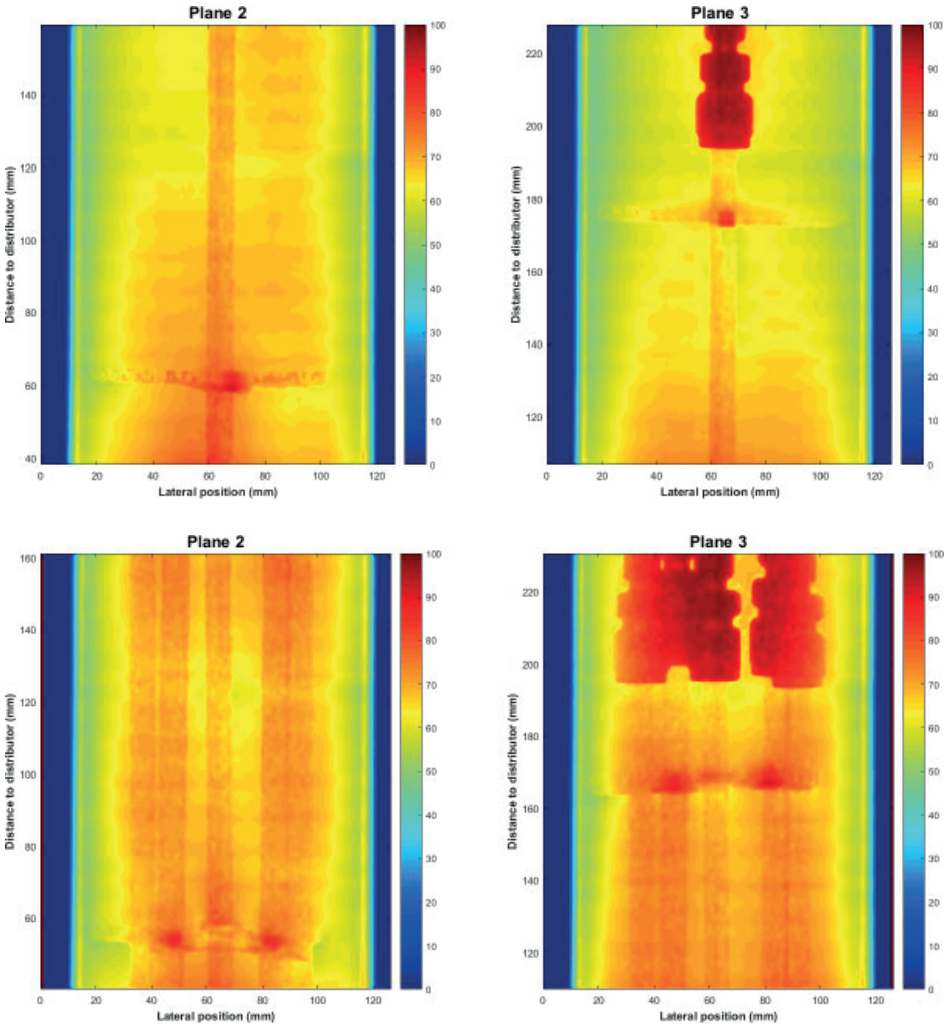

Figure 5.10 Average solids concentration maps inside the fluidized bed and along the membrane(s) (a) One single membrane immersed inside the fluidized bed (b) Membrane module with five membranes is immersed; H = 80 mm at plane 2 and H = 160 mm for plane 3, for all the cases the outlet velocity was kept the same at 2 U/U_{mf}. The color bars represent the normalized solids concentration in mm of particles path length (zero represents the empty bed and 100 stands for packed bed).

Figure 5.11a shows the obtained lateral solids concentration profiles for the case without immersed membranes at different axial distances from the distributor plate. For all the positions the average solids concentration decreases from the middle of the bed towards the reactor wall, as expected considering the relative small distance from the bottom distributor. Close to the reactor wall the solids concentration increases which is attributed to the solids back flow along the wall. Moving from the bottom of the reactor to higher bed axial positions, the solids concentration decreases related to bubble growth; only when passing through the

bottom spacer (63 mm above the distributor), the average solids concentration increases due to bubble cutting. Once more, this confirms the clear effect of the bottom spacer on the average bubble diameter.

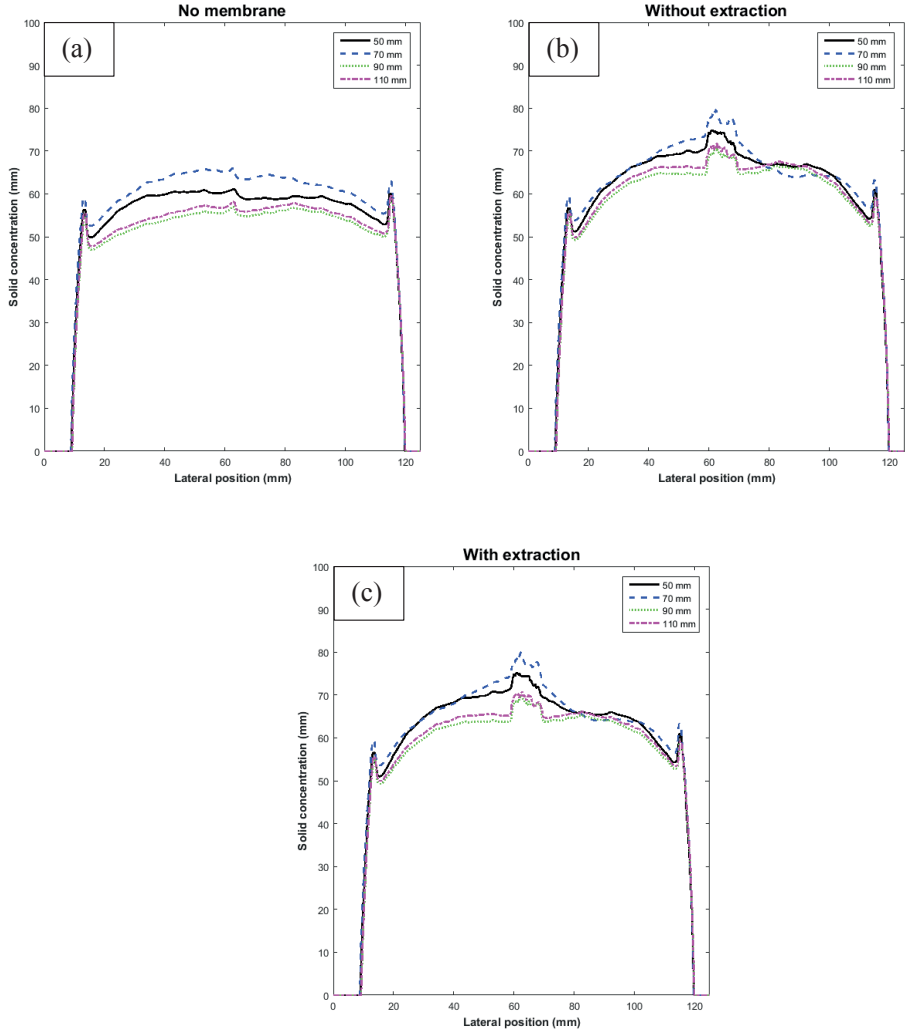

Figure 5.11 Time-averaged lateral solids concentration profiles at different heights from the distributor plate: (a) standard fluidized bed without membranes; (b) fluidized bed with one single membrane in the middle without gas extraction; (c) fluidized bed with one single membrane in the middle and 10 ln/min gas extraction. For all the cases the outlet velocity was kept at 2 U/U_{mf}.

When the membrane module with one single membrane was immersed inside the bed (Figure 5.11b), the solids concentration was strongly increased near the membrane wall, even for the case without gas permeation through the membranes. Thus it can be concluded that the formation of the so-called densified zones around the membrane(s) is not only due to gas extraction via the membranes, but also due to the presence of the membranes. Inspecting Figure 5.11c, no significant changes can be observed on the lateral solids concentration profiles related to the gas extraction (10 ln/min or 5% of the inlet flow), obviously related to the relatively small amount of gas extracted compared to the feed. To extend this study the experimental results from the case with the membrane module with five membranes (with and without gas extraction and up to 12.5% of the inlet flow rate) were analyzed (see Figure 5.12).

As evident from Figure 5.12a, and similar to the case with one single membrane submerged in the middle, higher average solids concentrations can be observed near the membranes. Moving from the reactor wall towards the middle of the reactor, the average solids concentration first increases to a maximum value and then decreases to a local minimum in the center of the reactor. This is related to the membrane module configuration, having five membranes located in a star shape without any membrane present in the middle of the module. Therefore, some bubbles will pass via the center of the module resulting in lower solids concentrations in the center.

Analyzing the effects of gas extraction via the membranes, the results for the case with gas extraction via the membranes (12.5 % of the inlet flow) showed no significant changes compared to the case without gas extraction in solids concentrations far from the bottom spacer (Figure 5.12b). However, very close to the bottom spacer (i.e. at 70 mm distance from the distributor plate), the effect of gas extraction on the lateral solids concentration profiles is more pronounced, where higher solids concentrations were observed close to the membranes when extraction was imposed.

Bubble phase dynamics

In the previous section the average solids concentration was investigated for the cases with and without submerged membranes varying the number of membranes and the relative amount extracted via the membranes. It was concluded that with the insertion of the membrane modules, higher solids concentrations was obtained along the reactor due to bubble cutting (reduced slug formation) when compared with the case without membranes present.

In order to substantiate this observation and to investigate the change in bubble phase behavior related to the presence of membranes, the average cycle time and the amplitude of the output signal at different bed positions can be used. Figure 5.13 shows a typical output intensity signal over a pixel pocket of 50x50 pixels in size (at $r/R = 0.5$, where r is the radial distance from the center of the reactor and R is the reactor radius) averaged over 3 s of continuous recording for two cases at 0 U/U_{mf} and at 2 U/U_{mf}. Inspecting the output signal for the case

at 2 U/U_{mf} (freely bubbling bed) reveals that the solids concentration is locally oscillating with an average amplitude and cycle time.

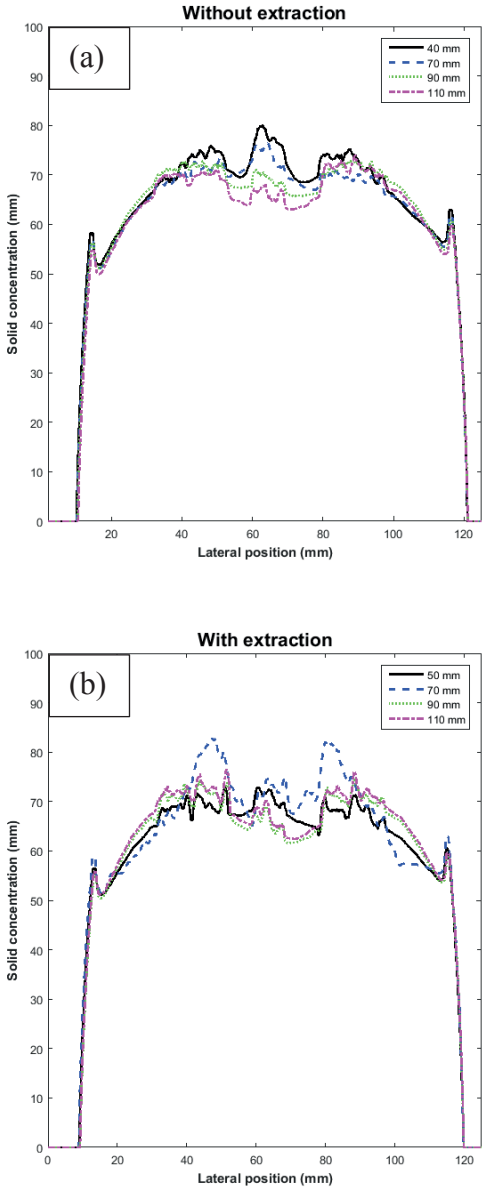

Figure 5.12 Time-averaged lateral solids concentration profiles at different heights from the distributor plate: (a) fluidized bed with the membrane module with 5 membranes in a star configuration and without gas extraction; (b) fluidized bed with the membrane module with 5 membranes in star configuration and 25 ln/min gas extraction (12.5% of the inlet flow). For all the cases the outlet velocity was kept at 2 U/U_{mf} .

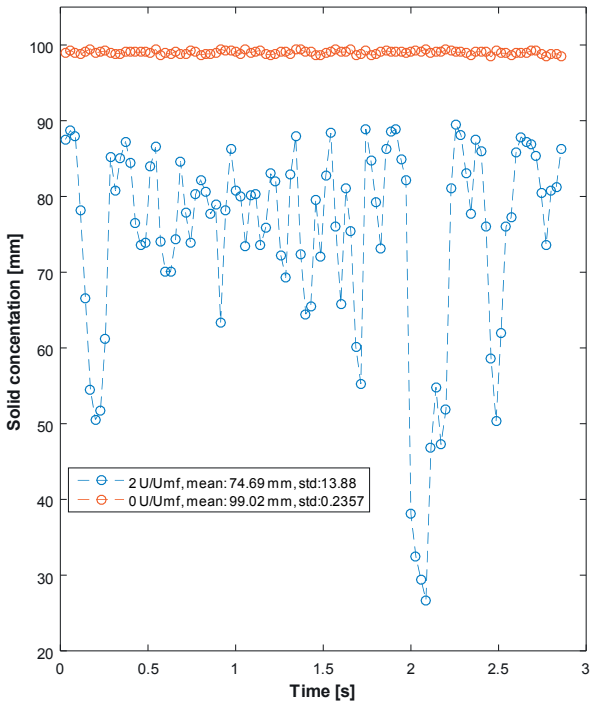

Figure 5.13 Output solids concentration signal in time at 0 U/U_{mf} and 2 U/U_{mf} (data was collected at 100 mm from the distributor plate and at r/R = 0.5).

The oscillations in time of the solids concentration is attributed to the passage of bubbles. When a bubble passes, the solids concentration decreases to a minimum value (depending on the bubble size) and goes through a maximum when the bubble has just passed. For the case at 0 U/U_{mf} (when the bed is stagnant), the standard deviation of the output signal was 0.2357 (mean: 99 mm of solid), while for the case at 2 U/U_{mf} the standard deviation increased to 13.88, confirming that the oscillations in solids concentrations is not caused by background noise (at 0 U/U_{mf}) and can be directly related to the passage of bubbles.

In order to quantify the bubble phase behavior at different experimental conditions, the output signal at the detector plate was monitored in time. Average cycle time and amplitude of the output signal was measured over 1 min of recording (2100 frames at 35 Hz) and at different axial positions along the reactor and in the middle of the annular space (r/R = 0.5). Three cases were selected for this analysis: 1) standard fluidized bed without internals; 2) Fluidized bed with one membrane in the middle without and with 10 ln/min gas extraction (5% of the inlet flow) through the membranes; 3) Fluidized bed with the membrane module consisting of five membranes without and with 25 ln/min gas extraction (12.5% of the inlet flow) via the

membranes. Figure 5.14 summarizes the obtained average cycle time and amplitudes for all these cases.

Figure 5.14a shows that for the case without membranes, at higher axial positions from the distributor plate, a higher average cycle time is measured. This is expected due to bubble growth along the reactor length. The same trend can be seen for the average amplitude at different axial positions (Figure 5.14b). This confirms the fact that at higher bed positions the bubble phase will grow to bigger bubbles that occupy a larger bed depth. In the presence of one single membrane in the middle of the reactor, the average output signal cycle time was reduced by 24% along the reactor (28% reduction in signal amplitude) in comparison with the case without immersed membranes. For the same case with gas extraction (5% of the inlet) the average cycle time was decreased by 20 % compared to the case without membranes.

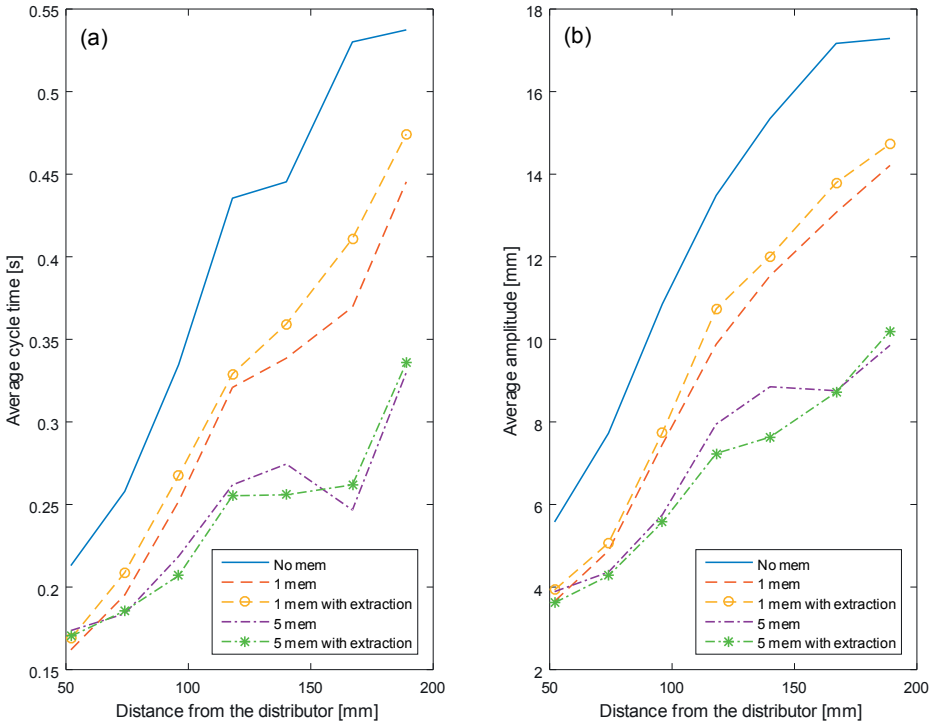

Figure 5.14 (a) Average cycle time and (b) average amplitude of the output signal at different axial positions along the reactor (for all the cases the inlet velocity was corrected for membrane(s) presence and gas extraction to keep the outlet velocity at 2 U/Umf. Each point in the graphs represents the average of 2100 frames (at 35 Hz) over a pixel pocket of 50x50 at r/R = 0.5.

When the membrane module with 5 membranes was immersed inside the bed (no extraction), the reduction in the average output signal cycle time was 36%, while the average signal

amplitude was reduced by 42%. This confirms that when a higher number of membranes are submerged, a higher degree of bubble cutting can be obtained. When 12.5% of the inlet gas was extracted via the membranes no significant changes in the average signal properties were observed (37% reduction in average cycle time and 45% reduction in amplitude compared with the case without membranes). In general, with submerged membranes a lower amplitude and cycle time was observed along the reactor length, with a more pronounced effect for the module with more membranes.

5.3.2 Geldart A/B

After the experiments with the polystyrene particles and at different operating conditions, the reactor was refilled with fine Al_2O_3 particles (Geldart A/B type). The stagnant bed height was 30 cm giving a bed aspect ratio of 3. Thus, it was ensured that the membrane module was fully immersed at minimum fluidization conditions. The lower minimum fluidization velocity for this type of particles required a lower inlet flow rate, allowing to achieve much higher values of gas extraction (up to 40% of the inlet flow).

Figure 5.15 shows the instantaneous solids concentration profiles from the experiment at 2 U/U_{mf} for the case without membranes. Compared to a similar case with Geldart B type particles at the same fluidization number and at the same height from the distributor plate, a clearly larger and more homogeneous average solids concentration was observed, without slug formation.

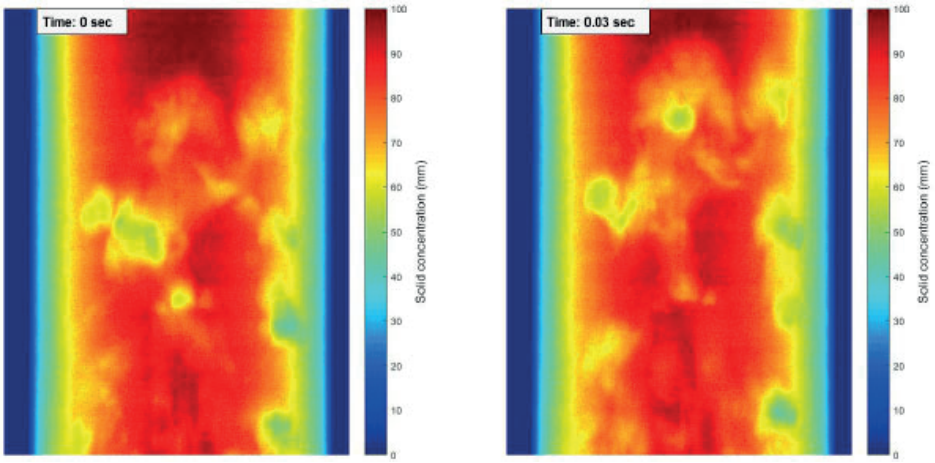

Figure 5.15 Instantaneous solids concentration profiles at different moments in time for the standard bubbling fluidized bed without membranes at 2 U/U_{mf}, where the bed was filled with fine Al_2O_3 particles (Geldart A/B), H = 80 mm.

The results shown in Figure 5.15 also imply that for fluidized bed reactors designed especially for micro heat and power applications (with similar reactor sizing as the fluidized bed used in

this study), a smaller average bubble diameter without slug formation can be obtained when using Geldart A/B type particles, with an expected positive effect on the bubble-to-emulsion phase mass transfer rate. In the next section the effect of the presence of and the permeation through a submerged membrane is investigated on the average solids concentration profiles.

Average solids concentration

The measured time-averaged solids concentration profiles for three different cases have been presented in Figure 5.16: a) standard fluidized bed without membranes; b) Fluidized bed with one single membrane in the middle and without gas extraction and c) Fluidized bed with one single membrane in the middle of the reactor and 40 % gas extraction (of the inlet flow). For all the cases the highest average solids concentration was found in the middle of the reactor. Note that these time-averaged solids concentrations are much higher than the solids concentrations measured for the polystyrene particles (Geldart B) at the same relative fluidization velocities, related to the smoother fluidization with smaller average bubble sizes.

When a membrane module with one single membrane was integrated inside the bed (Figure 5.16b), the average solids concentration was slightly decreased in the annular space between the membrane and the reactor wall, indicating that more bubbles pass between the membrane and reactor wall while far from the membrane and at the reactor wall no significant changes can be discerned.

In the presence of the membrane with gas extraction (40% of the inlet flow), a more clear change in the average solids concentrations was observed (Figure 5.16c). Especially near the surface of the membrane the average solids concentration shows a layer with maximum solids concentration. Far from the membrane surface and in the middle of the annular space (r/R = 0.5), a lower solids concentration was detected compared to the case without gas extraction. These results confirm that at sufficiently high extraction values, particles will accumulate near the membrane surface and form a densified layer which may impose an additional mass transfer resistance for gas components to reach the surface of the membranes [13]. Figure 5.17 shows the time-averaged lateral solids concentration profiles at different distances from the distributor plate and for the three different cases, supporting the above observations.

To investigate whether the densified solids layer near the membrane is stagnant or dynamic, the temporal evolution of the solids concentration was monitored at three different radial positions: 1) At the surface of the membrane at r/R = 0; 2) In the middle of the annular space at r/R = 0.5 and 3) Next to the reactor wall at r/R = 1 (all the points were located at 10 cm from the bottom distributor plate). For each case the solids concentration was measured and saved over 2100 frames (one minute of recording with 35 frames per second) and the histogram of the obtained solids concentration data, normalized by the total number of observations in each histogram bin, is given in Figure 5.18.

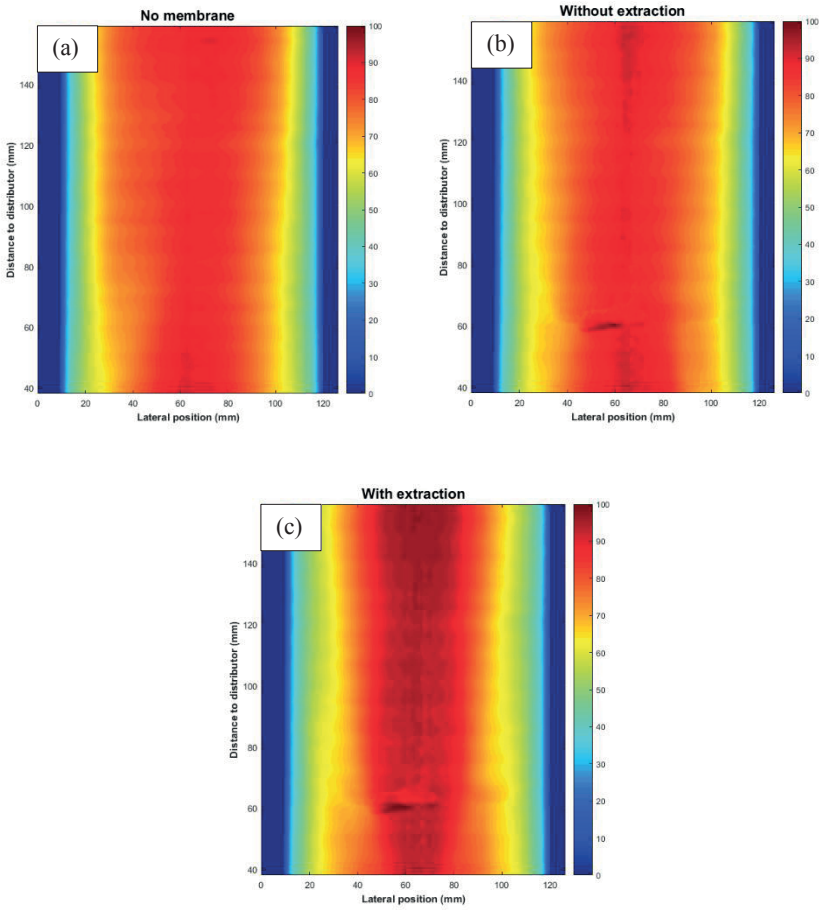

Figure 5.16 Time-averaged solids concentration profiles for: (a) Standard fluidized bed without membranes; (b) Fluidized bed with one single membrane in the middle of the reactor without gas extraction; (c) Fluidized bed with one single membrane in the middle of the reactor and with 40% gas extraction (of the inlet flow). At H = 80 mm and 2 U/U_{mf}. The color bar represents the normalized solids concentration (path length) in mm of particles, where zero indicates the empty bed and 100 the packed bed.

The probability distribution of the solids concentrations in the center of the column ($r/R = 0$) show for all the three different cases a skewness towards high solids concentrations, which increases due to the presence of the membrane and even more in case of gas extraction through the membrane. In case of gas extraction via the membrane in the center of the bed (Figure 5.18c), over 40% of the incidents the solids concentration reached the maximum value of 100 mm of bed depth, corresponding to the maximum packing of a packed bed, implying that for over 40% of the incidents no bubbles were passing near the membrane surface. Moving away from the surface of the membrane to the middle of the annular space ($r/R = 0.5$), the immersion of the membrane results in higher probabilities for lower solids concentrations compared with

the case without membrane in the bed. This confirms that the immersion of the membrane results in a higher gas bubble passage in the annular space. At the reactor wall ($r/R = 1$) a more Gaussian probability distribution can be observed for all the three scenarios. At the reactor wall no significant changes were observed when the membrane module was immersed inside the bed, or when 40% of the gas was extracted via the membrane.

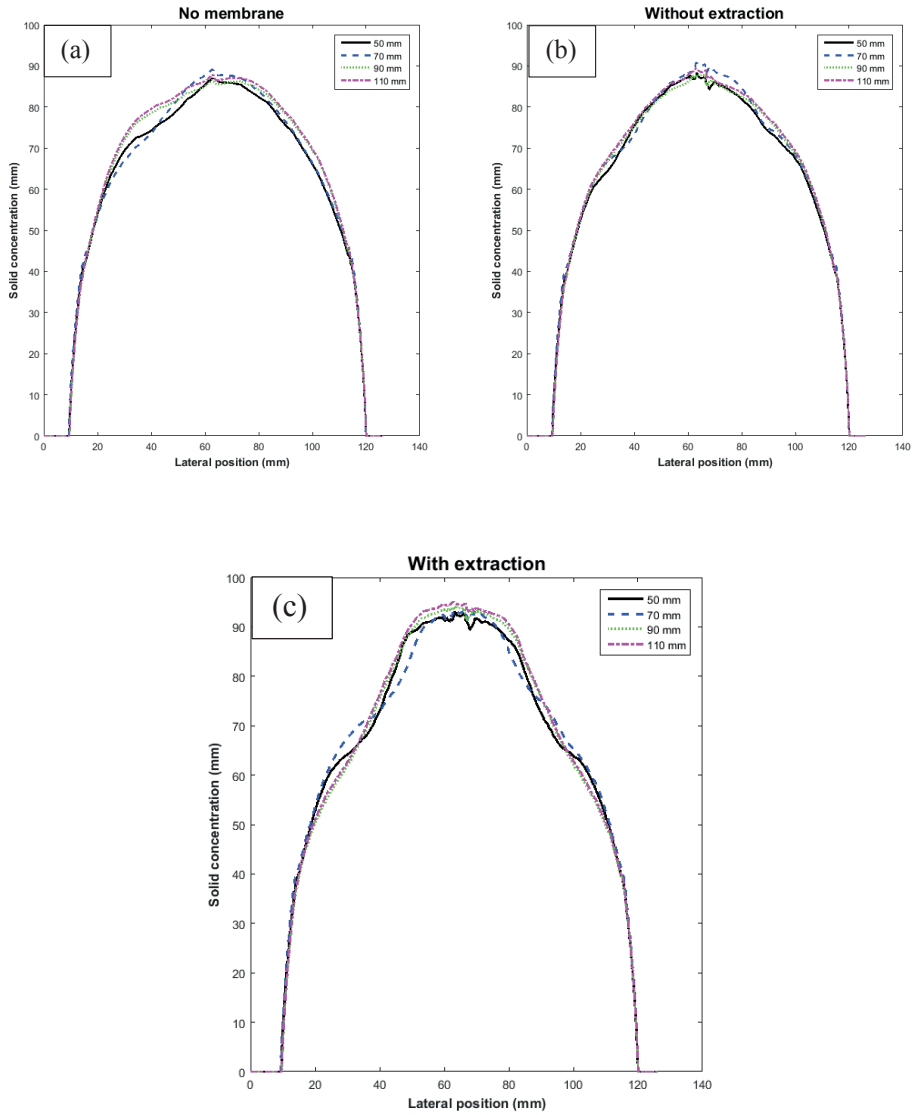

Figure 5.17 Average lateral solids concentration profiles at different distances from the distributor plate: (a) Standard fluidized bed without membrane (b) Fluidized bed with one single membrane in the middle without gas extraction (c) Fluidized bed with one single membrane in the middle with 40% gas extraction (of the inlet flow). For all the cases the outlet velocity was kept at 2 U/U_{mf}.

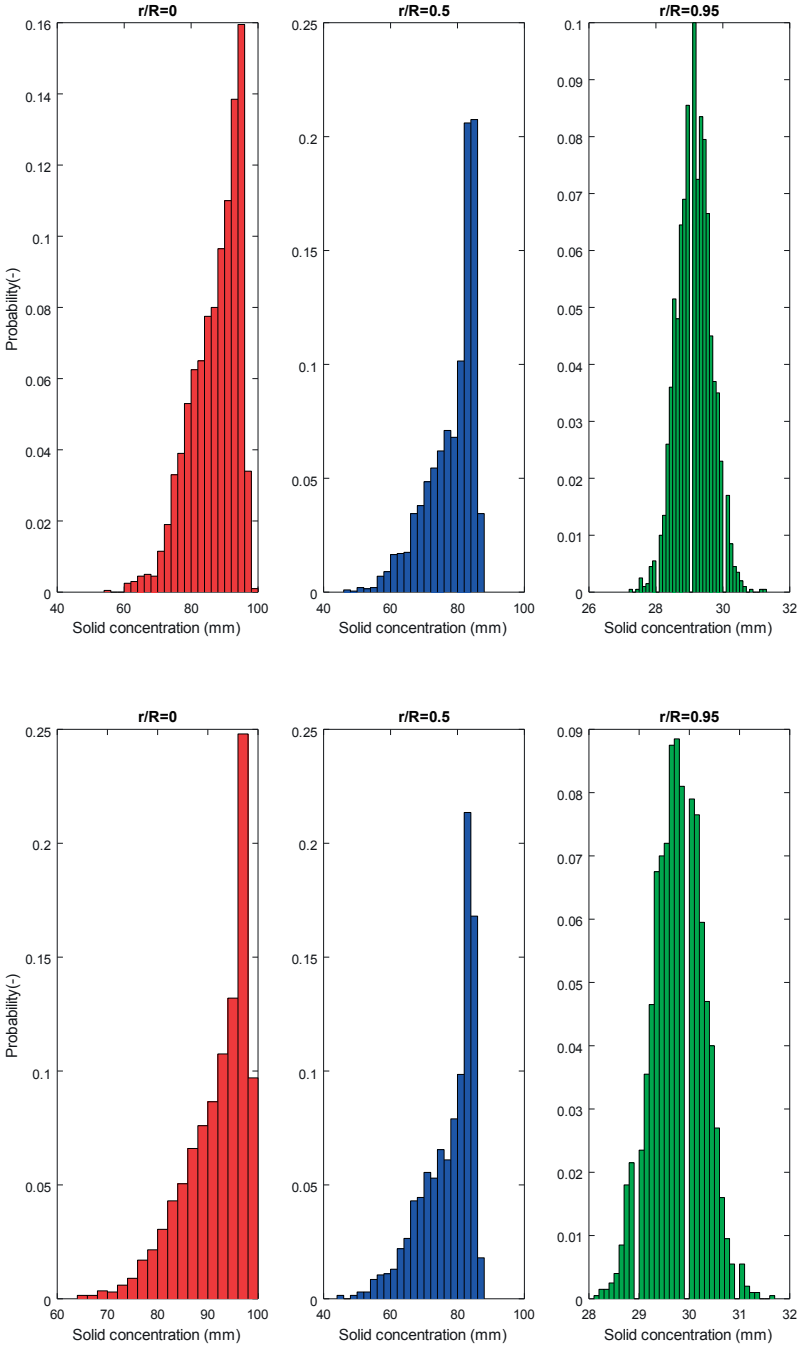

Figure 5.18 Normalized histograms at different lateral positions across the reactor width and for three different cases

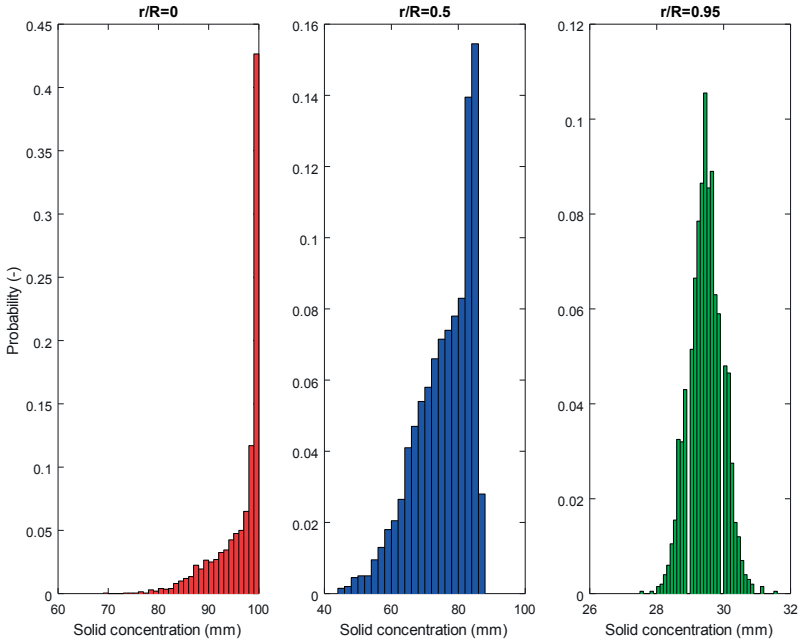

Figure 5.18 Normalized histograms at different lateral positions across the reactor width and for three different cases: (a) Standard fluidized bed without membrane; (b) Fluidized bed with one single membrane immersed in the middle of the reactor without gas extraction; (c) Fluidized bed with one single membrane in the middle of the reactor with 40% gas extraction (of the inlet flow). For all the cases the outlet velocity was kept the same at 2 $U/U_{mf.}$

5.4 Conclusions

The hydrodynamics of a 10 cm diameter membrane-assisted fluidized bed was investigated using a fast X-ray analysis technique. For each experiment the output attenutation of the X-ray beam was measured at the detector plate for over one min of continuous recording. A total number of 2100 frames (35 Hz) was saved for all experiements. The projected 2D solids concentration maps were obtained after a detailed image correction and calibration procedure.

Two different membrane modules with one and five membranes were designed and constructed to monitor the behavior of the fluidized bed in absence and in presence of the membrane modules and with and without gas extraction through the membranes. Two different particle types were investigated, viz. 400-600 µm polystyrene and 80-200 µm Al_2O_3 particles, belonging to type B and A/B of the Geldart classification, repectively.

The obtained results revealed the heavy slugs formation when using the Geldart B type particles without the membrane modules. The formation of these slugs corresponds with a strong decrease in the time-averaged solids concentrations inside the fluidized bed and may

increase the overall mass transfer resistance and increase gas bypass, thus possibly deteriorating the reactor performance. Once the membrane modules were immersed inside the fluidized bed, the extent of slugging was largely decreased attributed to increased bubble breakage.

At higher axial positions inside the fluidized bed, the average bubble diameter increased, which may impose or aggravate mass transfer limitations between the bubble and emulsion phases. In a research study by Gallucci et al. [24] it was proposed to circumvent these mass transfer limitations by using spacers (e.g. wire mesh) inside the bed. Results from our study indicated that the membrane modules (membranes/spacers) can be used not only to extract (and purify) gas from the reactor, but can simultaneously be exploited to limit bubble growth along the reactor height.

Placing the membrane spacers far from each other resulted in reduced bubble cutting along the bed. Decreasing the distance between the spacers (shorter membranes) may also be beneficial to keep the membranes better fixed and improve their lifetime depending on the membranes' mechanical stability. Thus, positioning more spacers with shorter membranes may improve both the hydrodynamics and the mechanical stability of the membranes. This will result in a smaller average bubble diameter and enhanced mass transfer between emulsion and bubble phases.

The obtained results for the time-averaged solids concentration fields for the case of the membrane module with one membrane in the center and using Geldart A/B type particles confirmed that at high extraction values, particles will accumulate near by the membrane and form a layer which may induce an additional mass transfer resistance for gas components to reach the surface of the membranes, whereas more bubbles were passing in the annular space between the membrane and the reactor wall. This was further supported by the probability density function of the solids concentration at different radial positions. The results from this study can help optimizing the positioning of the membrane and membrane spacers for optimal performance of fluidized bed membrane reactors.

Bibliography

[1] G. Di Marcoberardino, L. Roses, G. Manzolini, Technical assessment of a micro-cogeneration system based on polymer electrolyte membrane fuel cell and fluidized bed autothermal reformer, Appl. Energy. 162 (2016) 231–244. doi:10.1016/j.apenergy.2015.10.068.

[2] A. Brunetti, E. Drioli, G. Barbieri, Energy and mass intensities in hydrogen upgrading by a membrane reactor, Fuel Process. Technol. 118 (2014) 278–286. doi:10.1016/j.fuproc.2013.09.009.

[3] F. Gallucci, E. Fernandez, P. Corengia, M. van Sint Annaland, Recent advances on membranes and membrane reactors for hydrogen production, Chem. Eng. Sci. 92 (2013) 40–66. doi:10.1016/j.ces.2013.01.008.

[4] A. Helmi, E. Fernandez, J. Melendez, D.A. Pacheco Tanaka, F. Gallucci, M. van Sint Annaland, Fluidized Bed Membrane Reactors for Ultra Pure H_2 Production-A Step forward towards Commercialization., Molecules. 21 (2016). doi:10.3390/molecules21030376.

[5] E. Fernandez, J.A. Medrano, J. Melendez, M. Parco, J.L. Viviente, M. van Sint Annaland, F. Gallucci, D.A. Pacheco Tanaka, Preparation and characterization of metallic supported thin Pd-Ag membranes for hydrogen separation, Chem. Eng. J. (2015). doi:10.1016/j.cej.2015.09.119.

[6] E. Fernandez, A. Helmi, K. Coenen, J. Melendez, J.L. Viviente, D.A. Pacheco Tanaka, M. van Sint Annaland, F. Gallucci, Development of thin Pd-Ag supported membranes for fluidized bed membrane reactors including WGS related gases, Int. J. Hydrogen Energy. 40 (2015) 3506–3519. doi:10.1016/j.ijhydene.2014.08.074.

[7] E. Fernandez, J. Angel Sanchez-García, J. Melendez, V. Spallina, M. van Sint Annaland, F. Gallucci, D.A. Pacheco Tanaka, Development of highly permeable ultra-thin Pd-based supported membranes, Chem. Eng. J. Submited (2015). doi:10.1016/j.cej.2015.11.060.

[8] T. A. Peters, M. Stange, R. Bredesen, On the high pressure performance of thin supported Pd–23%Ag membranes—Evidence of ultrahigh hydrogen flux after air treatment, J. Memb. Sci. 378 (2011) 28–34. doi:10.1016/j.memsci.2010.11.022.

[9] T. A. Peters, T. Kaleta, M. Stange, R. Bredesen, Hydrogen transport through a selection of thin Pd-alloy membranes: Membrane stability, H_2S inhibition, and flux recovery in hydrogen and simulated WGS mixtures, Catal. Today. 193 (2012) 8–19. doi:10.1016/j.cattod.2011.12.028.

[10] J.F. De Jong, M. van Sint Annaland, J.A.M. Kuipers, Experimental study on the hydrodynamic effects of gas permeation through horizontal membrane tubes in fluidized beds, Powder Technol. 241 (2013) 74–84. doi:10.1016/j.powtec.2013.03.014.

[11] J.A. Medrano, R.J.W. Voncken, I. Roghair, F. Gallucci, M. van Sint Annaland, On the effect of gas pockets surrounding membranes in fluidized bed membrane reactors: An experimental and numerical study, Chem. Eng. J. (2015). doi:10.1016/j.cej.2015.04.007.

[12] N.T.Y. Dang, F. Gallucci, M. van Sint Annaland, Micro-structured fluidized bed membrane reactors: Solids circulation and densified zones distribution, Chem. Eng. J. 239 (2014) 42–52. doi:10.1016/j.cej.2013.11.001.

[13] L. Tan, I. Roghair, M. van Sint Annaland, Simulation study on the effect of gas permeation on the hydrodynamic characteristics of membrane-assisted micro fluidized beds, Appl. Math. Model. 38 (2014) 4291–4307. doi:10.1016/j.apm.2014.04.044.

[14] S.A. Wassie, F. Gallucci, S. Cloete, A. Zaabout, M. van Sint Annaland, S. Amini, The effect of gas permeation through vertical membranes on chemical switching reforming (CSR) reactor performance, Int. J. Hydrogen Energy. 41 (2015) 8640–8655. doi:10.1016/j.ijhydene.2015.12.003.

[15] S. Maurer, E.C. Wagner, T.J. Schildhauer, J.R. van Ommen, S.M.A. Biollaz, R.F. Mudde, X-ray measurements of bubble hold-up in fluidized beds with and without vertical internals, Int. J. Multiph. Flow. 74 (2015) 118–124. doi:10.1016/j.ijmultiphaseflow.2015.03.009.

[16] S. Maurer, E.C. Wagner, J.R. van Ommen, T.J. Schildhauer, S.L. Teske, S.M.A. Biollaz, A. Wokaun, R.F. Mudde, Influence of vertical internals on a bubbling fluidized bed characterized by X-ray tomography, Int. J. Multiph. Flow. 75 (2015) 237–249. doi:10.1016/j.ijmultiphaseflow.2015.06.001.

[17] S. Maurer, D. Gschwend, E.C. Wagner, T.J. Schildhauer, J. Ruud van Ommen, S.M.A. Biollaz, R.F. Mudde, Correlating bubble size and velocity distribution in bubbling fluidized bed based on X-ray tomography, Chem. Eng. J. 298 (2016) 17–25. doi:10.1016/j.cej.2016.02.012.

[18] R. F. Mudde, Bubbles in a Fluidized Bed: A Fast X-ray Scanner, AIChE J. 57 (2011) 2685–2690. doi:10.1002/aic.

[19] R.F. Mudde, J. Alles, T.H.J.J. van der Hagen, Feasibility study of a time-resolving x-ray tomographic system, Meas. Sci. Technol. 19 (2008) 85501. doi:10.1088/0957-0233/19/8/085501.
[20] RE4CELL, Advanced Multi-Fuel Reformer for Fuel CELL CHP Systems - ReforCELL, http://www.reforcell.eu/ (accessed August 8, 2016).
[21] E. Fernandez, J. Sanchez-Garcia, J. Viviente, M. van Sint Annaland, F. Gallucci, D. Tanaca, Morphology and N_2 Permeance of Sputtered Pd-Ag Ultra-Thin Film Membranes, Molecules. 21 (2016) 210. doi:10.3390/molecules21020210.
[22] DEMCAMER, Design and manufacturing of catalitic membranes reactors by developing new nano-architectured catalytic and selective membrane materials, http://demcamer.org/ (accessed August 8, 2016).
[23] D. Geldart, Types of gas fluidization, Powder Technol. 7 (1973) 285–292. doi:10.1016/0032-5910(73)80037-3.
[24] F. Gallucci, M. van Sint Annaland, J. A. M. Kuipers, Theoretical comparison of packed bed and fluidized bed membrane reactors for methane reforming, Int. J. Hydrogen Energy. 35 (2010) 7142–7150. doi:10.1016/j.ijhydene.2010.02.050.

I was dreaming I was awake. And then i woke up, and found myself asleep.

Stan Laurel

In “Oliver the eight” (1934)

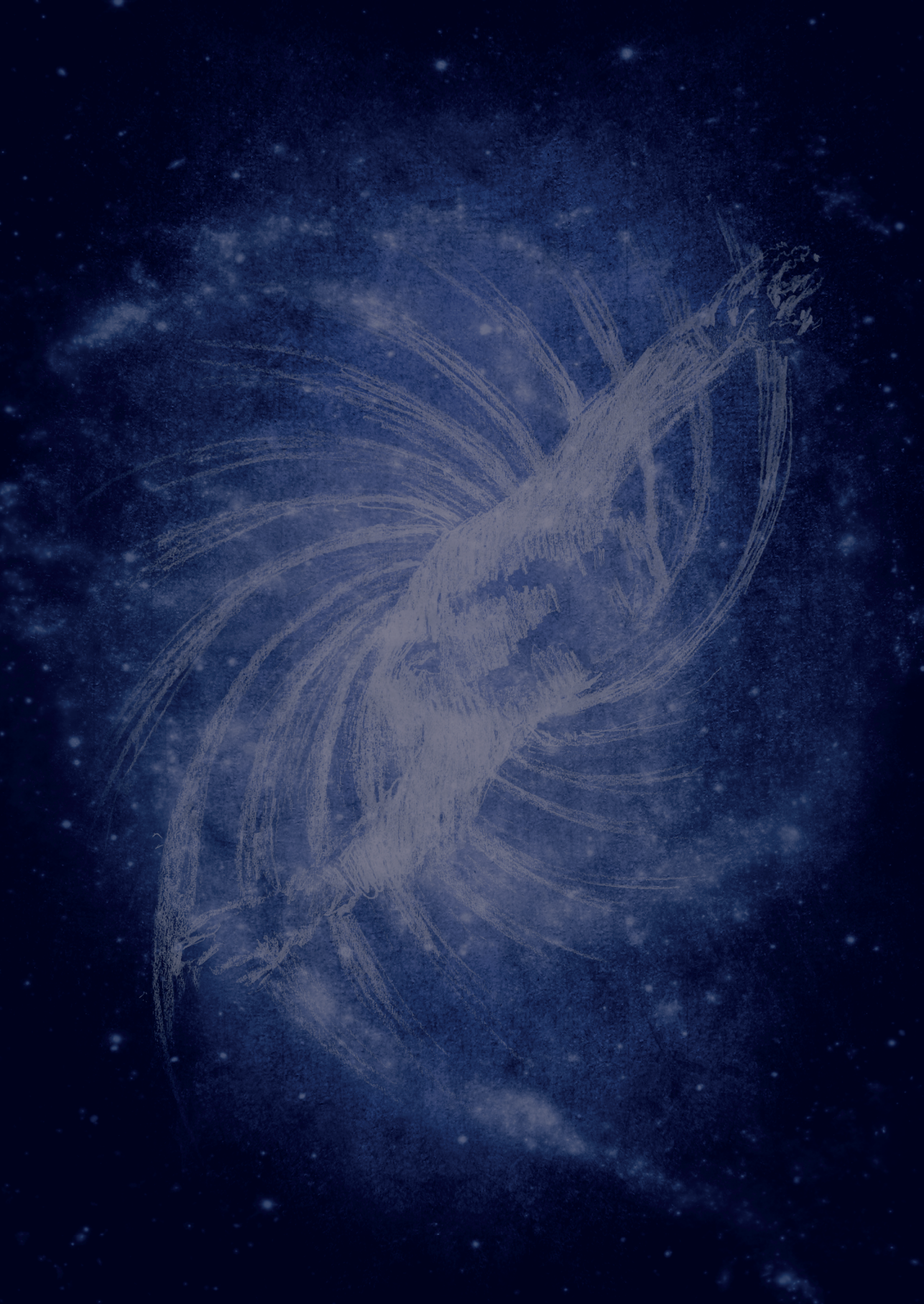

Chapter 6

Influence of vertically immersed membranes on hydrodynamics – a 2D PIV/DIA analysis

Abstract

The hydrodynamic behavior of a pseudo-2D bubbling gas-solid fluidized bed with vertically immersed membrane tubes has been studied using an endoscopic-laser PIV/DIA technique. The solids mass flux and hold-up profiles were determined together with the bubble phase properties (equivalent bubble diameter and bubble rise velocity) for different operating conditions and different membrane module configurations. The obtained results revealed that the lateral solids motion can be significantly hampered due to the presence of the membrane modules resulting in a very high solids hold-up near the walls and much diluted regions in the middle of the reactor. The obtained results from the experiments with a different number of membranes, membranes with a different outer diameter, and positioned with the bottom of the module at different axial positions give guidelines to optimize the module configuration to achieve the highest lateral gas dispersion and optimal bubble breakage. These experimental results have demonstrated the very important effect of the tube spacers. Moreover, the analysis of the bubble phase properties confirmed the enormous decrease in equivalent bubble diameter (up to a factor 3.5) for fluidized beds with immersed vertical tube modules with spacers in comparison with a fluidized bed without internals, showing the great potential for improvement of the bubble-to-emulsion phase mass transfer rate.

6.1 Introduction

It is widely accepted that fluidized bed membrane reactor configurations can outperform other membrane reactor configurations such as packed bed membrane reactors owing to their inherent superior mass and heat transfer characteristics. Specifically, once a highly permeable membrane is integrated inside a packed bed reactor configuration, mass transfer resistances from the bulk of the catalyst bed to the surface of the membranes (referred to as concentration polarization) can significantly hamper the performance of the reactor, resulting in a much higher membrane area required for the same hydrogen production rate [1]. Concentration polarization might also occur in fluidized bed membrane configurations when ultra-high flux membranes are employed (see chapter 5), which is caused by the formation of zones with higher solids hold-up near the membranes, so-called densified zones [2,3]. Nevertheless, still the mass transfer rate inside fluidized beds is much higher than in packed bed configurations, at least a factor of two (see chapter 4). The enhanced mass transfer in fluidized beds is related to the more intensified gas dispersion inside the reactor, which is caused by solids mixing induced by the motion of gas bubbles rising through the bed. Thus, the performance of fluidized bed membrane reactors is directly influenced by the intensity of the gas dispersion and hence the gas-solids mixing in the bed and the size of the bubbles along the reactor [4].

For the modeling of fluidized bed membrane reactors many simplified models have been proposed in open literature [5]. Most of the developed phenomenological models are based on constitutive equations including an average bubble diameter and bubble rise velocity. Most of the often used correlations were developed at cold-flow conditions and in absence of internals inside the fluidized bed. Especially the presence of membranes immersed in the bed can strongly affect the behavior of the bubble and emulsion phases. For small-scale membrane-assisted fluidized bed reactors this effect is predicted to be even more pronounced. There is a clear need to experimentally investigate the influence of the presence of submerged membranes on the hydrodynamics of fluidized bed reactors (solids circulation patterns and bubble phase properties) at different operating conditions and for different membrane module configurations. This is an important prerequisite to improve the phenomenological models and to be able to predict the behavior of this type of reactors and improve their design.

Various experimental techniques have been developed to study the hydrodynamics of fluidized bed reactors. These measurement techniques can be classified as either invasive or non-invasive. A major concern with the application of invasive techniques (e.g. techniques using immersed probes) in small-scale setups is the disturbance on the solids fluxes and bubble phase behavior [6]. Several non-invasive techniques to measure the gas voidage in dense gas-solid fluidized bed have been reviewed by van Ommen and Mudde [7]. These techniques can be divided in two categories such as tomography techniques and velocimetry techniques. The non-invasive tomography techniques such as X-ray computed tomography (XCT) or positron emission tomography (PET) have low spatial resolution, while they can measure

the characteristics of only one phase (either the bubble or the emulsion phase). Velocimetry techniques e.g. radioactive particle tracking (RPT) are able to provide information on the solids motion, while the measurement is based on single particle tracking instead of solids distributions. Velocimetry techniques such as Particle Image Velocimetry (PIV) are nowadays used quite frequently to study the hydrodynamics of fluidized beds. It was for the first time applied by Bokkers et al. to measure the emulsion phase circulation in a bubbling fluidized bed at room temperature [8]. However, PIV needs visual access to the bed and therefore it can only be applied to fluidized bed columns with shallow depth that can provide the visual access. Laverman et al. coupled PIV with Digital Image Analysis (DIA) to obtain information on both solids and gas phases at the same time with high temporal and spatial resolution [9]. Thus, whole-field information on both the solids circulation patterns and bubble properties can be obtained simultaneously. In a fluidized bed the solids and bubble phases interact strongly with each other. Therefore, to better understand the behavior of the fluidized bed, both the solids flux profiles and bubble phase behavior need to be investigated simultaneously. This is one of the major advantages of the coupled PIV/DIA technique, that has led to its frequent use to study the hydrodynamics of dense gas-solid fluidized beds at different operating conditions and reactor configurations [2,10–14].

De Jong [10] studied the effects of horizontally immersed membranes on the hydrodynamics of bubbling gas-solid fluidized beds. In this study he demonstrated that the presence of a bundle of horizontally integrated membranes decreased the average equivalent bubble diameter about three times compared to the case without membranes present. Later Medrano et al. extended this work and showed that due to the presence of horizontal tubes gas pockets can form around the tubes/membranes that need to be properly accounted for in the determination of the equivalent bubble size [11].

Wassie et al. [14] experimentally investigated the effect of gas extraction via flat plate filters mounted in the back side the fluidized bed. They studied the influence of gas extraction on the bubble phase behavior. In this study only DIA was used to characterize the average equivalent bubble diameter and bubble rise velocity for different gas extraction values and extraction locations. Although no significant effect was reported on the behavior of the bubble phase for different extraction values, altering the extraction locations significantly changed the bubble phase properties. In another research carried out by Julian and co-workers [12], the coupled PIV/DIA technique was applied to a two-section two-zone pseudo 2D fluidized bed to study the effect of geometry on the average bubble phase properties and solids circulation patterns. The PIV/DIA technique was also successfully applied to micro-structured fluidized bed reactors with gas extraction at the walls [2].

Despite the more frequent application of the coupled PIV/DIA technique on the hydrodynamics of membrane-assisted fluidized bed reactors, no systematic research has been performed so far on the hydrodynamics of the fluidized beds with vertically immersed tubular membranes. The current research aims to extend the application of the coupled PIV/DIA

technique to a dense bubbling gas-solid fluidized bed with vertically immersed internals at different operating conditions and various module configurations.

This chapter first describes the coupled PIV/DIA technique in detail, followed by a description of the experimental setup and used materials. Subsequently, the main results obtained for the solids flux and hold-up profiles and bubble phase properties, viz. equivalent bubble diameter and bubble rise velocity, will be described and discussed. Finally, conclusions are drawn based on the obtained results and recommendations for the design of such reactor units will be given.

6.2 Experimental

6.2.1 Coupled PIV/DIA

Particle image velocimetry (PIV) is a non-invasive measurement technique which was originally developed for the measurement of liquid velocity profiles [15]. The fundamental principle of this experimental technique is to take consecutive images with short inter-frame time using a CCD camera. The obtained frames are divided in number of zones (referred to as interrogation areas) and in each in each zone the most probable displacement of the particles is calculated by cross-correlation between the two consecutive frames. More information on the fundamentals of PIV techniques and the cross-correlation can be found in [16].

In this work the cross-correlation was applied using a third party software (Davis®). A standard multi pass PIV algorithm (50% decrease and overlap of interrogation areas) was used. The size of interrogation areas was 256x256 or 128x128 pixels (based on image resolution) to minimize the in-plane error [16]. The inter-frame time is 1 ms with a recording frequency of 2 Hz. For each set of double frames the cross-correlation was applied and the whole-field instantaneous solids velocity map was obtained (Figure 6.1). To obtain time-averaged solids velocity profiles, a total of 2500 double frames were recorded to have reliable statistics with minimum error from the mean [4].

An in-house Digital Image Analysis (DIA) algorithm developed elsewhere [4] was applied to separate the bubble and emulsion phases based on a preselected pixel intensity threshold [9]. The DIA algorithm firstly corrected images for inhomogeneous illumination and lens effects and subsequently calculates the equivalent bubble diameter and rise velocity for each frame. The DIA script excludes bubbles that are not entirely captured in the image (i.e. touching the top and/or bottom of the images) or with a size smaller than the depth of the column, since these bubbles are not fully visible.

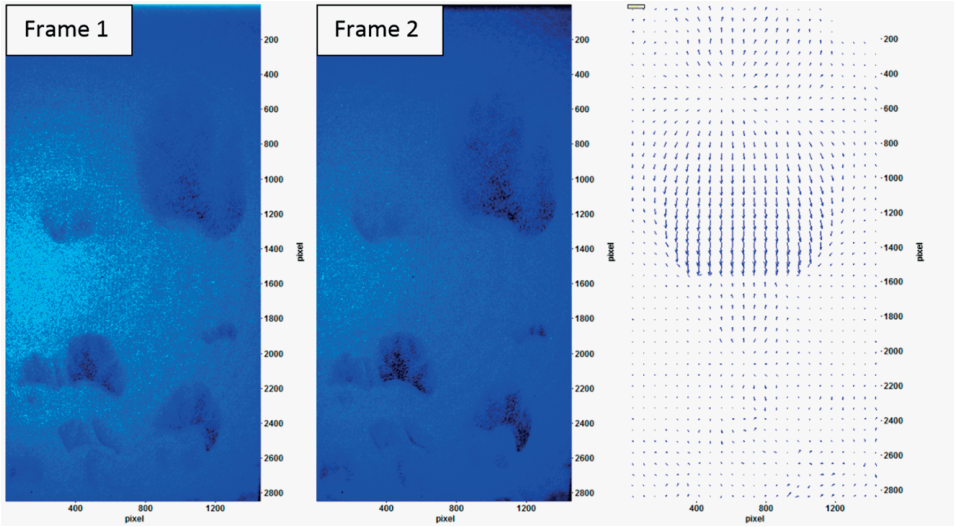

Figure 6.1 Frame one and two and the calculated instantaneous solids velocity profile from Davis®

To couple the PIV instantaneous velocity measurements with bed voidage information from DIA, initially and at each frame the intensities of the pixels were normalized between zero and one. We consider zero for the bubble phase and one for the emulsion phase. In the second step and using identical interrogation areas as the PIV (128x128 pixels), the intensities are averaged and converted to a solids hold-up using a correlation developed by De Jong [17]. At this stage the whole-field instantaneous solids hold-up map for each frame can be obtained. In the final step the instantaneous velocities from PIV were multiplied by the instantaneous solids hold-up for each interrogation area to obtain the instantaneous solids flux for each frame. The time-averaged emulsion phase flux was calculated by averaging over the frames for each interrogation area (see Figure 6.2).

6.2.2 Setup

An endoscopic-laser PIV/DIA setup which was already developed and validated elsewhere [4] was used in this study. The setup was originally designed to study the hydrodynamics of gas-solid fluidized beds at elevated temperatures, but in the current study the experimental technique is only applied at cold-flow conditions. In the future, this study will be extended to elevated temperatures and reactive conditions. Figure 6.3 shows a schematic representation of the endoscopic-laser PIV/DIA setup used in this study.

A pseudo-2D borosilicate glass column was constructed, 0.25x0.015x0.60 m in width, depth and height respectively. The glass column can work up to 300 °C due to the maximum operating temperature of the used silicon sealant. For homogeneous distribution of the inlet gas, a distributor plate was made from sintered stainless steel (40 µm average pore size and 3.2 mm thickness, purchased from van Borselen Filters) and placed at the bottom of the bed. The

air chamber at the bottom of the column and the freeboard at the top were made of stainless steel. The glass column was placed inside a high temperature industrial electrical furnace (N660 Nabertherm, Maximum operating temperature of 1000 °C) to obtain a homogeneous heating of the column with minimum heat losses. The furnace is equipped with a N_2 purge line for emergency flushing of the system.

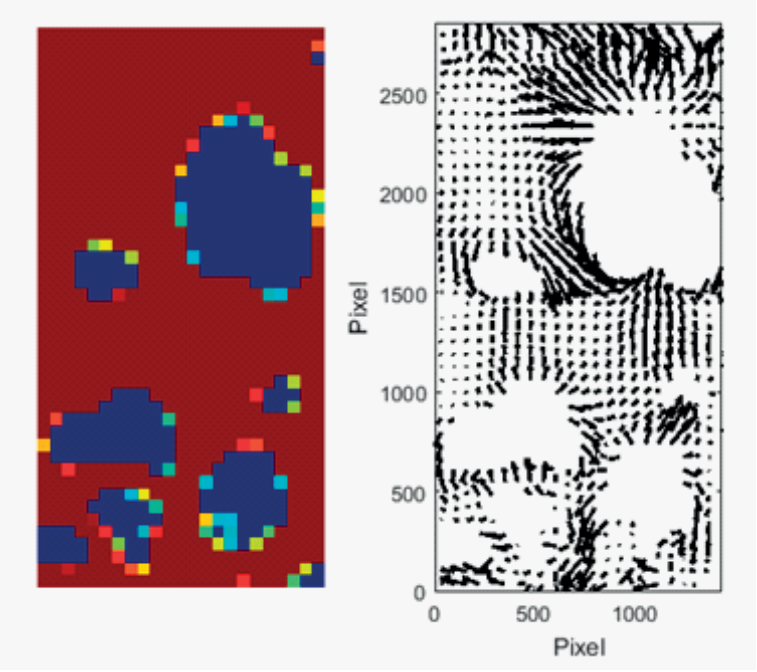

Figure 6.2 (a) Solids hold-up map from the DIA algorithm (b) the subsequent instantaneous solids flux profile from the coupled PIV/DIA technique

For the experiments the camera and laser were placed outside the furnace chamber while the optical access to the column was obtained by inserting high temperature optical and laser endoscopes through two holes at the front door of the furnace. The optical endoscope connected to the camera was provided by Cesyco Kinoptic Endoscopy, France (940 mm in length with a 16 mm tip lens). In addition, a co-axial flow of air was fed at the tip lens of the endoscope to protect it against the elevated temperatures (this also helps to prevent dust formation at the tip lens). The rest of the optics inside the endoscope are protected with a cooling water jacket. To capture images a Dantec Flowsense 16M (1700x3048 px) camera was connected to the C-mounted end of the optical endoscope. In an independent study [4], it was confirmed that a camera resolution of 2-3 pixels/particle ensures a reliable application of PIV for particles of 400-600 μm diameter [16].

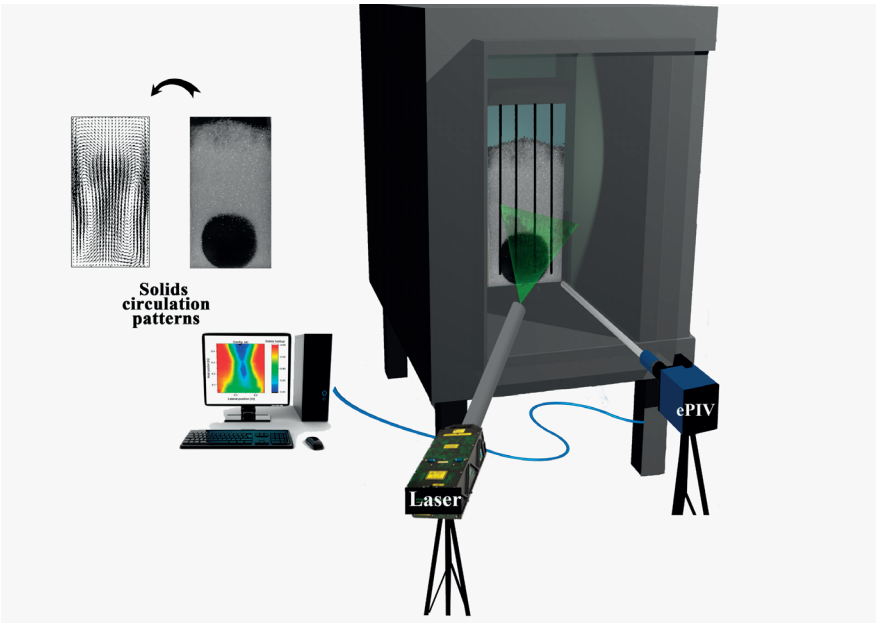

Figure 6.3 Schematic representation of the endoscopic-laser PIV/DIA setup [18]

To illuminate the bed with high contrast between the emulsion and bubble phases a double-pulse Nd:Yag laser providing 532 nm light (Evergreen) was used. The laser was connected to a high temperature endoscope (provided by OptoPrecision Gmbh). The laser power was adjustable while for the current study it was set at the maximum of 70 mJ/pulse. Also to minimize the inherent pulse to pulse incoherency of the Nd:Yag laser [4], a laser beam homogenizer was designed and provided by Bayerisches Laserzentrum [19]. The homogenizer was connected to a carbon tube of 65 cm in length coupled with the laser source. Both homogenizer and the carbon tube were protected by a cooling water jacket to keep the optics protected from the heat at elevated temperatures.

As shown in Figure 6.3, for this study, a single laser source was used to illuminate the column from the left side. This configuration results in higher intensities on the left side of the column in comparison with the upper and lower right corners. To eliminate the non-homogenous illumination, an intensity normalization protocol was conducted in the DIA script using the time-averaged intensity plot for each experiment. For each set of frames, the first frame is assumed to be the time-averaged intensity and is compared with the second frame. If the difference between the relative intensities of the same pixel is below a predefined threshold, then it is assumed that emulsion phase was present and it will be used in the averaging (for the averaging only the intensity of the emulsion phase was needed). Otherwise, it was assumed that a bubble was present and it was not included in the averaging.

Experiments were performed using glass beads with two particle size distributions: 100-200 μm and 400-600 μm. The experiments showed that a reliable PIV measurement was only possible for the bigger particle size range due to lack of sufficient illumination for the smaller particle size and probable out-of-plane errors due to the large number of particles per depth of the column. Therefore, in the current study only results with the larger particle size are reported.

A membrane module with the capacity of seven vertical tubes of 6 mm in outer diameter and 30 cm in length, was designed. Figure 6.4 shows the actual view of the glass column with 7 tubes. For the current research no gas extraction was applied via the tubes. The tubes were standard steel tubes (o.d. 6 mm) painted in black (a high temperature paint is used that can work up to 750 °C), which avoids the need to correct the intensity maps for the presence of the internals. Spacers were installed at two different axial positions along the membrane module to keep the tubes in place. The effect of spacers were minimized by keeping the thickness of the connections at 0.5 mm, although the presence of the spacers might influence the bed behavior.

Figure 6.4 Front view of the glass column with immersed vertical tubes and spacers (distance between the membranes: 31 mm, distance from the reactor wall for the most right and left membranes: 32 mm)

To obtain a better understanding of the hydrodynamics of the fluidized bed at the presence of vertically immersed tubes, experiments with different module configurations were conducted. For all the experiments the superficial gas velocity inside the column was kept the same. When membrane modules were present, the inlet flow was corrected for the projected area of the

membranes. Table 6.1 summarizes the operating conditions and module configurations for the experiments performed using 2.45 U/U_{mf} (U_{mf}: 0.23 m/s).

Table 6.1 Design of experiments

Configuration [-]	Number of Membranes [-]	Membranes outer diameter [mm]	Membranes bottom from the distributor [mm]	Bottom spacer from the distributor [mm]	Upper spacer from the distributor [mm]	Bed aspect ratio [-]
Reference	0	n.a.	n.a.	n.a.	n.a.	1.5
a	7	6	0	30	300	1.5
b	7	6	60	90	360	1.5
c	7	6	60	60	330	1.5
d	5	6	60	60	330	1.5
e	7	6	0	30	300	1.2
f	7	3	0	30	300	1.2

6.3 Results and discussion

In this section, results from the experiments with constant superficial gas velocity and different membrane module configurations, will be presented in two parts. In part one, the obtained results for the emulsion phase, viz. the solids flux and circulation patterns, are given and discussed, followed by the time-averaged solids hold-up maps. In the second part, the average bubble phase properties (equivalent bubble diameter and bubble rise velocity) are analyzed for all above mentioned experiments.

6.3.1 Solids flux and hold-up

The time-averaged solids flux profiles for the standard fluidized bed without internals (reference case) and with different immersed membrane modules (as specified in Table 6.1) are shown in Figure 6.5. All the cases show the expected solids circulation patterns with upwards solids motion in the center of the bed and downwards motion near the walls, related bubble coalescence and growth. The symmetry in the solids circulation patterns is a good indication of a homogeneous distribution of the inlet gas flow at the porous distributor plate at the bottom of the reactor. The time-averaged solids fluxes below 0.05 m above the distributor plate are downwards in the center of the bed, which is attributed to the downwards movement of the solids at the front wall of the column at this bed position, since the bubbles are too small to occupy the entire bed depth and the DIA script does not account for bubbles with an equivalent diameter smaller than the column depth (0.015 m).

Focusing on module configuration (a) (7 uniformly spaced tubes with 6 mm outer diameter), it is evident in Figure 6.5 that at all different heights from the distributor plate, the

upwards time-averaged solids flux in the middle of the bed is enhanced in comparison with the reference case, while at the same time the width of the zones with solids downwards motion is increased. Figure 6.6 presents the lateral solids flux profiles for the two cases at different heights from the distributor plate. At lower axial positions (H = 10 cm above the distributor plate), the difference in solids fluxes profiles for the two cases is still small, but moving along the bed to higher axial positions in the bed the difference becomes much more pronounced (up to H = 30 cm, where the upper membrane spacer is positioned). Passing over the upper spacer of the membrane module, the upwards solids flux in the middle of the bed is somewhat decreased attributed to the effect of the spacer on the solids motion. Due to the inter-play between the bubble and emulsion phases inside a fluidized bed, a noticeable effect is also observed for the time-averaged bubble phase properties, which will be discussed in detail later in the next section.

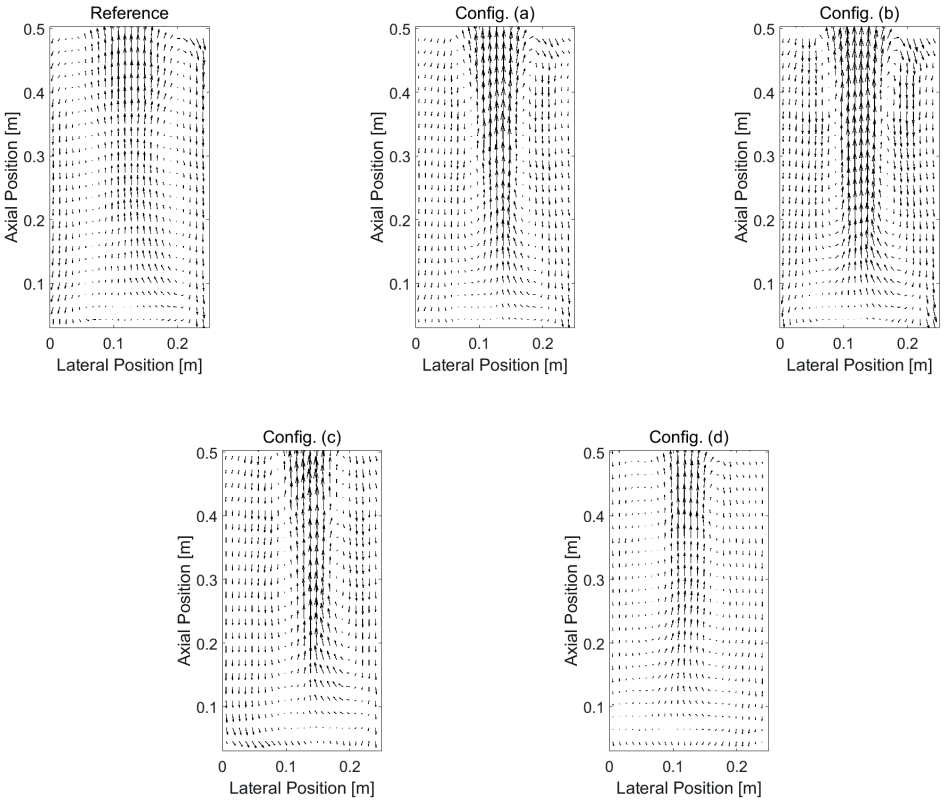

Figure 6.5 Time-averaged solids flux profiles for the standard fluidized bed (reference) and for the fluidized bed with different immersed membrane modules (config. a-d, see Table 6.1).

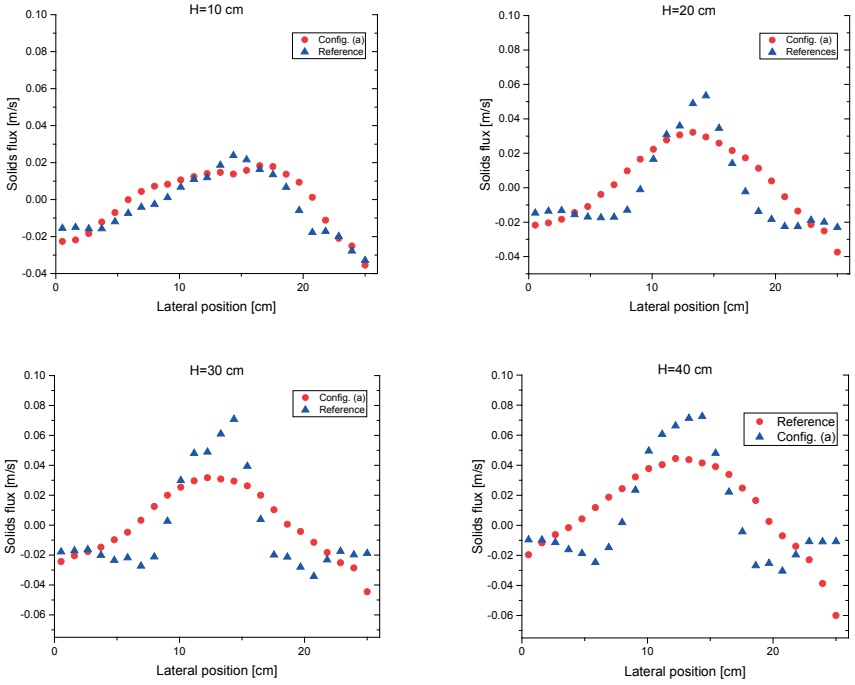

Figure 6.6 Time-averaged lateral solids flux profiles at different heights from the distributor plate (H) for the reference case and module configuration (a)

As expected, the solids flux decreases and becomes negative close to the column walls, but for the case with the module immersed in the bed, the decrease is much more abrupt resulting in a typical core-annulus velocity profile and the magnitude of the downwards negative solids flux is much larger in comparison with the reference case without internals. This observed deviation is strongly related to the hindered lateral solids and bubble motion caused by the presence of the membrane module. To further elucidate this, the time-averaged solids hold-up profiles for the reference case and the cases with different immersed modules are compared in Figure 6.7.

The time-averaged solids hold-up map for the reference case clearly shows more diluted regions in the middle of the bed and thin zones with higher solids hold-up near the reactor walls, consistent with the time-averaged solids flux profiles with a more spatially distributed upwards solids motion in the middle part of the bed. Also the homogeneity of the obtained time-averaged solids hold-up in the diluted region in the center confirms that in the absence of the membrane module bubbles can grow and move more freely in the lateral direction.

The solids hold-up map for configuration (a) reveals that, in comparison with the reference case, the immersion of the membrane module leads to the formation of much thicker zones

with very high solids hold-up near the walls. Bubbles mostly move in the center of the bed and bubble meandering is largely decreased. Hence both the horizontal solids and bubble motion is hampered due to the presence of the module.

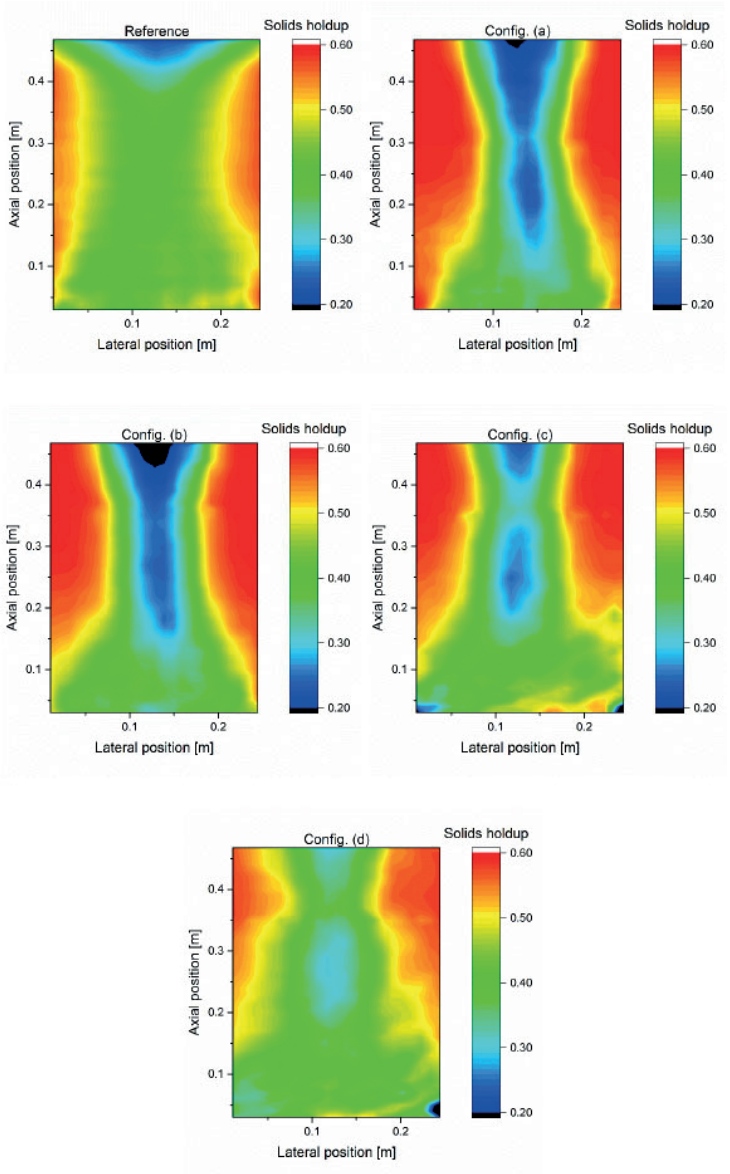

Figure 6.7 Time-averaged solids hold-up map for the reference case and different module configurations

The above described observations indicate that the presence of immersed membrane modules can significantly change the hydrodynamic behavior of the fluidized bed. Specifically

the average solids flux and solids hold-up profiles can change drastically. The influence of the position and configuration of the immersed module is investigated systematically in the next sections.

6.3.1.1 Effect of axial position of the membrane module

For configuration (a) the module was fully immersed inside the bed, all the way down to the distributor plate. To investigate the influence of the axial position of the membrane module on the solids flux profiles, an experiment was performed where the membrane module was moved 60 mm upwards, which is referred to as configuration (b) in Table 6.1. Figure 6.5 also shows the time-averaged solids flux profiles for configuration (b). In comparison with configuration (a) no significant changes in the solids flux profiles can be seen at the bottom part of the bed. However, moving towards higher axial positions, the solids upwards flux is slightly increased in the middle of the bed for the case when the membranes were lifted upwards, while near the reactor walls somewhat more enhanced downwards movement can be identified but without remarkable difference in the thickness of the zones of downwards solids flow.

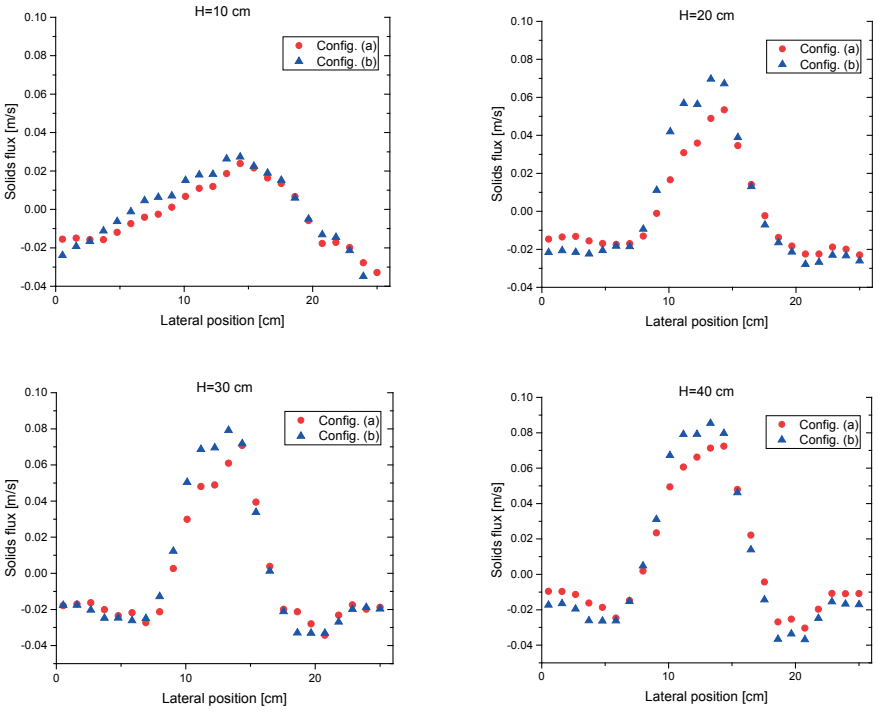

Figure 6.8 Time-averaged lateral solids flux profiles at different heights from the distributor plate (H) for module configurations (a) and (b)

In Figure 6.8, the time-averaged lateral solids flux profiles at different heights from the distributor plate are plotted for configurations (a) and (b). Due to bubble growth and coalescence the solids upwards flux increases at higher axial positions for both configurations. Although a careful inspection at the axial positions where the upper membrane spacer is located (H = 30 cm for configuration (a) and H = 36 cm for configuration (b)), reveals a small decline in the upwards positive solids flux (related to the slightly reduced available area). Overall it can be concluded that no significant changes in the time-averaged solids flux profiles can be discerned for cases with the module placed at different axial positions. This is further confirmed by the similarities for both cases in the time-averaged solids hold-up profiles shown in Figure 6.7, underlining the minimal effect on the extent of lateral solids mixing and bubble motion (although the bubble properties are slightly affected, as will be discussed later in this chapter).

6.3.1.2 Effect of axial position of the spacer

Subsequently we have kept the membranes at exactly the same axial position, but relocated the position of the spacers 3 cm downwards to further investigate the effect of the spacers, indicated as configuration (c). Figure 6.5 compares the time-averaged solids flux profiles for configuration (b) and (c). Qualitatively, it is apparent that repositioning the membrane spacers at lower bed positions decreases somewhat the upwards solids flux in the middle of the reactor and decreases the downwards solids motion near the reactor walls. Figure 6.9 gives a quantitative comparison between the time-averaged lateral solids flux profiles for both cases and at four different heights from the distributor plate. Inspecting these results, configuration (c) shows a lower upwards solids flux in the middle of the reactor and lower downwards flux near the walls for all axial positions. Moving from the bottom the reactor towards the top part of the bed, the lateral solids flux profiles approach each other again after the top spacer at H = 40 cm.

At H = 40 cm the lateral solids upwards and downwards flows show similar values for both cases. While in configuration (b), the upwards solids flux increases above the upper membranes spacer (due to bubble growth), in configuration (c), the upwards solids flux will decrease and due to the presence of the membranes spacer (see Table 6.1).

Figure 6.7 shows the time-averaged solids hold-up profiles for configuration (c). In the middle part of the bed a higher solids hold-up can be observed in comparison with configuration (b) with higher positions of the membrane spacers. Specifically at H = 33 cm where the upper membrane spacer is located, a strong increase in the solids hold-up in the middle of the reactor can be observed. This is strongly correlated to the effect of the membrane spacer on the average bubble phase properties.

The results have shown that the axial location of the membranes and spacers can significantly affect the upwards and downwards solids movement, whereas the time-averaged lateral solids motion was hardly influenced. It appears that the presence of the membranes and spacers largely limits the solids lateral movement. Consequently, bubbles tend to pass more in the middle part of the reactor with a lower likelihood to pass near the walls. In a fluidized bed

the degree of gas-solids mixing is induced by the motion of the bubbles in axial and lateral directions, so that any limitation in the solids and bubbles motion will noticeably decrease the extent of mixing inside the reactor and hence deteriorate the heat and mass transfer characteristics accordingly.

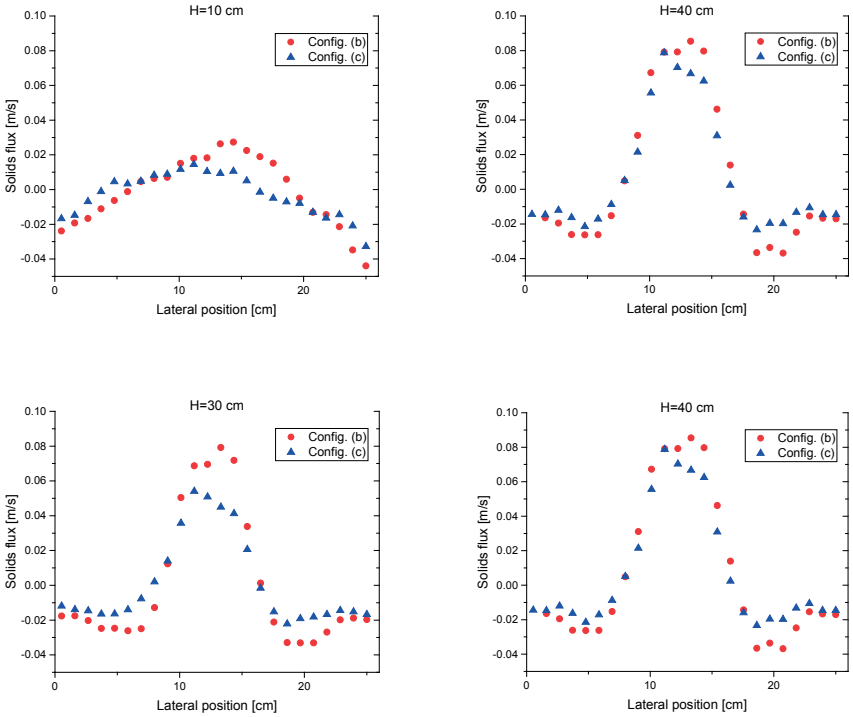

Figure 6.9 Time averaged lateral solids flux profiles at different heights from the distributor plate (H) for configurations (b) and (c)

6.3.1.3 Effect of number of membranes

In another experiment the number of tubes was decreased, indicated as configuration (d) in Table 6.1. In comparison with configuration (c), the two membranes on the most right and left side the module were removed leaving only the five tubes in the middle (distance from the wall for the extreme right and left membranes was thus increased to 63 mm vs. 32 mm in configurations a-c). Both the upper and lower membrane spacers were kept at identical locations as for configuration (c). Moreover, the inlet flow rate was slightly adjusted to correct for the modified projected area of the membranes in order to keep the superficial gas velocity identical for both cases.

Figure 6.5 depicts the time-averaged solids circulation patterns for both configurations. In comparison with configuration (c), the change in average solids velocity profiles is quite

remarkable: in the middle of the bed the upwards positive velocity of the solids phase is clearly decreased, while simultaneously the downwards solids velocity near the walls is decreased. In Figure 6.10 we have plotted the time-averaged lateral solids flux profiles for both configurations.

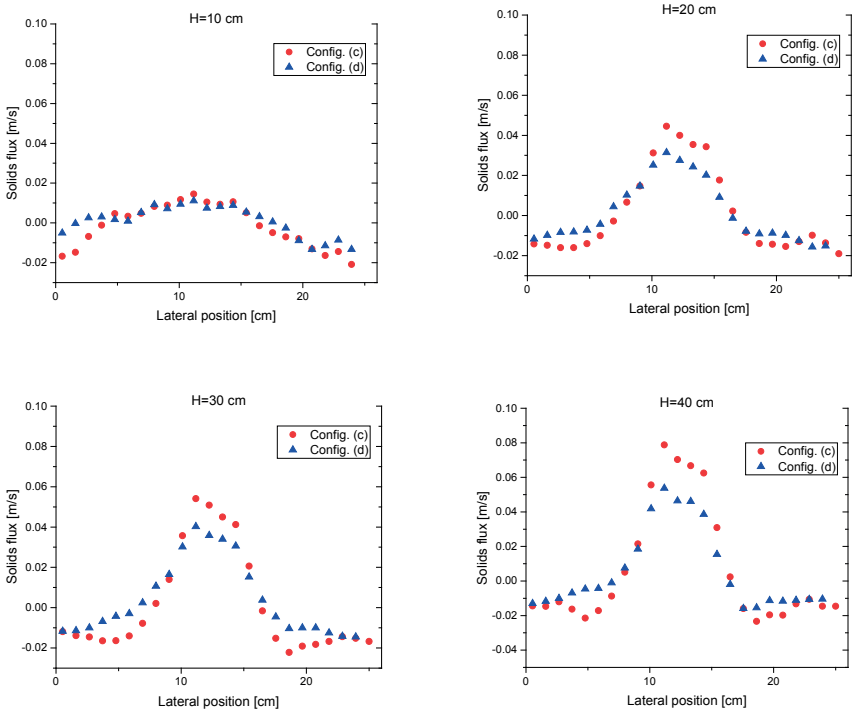

Figure 6.10 Time-averaged lateral solids flux profiles for configuration (c) and (d). H represents the height from the distributor plate in cm.

As can be seen from the plots, removing the two tubes near the walls affect the time-averaged solids flux profiles minimally close to the distributor plate (at $H = 10$ cm), but at higher axial positions, the upwards positive solids flux is largely reduced. Interestingly, moving from the middle part of the bed towards the reactor walls in the lateral direction, a smoother drop in the lateral solids flux can be identified in comparison with configuration (c). Also the time-averaged solids hold-up profiles (see Figure 6.7) were drastically changed in comparison with configuration (c) and especially near the walls. Essentially, the results show that in case the number of membranes was reduced by removing the outermost tubes the lateral solids (and bubble) motion was largely enhanced. The homogeneity of the solids hold-up profiles resemble those of the reference case without any internals in the bed.

6.3.1.4 Effect of membranes outer diameter

To investigate the effect of the membranes outer diameter on the time-averaged solids flux and hold-up profiles, two additional experiments were conducted, referred to as configuration (e) and (f) in Table 6.1. For both cases, the number of membrane tubes, the axial positioning of the spacers and the superficial gas velocity was kept the same. In configuration (e) the outer diameter of the membrane tubes was 6 mm vs. 3 mm in configuration (f). Figure 6.11 presents the time-averaged lateral solids flux profiles for both cases up to 30 cm above the distributor plate. It should be noted that after the experiment with configuration (e) the glass column was repaired and the distributor plate at the bottom of the reactor was replaced. The shift in the lateral position of the maximum solids flux (for all different axial positions), is attributed to a somewhat less homogeneous gas distribution.

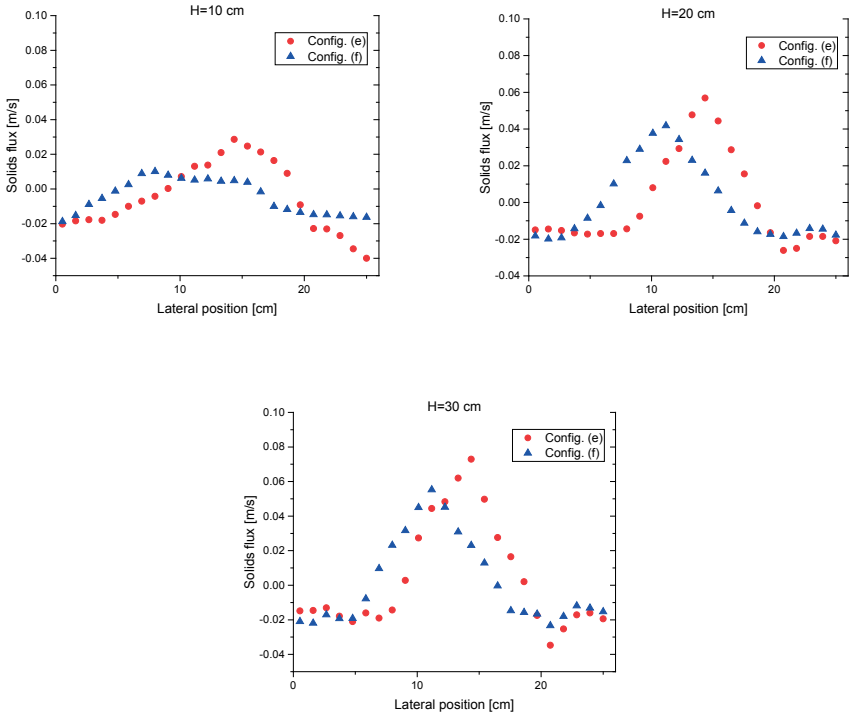

Figure 6.11 Time-averaged lateral solids flux profiles for configurations (e) and (f)

However, the obtained results from these experiments, confirmed that in the presence of tubes with a smaller outer diameter, the time-averaged upwards solids flux decreases in comparison with a similar case with larger diameter tubes. At the same time a slight increase in the downwards solids motion can be observed. A qualitative observation of the obtained snapshots of the bed for both cases, revealed that in the case of the module with smaller

diameter tubes, the bubbles can move more freely in the lateral direction, while for the case with the larger diameter tubes, the bubbles rise mostly in the middle of the bed with a higher upwards velocity.

Figure 6.12 shows the time-averaged solids hold-up contour plots for both configurations. The results for configuration (e), that correspond closely to the results obtained before for configuration (a) as expected, differ however much from the results obtained for configuration (f). A distinct increase in the solids hold-up in the diluted region in the middle part of the bed can be observed smoothing out the lateral solids concentration gradients because of the increased lateral solids motion in case of the module with smaller diameter tubes.

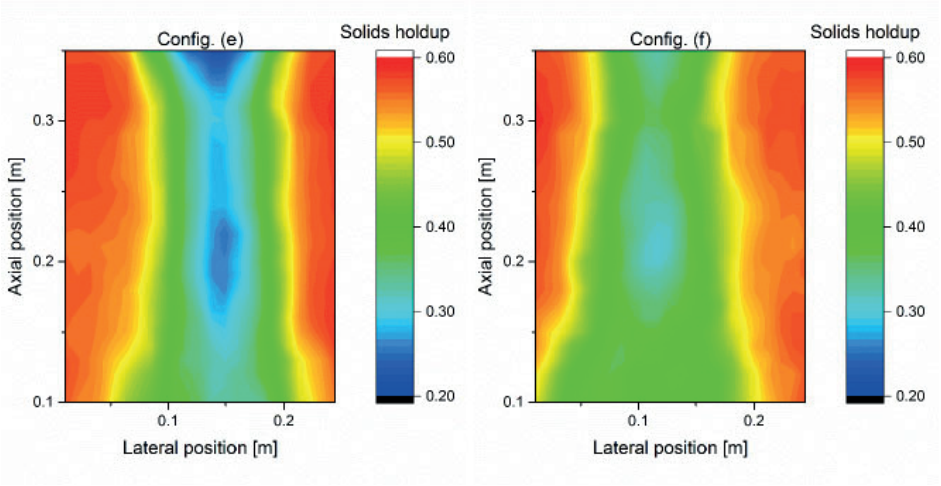

Figure 6.12 Time-averaged solids hold-up contour plots for configurations (e) and (f)

6.3.2 Bubbles phase properties

In addition to the solids flux and hold-up profiles, also the bubble phase properties, viz. the average equivalent bubble diameter and rise velocity, have been determined for the different module configurations as function of the axial position in the bed. First the results for the equivalent average bubble diameter for all the cases and as a function of bed height will be discussed, followed by a discussion on the bubble rise velocity for the different immersed modules. For all these cases, the estimated values from our experiments are compared with predictions based on the correlations by Shen and co-workers [20].

Figure 6.13 depicts two sets of snapshots randomly chosen among 50 double frames for the reference case without internals and for the case with module configuration (c). For the reference scenario (Figure 6.13a) bubbles are formed at the bottom part of the bed and coalesce and grow along the axial direction (clearly much larger bubbles can be identified at higher axial positions for the reference case). Interestingly, for the case with the immersed membrane module (Figure 6.13b), the presence of the tubes and spacers the bubbles are cut

into several neighboring bubbles with stalactite solids zones in between. The DIA protocol detects these zones as separate daughter bubbles based on the difference in pixel intensity. In the next section, the measured bubble phase properties for the cases with different immersed modules will be discussed and analyzed.

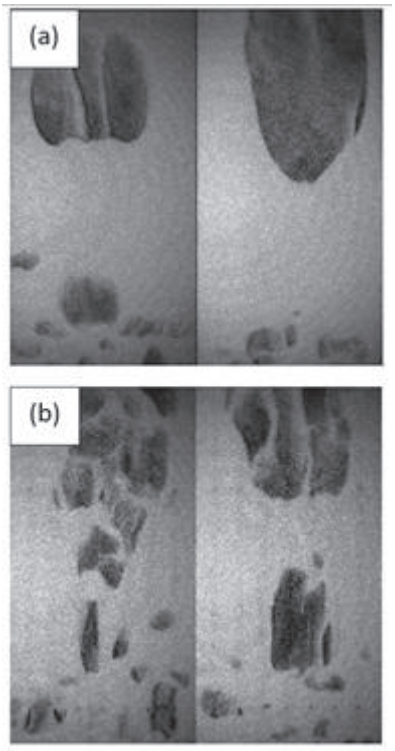

Figure 6.13 Snapshots from the recordings: (a) reference case (b) configuration c

6.3.2.1 Equivalent bubble diameter

The measured equivalent average bubble diameter at different axial bed positions (up to 0.4 m above the distributor plate) for the different experiments are shown in Figure 6.14. For the reference case without internals, the average equivalent bubble diameter increases as a function of the axial position as expected [9,20], but when comparing our experimental results with estimates using the correlation by Shen and co-workers, our experiments are largely underestimated at higher axial positions. One possible reason for this discrepancy is the smaller reactor depth (0.015 m) used in our study in comparison to the one used by Shen and co-workers (0.07 m). In our experiments bubble growth in the depth direction was more restricted, possibly increasing their expansion in the reactor width and height directions leading to bubbles with a much larger equivalent bubble diameter.

For all the cases with immersed membrane modules (configurations a-d), the equivalent bubble diameter is significantly reduced in comparison with the reference case without internals. At lower bed positions (between 0.1-0.25 m), the estimated average equivalent bubble diameter shows very close values for all the different configurations (a-d) irrespective of the axial positioning of the tube bundle and positioning of the spacers (see Table 6.1). This finding underlines that, although the presence of the membranes reduces the equivalent bubble diameter close by the distributor plate, relocating the membrane modules hardly affects the average size of the bubbles. However, at higher axial positions the estimated average equivalent bubble size differs greatly for the different module configurations. Specifically when the upper spacer is re-located to higher bed positions, as for example in configurations (b) and (c) in contrast with configuration (a), the strong decrease in the equivalent bubble diameter is evident. This is in accordance with the qualitative observations shown in Figure 6.13 and shows the enormous effect of the upper spacer on the extent of bubble cutting.

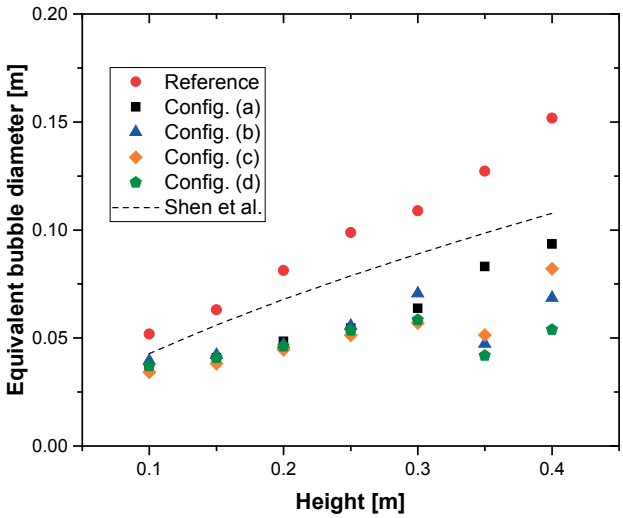

Figure 6.14 Equivalent bubble diameter at different axial bed positions for different membrane module configurations

Among the different module configurations, the minimum equivalent bubble diameter was found for configuration (d), which is the module where the two outer membranes left and right were removed. This is attributed to enhanced solids motion and bubble meandering in the lateral direction. It appears that bubble coalescence in the center of the bed is reduced and more independent bubbles with a smaller equivalent diameter can move simultaneously through the emulsion phase across the width of the bed. Therefore, the extent of solids and gas mixing

is strongly improved, which can lead to a remarkable increase in the overall performance of the membrane reactor unit. Thus, not so much the design of the tube bundle, but the design of the spacer and the axial positioning of the spacers plays an important role in the design of fluidized bed membrane reactors.

The average bubble size determined by DIA at 0.1 m above the distributor plate can be reduced by up to 29% in comparison with the reference case without internals, whereas at higher axial positions at 0.4 m above the distributor plate, this reduction can increase even further up to 65%. The observed decrease in the average bubble diameter by a factor of about 3.5 corresponds to other findings in the literature for horizontally immersed membrane tubes [17].

Figure 6.15 presents the measured equivalent bubble diameter as a function of the axial position for configurations (e) and (f). Similar to the previously presented results for configurations a-d, a reduced equivalent bubble diameter was found for both immersed module configurations in comparison with the reference case without internals, and the difference in the equivalent bubble size for the two configurations is negligible. While the immersion of tubes with a smaller outer diameter (configuration (f)) enhanced the gas-solids mixing as deduced from the solids flux and hold-up profiles, the equivalent bubble diameter remained unaffected. In other words, the outer diameter of the tube had a minimal effect on the average bubble diameter for the experimental conditions used in this research. These results essentially suggest that more attention has to be paid on the specifications of the membranes spacers. Further research is required to determine the optimal number, axial positioning and configuration

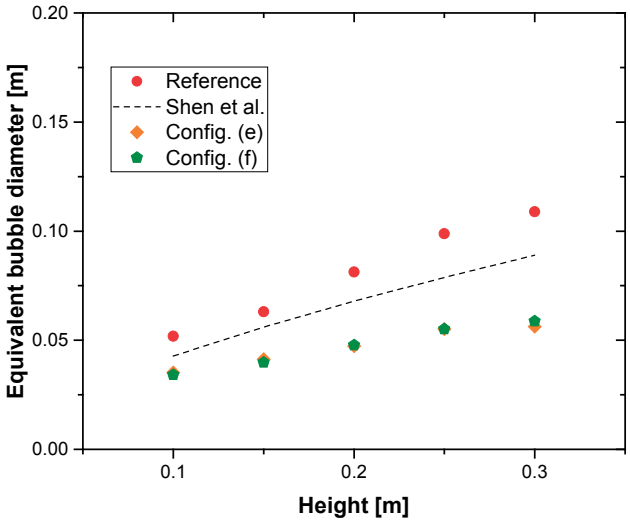

Figure 6.15 Equivalent bubble diameter at different axial positions for configurations (e) and (f)

of the membrane spacers to achieve maximum reduction in the average bubble diameter to enhance the bubble-to-emulsion mass transfer, while maintaining sufficient gas-solids mixing for lateral gas dispersion.

6.3.2.2 Bubble rise velocity

Also the bubble rise velocity was determined for the different module configurations, considering only bubbles with an equivalent bubble diameter of 0.02-0.10 (Figure 6.16). For all the investigated cases, the bubble rise velocity increases for larger bubbles. The correlation by Shen and co-workers [20] over predicts the measured bubble rise, as was also reported elsewhere [9].

In particular, for larger bubbles (exceeding 0.08 m equivalent bubble diameter) a distinct difference between the obtained bubble rise velocities for the different module configurations can be seen. This is attributed to difference in the bubble size distribution for the different module configurations [21]. Specifically for the module with reduced number of tubes and the module with the spacers located at different axial positions, a different bubble size distribution was observed related to the different bubble cutting patterns.

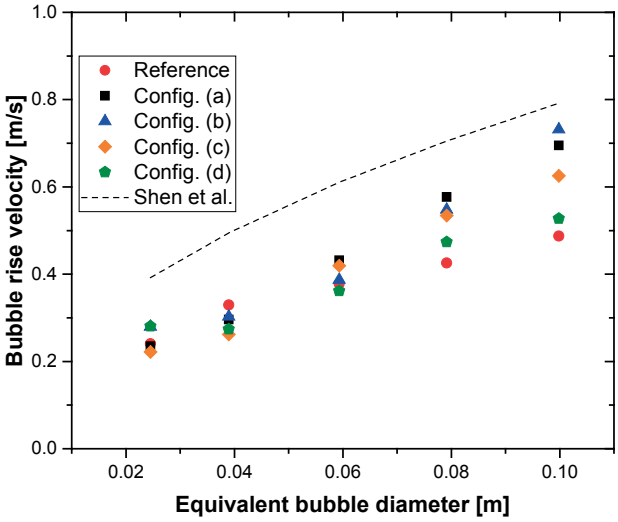

Figure 6.16 Bubble rise velocity as a function of equivalent bubble diameter

6.3.2.3 Effect on bubble-to-emulsion phase mass transfer

In a bubbling fluidized bed the overall efficiency of the reactor is often heavily dependent on the bubble-to-emulsion phase mass transfer rate (K_{be}). The closures for the determination of K_{be} on its turn rely on the average bubble diameter and corresponding bubble rise velocity.

Any change in average properties of the bubble phase will directly influence the overall mass transfer properties of the bed. In Table 6.2 we estimate the relative increase in K_{be} as a result of a reduction in the average bubble diameter using correlations listed in appendix B of Chapter 4.

Table 6.2 Effect of average bubble size (D_b) on the bubble-to-emulsion mass transfer coefficient (K_{be})

D_b [m]	0.05			0.075			0.10		
Reduction in D_b [%]	20	40	60	20	40	60	20	40	60
K_{be}/K_{be0} [-]	1.3	2.0	3.4	1.4	2	3.5	1.4	2	3.6

The obtained theoretical calculations in Table 6.2 clearly demonstrate the enormous potential of the presence of the membrane bundle with spacers on improving the overall bubble-to-emulsion phase mass transfer rate. Specifically this can largely affect the amount of catalyst and membrane area required for certain reactor capacity. This finding is promising and should be further explored and validated experimentally.

6.4 Conclusions

An endoscopic-laser PIV/DIA technique was used to study the hydrodynamic behavior of a dense bubbling gas-solid fluidized bed with vertically immersed membranes at different operating conditions and various membrane module configurations. For all the experiments the superficial gas velocity inside the reactor was kept the same by correcting the inlet flow for the projected area of the membranes at the distributor plate. Glass beads of 400-600 μm in diameter were used ensuring enough resolution (2-3 pixels/particle) for a reliable PIV measurement.

The obtained results from the experiments confirmed that the hydrodynamic behavior of the fluidized bed can be significantly influenced by the presence of the membrane modules. In particular, the upwards solids flux in the middle of the bed can be largely increased and the downwards negative solids flux near the walls can be considerably hindered. Bubbles will be pushed towards the middle of the reactor with less likelihood to pass near by the walls leading to the formation of thick zones with very high solids hold-up near the walls. Thus the degree of gas-solid mixing inside the bed may be decreased to a very large extent.

We extended our study to systematically observe the effect of the axial positioning of the membrane modules, number and outer diameter of the tubes on the time-averaged solids and bubble phase behavior. For the solids phase, the axial location of the membrane modules strongly changed the upwards and downwards solids fluxes, while at the same time the lateral motion of the particles remained limited. With a reduced number of membranes immersed inside the bed by increasing the distance between the membrane module and the reactor wall,

the degree of gas-solid mixing was strongly increased in the lateral position resulting in a more homogeneous solids hold-up inside the bed. The same finding was obtained when the outer diameter of the membranes was reduced (3 mm vs. 6 mm).

The analysis of the time-averaged bubble phase properties for all the membrane module configurations, confirmed a remarkable reduction in the equivalent bubble diameter in comparison with the case without internals (up to 65%). We observed that this reduction is more pronounced at higher axial positions related to the position of the upper spacer of the module, underlining the very important role of the spacers on the behavior and properties of the bubble phase. Our experimental observations on the average bubble phase properties largely deviate from estimated values based on frequently used closure correlations from literature [20], encouraging future studies to determine closures that account for internals for a more accurate prediction of the reactor behavior.

The experiments with the different modules have shown up to 3.5 times lower equivalent bubble diameter in comparison with the case without internals. Since the mass transfer characteristics depend strongly on the average bubble diameter, we demonstrated the potential of the membrane modules and spacers to increase the overall reactor efficiency by enhancing the bubble-to-emulsion phase mass transfer rate. This finding is very promising and should be further explored experimentally.

Bibliography

[1] F. Gallucci, M. van Sint Annaland, J. A. M. Kuipers, Theoretical comparison of packed bed and fluidized bed membrane reactors for methane reforming, Int. J. Hydrogen Energy. 35 (2010) 7142–7150. doi:10.1016/j.ijhydene.2010.02.050.

[2] N.T.Y. Dang, F. Gallucci, M. van Sint Annaland, Micro-structured fluidized bed membrane reactors: Solids circulation and densified zones distribution, Chem. Eng. J. 239 (2014) 42–52. doi:10.1016/j.cej.2013.11.001.

[3] L. Tan, I. Roghair, M. van Sint Annaland, Simulation study on the effect of gas permeation on the hydrodynamic characteristics of membrane-assisted micro fluidized beds, Appl. Math. Model. 38 (2014) 4291–4307. doi:10.1016/j.apm.2014.04.044.

[4] I.C. Velarde, F. Gallucci, M. van Sint Annaland, Development of an endoscopic-laser PIV/DIA technique for high-temperature gas–solid fluidized beds, Chem. Eng. Sci. 143 (2016) 351–363. doi:10.1016/j.ces.2016.01.002.

[5] C.S. Patil, M. van Sint Annaland, J. A. M. Kuipers, Fluidised bed membrane reactor for ultrapure hydrogen production via methane steam reforming: Experimental demonstration and model validation, Chem. Eng. Sci. 62 (2007) 2989–3007. doi:10.1016/j.ces.2007.02.022.

[6] J. Werther, Measurement Techniques in Fluidized Beds, Powder Technol. 102 (1999) 15–36. doi:10.1016/S0032-5910(98)00202-2.

[7] J.R. Van Ommen, R.F. Mudde, Measuring the Gas-Solids Distribution in Fluidized Beds - A Review, in: 12th Int. Conf. Fluid. - New Horizons Fluid. Eng., 2007.

[8] G.A. Bokkers, M. van Sint Annaland, J.A.M. Kuipers, Mixing and segregation in a bidisperse gas-solid fluidised bed: A numerical and experimental study, Powder Technol. 140 (2004) 176–186. doi:10.1016/j.powtec.2004.01.018.

[9] J. A. Laverman, I. Roghair, M. van Sint Annaland, J. A. M. Kuipers, Investigation into the hydrodynamics of gas–solid fluidized beds using particle image velocimetry coupled with digital image analysis, Can. J. Chem. Eng. 86 (2008) 523–535. doi:10.1002/cjce.20054.

[10] J.F. De Jong, M. van Sint Annaland, J.A.M. Kuipers, Experimental study on the effects of gas permeation through flat membranes on the hydrodynamics in membrane-assisted fluidized beds, Chem. Eng. Sci. 66 (2011) 2398–2408. doi:10.1016/j.ces.2011.02.059.

[11] J.A. Medrano, R.J.W. Voncken, I. Roghair, F. Gallucci, M. van Sint Annaland, On the effect of gas pockets surrounding membranes in fluidized bed membrane reactors: An experimental and numerical study, Chem. Eng. J. (2015). doi:10.1016/j.cej.2015.04.007.

[12] I. Julian, F. Gallucci, M. Van Sint Annaland, J. Herguido, M. Menendez, Hydrodynamic study of a Two-Section Two-Zone Fluidized Bed Reactor with an immersed tube bank via PIV/DIA, Chem. Eng. Sci. 134 (2015) 238–250. doi:10.1016/j.ces.2015.05.009.

[13] I. Julián, F. Gallucci, M. van Sint Annaland, J. Herguido, M. Menéndez, Coupled PIV/DIA for fluid dynamics studies on a Two-Section Two-Zone Fluidized Bed Reactor, Chem. Eng. J. 207–208 (2012) 122–132. doi:10.1016/j.cej.2012.06.015.

[14] S.A. Wassie, F. Gallucci, S. Cloete, A. Zaabout, M. van Sint Annaland, S. Amini, The effect of gas permeation through vertical membranes on chemical switching reforming (CSR) reactor performance, Int. J. Hydrogen Energy. 41 (2015) 8640–8655. doi:10.1016/j.ijhydene.2015.12.003.

[15] R.J. Adrian, Twenty years of particle image velocimetry, Exp. Fluids. 39 (2005) 159–169. doi:10.1007/s00348-005-0991-7.

[16] J. Westerweel, Fundamentals of digital particle image velocimetry, 8 (1997) 1379–1392.

[17] J.F. De Jong, S.O. Odu, M.S. van Buijtenen, N.G. Deen, M. van Sint Annaland, J.A.M. Kuipers, Development and validation of a novel Digital Image Analysis method for fluidized bed Particle Image Velocimetry, Powder Technol. 230 (2012) 193–202. doi:10.1016/j.powtec.2012.07.029.

[18] I.C. Velarde, F. Gallucci, M. van Sint Annaland, Development of an endoscopic-laser PIV/DIA technique for high-temperature gas-solid fluidized beds, Chem. Eng. Sci. 143 (2016) 351–363. doi:10.1016/j.ces.2016.01.002.

[19] M. Zimmermann, N. Lindlein, R. Voelkel, K.J. Weible, Microlens Laser Beam Homogenizer: From Theory to Application, Proc. SPIE, Int. Soc. Opt. Eng. 6663 (2007) 666301–666302. doi:10.1117/12.731391.

[20] L. Shen, F. Johnsson, B. Leckner, Digital image analysis of hydrodynamics two-dimensional bubbling fluidized beds, Chem. Eng. Sci. 59 (2004) 2607–2617. doi:10.1016/j.ces.2004.01.063.

[21] S. Maurer, D. Gschwend, E.C. Wagner, T.J. Schildhauer, J. Ruud van Ommen, S.M.A. Biollaz, R.F. Mudde, Correlating bubble size and velocity distribution in bubbling fluidized bed based on X-ray tomography, Chem. Eng. J. 298 (2016) 17–25. doi:10.1016/j.cej.2016.02.012.

Ideas have consequences.

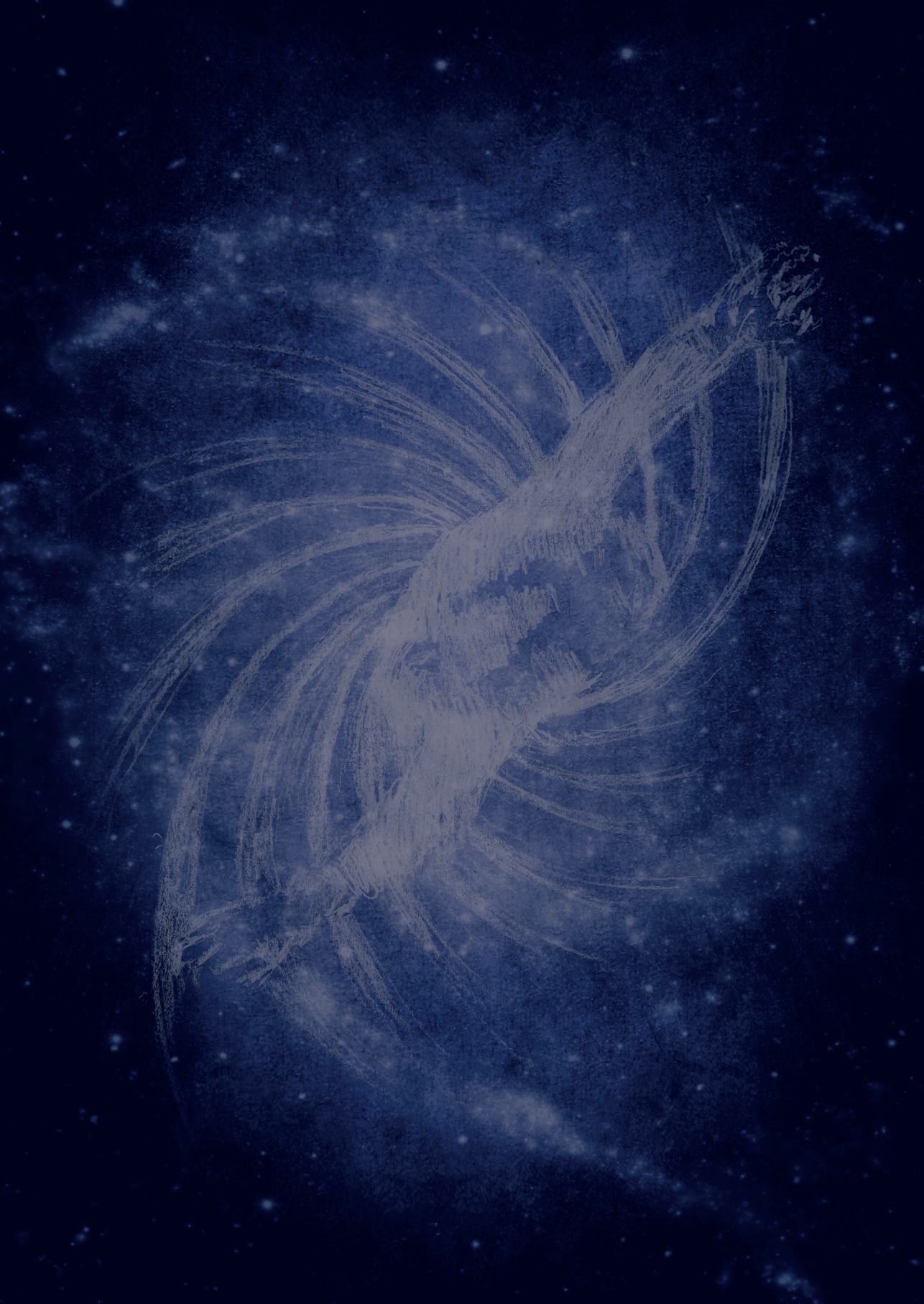

Chapter 7

Fluidized bed membrane reactors for ultra-pure H_2 production - A step forward towards commercialization

Abstract

In this research the performance of a fluidized bed membrane reactor for high temperature water gas shift and its long term stability was investigated to provide a proof-of-concept of the new system at lab scale. A demonstration unit with a capacity of 1 Nm^3/h of ultra-pure H_2 was designed, built and operated over 900 h of continuous work. Firstly, the performance of the membranes were investigated at different inlet gas compositions and at different temperatures and H_2 partial pressure differences. The membranes showed very high H_2 fluxes (3.89×10^{-6} $mol \cdot m^{-2} \cdot Pa^{-1} \cdot s^{-1}$ at 400 °C and 1 atm pressure difference) with a H_2/N_2 ideal perm-selectivity (up to 21,000 when integrating five membranes in the module) beyond the DOE 2015 targets. Monitoring the performance of the membranes and the reactor confirmed a very stable performance of the unit for continuous high temperature water gas shift under bubbling fluidization conditions. Several experiments were carried out at different temperatures, pressures and various inlet compositions to determine the optimum operating window for the reactor. The obtained results showed high hydrogen recovery factors, and very low CO concentrations at the permeate side (in average <10 ppm), so that the produced hydrogen can be directly fed to a low temperature PEM fuel cell.

7.1 Introduction

With the still increasing consumption of fossil fuels and the associated rising energy costs, renewable energy sources are becoming more and more important. Different renewable energy sources are already in use like solar, wind, hydro, etc., but this is not enough to completely replace fossil fuels in the short term. Hydrogen as an energy carrier is widely considered to play an important role in the near future. High purity hydrogen can be used in fuel cells as a substitute for conventional internal combustion engines and gas turbines because of, for example, higher power density and cleaner exhausts [1].

Hydrogen is nowadays mostly used in oil refineries or to produce methanol and ammonia, while the demand for hydrogen is rising. Hydrogen can be produced from different feedstocks, fossil based such as natural gas or coal and non-fossil based such as biomass [2]. The conventional large scale hydrogen production process consists of mainly two steps, the processing of the feedstock (for example reforming or gasification) and the water gas shift (WGS) reaction to upgrade CO to H_2. The basic reactions for hydrogen production from natural gas (primarily methane) are as follows:

Endothermic reforming of methane

$$CH_4 + H_2O \leftrightarrow 3H_2 + CO \quad \Delta H^0_{298} = +205.9\ kJ/mol \qquad \text{Eq.(7.1)}$$

Exothermic water gas shift reaction

$$CO + H_2O \leftrightarrow H_2 + CO_2 \quad \Delta H^0_{298} = -41\ kJ/mol \qquad \text{Eq.(7.2)}$$

The WGS reaction is a very important step in this conversion as it converts carbon monoxide with steam to hydrogen and carbon dioxide. By using a two-stage WGS system with two different catalysts, CO can be almost fully converted reducing its content to values as low as 0.5%. Indeed, the WGS reaction is an exothermic equilibrium-limited reaction, where the CO conversion and H_2 production are favored at lower temperatures as can be deduced from the temperature dependency of the equilibrium constant (K_p) [3]:

$$K_p = \exp\left(\frac{4577.8}{T} - 4.33\right) \qquad \text{Eq.(7.3)}$$

The WGS reaction is however controlled by kinetics at low temperatures, which implies that a highly active and stable catalyst is required. The WGS reaction is traditionally carried out in a two-stage reactor. This allows a smaller adiabatic temperature rise and a better steam management making the process more economical. The first stage is a high temperature (300–450 °C) converter for fast CO conversion while minimizing the catalyst bed volume.

The next stages are at lower temperatures (190–250 °C) to achieve a higher conversion, which is limited by the reaction equilibrium, *i.e.*, temperature and feed composition. Afterward, the produced hydrogen needs to be purified (Pressure swing adsorption (PSA) or Preferential Oxidation (PROX) are the most often used).

The WGS system could be improved by integrating the reaction and separation of hydrogen steps in a single stage [4]. The combination of membrane separation and WGS in membrane reactors have become very interesting, since the membrane separation makes it possible to continuously remove hydrogen which allows conversions beyond the equilibrium conversion of conventional systems thus achieving complete CO conversion in a single high-temperature unit [2,5].

Different types of membrane reactors have been proposed in the literature such as packed bed membrane reactors and fluidized bed membrane reactors. The simplest membrane reactor configuration for WGS is a packed bed membrane reactor where one or more membranes are accommodated in a packed catalytic bed. While this configuration has been proven at lab scale by different authors, still some limitations hamper the application of such configuration when applying highly permeable membranes [4]. In particular, for exothermic reactions, hot spot formation inside the bed (due to the relatively poor heat dispersion in packed bed reactors) can cause damage to the membranes resulting in a decrease in the perm-selectivity and catalyst performance. Additionally, mass transfer limitations from the catalyst bed to the surface of the membrane may prevail when using highly permeable membranes, with the consequent increase in the required membrane area for a given hydrogen recovery [5–7].

To overcome the limitations of packed bed membrane reactors, membrane assisted fluidized beds have been proposed in the literature and are being used mostly for methane reforming reactions. In Figure 7.1, a schematic overview of a fluidized bed membrane reactor for WGS is shown. At the bottom, the reactants are fed to the reactor where the reaction takes place. Palladium (Pd) based membrane tubes are immersed inside the catalyst bed to extract the hydrogen from the reaction zone. To have a successful industrial implementation of such a unit, it is crucial to minimize the required membrane area and the Pd membrane layer thickness for a specific H_2 production capacity, related to the very high cost of Pd and its scarcity in nature [8].

Negligible pressure drop, reduced intra particle mass and heat transfer resistances, nearly isothermal operating conditions and flexibility in membrane module arrangement are the main advantages of the fluidized bed configuration. In addition, the membrane module can improve the bubble to emulsion mass transfer rate due to increased bubble breakage at the membrane module[9]. Difficulties in reactor construction, membranes sealing and long term stability under fluidizing conditions and erosion of reactor internals and catalyst attrition are the main disadvantages reported for fluidized bed membrane reactor applications, which has thus far hampered the commercialization of these units.

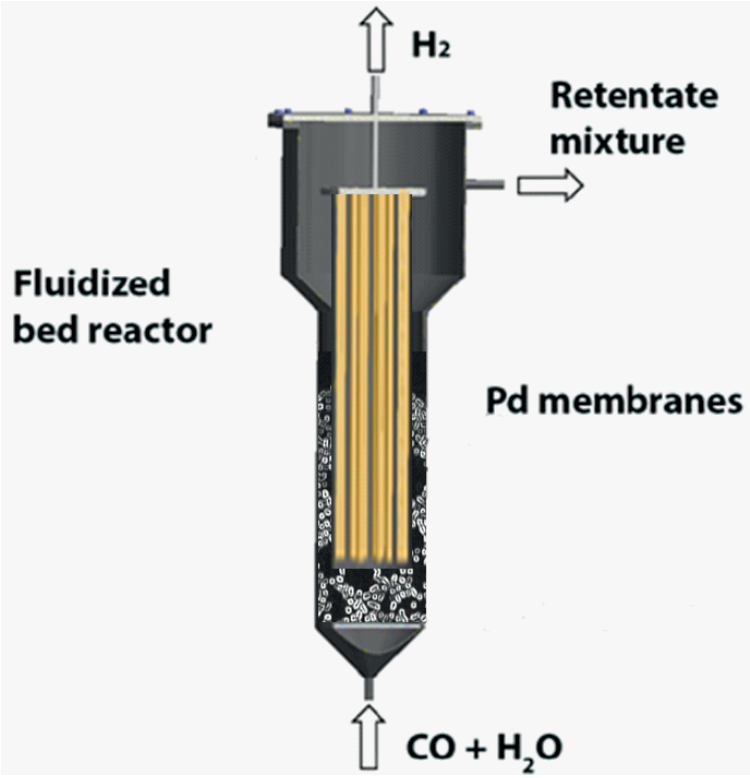

Figure 7.1 A schematic representation of a fluidized bed membrane reactor for water gas shift reaction.

Although membrane assisted fluidized bed reactors have been demonstrated for methane reforming and autothermal reforming reactions with metallic supported Pd-based membranes [10,11], the long term performance of these promising reactors have not yet been demonstrated for WGS using highly permeable ceramic supported Pd-based membranes with high hydrogen recovery factors and selectivities. Therefore, the main objective of this research is to demonstrate a membrane assisted fluidized bed reactor with the capacity of 1 Nm^3/h of ultrapure H_2 production with high-temperature WGS to provide a proof-of-principle at lab scale. The long-term performance of the membranes (permeance and selectivity) and the catalyst is monitored in a lab scale test rig. Subsequently, the performance of the membrane reactor is assessed for different inlet compositions and operating conditions to determine the optimum operating window for the process. In the following sections, first results will be presented and discussed, followed by a summary of the main conclusions. Then the experimental setup and procedure is described in detail, discussing practical challenges and possible solutions.

7.2 Materials and Methods

A membrane assisted fluidized bed reactor setup was designed and built. The setup consists of three main sections: a feed section, reactor section and analysis section (Figure 7.2 and Figure 7.3). The feed section consists of a feed gas supply from cylinders and mass flow controllers (Bronkhorst® Bronkhorst Nederland B.V., The Netherlands) to set the desired flow and feed composition at the inlet. The mass flow controllers are also equipped with shut off valves (Nypro type) to cut off the flow in case of an emergency. A Bronkhorst® Controlled evaporator and mixer (CEM) system was used to feed the reactor with a precise and very stable amount of steam. All the lines were electrically traced to ensure that the temperature remains above the dew point of the gas mixture.

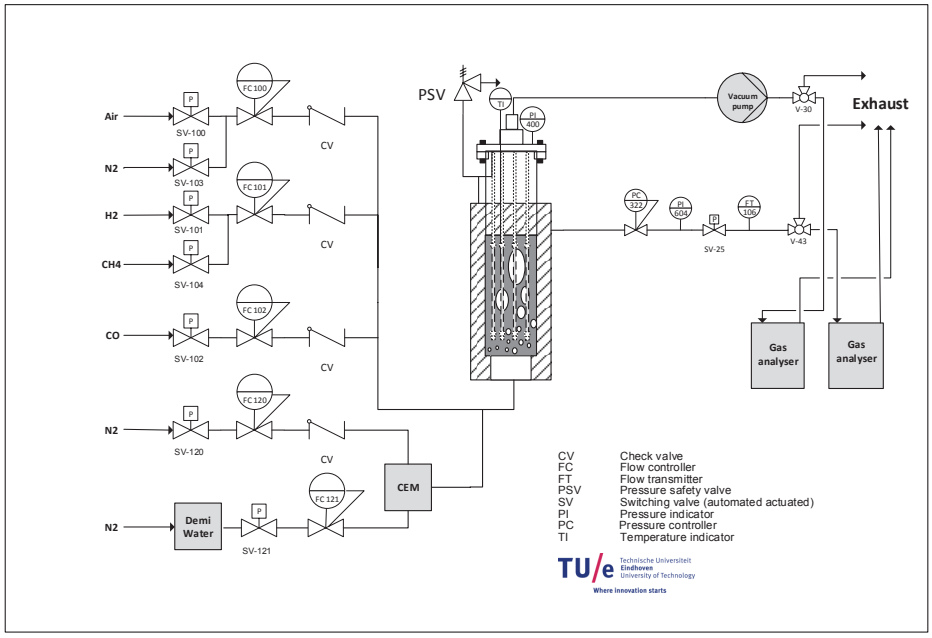

Figure 7.2 A process flow diagram of the membrane assisted fluidized bed setup.

The reactor was constructed with a geometry of 102 mm in diameter and 100 cm in height from AISI310 (CORO METAALTECHNIEK, Veenendaal, The Netherlands). The porous plate distributor was made of Hastelloy X (Ø 102 × 5 mm) with 40 µm pore size. Three electric baby ovens with a capacity of 2.2 kW were used to keep the reactor at the desired temperature. Pressure transmitters (PTX 1400 from Druck Nederland B.V., The Netherlands) were used to measure the pressure at the top and bottom of the reactor (at the porous plate position). The feed can be set to bypass the reactor using a three-way valve (Parker type) to measure the composition with an analyzer.

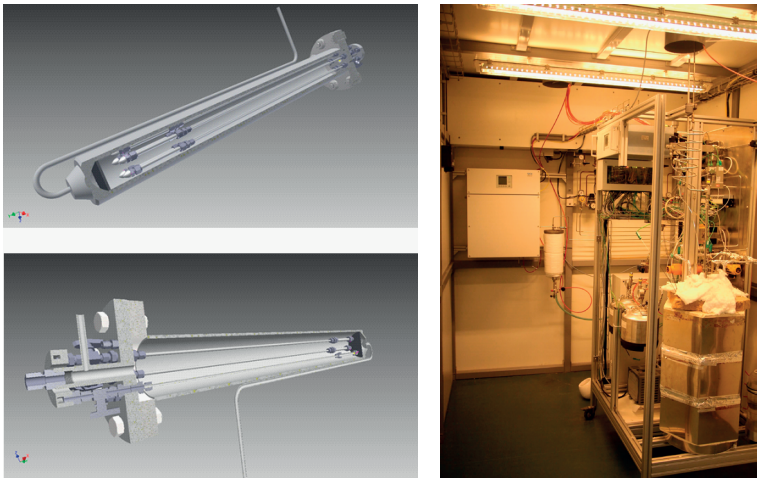

Figure 7.3 Fluidized bed membrane reactor setup (right); and membrane reactor module (left). To control the system remotely, the InTouch program (InTouch 2012 V10.6, Houston, TX, USA) was used on a PC. In the permeate side the CO content (in ppm) was continuously measured to be able to assess the stability of the membrane performance.

The setup was designed to have the possibility to sample both the retentate and permeate streams. The analysis section consists of two inline GMS800 series extractive gas analyzers (© SICK GmbH, Reute, Germany). In the retentate side, the analyzer was calibrated for CO, CO_2, CH_4 and H_2 with a precision of 1 vol%. In the permeate side the analyzer was calibrated for H_2 between 0 to 100 volume % and for CO between zero and 100 ppm. Therefore, traces of CO impurity at the permeate side can be detected with the analyzer (with a lower detection limit of 0.2 ppm). CO_2 is also measured in the permeate side stream in the range 0–200 ppm.

Catalyst and filler particles were supplied by Johnson Matthey® (Johnson Matthey Fuel Cells Research, Reading, UK). The catalyst was 2 wt % Pt loading impregnated onto 80–200 micron alumina particles (Table 7.1). Due to high activity of the catalyst, it was diluted with inert alumina (the catalyst support) to have enough bed height for complete immersion of the Pd-based membrane module inside the gas-solid suspension at minimum fluidization velocity. Thus a mixture of 954 g of the catalyst and the filler (9.2%/90.8%) was integrated inside the reactor for these experiments. Separate tests with different amount of catalyst material confirmed the absence of mass transfer limitations.

Table 7.1 Catalyst and alumina particles physical properties.

	Material	Avg. Particle Diameter (μm) [1]	Average Skeletal Density (g/cc) [2]	std. dev. (g/cc)	Apparent Density [3] (g/cm^3)	Geldart Classification (-)
Filler	Al_2O_3	160	3.300	0.009	1.691	A/B
Catalyst	$2\%Pt/Al_2O_3$	180	3.321	0.016	1.443	A/B

[1] FRITSCH ANALYSETTE22 + Quantachrome instruments, Upyc 1200e V5.04; [3] ThermoFisher SCIENTIFIC Pascal 140 series.

Regarding the hydrodynamics of the fluidized bed, separate experimental results (not reported here for brevity) confirmed homogeneous fluidization of the catalyst and alumina filler particle mixture. The minimum fluidization velocity (U_{mf}) was determined experimentally for the catalyst and inert material at the temperature range of 20–400 °C with compressed air using the standard pressure drop method (see Table 7.2). Later, the determined values were used to predict the inlet flow rate necessary to keep the catalyst bed at bubbling fluidization conditions.

Table 7.2 Minimum fluidization velocity *vs.* temperature.

Temperature (°C)	22	102	204	296	397
U_{mf} (cm/s)	2.41	2.14	1.90	1.63	1.49

Before integration of the catalyst batch inside the reactor a small batch of the catalyst/filler (1/3) mixture was used for a segregation test. After a 24 h test under bubbling fluidization conditions at room temperature and atmospheric pressure no segregation was observed, ensuring a homogenous catalyst distribution inside the fluidized bed during the experiments.

Five Pd-Ag alloy membranes (4–5 μm of selective layer thickness, 13%–15% Ag) were prepared onto ceramic supports provided by Rauschert Kloster Veilsdorf (alumina 100 nm pore size top layer, 10/7 mm outer diameter/inner diameter). The membranes were sealed following a sealing technique reported by Fernandez et al. [12]. After sealing, each membrane had an average net length of 10 cm.

Three sets of experiments were performed: (a) The catalyst batch was firstly integrated inside the reactor to be operated in absence of the membrane module (conventional fluidized bed reactor); (b) The catalyst batch was removed from the reactor and the membrane module was integrated inside the reactor. Membranes were first activated under pure H_2 atmosphere ensuring stable performance of the membranes. Subsequently, the permeation properties of the membranes were checked and the inhibitory effect of CO and H_2O on the H_2 permeation flux was measured; (c) The catalyst batch was re-integrated into the reactor in the presence of the membrane module to study the reactor performance with internals (membranes were closed at the top so that the membranes acted as non-permeable internals). Finally, the membrane

module was opened at the permeate side and the performance of the fluidized bed membrane reactor was investigated for different operating conditions. After the tests, the morphology of the membranes was analyzed by SEM and compared with the fresh membranes.

7.3 Results and Discussion

7.3.1 Conventional Fluidized bed Reactor

Figure 7.4 illustrates the performance of the catalytic fluidized bed reactor (without membranes) at different temperatures and at different excess velocities (i.e., different $U\text{-}U_{mf}$ values, where U is the fluidization velocity and U_{mf} the minimum fluidization velocity) to have a similar initial equivalent average bubble size at different temperatures. According to the obtained results, the performance of the reactor was mainly limited by thermodynamics, where a CO conversion close to the equilibrium value was achieved, especially at higher temperatures. In addition, at constant temperature, the performance of the reactor was similar for different excess velocities, since the CO conversion is not limited by the mass exchange rate between the emulsion and the bubble phases. Therefore, increasing the inlet flow rate will not result in higher CO to H_2 conversion rates.

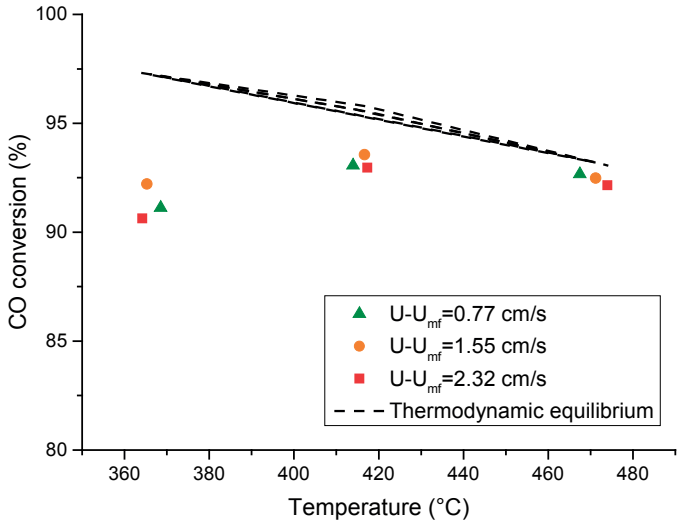

Figure 7.4 Performance of the conventional fluidized bed reactor a function of the operating temperature at different excess velocities ($U\text{-}U_{mf}$) for WGS. Feed: CO (10%), H_2O (30%), N_2 (balance), reactor at 1 bar.

Later the performance of the conventional fluidized bed reactor will be compared at similar conditions with the performance of a fluidized bed reactor in the presence of internals and in the last step in the presence of membranes with extraction. After the conventional fluidized bed

reactor test, the reactor was cooled down and the catalyst batch was removed from the reactor. Therefore, the membrane module could be integrated for activation protocol under pure H_2 flow.

7.3.2 Membrane Permeation Properties

In order to characterize the permeation properties of the membranes, initially the membranes have to be activated. The activation protocol includes the reduction under pure H_2 while imposing a pressure difference between the retentate and permeate sides of the membranes (in this case at 400 °C and 1 bar pressure difference) followed by air treatment of the surface of the membranes (at the same condition). After reaching to a stable performance of the membranes the permeation properties of the membranes were characterized at different temperatures and pressure differences. Table 7.3 compares the permeation properties of some of the best reported membranes in the open literature with the performance of the used membrane module. Comparing with the reported values, the used membrane module shows a very high H_2 permeance that can ensure very high H_2 recovery values. In addition, due to the excellent H_2/N_2 ideal selectivity obtained a very high H_2 purity suitable for low temperature fuel cell applications can be achieved in the permeate side.

To have a fair prediction of the membranes performance at WGS conditions, it is essential to investigate the behavior of the membranes in the presence of WGS related gases. More specifically, the poisoning effect of CO and the inhibitory effect of H_2O should be quantified. In addition, the external mass transfer limitations for H_2 molecules to reach the membrane surface have to be taken into account. Therefore, a series of experiments were designed to independently investigate the effects of external mass transfer limitations, CO poisoning and H_2O inhibition on the permeation properties of the membrane module for different gas compositions at different temperatures.

The poisoning effect of CO was quantified by adding different percentages of CO (2.5%–10%) to a mixture of H_2 and N_2 with different compositions and at different temperatures (N_2 was used as the balance). Inspecting the obtained results shown in Figure 7.5a&b, it can be inferred that, for all cases, CO had a poisoning effect on the performance of the membranes. It can be seen that the poisoning effect of CO is more pronounced at lower CO concentrations. This is in line with the current knowledge on CO interaction with the membrane surface. In fact, CO can easily jump between the hollow and the bridge positions of the Pd cluster, and this permits a small amount of CO to inhibit the interaction of H_2 with a large part of the Pd surface [26]. At higher temperatures, a less pronounced CO poisoning effect was also observed, as has already been reported by many authors [27]. The possible inhibitory effect of H_2O on the performance of the membrane was studied as well by addition of certain percentages of H_2O (30%–50%) to a mixture of H_2 and N_2 with different compositions and at a temperature range of 350–450 °C (Figure 7.5c&d). The addition of H_2O had a negligible effect on the hydrogen permeance of the membranes.

Table 7.3 Hydrogen permeation properties of commercial and the best thin Pd based membranes (membranes reported in order of permeance, the units of the permeance have been taken from DOE 2015 [13] and used to compare the different membranes).

Membrane	Support	Thickness µm	Technique	Temp. °C	Permeance × 10^{-7} mol·m^{-2}·s^{-1}·Pa^{-1} at 1 atm	Selectivity H_2/N_2	Producer	Ref.
$Pd_{77}Ag_{23}$	No	1.9–3.8	PVD 2 steps	400	190	2900	Sintef	[14]
Pd_{93}-Ag_7	α-Al_2O_3	0.78	ELP	400	114	640	TECNALIA	[15]
$Pd_{77}Ag_{23}$	Micro-channels	2.2	PVD 2 steps	400	88	----	Sintef	[16]
Pd_{92}-Ag_8	γ-Al_2O_3/YSZ	0.9	ELP	400	65	1100	TECNALIA	[17]
Pd-Au	Al_2O_3	2–3	ELP	500	62	1400	Dalian	[18]
Pd-Au	YSZ/PSS	1–5	ELP	400	43–52	10000–20000 (H_2/Ar)	PALL *	[19]
Pd_{85}-Ag_{15}	α-Al_2O_3	3.2	ELP	400	31	8000–10000	TECNALIA	[20]
Pd-Ag	α-Al_2O_3	2–10	ELP	350	6–31	500 to >1000	Media and process *	[21]
Pd	γ-Al_2O_3	2–4	ELP	400	27	500	Dalian	[22]
Pd	Metallic	3–5	ELP	450	20	450 H_2/He	CRI/Criterion *	[23]
Pd-Ru	Al_2O_3/PSS	6.4	ELP	400	19	15000 @ 10 bar	NORAM * (former MRT)	[24]
Pd-Ag	α-Al_2O_3	3–9	ELP	350	15	>7600	Hysep *	[25]
Pd	Metallic	12	PVD-ELP	417	11	1100	Plansee/KIT/Linde	[26]
Pd_{85}-Ag_{15}	Metallic	4–5	ELP	400	10	>200000	TECNALIA	[10]
Pd	Metallic	7.6		450	9	Infinite after 3500 h >6000 H_2/He	CRI/Criterion *	[23]
Pd	No	76	Self-supported	600	4	>>10000	REB Research *	[6]
Pd_{85}-Ag_{15}	α-Al_2O_3	4	ELP	400	42	20000	TECNALIA	This work

* Commercial Pd-based membranes.

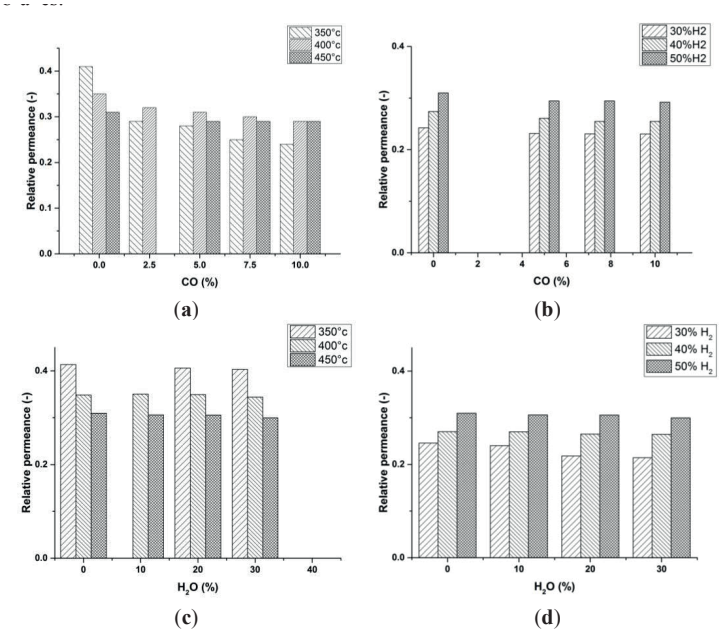

Figure 7.5 CO poisoning and H_2O inhibitory effect on the performance of the membranes at different temperatures with $H_2/CO/N_2$ and $H_2/H_2O/N_2$ feed gas compositions. (a) CO poisoning effect at different temperatures and constant H_2 concentration in feed (50%), N_2 (balance); (b) CO poisoning at different H_2 concentration in the feed at 450 °C; (c) H_2O inhibitory effect at different temperatures and constant H_2 in the feed (50%), N_2 (balance); (d) H_2O inhibitory effect at different H_2 concentration in the feed at 450 °C. Relative permeance is the performance of the membrane module at the specified condition normalized with the case when only pure H_2 was used with exactly the same partial pressure difference.

According to the obtained results (Figure 7.5), the external mass transfer for H_2 molecules to reach the membranes surface is affecting the H_2 permeation flux and this effect is more pronounced for higher temperatures and lower H_2 concentrations inside the reactor. This is due to the fact that at higher temperatures the membrane has a higher permeance increasing the concentration gradient from the gas bulk to the surface of the membranes (larger extent of concentration polarization). This can be improved by employment of fluidizing particles inside the reactor. Due to a much better mixing of the gas mixture due to solids circulation patterns, the external mass transfer resistance will be largely decreased [19]. Although when immersing very high flux membranes, a dynamic zone with a locally higher solids holdup could be formed (densified zones) in the vicinity of the membranes, which may impose a mass transfer resistance for H_2 to reach the membrane surface. To mitigate this effect, use of larger particles or operation in the turbulent fluidization regime could to be considered [28].

7.3.3 Long Term Membrane Performance

After characterization of the membranes permeation properties, the module was cooled down to room temperature and the catalyst batch was integrated inside the reactor. The performance of the membrane module was investigated in the presence of the catalyst in the continuous bubbling fluidization regime at high temperature WGS conditions. Figure 7.6 summarizes the long-term performance of the membrane module under the specified conditions.

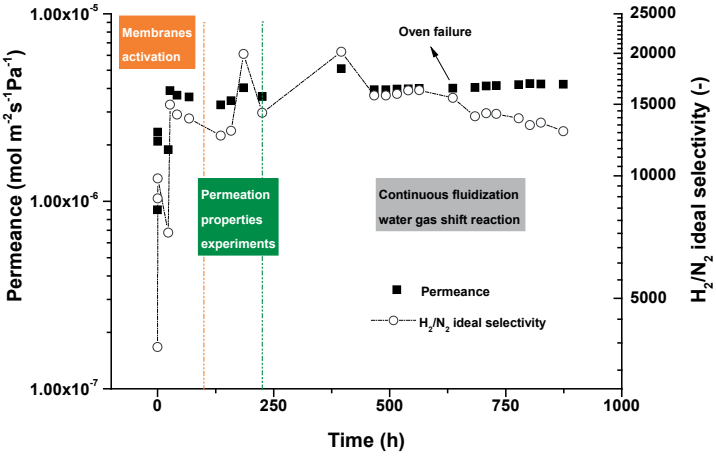

Figure 7.6 Long-term performance of the membrane module during 900 h of continuous operation in the bubbling fluidization regime at high-temperature WGS conditions. Temperature: 400 °C, Ppermeate: 1 bar, Pretentate: 2 bar; feed: 10 NL/min of pure H_2.

The membrane module showed a very stable performance during nearly 900 h of continuous operation in the bubbling fluidization regime at high temperature WGS conditions (including the initial time used for membrane activation). For such thin and high flux membranes, this is one the longest ever reported stability tests in the literature with an outstanding H_2/N_2 selectivity throughout the testing period. Although after 550 h work due to a failure in one of the ovens around the reactor, the membrane module experienced a high thermal shock over night increasing the N_2 leakage somewhat. This confirms the importance of nearly isothermal conditions to achieve stable performance of the membranes, since hot spot formation by the membranes (which is prone to occur in packed bed membrane reactor modules) could be detrimental for the lifetime and perm-selectivity of the membranes.

7.3.4 Fluidized Bed Membrane Reactor Performance

For all sets of experiments a standard operating procedure was followed to maintain consistency and comparability between the results. First of all, the reactor was set at a desired temperature to be stabilized. Three temperature sensors at the top, middle and bottom of the catalytic bed along the membrane module were placed to continuously monitor the ovens and

reactor temperatures to be at the specified set points. Before starting with each experiment, the inlet gas mixture was bypassed to the analyzer to measure the inlet dry gas composition. After inlet gas stabilization in the bypass mode, the feed gas was redirected to the reactor while the membranes were blocked in the permeate side to avoid H_2 permeation through the membranes as is the case in the conventional fluidized bed reactor (in this case with internals).

In the next step, the membranes were opened from the top part and a vacuum pump was used to generate the trans-membrane pressure difference to investigate the effect of H_2 permeation on the performance of the reactor. Table 7.4 illustrates the operating window in which the experiments were performed. In the following section, results from the experiments are plotted and discussed in terms of the main reactor performance characteristics, viz. CO conversion and H_2 recovery factor, defined in Table 7.5. In addition, for all sets of the experiments the carbon balance was checked to ensure that carbon deposition was always below 2%.

Table 7.4 Overview of the operating window for the experiments.

Parameter	Unit	Value
Pressure Range	bar	1–3
Temperature Range	°C	350–450
U/U_{mf}	-	1.5–5
Steam/Carbon (S/C)	-	1.5–3

Table 7.5 Parameters to quantify the reactor performance (ϕ: Molar flow)

CO Conversion	$\frac{\boldsymbol{\Phi_{co,in} - \Phi_{co,out}}}{\boldsymbol{\Phi_{co,in}}}$
H_2 Recovery Factor	$\frac{\phi_{H_2,permeated}}{\phi_{H_2,in} + \phi_{H_2,produced}}$

7.3.5 Long Term Performance of the Membrane Reactor

The long term performance of the membrane reactor module was monitored for a base case during the 900 h of continuous operation. The reactor performance was monitored for the base case initially with the membranes closed (a fluidized bed the with membrane module only as internals) and later the membranes were opened in the permeate side to have permeation through them. Figure 7.7 depicts the performance of the catalyst and membrane reactor over the specified time and for both the fluidized bed reactor (FBR) and fluidized bed membrane reactor (FBMR) cases.

Over roughly 900 hours of continuous operation in the bubbling fluidization regime and WGS operating conditions, the catalyst and the membrane module have shown a very stable performance without any decrease in the performance of the catalyst and permeation properties of the membranes. The CO impurity of the permeate stream was 15 ppm in average during the whole time span (min: 10, max: 28). It should be noted that the CO impurity depends on the CO conversion at the retentate side, so that much lower impurities can be obtained at higher CO conversions at the retentate side (see next section).

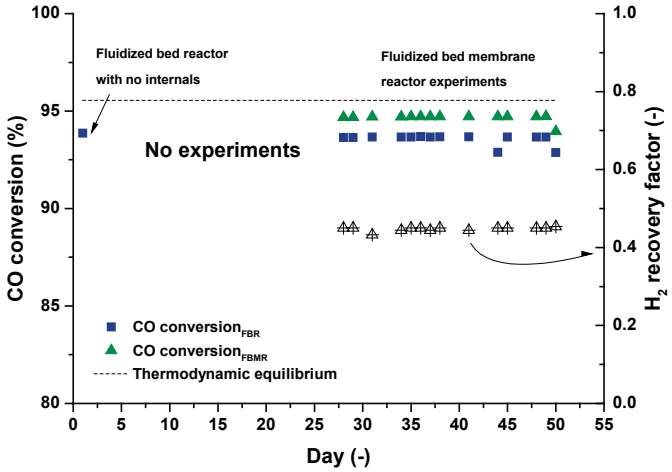

Figure 7.7 The long term performance of the a fluidized bed membrane reactor (FBMR) module in comparison with a fluidized bed reactor (FBR) module over 900 h of continues work. Temperature: 400 °C, CO (10%), H_2O (30%), N_2 balance, U/U_{mf}: 2.1, Pperm: 30 mbar, P:1 bar

A H_2 recovery factor of 45% in average was measured for the reference case during the experimental work over 900 h. The recovery factor can be either enhanced with increasing the partial pressure of H_2 at the retentate side (working at elevated pressures), installing more membrane area or increasing the operating temperature of the module which will be explained in the next part of result and discussion.

7.3.6 Fluidized Bed Reactor vs. Fluidized Bed Membrane Reactor

The performance of the membrane reactor was studied at different operating conditions. Firstly experiments were carried out at 1 bar inside the reactor and S/C: 3 for different excess velocities $U\text{-}U_{mf}$: 0.77–2.32 and at different temperatures of 350, 400 and 450 °C (see Figure 7.8). The CO conversion of the conventional fluidized bed without internals (FBR, w/o) is considered as the reference case, which is compared to the case of a fluidized bed with internals (FBR, w) where the membrane module is just immersed but no gas is extracted via the membranes, and the case of a fluidized bed membrane reactor (FBMR) with extraction via the membranes. FBR, w/o showed higher CO conversions at elevated temperatures. The same behavior can be observed for FBR, w due to the increased catalytic activity as well. In both cases the conversion of CO is limited by thermodynamic equilibrium while only a small change in reactor performance was observed in absence (FBR, w/o) and in presence (FBR, w) of internals. This could be due to the fact that the presence of internals did not improve the mass transfer inside the bed. More studies need to be performed to figure out the optimum placement of the membrane module (bubble size vs. membranes pitch) to improve the mass

transfer inside the bed. Possibly to have smaller average bubble size along the bed which will result in higher bubble to emulsion mass transfer rates as described by Maurer et al. [9].

The main advantage of utilizing hydrogen selective membrane (FBMR) to circumvent the thermodynamic equilibrium limitation is clearly shown in Figure 7.8a-c where at elevated temperatures, higher CO conversions than the equilibrium value can be achieved. More specifically, at elevated temperatures, the permeation through the membranes was the rate limiting factor and determined the membrane reactor performance. This also suggests to work at higher temperatures where the H_2 recovery increases as a result of increase in membrane permeation, while at higher excess velocities the H_2 recovery factor decreases due to lower ratio of the membrane area to inlet flow rate. This ratio is indeed one of the key parameters determining the membrane reactor performance [7].

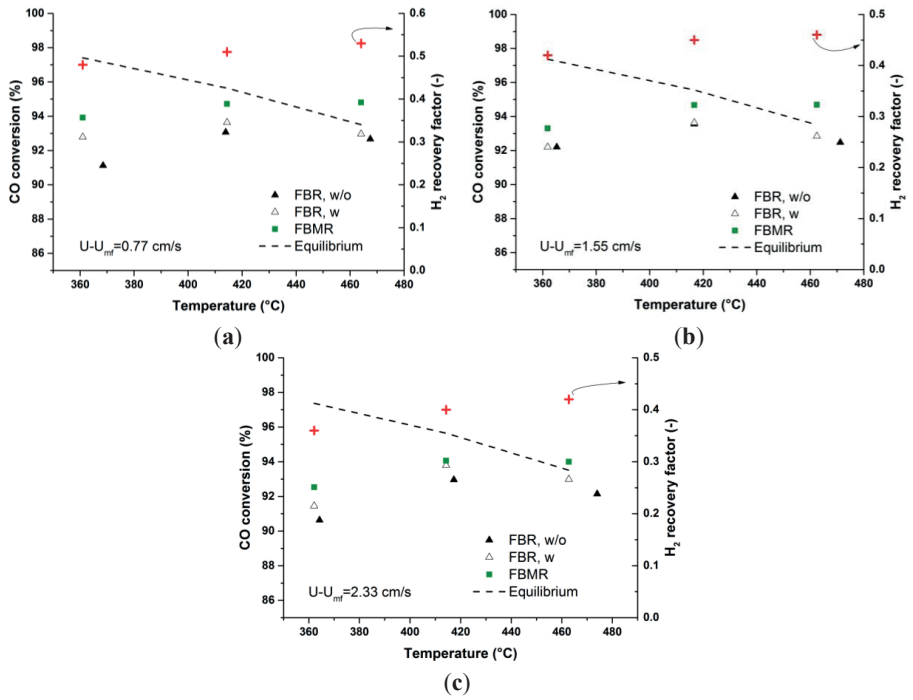

Figure 7.8 (a) Performance of the fluidized bed reactor without internals (FBR, w/o) in comparison with (b) fluidized bed reactor with internals (FBR, w) and (c) fluidized bed membrane reactor (FBMR) performance at various U-U_{mf}. P: 1 bar, CO (10%), H_2O (30%), N_2

During the fluidized bed membrane reactor experiments the quality of H_2 in the permeate stream was monitored. The average CO impurity during the experiments at different temperatures was 13 ppm (min: 6 ppm, max: 25 ppm), which is very suitable for most H_2 applications. The performance of the membrane reactor was investigated at different pressures from 1–2.5 bar.

To have similar hydrodynamics inside the reactor, the inlet flow rate was modified at different temperatures to keep the U/U_{mf} = 2.1 and constant for all the cases. Figure 7.9 illustrates the performance of the membrane reactor at different pressures where increasing the reactor pressure will result in lower hydrogen recovery factors (average CO impurity: 21 ppm; min: 19, max: 25 ppm). This is due to the fact that at higher pressures the inlet flow rate was increased to keep the $U\text{-}U_{mf}$ value constant for different cases. Although the hydrodynamics will be similar for the different cases, the ratio between the inlet flow rate and the membrane area is different for the different cases. Increasing the inlet flow rate at higher pressures will result in a lower ratio of the membrane area over the inlet flow rate.

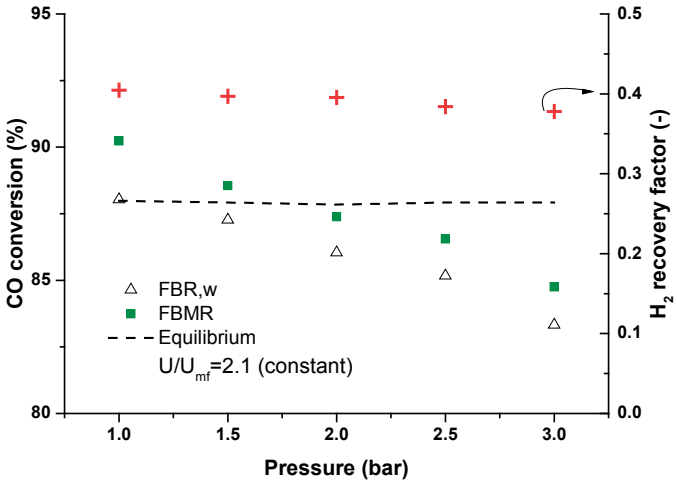

Figure 7.9 Effect of pressure on the performance of the membrane reactor at constant U/U_{mf} at 400 °C, CO (10%), H_2O (15%), N_2 balance, Ppermeate: 30 mbar.

To show this more clearly, a new test with constant inlet flow rate was carried out for different operating pressures. Figure 7.10 clearly shows higher CO conversions at higher membrane reactor pressures when keeping the inlet flow rate constant. In this case at higher pressures the hydrogen recovery will be higher as well (average CO impurity: 7 ppm, min: 3 ppm, max: 9 ppm). Although increasing the pressure above 2 bar inside the reactor did not affect the performance of the membrane reactor much. This is due to the fact that at higher pressures (with constant inlet flow rate) the U/U_{mf} ratio will be lower. Therefore, at higher pressures the mixing will be worse and this will induce the mass transfer limitation inside the catalytic bed. Although CO conversions above the equilibrium can be achieved for higher inlet flow rates, due to limitations in the CO mass flow controller, experiments for higher inlet flow rates were not feasible with the specified inlet gas composition. Therefore, experiments were continued with a semi-industrial WGS inlet gas composition.

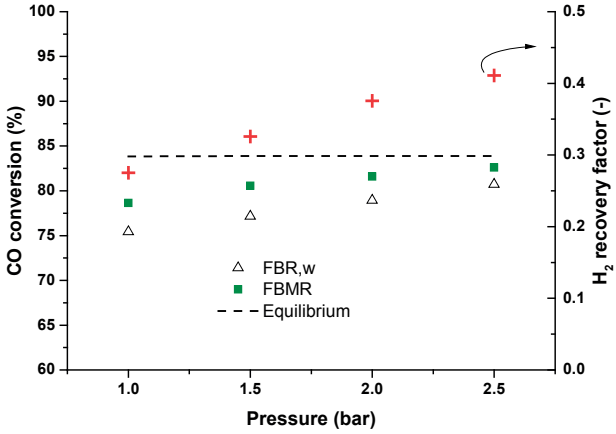

Figure 7.10 Membrane reactor performance at different pressures up to 2.5 bar and at 400 °C, CO (5%), H_2O (15%), CH_4 (0%), H_2 (18%), N_2 balance, U/U_{mf}:1.71–6, Ppermeate: 30 mbar.

7.3.7 Reactor Performance for Industrial Inlet Composition

The membrane reactor performance was also studied by feeding a semi-industrial WGS feed composition (WGS gas as outlet of a steam methane reformer) at different pressures. The inlet flow rate was kept the same for all the cases to keep the ratio of the inlet flow rate to the membrane area constant, as in the previous study. The obtained results (Figure 7.11) confirmed the better performance of the membrane reactor at higher pressures, although the maximum total pressure was 2 bar due to limitations with the current setup. The CO content in the permeate is below 10 ppm (average CO impurity: 5.6 ppm, min: 4.5 max: 7 ppm), which guarantees the H_2 quality for fuel cell applications.

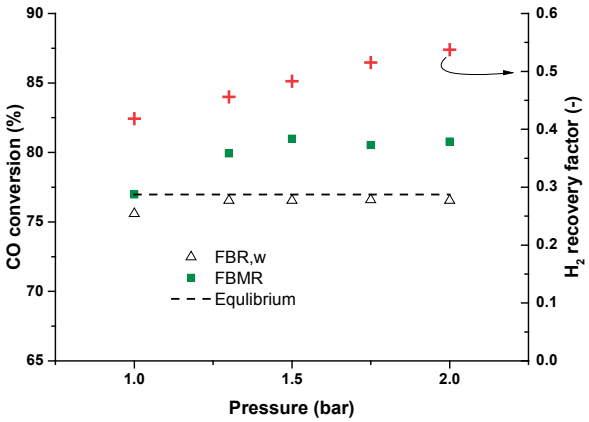

Figure 7.11 Membrane reactor performance for a semi-industrial inlet composition at 400 °C, CO (9.2%), H_2O (19%), CH_4 (4%), H_2 (30%), N_2 balance, U/U_{mf}: 1.67-5, Ppermeate: 30 mbar

A similar experiment was carried out at 450 °C to assess whether the performance of the membrane reactor can be improved at higher temperatures. Although an increase in the temperature results in better performance of the membrane reactor in terms of CO conversion and H_2 recovery factor, a high degree of methanation occurs at higher reactor temperatures. Apparently, the catalyst used in this study is active for methanation only at temperatures around and above 450 °C. Therefore, for the inlet composition similar to industrial WGS reactors it is recommended to operate at around 400 °C to minimize methanation.

7.3.8 Post-Mortem Analysis

7.3.8.1 Membranes

After completion of membrane reactor tests the module was cooled down to room temperature and the membranes and catalyst particles were removed for further post-mortem analysis. Figure 7.12 and Figure 7.13 show the actual and SEM images of the membranes surface before and after 900 h of continuous operation. It is clear that the surfaces of the membranes are contaminated with traces of fluidizing particles. Despite the contamination with parts of fluidization particles the membrane has shown a very stable permeation throughout the entire experimental program.

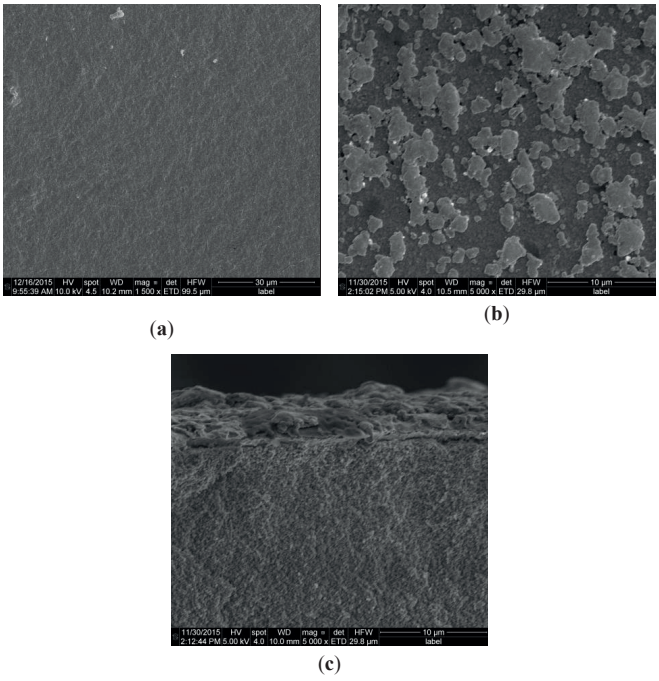

(**a**) (**b**)

(**c**)

Figure 7.12 SEM images: (a) fresh membrane surface; (b) membrane surface after 900 h of continuous operation under bubbling fluidization conditions and WGS; and (c) membrane cross section.

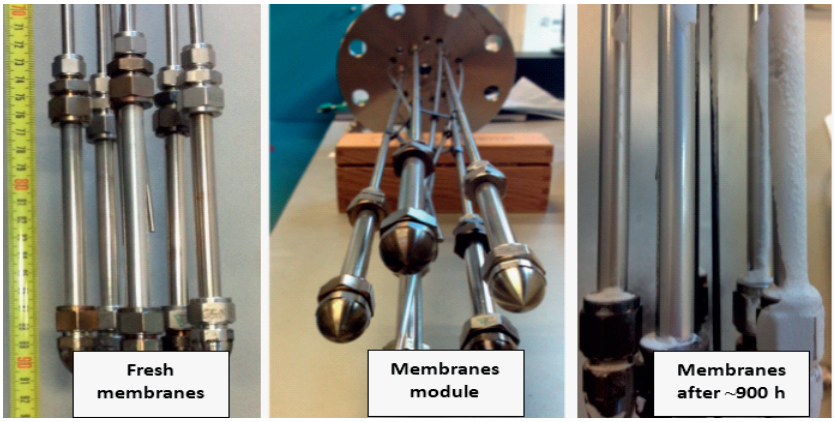

Figure 7.13 Fresh membranes surface and after 900 h of continuous operation under bubbling fluidization conditions and high temperature WGS.

7.3.8.2 Catalyst

Figure 7.14 compares the particle size distribution of the fresh catalyst with the particle size distribution after 900 h of continuous operation under bubbling fluidization conditions and high temperature WGS. The particle size distribution before and after the long term performance check of the fluidized bed membrane reactor module confirms the very good mechanical stability of the catalyst. Therefore, the attrition of the particles inside the column was negligible for the selected experimental conditions. Due to limitations in the setup, experiments at high inlet flow rates to attain the turbulent fluidization regime were not possible.

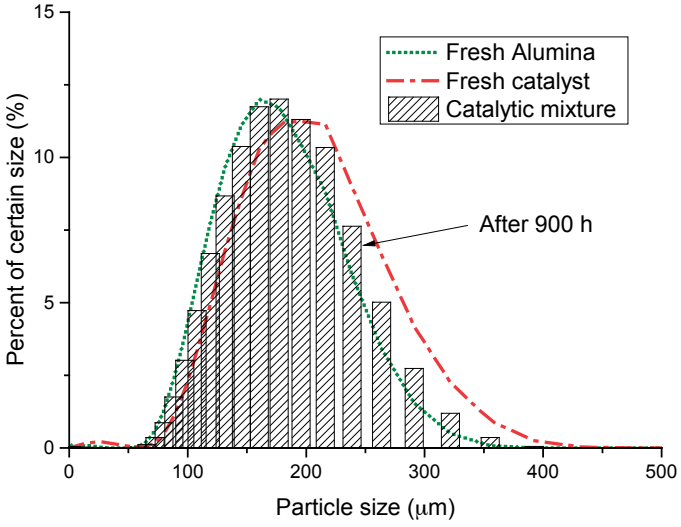

Figure 7.14 Particle size distribution of fresh alumina, catalyst and the catalytic batch after 900 h of continuous operation (FRITSCH ANALYSETTE 22).

7.4. Conclusions

A fluidized bed Pd-based membrane reactor unit with a capacity of 1 Nm^3/h of ultra-pure H_2 was designed, built and operated for over 900 h of work. Initially, the permeation properties of the membranes were measured in absence of catalytic particles, confirming a very high H_2 permeance and outstanding H_2/N_2 ideal perm-selectivities (up to 21,000 when integrating five membranes in the module) in comparison with the best ever reported Pd based membranes in the literature. Independent effects of external mass transfer limitations (concentration polarization), CO poisoning and H_2O inhibition on the performance of the membranes were investigated in the single-phase module over a temperature range of 350–450 °C and for different H_2 concentrations in the feed. The obtained results revealed that concentration polarization is the rate limiting factor for H_2 molecules to reach the surface of the membranes and a better mixing inside the membrane reactor module is essential, which can be achieved with fluidization. In line with other findings in the open literature, the poisoning effect of CO was decreased at higher temperatures while the inhibitory effect of H_2O was negligible over the investigated temperature range.

Monitoring the performance of the membrane reactor for a reference case over 900 h of continuous work under bubbling fluidization and high-temperature WGS conditions confirmed a very stable performance of both the membranes and the catalyst. The membrane reactor performance was studied at different operating conditions and compared with the performance of a conventional fluidized bed reactor and used to evaluate the optimal operating conditions. The fluidized bed reactor performance with and without and the membranes as internals without permeation was practically the same, indicating that the presence of the membranes tubes did not improve the bubble-to-emulsion phase mass transfer, possibly related to the suboptimal positioning of the membrane module inside the reactor. Further studies are required to optimize the positioning of the membrane module.

In general, increasing the temperature to between 350 and 450 °C results in higher CO conversions and improved H_2 recovery factors, although at higher temperatures the performance can be deteriorated due to the increasing importance of methanation (at least for the catalyst used in this work). In addition, it is recommended to operate at higher pressures to enhance the permeation through the membranes thereby shifting the equilibrium more towards the products. Analysis of the H_2 quality in the permeate stream has shown very low CO concentrations (in average <10 ppm), so that the produced hydrogen can be directly fed to a low temperature PEM fuel cell.

Bibliography

[1] C.S. Patil, M. van Sint Annaland, J. A. M. Kuipers, Design of a Novel Autothermal Membrane-Assisted Fluidized-Bed Reactor for the Production of Ultrapure Hydrogen from Methane, Ind. Eng. Chem. Res. 44 (2005) 9502–9512. doi:10.1021/ie050244y.

[2] R.S.C. Advances, G. Barbieri, A. Brunetti, A. Caravella, E. Drioli, RSC Advances Pd-based membrane reactors for one-stage process of water gas shift, (2011) 651–661. doi:10.1039/c1ra00375e.

[3] J.M. Moe, Design of Water-Gas-Shift Reactors, Chem. Eng. Prog. 58 (1962) 33–36.

[4] F. Gallucci, E. Fernandez, P. Corengia, M. van Sint Annaland, Recent advances on membranes and membrane reactors for hydrogen production, Chem. Eng. Sci. 92 (2013) 40–66. doi:10.1016/j.ces.2013.01.008.

[5] T.P. Tiemersma, C.S. Patil, M. van Sint Annaland, J. A. M. Kuipers, Modelling of packed bed membrane reactors for autothermal production of ultrapure hydrogen, Chem. Eng. Sci. 61 (2006) 1602–1616. doi:10.1016/j.ces.2005.10.004.

[6] F. Gallucci, M. van Sint Annaland, J. A. M. Kuipers, Autothermal Reforming of Methane with Integrated CO_2 Capture in a Novel Fluidized Bed Membrane Reactor. Part 2 Comparison of Reactor Configurations, Top. Catal. 51 (2008) 146–157. doi:10.1007/s11244-008-9127-7.

[7] F. Gallucci, M. van Sintannaland, J. A. M. Kuipers, Theoretical comparison of packed bed and fluidized bed membrane reactors for methane reforming, Int. J. Hydrogen Energy. 35 (2010) 7142–7150. doi:10.1016/j.ijhydene.2010.02.050.

[8] A. Helmi, F. Gallucci, M. van Sint Annaland, Resource scarcity in palladium membrane applications for carbon capture in integrated gasification combined cycle units, Int. J. Hydrogen Energy. 39 (2014) 10498–10506. doi:10.1016/j.ijhydene.2014.05.009.

[9] S. Maurer, E.C. Wagner, T.J. Schildhauer, J.R. van Ommen, S.M.A. Biollaz, R.F. Mudde, X-ray measurements of bubble hold-up in fluidized beds with and without vertical internals, Int. J. Multiph. Flow. 74 (2015) 118–124. doi:10.1016/j.ijmultiphaseflow.2015.03.009.

[10] E. Fernandez, J.A. Medrano, J. Melendez, M. Parco, J.L. Viviente, M. van Sint Annaland, F. Gallucci, D.A. Pacheco Tanaka, Preparation and characterization of metallic supported thin Pd-Ag membranes for hydrogen separation, Chem. Eng. J. (2015). doi:10.1016/j.cej.2015.09.119.

[11] J.A. Medrano, E. Fernandez, J. Melendez, M. Parco, D.A.Pacheco Tanaka, M. van Sint Annaland, F. Gallucci, Pd-based metallic supported membranes: High-temperature stability and fluidized bed reactor testing, Int. J. Hydrogen Energy. (2015) 1–13. doi:10.1016/j.ijhydene.2015.10.094.

[12] E. Fernandez, J. A. Sanchez-García, J. Melendez, V. Spallina, M. van Sint Annaland, F. Gallucci, D.A. Pacheco Tanaka, Development of highly permeable ultra-thin Pd-based supported membranes, Chem. Eng. J. Submited (2015). doi:10.1016/j.cej.2015.11.060.

[13] US department of energy, DOE, Hydrogen and Fuel Cells Program Annual progress report, (2011). https://www.hydrogen.energy.gov/annual_progress11.html (accessed March 13, 2016).

[14] T. A. Peters, M. Stange, R. Bredesen, On the high pressure performance of thin supported Pd–23%Ag membranes—Evidence of ultrahigh hydrogen flux after air treatment, J. Memb. Sci. 378 (2011) 28–34. doi:10.1016/j.memsci.2010.11.022.

[15] J. Melendez, E. Fernandez, A. Helmi, F. Gallucci, P.L. Arias, D.A. Pacheco Tanaka, Preparation and characterization of ultra-thin (<1 micron) Pd-Ag membranes on porous alumina support (100 nm pore size)., in: 12th Int. Conf. Catal. Membr. React., Szczecin, Poland, 2015.

[16] N. Vicinanza, I.H. Svenum, L.N. Næss, T.A. Peters, R. Bredesen, A. Borg, H.J. Venvik, Thickness dependent effects of solubility and surface phenomena on the hydrogen transport properties of sputtered Pd77%Ag23% thin film membranes, J. Memb. Sci. 476 (2015) 602–608. doi:10.1016/j.memsci.2014.11.031.

[17] D.A. Pacheco Tanaka, J. Okazaki, M.A. Llosa Tanco, S.T. M., Fabrication of supported palladium alloy membranes using electroless plating techniques, in: Palladium Membr. Technol. Hydrog. Prod. Carbon Capture Other Appl., 2015: pp. 83–99. doi:10.1533/9781782422419.1.83.

[18] L. Shi, A. Goldbach, H. Xu, High-flux H_2 separation membranes from (Pd/Au)n nanolayers, Int. J. Hydrogen Energy. 36 (2011) 2281–2284. doi:10.1016/j.ijhydene.2010.11.056.

[19] A. Damle, J. Acquaviva, Membrane Reactor for Hydrogen Production, in: AICHE, Philadelphia, PA, USA, 2008.

[20] E. Fernandez, A. Helmi, K. Coenen, J. Melendez, J.L. Viviente, D.A. Pacheco Tanaka, M. van Sint Annaland, F. Gallucci, Development of thin Pd-Ag supported membranes for fluidized bed membrane reactors including WGS related gases, Int. J. Hydrogen Energy. 40 (2015) 3506–3519. doi:10.1016/j.ijhydene.2014.08.074.

[21] Media and Process Technology Inc. Hydrogen Selective Ceramic Membranes For High Temperature Applications,http://www.mediaandprocess.com/products/products02.html (accessed March 14, 2016).

[22] A. Goldbach, F. Bao, C. Qi, C. Bao, L. Zhao, C. Hao, C. Jiang, H. Xu, Evaluation of Pd composite membrane for pre-combustion CO_2 capture, Int. J. Greenh. Gas Control. 33 (2015) 69–76. doi:10.1016/j.ijggc.2014.12.003.

[23] P. Veenstra, M. Iyer, A. Nijmeijer, F. Geuzebroek, R. Moene, J. Saukaitis, Integrated approach to CO_2 capture: Fuel gas decarbonisation, Energy Procedia. 63 (2014) 2054–2059. doi:10.1016/j.egypro.2014.11.221.

[24] B. A. Li, T. Boyd, A. Gulamhusein, Towards Industrial Applications: Membrane and Fluidized Bed Reactor, in: Pd-Membrane Technol. Scale-Up, 2015.

[25] Hysep, Hydrogen separation modules, (2016). http://www.hysep.com/fileadmin/hysep/user/documents/B-09 010_hysep_A4_wb.pdf.

[26] B. Dittmar, A. Behrens, N. Schödel, M. Rüttinger, T. Franco, G. Straczewski, R. Dittmeyer, Methane steam reforming operation and thermal stability of new porous metal supported tubular palladium composite membranes, Int. J. Hydrogen Energy. 38 (2013) 8759–8771. doi:10.1016/j.ijhydene.2013.05.030.

People say to me, "Are you looking for the ultimate laws of physics?" No I am not. I am just looking to find out more about the world. And if it turns out there is a simple ultimate law that explains everything so be it. That would be very nice to discover. If it turns out it's like an onion with millions of layers and we just sick and tired of looking at the layers then that's the way it is! But whatever way it comes out it's nature, it's there, and she's going to come out the way she is. And therefore when we go to investigate we shouldn't pre-decide what it is we are trying to do except to find out more about it.

Professor Richard Feynman

1908-1988, Theoretical Physicist

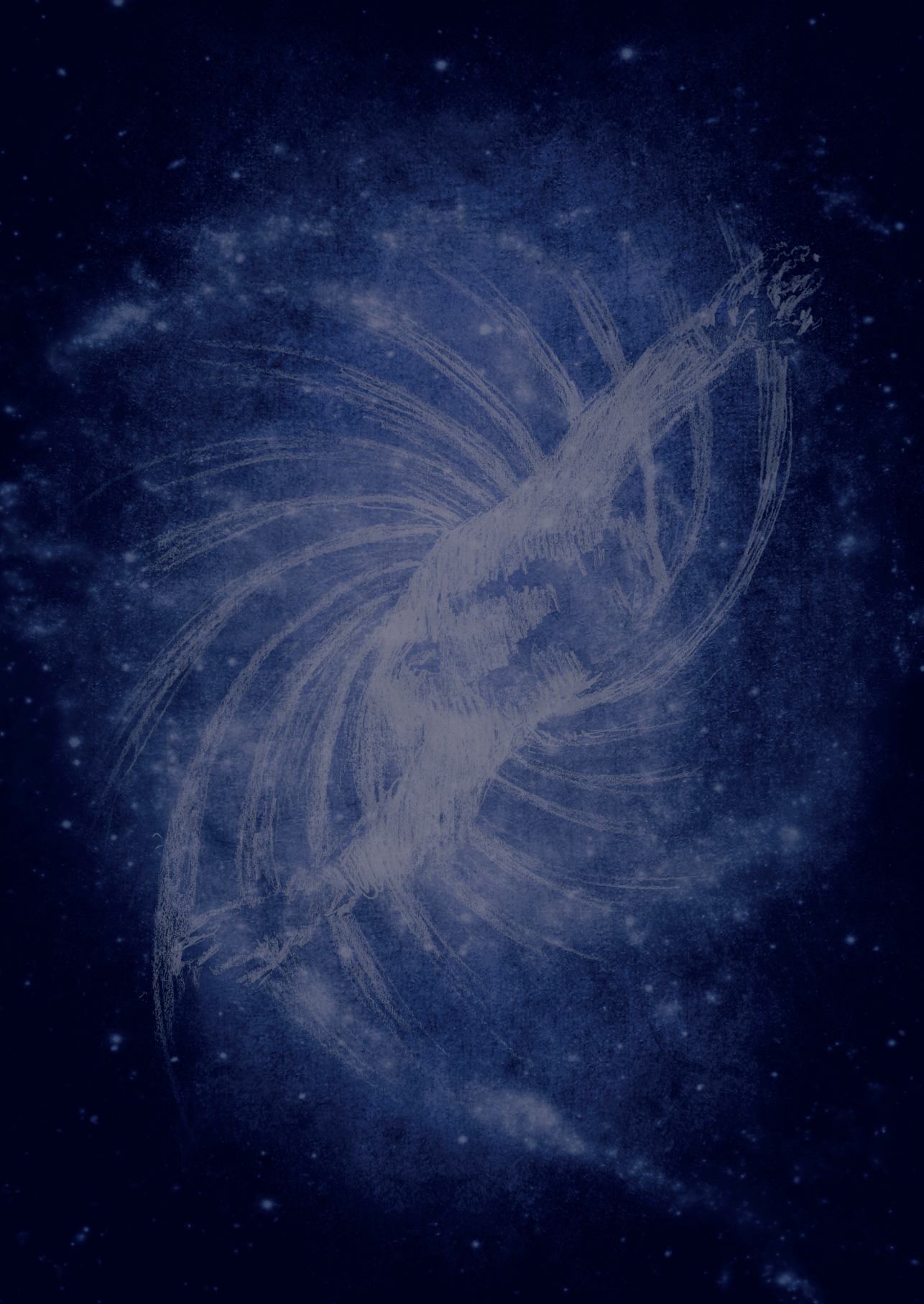

Chapter 8

Epilogue

8.1 Scope

Within last few years H_2 has attracted considerable attention as a promising future energy career. Highly pure H_2 can be produced from many different primary energy resouces and once is highly purified can be fed to PEM fuel cells and internal combustion engines with very high energy efficiencies and near zero greenhouse gas emissions. The conventional technology for H_2 production is optimised for large scales (>100 000 Nm^3/h) with a large carbon footprint. Downscaling of such process for smaller scales (5-250 Nm^3/h) is not economically viable and require innovations in the production methodology.

Fluidized bed membrane reactor technology is intended to overcome the limitations of the conventional H_2 production process providing high process efficiencies for on-site production of H_2 at small scales. This last chapter of the thesis contains an overview of the most significant findings on the application of Pd-based membranes in fluidized bed reactors for small scale ultra-pure H_2 production via water gas shift (WGS). A discussion will be provided on the potential impact of the current technology on the European economy and environment.

8.2 This thesis

It was shown that the large scale application of Pd membranes lead to a tremendous increase in the world supply of Pd to redirect the traditional IGCC power plants without CO_2 capture to the new membrane technology. Pre-combustion CO_2 capture using WGS membrane reactors with palladium membranes seems a non-practical option for relatively large-scale plants. On the other hand, smaller scales application of WGS membrane technology showed to be still very interesting, since it will not greatly influence the Pd market.

Electroless plating technique was successfully demonstrated for fabrication of thin Pd based membranes with very high and stable permeation rates (with outstanding perm-selectivities). It was shown that there may be chemical interaction between some bed materials and the membranes, which may result in strong decline in the membrane performance. Thus the reactor should be operated with catalyst/supports that have no interaction with the membrane(s).

Despite the promising gas-solid mixing inside fluidized bed reactors, the computed concentration profiles (from the models) near by a membrane with very high permeation rate, confirmed the existence of a concentration boundary layer in the vicinity of the membrane that imposes a mass transfer resistance from the bulk of the fluidized bed to the surface of the membranes. Although the bubble-to-emulsion phase mass transfer limitations were found to be less pronounced relative to the emulsion-to-membrane wall mass transfer resistances.

The X-ray analysis of bubbling fluidized bed reactors confirmed that the hydrodynamics of the reactor can be strongly improved when membrane modules (membranes/spacers) are immersed inside the bed. For Geldart B type of particles, positioning more spacers with

shorter membranes is advised to decrease the extent of slugging attributed to increased bubble breakage leading to enhanced mass transfer limitations between the bubble and emulsion phases. Thus membrane modules can be used not only to extract (and purify) gas from the reactor, but simultaneously to limit bubble growth along the reactor height. Similar analysis for Geldart A/B particles, confirmed that particles will form a layer near by the membranes at high gas extraction values (about 40% of the inlet flow) inducing an additional mass transfer resistance for gas components to reach the surface of the membranes.

Despite the positive role that membranes can perform to enhance the performance of the reactor, our endoscopic PIV/DIA results revealed that the degree of gas-solid mixing inside the bed may be decreased to a very large extent if no attention has being paid on the design features of the membrane module. A remarkable reduction in the equivalent bubble diameter in comparison with the case without membranes was found (up to 3.5 times) in comparison with the case without membrane modules. The obtained results once more demonstrated the potential of the membrane modules and the spacers to increase the overall reactor efficiency by enhancing the bubble-to-emulsion phase mass transfer rate.

In this research the long term (>900 h) performance of a fluidized bed membrane reactor with a capacity of 1 Nm^3/h was successfully demonstrated for production of ultra-pure H_2 for high temperature WGS. The membranes showed very high H_2 fluxes (3.89×10^{-6} $mol \cdot m^{-2} \cdot Pa^{-1} \cdot s^{-1}$ at 400 °C and 1 atm pressure difference) with a H_2/N_2 ideal perm-selectivity (up to 21,000 when integrating five membranes in the module) beyond the DOE 2015 targets. We obtained a high H_2 recovery factors, and very low CO concentrations at the permeate side (in average <10 ppm), so that the produced H_2 can be directly fed to a low temperature PEM fuel cell. These results are promising and once more proof the potential of the current technology for small scale production of H_2 with very high purity suitable for many industrial sectors.

8.3 Outlook

Considering the scarcity of Pd metal in nature, recyclability and reusability of the Pd-based membranes should be considered as an important option to avoid increase in the market prices. Recently Li et al. [1] demonstrated that not only the Pd metal can be recycled via a treatment with HNO_3 and HCl-H_2O_2 agents, but also the membranes support (e.g. porous Al_2O_3 tubes) can be reused for preparation of new batch of membranes. This might be an important step to solve the key limitation of the large scale application of Pd based membranes. More research needs to be performed for full commercial demonstration of the recycling process.

Also to improve the durability and stability of the membranes especially at fluidization conditions and to reduce the interaction between membranes and catalyst particles, novel ‘’pore-fill’’ Pd-based membranes can be considered as a promising option. This can

be achieved by filling Pd into the nano-pores of the porous support layer utilisng a vacuum-assisted electroless plating technique [2]. Therefore, the selective Pd layer will not be exposed to the fluidizing particles leading to minimum interaction between the particles and the Pd selective layer. Typically these membranes show much lower perm selectivities in comparison with the Pd based membranes fabricated in this work via electroless plating technique. To obtain an ultra-pure H_2 stream more attention has to be paid to improve the selectivity of such membranes.

In the modeling part, the obtained results from the TFM should be validated using non-invasive techniques such an infra-red [3,4], with a special focus on the determination of densified layer thickness at different relative extraction values and mean particle sizes. In addition, ideally a closure correlation for gas-phase dispersion coefficient from bed-to-membrane has to be derived to precisely account for inside a fluidized bed membrane reactors and at the presence of densified zones. The obtained knowledge can be further used in the one-dimensional (1D) model for precise prediction the performance of the membranes at different operating conditions.

The obtained time-averaged results from the fast X-ray analysis can be further extended by performing the experiments in triggered mode and from at least three different angles. Results from these experiments can be used to reconstruct the bubbles size and rise velocity at different axial positions of the membrane reactor and different inlet gas velocities. More specifically, correlations can be derived accordingly which include the effect of membrane modules with various configurations and gas extraction values [5].

The X-ray tomography technique can be applied only at room temperature while the endoscopic PIV/DIA results can be used to consider the effect of temperature on the dynamics of the bed (initially both techniques should be compared at room temperature) at higher temperatures representing the actual operating condition inside the high temperature membrane reactor. It is expected that at higher temperatures (especially above 300 °C) the hydrodynamics of the bed strongly be influenced by change in inter-particles forces at elevated temperatures [6].

8.4 Expected impacts

In this thesis the potential application of Pd-based fluidized bed membrane reactor technology was demonstrated for ultra-pure H_2 production via WGS. The successful exploitation of the current technology will directly reduce the environmental footprint associated with the conventional H_2 production technology. The number of process steps will be reduced from four steps WGS to two steps (including the feedstock cleaning).

Due to in-situ separation of H_2 via the membranes, higher feedstock conversions with higher selectivity can be achieved. Therefore, lower fuel consumption at milder reactor oper-

ating conditions (lower temperatures) can be realized. As a result, a tremendous reduction in energy usage can be obtained. Also due to possible intrinsic CO_2 capture at the outlet of the reactor (CO_2 enrich stream), a large reduction in CO_2 emission can be present. In addition, due to milder operating condition of the reactor, a safer production process is guaranteed leading to reduction in process risks.

Bibliography

[1] Y. Li, W. Ding, X. Jin, J. Yu, X. Hu, Y. Huang, Toward extensive application of Pd/ceramic membranes for hydrogen separation: A case study on membrane recycling and reuse in the fabrication of new membranes, Int. J. Hydrogen Energy. 40 (2015) 3528–3537. doi:10.1016/j.ijhydene.2014.09.017.

[2] D.A. Pacheco Tanaka, M.A. Llosa Tanco, J. Okazaki, Y. Wakui, F. Mizukami, T.M. Suzuki, Preparation of "pore-fill" type Pd-YSZ-Al2O3 composite membrane supported on Al2O3 tube for hydrogen separation, J. Memb. Sci. 320 (2008) 436–441. doi:10.1016/j.memsci.2008.04.044.

[3] T.Y.N. Dang, T. Kolkman, F. Gallucci, M. van Sint Annaland, Development of a novel infrared technique for instantaneous, whole-field, non invasive gas concentration measurements in gas-solid fluidized beds, Chem. Eng. J. 219 (2013) 545–557. doi:10.1016/j.cej.2012.12.036.

[4] J.A. Medrano, N.C.A. de Nooijer, F. Gallucci, M. van Sint Annaland, Advancement of an infra-red technique for whole-field concentration measurements in fluidized beds, Sensors (Switzerland). 16 (2016). doi:10.3390/s16030300.

[5] S. Maurer, D. Gschwend, E.C. Wagner, T.J. Schildhauer, J. R. van Ommen, S.M.A. Biollaz, R.F. Mudde, Correlating bubble size and velocity distribution in bubbling fluidized bed based on X-ray tomography, Chem. Eng. J. 298 (2016) 17–25. doi:10.1016/j.cej.2016.02.012.

[6] I.C. Velarde, F. Gallucci, M. van Sint Annaland, Development of an endoscopic-laser PIV/DIA technique for high-temperature gas-solid fluidized beds, Chem. Eng. Sci. 143 (2016) 351–363. doi:10.1016/j.ces.2016.01.002.

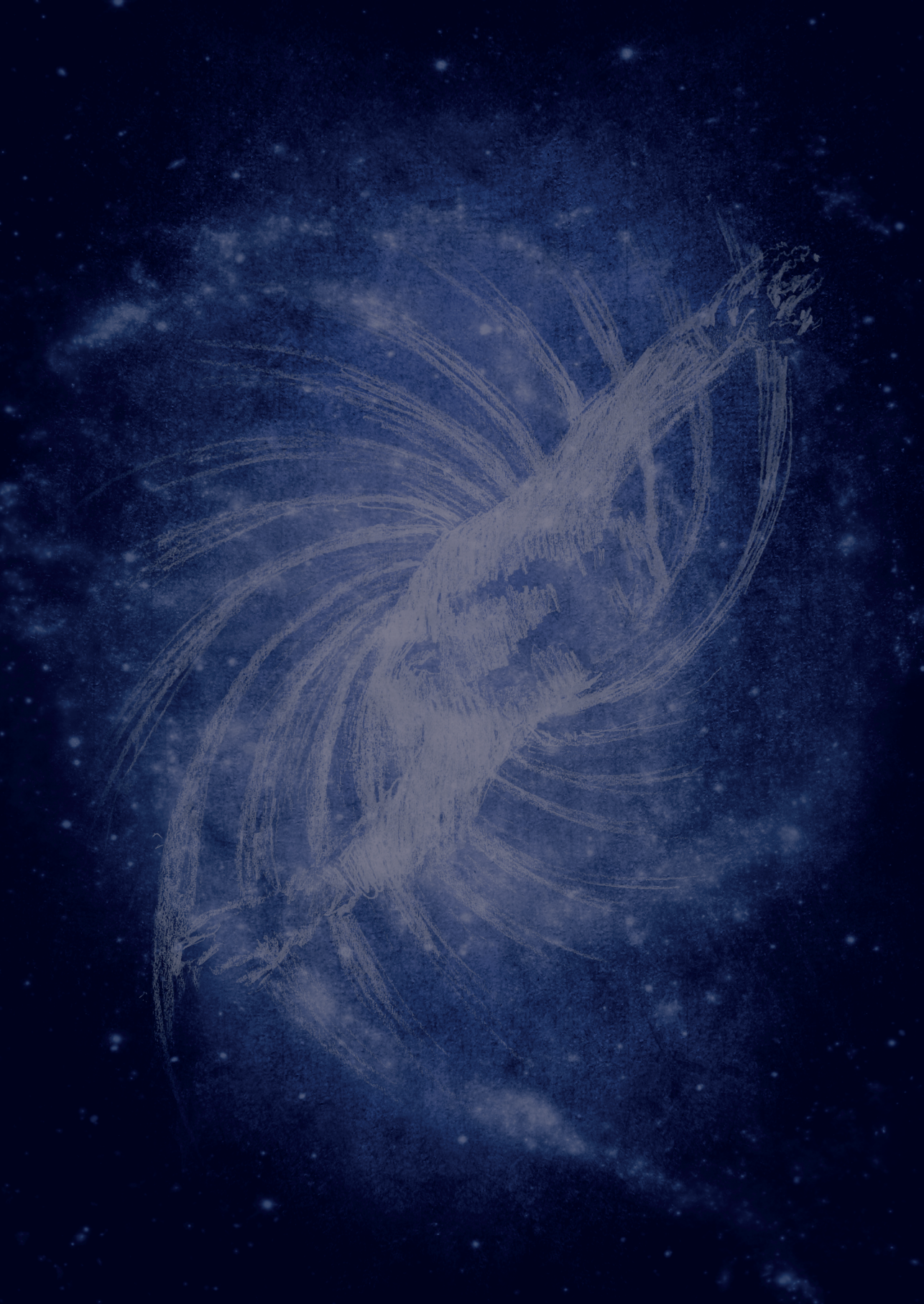

Biography

Arash Helmi was born on March 27th, 1984 in Mashhad, Iran. After obtaining his high school diploma in Mathematics and Physics, he was admitted to continue with his education at the distinguished BSc. Program in Chemical Engineering at Isfahan University of Technology, Isfahan, Iran. After successful completion of his BSc. degree with specialization in Petrochemical processes, he moved to Europe seeking for an international top level professional experience. In August 2008 he joined a master program in Resource Recovery at the University of Borås, Sweden and later in September 2009 he continued with his Master of Science degree in Innovative and Sustainable Chemical Engineering at Chalmers University of Technology, Gothenburg, Sweden.

The focus of his master thesis was on the development of a simulation methodology based on large eddy and volume of fluid simulations to study the breakup mechanism of fluid particles in turbulent flows. The research was performed under supervision of Prof. Bengt Andersson and Dr. Ronnie Andersson at the Chemical Reaction Engineering group. The output of the work was outstanding and results from the simulations agreed well with experimental high-speed measurement data. The obtained knowledge helps developing new, more physically sound models for the breakup phenomena required to solve scale separation problems in computational fluid dynamics simulations. Directly after completion of his master degree, he got employed as a research assistant at the same group to continue with his research topic funded by the Swedish research council.

In March 2012, he got an opportunity to pursue his Ph.D. in the Multiphase reactors group (Chemical Process Intensification, SPI) under supervision of Prof. Martin van Sint Annaland and Dr. Fausto Gallucci. Research was performed in collaboration with 9 top level European universities and research institutes together with representatives of top industries. Two membrane reactor technologies for ultra-pure H_2 production were studied in detail utilizing in-house validated numerical reactor models. Both reactors were demonstrated successfully at lab-scale. Detailed hydrodynamics and mass transfer studies inside fluidized bed mem-

brane reactors were performed, using particle image velocimetry, digital image analysis and X-ray tomography experimental techniques. Since May 2016, he has joined the SPI group as a post-doctoral research fellow under supervision of Dr. Ivo Roghair on hydrodynamics and heat transfer studies inside a fluidized bed dryer in collaboration with SABIC.

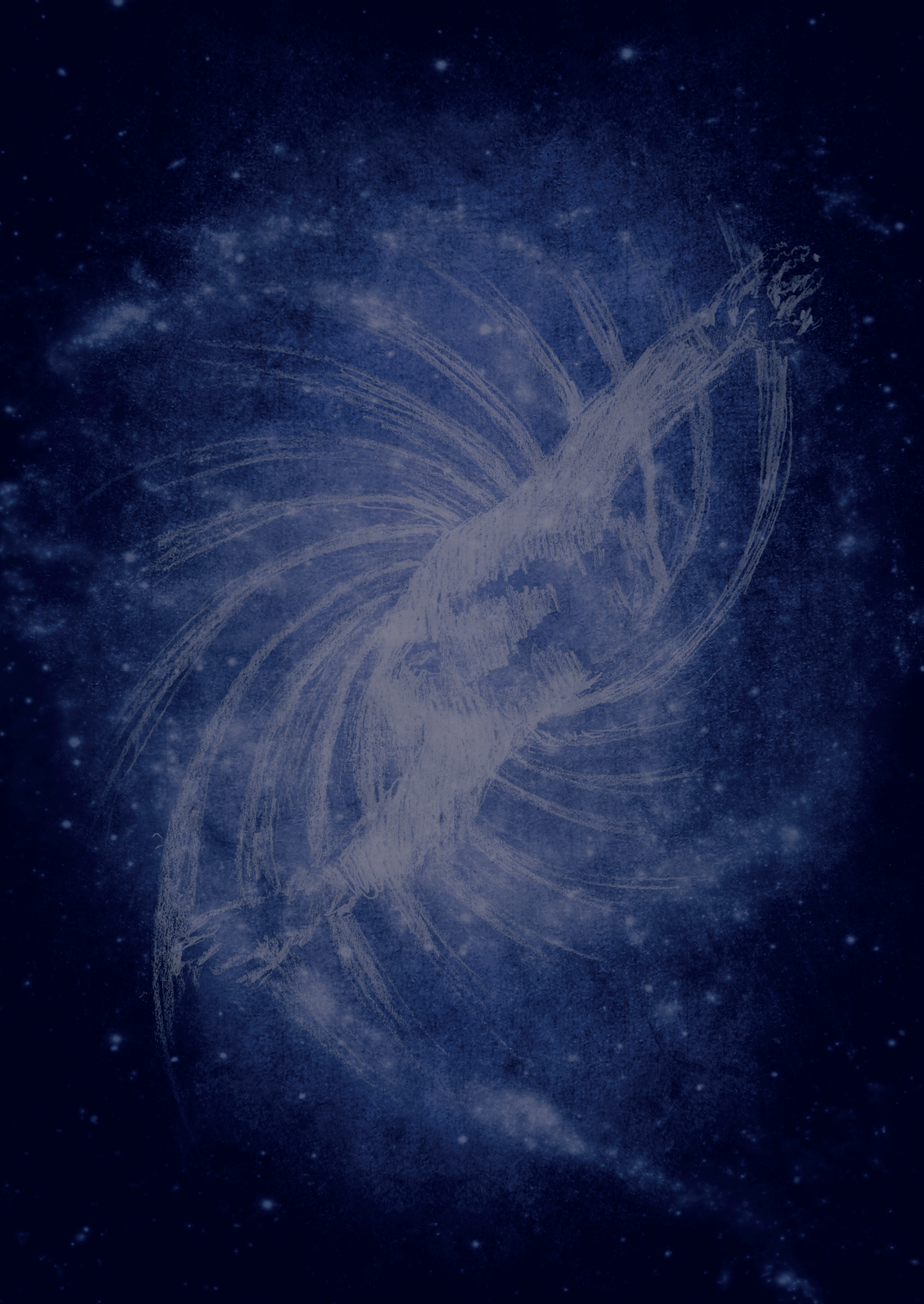

List of scientific publications

I. **Helmi, A.**, Gallucci, F., van Sint Annaland, M., Resource scarcity in palladium membrane applications for carbon capture in integrated gasification combined cycle units (2014) *International Journal of Hydrogen Energy*, 39 (20), pp. 10498-10506. DOI: 10.1016/j.ijhydene.2014.05.009

II. Fernandez, E., **Helmi, A.**, Coenen, K., Melendez, J., Viviente, J.L., Pacheco Tanaka, D.A., van Sint Annaland, M., Gallucci, F., Development of thin Pd-Ag supported membranes for fluidized bed membrane reactors including WGS related gases (2015) *International Journal of Hydrogen Energy*, 40 (8), pp. 3506-3519. DOI: 10.1016/j.ijhydene.2014.08.074

III. Fernandez, E., Coenen, K., **Helmi, A.**, Melendez, J., Zuñiga, J., Pacheco Tanaka, D.A., van Sint Annaland, M., Gallucci, F., Preparation and characterization of thin-film Pd-Ag supported membranes for high-temperature applications (2015) *International Journal of Hydrogen Energy*, 40 (39), pp. 13463-13478. DOI: 10.1016/j.ijhydene.2015.08.050

IV. Del Villar, V., Barrio, L., **Helmi, A.**, van Sint Annaland, M., Gallucci, F., Fierro, J.L.G., Navarro, R.M., Effect of Re addition on the WGS activity and stability of Pt/CeO_2-TiO_2 catalyst for membrane reactor applications (2016) *Catalysis Today*, 268, pp. 95-102. DOI: 10.1016/j.cattod.2015.11.013

V. **Helmi, A.**, Fernandez, E., Melendez, J., Pacheco Tanaka, D.A., Gallucci, F., van Sint Annaland, M., Fluidized bed membrane reactors for ultra-pure H_2 production - A step forward towards commercialization (2016) *Molecules*, 21 (3), art. no. 376, . DOI: 10.3390/molecules21030376

VI. Fernandez, E., **Helmi, A.**, Antonio Medrano J., Coenen K., Arratibel A., Melendez J., de Nooijer N., Spallina V., Viviente J.L., Zuñiga J., van Sint Annaland M., Pacheco Tanaka D.A., Gallucci F., Palladium based membranes and membrane reactors for hydrogen production and purification (*submitted to International Journal of Hydrogen energy)*

VII. **Helmi A.**, Voncken R., Raijmakers T., Roghair I., F. Gallucci, van Sint Annaland M., On concentration polarization in fluidized bed membrane reactors (*submitted to Chemical Engineering Journal)*

VIII. **Helmi A.**, Wagner E. C., Gallucci F., van Sint Annaland M. , van Ommen J. R., Mudde R. F., On the hydrodynamics of membrane assisted fluidized bed reactors - A 3D X-ray analysis (*submitted to Chemical Engineering & Processing: Process Intensification)*

IX. **Helmi A.**, Campos Velarde I., Gallucci F., van Sint Annaland M., Fluidized bed membrane reactors – hydrodynamics study with immersed tubular membranes (*submitted to Chemical Engineering Science)*

X. **Helmi A.**, van Meurs M., Gallucci F., van Sint Annaland M., On concentration polarization in packed bed membrane reactors *(will be submitted to Chemical Engineering Journal)*

XI. Gallucci F., Medrano J. A., **Helmi A.**, Spallina V., van Sint Annaland M., Chemical looping for hydrogen production and purification in "Membrane Engineering for the Treatment of Gases", 2nd Edition, Royal Society of Chemistry, Cambridge, UK (2017)

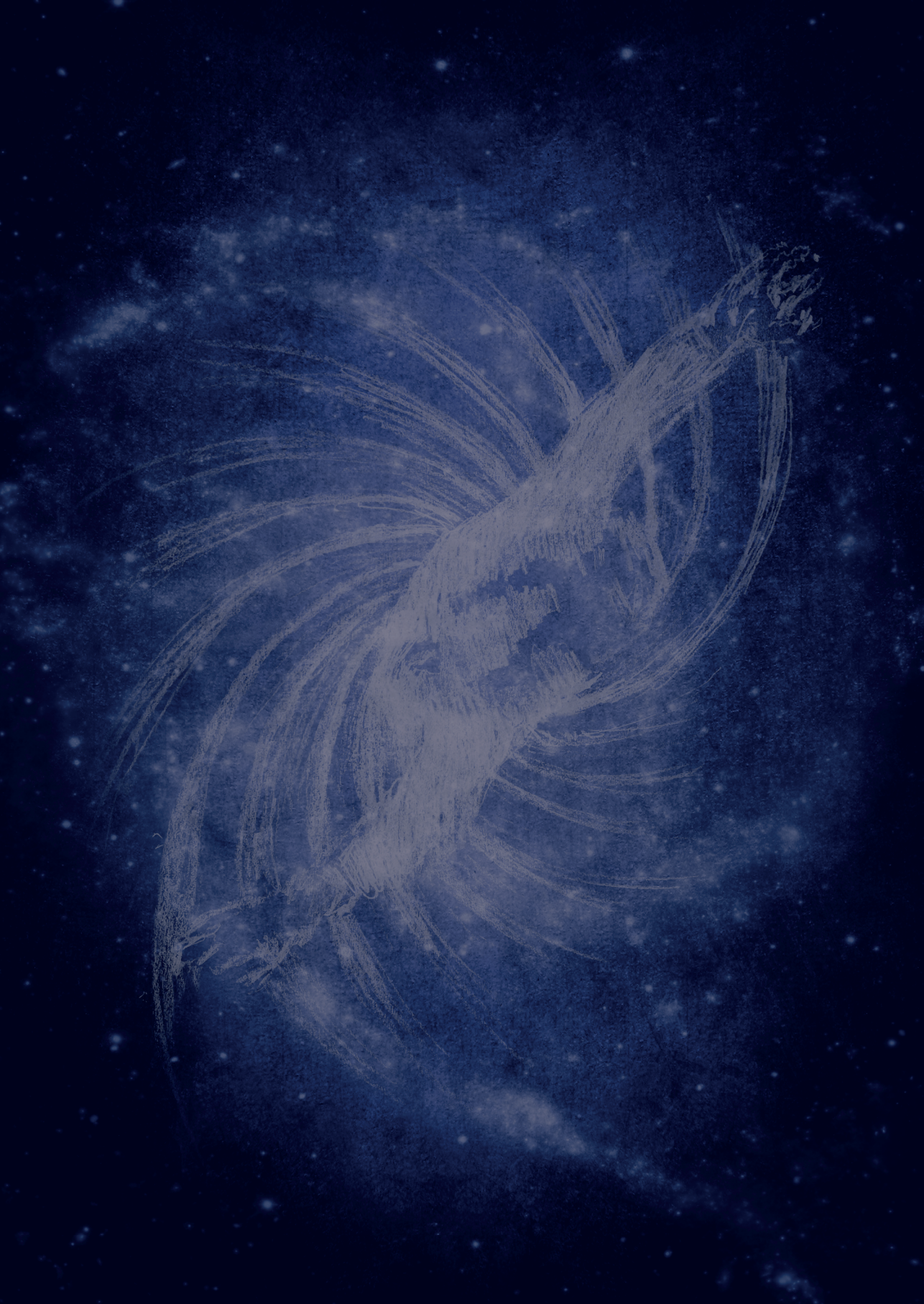

Acknowledgement

This section is specially dedicated to all the people who have directly or indirectly supported me and encouraged me to finalize this thesis. Without their contributions, this success wouldn't have been possible.

First of all, I would like to express my sincere gratitude to my promoter Prof. Martin van Sint Annaland for giving me the opportunity to do my doctoral research under his supervision. Over last few years we have had many meetings and discussions together on each part of the work. You were always prepared with many great ideas and very critical points on the very details of the work (as you always say: 'It's all in the details'). I am very thankful for all the freedom you gave me during the project to redefine our research questions and at the same time honored to have your support to peruse my research objectives.

Dr. Fausto Gallucci was my daily supervisor during my PhD work at the SPI group. It was my great pleasure working with you at all time and to have your insights on the project's goals and objectives. You were always ready with new proposals and practical ideas on how to finalize the open points. Also, we spent many nice moments together with other project partners during the consortium meetings in different countries. I would like to specially thank you and your family for the visit to your village in Calabria-Italy. Thanks for your memorable hospitality.

I did my PhD in the context of a European project (DEMCAMER) with many project partners from different disciplines and countries. Here I would like to thank all of them for the excellent collaboration, outstanding discussions and their technical support during the project. Together we achieved many milestones within the roadmap of the project.

I spent two weeks of my PhD work at TECNALIA research center in San Sebastian / Donostia, Spain. During this short visit, I practiced the fundamentals of Electroless plating technique for Pd-based membrane fabrication under supervision of Dr. David Alfredo Pacheco Tanaka. Thank you very much Alfredo for giving me a distinct view on the fabrication process of the Pd-based membranes. Also, during this period, many other people at TECNALIA did everything they possibly could to make me feel at home. Ekain and Ainara, Jon Zuñiga, Jon Melendez, Jose Luis, Alba, Alfredo and Margot: Milesker!

Also I spent few weeks of my PhD work at TU Delft to study the hydrodynamics of fluidized bed membrane reactors using a 3D X-ray analysis setup available at the Transport Phenomena group. During this time I had the honor and privilege of working with Prof. Rob Mudde and Prof. Ruud van Ommen. I am very thankful for your very critical view and very important feedbacks on post processing of the obtained experimental data. Also, to perform the experiments I had an excellent technical assistance form Evert Wagner. Thank you Evert for all the help and all the fruitful discussions during the very long days of experimental work.

For experimental work at TU/e, I would like to thank Joris Garenfeld , Joost Kors, Lee McAlpine, Thijs van Moll and Herbert Fiedler. Joris helped me to build the setup that was used for demonstration of the fluidized bed membrane reactor concept for water gas shift reaction. Many thanks for all your patience, clever ideas and all the nice talks. Joost, you

helped me a lot when I was very stressed to design and build the reactor for the X-ray tests at TU Delft. In addition, for the PIV/DIA analysis experiments, you put a lot of effort to seal the glass reactor enabling me to finalize the study. You were always fast and very skillful. Thank you very much for all the work.

During my work at the SPI group, I also supervised quite number of students and had close collaboration with some of my colleagues. Ramon Voncken, Frank van Wijk, Joel Silva, Roghelio Gonzalez Lua, Remco Fijneman, Kai Coenen, Caroline Supplis, Maarten van Meurs, Paulus Hamstra and Teun Raijmakers: Your contributions are the foundations of this doctoral research. I was very fortunate to work with you with different backgrounds, cultures and mindsets. I truly appreciate all your great efforts.

I would like to also thank all my colleagues at the SMR group for all the great moments that we spent together. Working at this group, gave me a unique opportunity to meet many people from all over the world with very diverse backgrounds and mindsets. I would like to express my special gratitude to some of you who I personally have spent more time with them.

Giulia, you were my closest and best friend during last years of work here at the group. Thanks for being next to me at all the very though and very good moments. In the last phase of my work, you truly helped me in my journey to recover from my illness and to finalize my thesis. Your presence means a lot to me since you are part of my family now.

Vincenzo, Maria Ortiz, Ildefonso and Luca: Thank you for being such amazing bodies. I am so blessed to have you in my life.

Lizzy, you showed me many times that I can count on you as a very true friend. You will always remain a very true friend of mine. Next to Lizzy, of course is Mariet. We shared many good moments all together at the office, you were always the great one who was initiating to have fun. Bedankt Blondie!

Marian and Michela: I could not be luckier to have you at the office. Thanks for making the office my second home and thanks for being supportive at all time. Your friendship is precious for me.

Paul, Maria Nordio, Jose and Elisa, Aitor, Alvaro and Maria, Maxim and Polly, Mohammad, Kay, Rhea, Judith, Martin Korevar, Abdel Ivan, Milan and Solomon: you were very special friends for me. You will remain special.

At the end I would like to thank my dear parents, family and relatives. Zohreh and Khosrow, Cina and Amanda, Saleh, Abas and Mohammad: I feel your love and support far from you, at all the moments of my life. My parents, Farokh and Ahmad: your presence is the most valuable gift in my life. I have you in my heart every second of my life. My sister and brothers, Toktam, Amin and Omid, and their beloved spouses and children: Ebrahim, Hanieh, Parsa, Pouya, Makan and Tania. Love you so much.

Yours truly,

Arash Helmi.

Eindhoven, March 2nd 2017